LASER DIRECT METAL DEPOSITION OF DISSIMILAR AND FUNCTIONALLY GRADED ALLOYS

A thesis submitted to

The University of Manchester

For the degree of

Doctor of Philosophy (PhD)

in the Faculty of Engineering and Physical Sciences

2011

KAMRAN SHAH

School of Mechanical, Aerospace and Civil Engineering

Table of Contents

Word Count: 45,165

List Of Figures

List of Tables

Abstract

Name of the University:	The University of Manchester
Submitted by:	Kamran Shah
Degree Title*:*	Doctor of Philosophy
Thesis Title:	Laser direct metal deposition of dissimilar and functionally graded alloys
Date:	01-03-2011

The challenges in the deposition of dissimilar materials are mainly related to the large differences in the physical and chemical properties of the deposited and substrate materials. These differences readily cause residual stresses and intermetallic phases. This has led to the development of functionally graded materials which exhibit spatial variation in composition. Laser direct metal deposition due to its flexibility, it offers wide variety of dissimilar and functionally graded materials deposition.

Despite considerable advances in process optimization, there is a rather limited understanding of the role of metallurgical factors in the laser deposition of dissimilar and functionally graded alloys. The aim of this work is to understand and explain mechanisms occurring in diode laser deposition of dissimilar materials and functionally graded materials. The first part of this work addressed diode laser deposition of Inconel 718 nickel alloy to Ti-6Al-4V titanium alloy. Here, the effect of laser pulse parameters and powder mass flow rates on the stress formation and cracking has evaluated by experiment and numerical techniques. Results showed that the clad thickness was an important factor affecting the cracking behaviour. In the second part of this study, an image analysis technique has been developed to measure the surface disturbance and the melt pool cross section size during laser direct metal deposition of Inconel 718 on a Ti-6Al-4V thin wall. It was noted that under tested conditions the overall melt pool area increased with the increase in powder flow rate; the powder carrier gas flow rates also seemed to play important roles in determining the melt pool size. In the third part of this study, a parametric study on the development of Inconel 718 and Stainless steel 316L continuously graded structure has been carried out. Results suggested that microstructure and other mechanical properties can be selectively controlled across the deposited wall.

The results presented in this dissertation can be used as a metallurgical basis for further development of dissimilar and functionally graded manufacturing using LDMD technique, guiding future manufacturing engineers to produce structurally sound and microstructurally desirable laser deposited samples.

Declaration

No portion of the work referred to in this thesis has been submitted in support of an application for another degree or qualification of this or any other university or other institution of learning.

Copyright Statement

I. The author of this thesis (including any appendices and/or schedules to this thesis) owns any copyright in it (the "Copyright") and he has given The University of Manchester the right to use such Copyright for any administrative, promotional, educational and/or teaching purposes.

II. Copies of this thesis, either in full or in extracts, may be made **only** in accordance with the regulations of the John Rylands University Library of Manchester. Details of these regulations may be obtained from the Librarian. This page must form part of any such copies made.

III. The ownership of any patents, designs, trademarks and any and all other intellectual property rights except for the Copyright (the "Intellectual Property Rights") and any reproductions of copyright works, for example graphs and tables ("Reproductions"), which may be described in this thesis, may not be owned by the author and may be owned by third parties. Such Intellectual Property Rights and Reproductions cannot and must not be made available for use without the prior written permission of the owner(s) of the relevant Intellectual Property rights and/or Reproductions.

IV. Further information on the conditions under which disclosure, publication and commercialisation of this thesis, the Copyright and any Intellectual Property and/or Reproductions described in it may take place is available in the University IP Policy (see http://www.campus.manchester.ac.uk/medialibrary/policies/intellectualproperty.pdf), in any relevant Thesis restriction declarations deposited in the University Library, The University Library's regulations (see http://www.manchester.ac.uk/library/aboutus/regulations) and in The University's policy on presentation of Theses.

List of publications

Journal Paper

- Shah, K., J.P. Andrew, A. Salman, and L. Li, 2010. Effects of Melt pool Variables and Process Parameters in Laser Direct Metal Deposition of Aerospace Alloys. Journal of Materials and Manufacturing processes. 25(12): p. 1372-1380.

Conference Papers

- Shah, K., A. Salman, A.J. Pinkerton, and L. Li, 2009. The significance of melt pool variables in laser direct deposition of functionally graded aerospace alloys. Orlando, FL, United states: Proceedings of 28th Int, Congress on Applications of Laser and Electro-Optics, ICALEO pp CD (1304).
- Shah, K., A. Pinkerton, R. Moat, L. Li, and M. Preuss, 2008. Direct diode laser deposition of functionally graded Ti-6Al-4V and Inconel 718 components. Proceedings of the 3rd Pacific International Conference on Application of Lasers and Optics pp CD (504) Beijing, China.
- Pinkerton A, Kamara A M, Shah K, Safdar S, L Li, 2008. Three dimensional analytical and finite element methods for simulating a moving melt pool with mass addition. Proceedings of the 3rd Pacific International Conference on Applications of Lasers and Optics. pp CD (806) Beijing, China.
- Pinkerton, A.J., R. Moat, K. Shah, L. Li, M. Preuss, and P.J. Withers, 2007. A verified model of laser direct metal deposition using an analytical enthalpy balance method. Orlando, FL, United states: 26th International Congress on Applications of Lasers and Electro-optics (ICALEO).

DEDICATION

First and foremost, I am extremely thankful to ALLAH that He gave me a chance and patience to carry out this work.
First, I would like to express my sincere gratitude to my dad for his support and guidance throughout my life that enabled me to reach at this stage. I am thankful to my mother for her prayers and to my uncle Dr. Inayat Ali Shah for his encouragement and support through thick and thin. Special thanks to my grand-parents for their never ending support and prayers. I want to thank my wife for her profound love, understanding, and patience during the passage of this work. Finally and most importantly, I would like to express deep love for my daughter Hibba, whose smile always brought so much joy to me and enabled me to forget all the pressures and maintain a positive perspective.

Acknowledgements

I would like to take this opportunity to thank all those who were involved with this project directly or indirectly and who helped me to successfully complete this work. I specially wish to express my deep gratitude to my supervisors, Professor Lin Li and Dr. Andrew Pinkerton for their sterling support, consistent help, invaluable guidance and excellent advice and supervision throughout this project. I would also like to thank Dr.M.A. Sheikh for his input and excellent advice on my work. I would also take this opportunity to thank all my friends and colleagues, especially in Laser Processing Research Centre and in The University of Manchester in general, with whom I spend a memorable time and remain involve in social and technical discussions (Dr. Usman Wajid, Dr. Mohammad Ali, Dr. Yasir Farooq, Dr. Rizwan Saeed Chaudry, Dr. Salman Nisar, Dr. Sohaib Zia Khan, Sohel Vhora, Ashfaq Khan, Naveed Ahsan, Khalid Mehmood and all others who become friends during my stay in Manchester). I wish them success in their lives.

NOMENCLATURE

AVI	Audio Video Interleave
B	Brightness of the beam ($W/m^2\ sr$)
c	Velocity of light (2.998×108 $m.s^{-1}$)
C_p	Specific heat ($J/kg{\cdot}K$)
d_w	Beam waist diameter(m)
d	Grain size (μm)
d_t	Track diameter (mm)
d_ψ	d-spacing measured at tilt angle Ψ, ($\AA$)
d_n	Stress free d-spacing measured at Ψ=0 ($\AA$)
E	Young's Modulus (GPa)
fps	Frames per second
G	Thermal gradient (K/m)
h	Planck's Constant (6.626×10-34 $J.s^{-1}$)
λ	Wavelength of electromagnetic radiation
ν	Frequency of electromagnetic radiation
θ	Beam divergence angle
N_1 and N_2	Number of electrons at energy states 1 & 2
H	Surface hardness (HV)
k	Thermal conductivity of material (W/mK)
n	Rotating speed (rpm)
R	Solidification velocity (m/s)
SDAS	Secondary dendritic arm spacing (μm)
SWR	Specific wear rate ($m^3N^{-1}m^{-1}$)
w	Wear track width (m)
w_d	Wear track depth (m)
W	Wear rate (m^3m^{-1})
$\partial T/\partial t$	Solidification cooling rate (K/s)
α	Thermal diffusivity (m^2/s)
σ_ϕ	Stress in ϕ direction
v	Poisson's ratio
Ψ	Tilt angle ($degrees$)
ρ	Material density (kg/m^3)
σ_y	Yield stress (MPa)

ACRONYM

APDL	ANSYS parametric design language
BCC	Body centred cubic
BCT	Body-centred tetragonal
BSE	Back scattered electron
CTE	Coefficient of thermal expansion
CW	Continuous wave
CNC	Computer numerically controlled
CCD	Charge-coupled device
FEM	Finite element modelling
FCC	Face centred cubic
GA	Gas atomised
Laser	Light amplification by stimulated emission of radiations
LDMD	Laser direct metal deposition
Nd:YAG	Neodymium-doped yttrium aluminium garnet
PW	Pulsed wave
PID	Proportional–integral–derivative
PREP	Plasma rotation electrode preparation
SEM	Scanning electron microscope
TEM	Transverse electromagnetic mode
WA	Water atomised

Chapter 1. Introduction

1.1 Research Rationale

Rapid prototyping is the most common name given to the host of related technologies that are used to fabricate physical objects directly from CAD data sources. These methods are unique in that they add and bond materials in layers to form objects. Today's additive technologies offer advantages in many applications compared to classical subtractive fabrication methods such as milling or turning.

Laser Direct Metal Deposition (LDMD) is one of such techniques that employs laser for creating solid object in the form of layers. Because of its ability to form fully dense structures, considerable interest has been shown for its use in producing near net shape, fully functional components. A variety of materials can be used such as stainless steel, Inconel, copper, titanium and aluminium. Materials composition can be changed dynamically and continuously, leading to objects with certain properties which are not possible to achieve using classical fabrication methods. Direct laser deposition has been proven more successful than the conventional manufacturing methods due to its flexibility in various manufacturing modes.

Functionally graded materials (FGMs) are the class of materials, in which the composition or the microstructure are locally varied so that a controlled variation of the local material properties is achieved. Various fabrication techniques for functionally graded materials have been developed in past twenty years or so. The graded change of structure inside an object allows the imparting of different functional properties to certain parts of an object

accordingly to their functional role, significantly increasing a part's productivity and performance [4].

Powder metallurgy is the most common method to manufacture functionally graded materials [5]. However, owing to several limitations of powder metallurgy, use of the direct laser deposition process to manufacture functionally graded materials is increasing in industry [6].

1.2 Aims and Major Challenges

Due to the ever increasing applications of laser deposited materials, laser fabrication of dissimilar and graded structures have received more attention recently. However, due to the differences in physical and chemical properties between dissimilar materials, variety of challenges still exist for the development in LDMD of dissimilar and functionally graded structures. For instance, the creation of brittle intermetallic phases and the residual stresses in the final component are still not fully understood. Dimensional accuracy, stability and structural integrity of the finished components are of great importance in developing LDMD parts. Therefore, parameters such as surface morphology, mechanical properties, and residual stress become important.

The work reported in this dissertation aims to understand and explain the phenomena and mechanisms involved in LDMD of dissimilar and functionally graded alloys. Inconel 718 and Ti-6Al-4V have previously been functionally graded by a few researchers but they reported limited success. In this work, instead of grading these alloys, variety of process parameters have been tested to successfully deposit these dissimilar alloys.

Despite considerable progress in of laser direct metal deposition (LDMD) process optimisation, there is rather limited work reported on the effects of melt pool variables on the final deposit characteristics. Effects of process

parameters and melt-pool characteristics on the deposition of Inconel 718 powder on a Ti-6Al-4V thin wall has been carried out. Welding nickel and steel alloys often results in solidification cracking. To overcome this problem, a parametric study on the development of graded structure of Inconel 718 and Stainless Steel 316L has been carried out.

1.3 Objectives of project

The objectives of this research are summarised below:

- To investigate the effects of processing parameters and their interaction in the LDMD process
- To identify the feasibility of LDMD of functionally graded materials
- To model the thermal and mechanical behaviour of the LDMD process
- To develop a scientific understanding of this process, and use of this knowledge for further LDMD applications.
- To contribute to the development of functionally graded structures for various applications including aerospace and automotive industries.

1.4 Layout of the dissertation

This thesis addresses a number of technological and scientific aspects of the diode laser direct laser metal deposition process. Chapter 2 gives a brief review of the principles and operation of lasers and some of the important laser beam parameters. Chapter 3 begins with a detailed description of the physical phenomena of direct laser. Different types of direct laser deposition, process characteristics and effects of various parameters on the system have been detailed. Chapter 4 describes the materials, equipments and their underlying principles used throughout this project. Chapter 5 presents an experimental study for the deposition of Inconel 718 on Ti-6Al-4V substrate.

Detailed experimental procedure and results are included in this chapter. This is followed by the development of finite element model and its theory for laser direct metal deposition process of Inconel 718 on Ti-6Al-4V in Chapter 6. Chapter 7 presents an investigation of the effects of process parameters into melt pool stability during the laser direct metal deposition process. In Chapter 8 Ni-steel function gradation and its microstructural and mechanical properties have been explored. A general summary of the outcomes of the programme of work is then made in Chapter 9.

Chapter 2. LASER FUNDAMENTALS

2.1 Introduction

During the last few decades, laser material processing has shown a rapid development. The interaction of laser light with matter is in many ways like the interaction of normal light with matter. The difference between them is the fact that laser light can be much more intense and concentrated than the light from other sources. This property of laser light has made laser as viable and efficient alternative to other processes like cutting, drilling, welding, cladding and heat treating. In this chapter, fundamental principles of laser, laser material interaction and types of lasers used in the study will be discussed.

2.2 Principles of laser

Light is an energy source consisting of electromagnetic waves. The electromagnetic spectrum is divided into gamma-rays, X-rays, ultra violet, visible, infrared, microwave and radio with respect to the increasing magnitude of the wavelength. Figure 2.1 shows the electromagnetic spectrum and their respective wave length [7]. To selectively produce these individual wavelengths has created wide variety of applications depending upon its use.

A laser is a device that emits light by optical amplification based on the stimulated emission of photons. The word LASER is actually an acronym of "Light Amplification by Stimulated Emission of Radiation" and was first

demonstrated by Theodore Maiman of Hughes Research Laboratories in 1960 in California, U.S.A. [8].

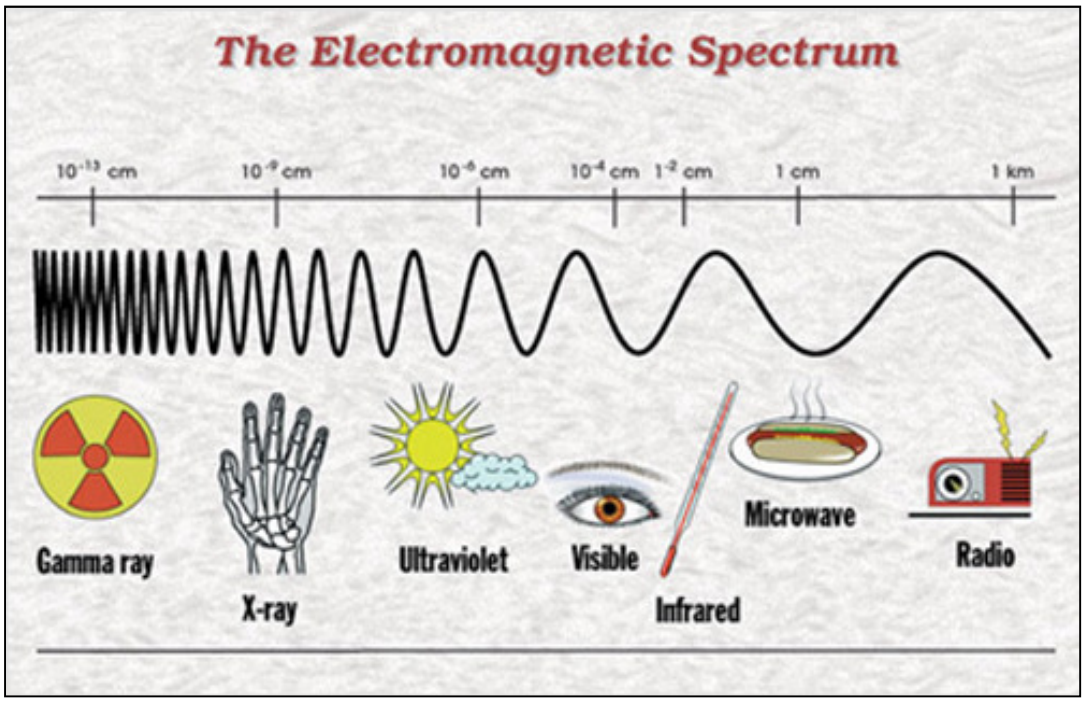

Figure 2.1: Schematic illustration of electromagnetic spectrum [7]

The underlying concept of working of laser can be understood from an example of a candle. Normally, a burning candle radiates light in all directions and therefore, illuminates objects around it. Obtaining a directed monochromatic light with single wavelength and frequency is literary the most efficient use of this power source. So, laser takes light that would normally be emitted in all directions, such as from a candle, and concentrates that light into a single direction [9]. Lasers generally have a narrower frequency distribution, or much higher intensity, as compared to other sources of light.

In order for a laser to function, a variety of necessary prerequisites must be in place. These working requirements include the presence of an active medium to support lasing, the accomplishment of stimulated emission and

amplification, the attainment of population inversion, a non-equilibrium pumping mechanism, and a resonant cavity.

2.3 Stimulation Emission and Amplification

To understand the laser mechanism, it is important to understand the principle of absorption and emission of light. For simplicity, if an atom is considered as having only two possible energy states, an upper state, E_2, and lower state, E_1, then if an atom in the upper state makes a transition to the lower state, then the energy of the electromagnetic radiation or photon emitted is given by [10]:

$$E' = E_2 - E_1 = \frac{hc}{\lambda} = h\nu \tag{2.1}$$

Where, "h" is Planck's constant (4.13566733×10^{-15} $eV.s$), "c" is the velocity of light (3×10^{8} m/s), "λ (μm)" is wavelength of electromagnetic radiation, and "ν" is frequency of electromagnetic radiation and E'(eV) is the energy of electromagnetic radiation.

Whilst the frequency of the emitted radiation "ν" is given by [11]:

$$\nu = \frac{E_2 - E_1}{h} = \frac{E'}{h} \tag{2.2}$$

Similarly, if an atom is initially in the lower energy state and makes a transition to the higher energy state, then the energy in the form of photons or electromagnetic radiation of frequency must be absorbed by the atom or the molecule as given in equation (2.2). Such energy level transitions of atoms from the lower energy states to the higher energy states can be achieved through the absorption of electromagnetic radiation with an energy level of, as shown in Figure 2.2(a).

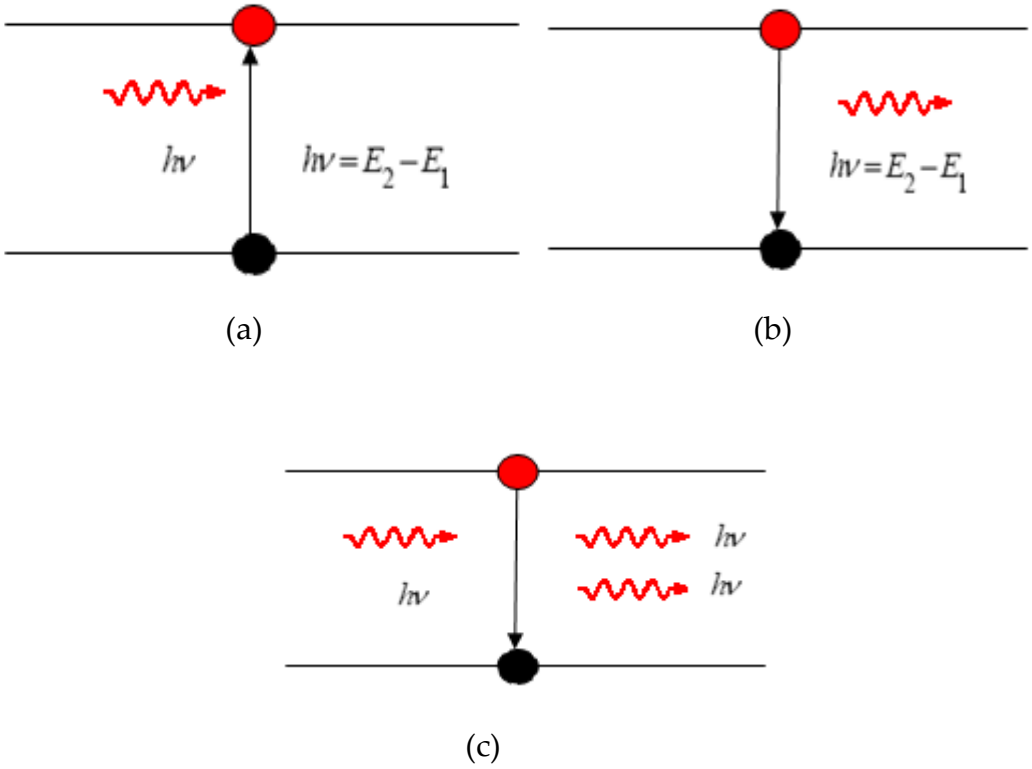

Figure 2.2: Schematic of the phenomena of electromagnetic radiation: (a) absorption, (b) spontaneous emission and (c) stimulated emission

According to Einstein [12], once in the excited state there are only two independent processes through which the excess energy may be emitted. Firstly, the excited atom will eventually decay spontaneously to the state of lower energy, E_1, emitting an electromagnetic wave (photon) with an energy of $E' = vh$ as shown in Figure 2.2(b). This process is known as spontaneous emission and inverse of the absorption process.

Secondly, the atom can be impelled to decay to lower energy level before its natural time by a photon having energy equal to E' interacting with the atom in the upper state and causing it to change to the lower state with the creation of a second photon as shown in Figure 2.2(c). These two photons not only have the same energy E' but also travel in the same direction with the same frequency and exactly in phase with each other. As such, the light wave representing the stimulated photon adds to the incident light wave on a constructive basis, thereby increasing its amplitude, and thus giving rise to

the possibility of Light Amplification by Stimulated Emission of Radiation – LASER.

2.4 Population Inversion and Laser Cavity

In reality the likelihood of a photon with energy of ΔE incident upon an atom in an upper energy level inducing stimulated emission or absorption are of equal probabilities. Thus, in a system containing a very large number of atoms, the dominant process will depend upon relative number of atoms in the upper and lower states. A large population of atoms in the upper state will result in stimulated emission dominating, while if there are more atoms in the lower state there will be a greater probability of absorption rather than stimulated emission.

Under normal conditions of thermal equilibrium, the population of atomic energy levels obey the Boltzman distribution. Therefore, for any two levels of energy E_1 and E_2 (assuming $E_2 > E_1$) and population N_1 and N_2 [13]:

$$\frac{N_2}{N_1} = \exp\left[\frac{-(E_2 - E_1)}{k_b T}\right] \tag{2.3}$$

Where, "k_b" (1.38×10^{-23} J/K)" is Boltzman's constant and T is temperature. For most metallic atoms, the first level above the lowest possible (the ground state) is separated by a gap of $1.25eV$ [13]. This amount of energy corresponds to that of a photon of visible light. Therefore under normal equilibrium conditions and at room temperature, the population of the excited state N_2 will be very small compared to the lower energy state N_1, according to Equation 2.3. For this reason, any photons of visible light are more likely to be absorbed rather than giving rise to stimulated emission. For stimulated emission to dominate, it is necessary to increase the population of

the upper energy level so that it is greater than that of the lower energy level. This situation is called population inversion.

To achieve a population inversion, the atoms within the laser medium must be excited or pumped into a non-equilibrium distribution through the application of a large amount of energy to the medium from an external source. There are a number of ways of pumping a collection of atoms into a higher energy level, these include; pumping by optical radiation, collisions induced by an electrical discharge, resonant energy transfer, plasma generation, passage of an electric current, electron bombardment and the release of chemical energy.

A laser works on the principle of light amplification by stimulated emission and it can only occur if emission takes place in an optical/laser cavity [14]. To achieve a continuous laser beam without constantly being dependent upon a spontaneous emission to initiate lasing, a laser (optical) cavity with feedback end mirrors is required. The basic components of optical cavity are tube containing gain medium (solid, liquid and gas) commonly known as a lasing material and two parallel mirrors. One of the mirrors being totally reflective and curved reflects almost all of the light that falls upon it (total reflector) and the other being either flat or curved and partially transitive to allow some of the oscillating power to emerge as the laser beam. Schematic of the whole laser generation process is shown in Figure 2.3.

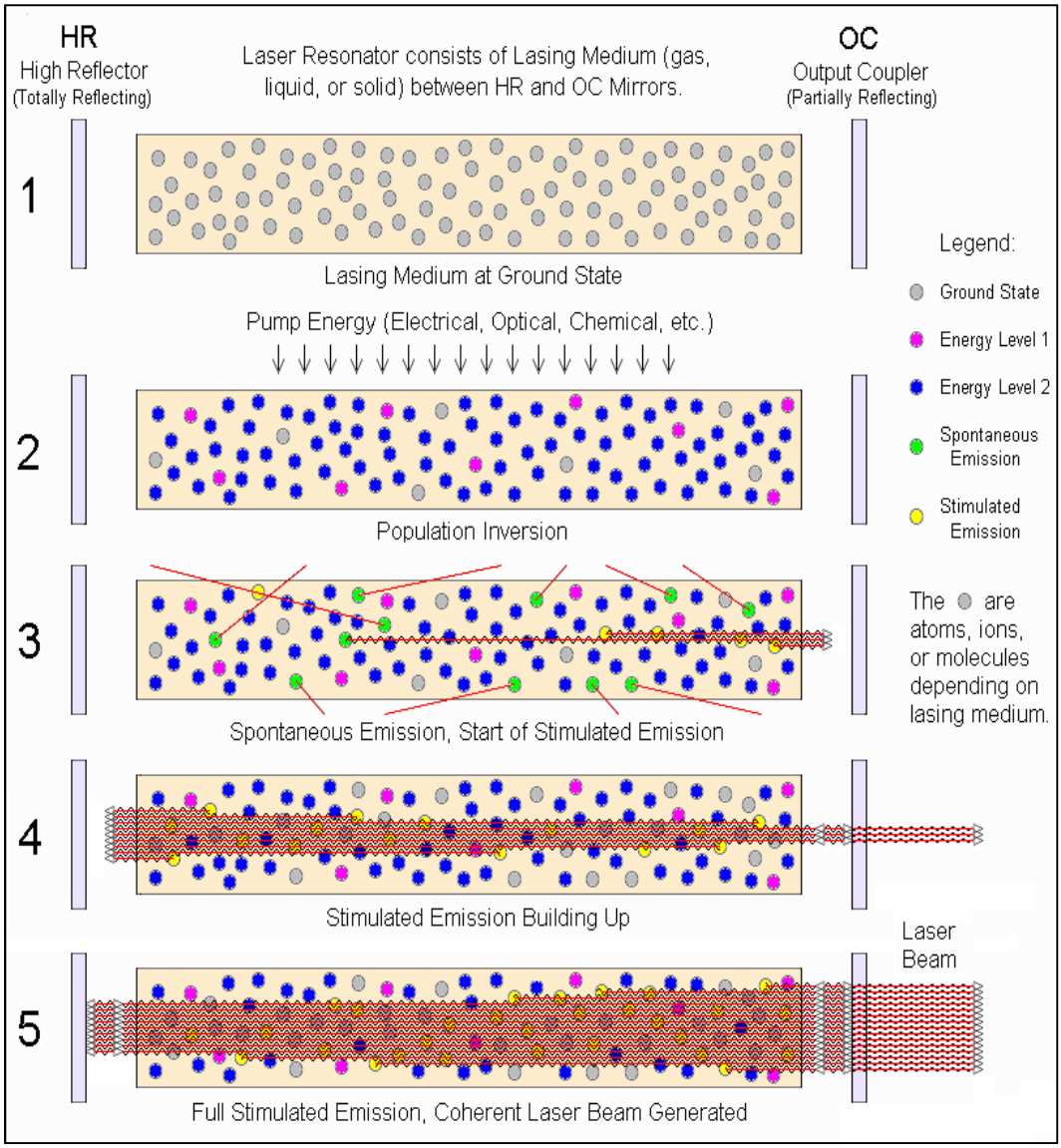

Figure 2.3: Basic Laser operation [7]

2.5 Laser configuration

Laser systems generally consist of a lasing medium, energy (pumping) source, resonators, cavity and a cooling system to work properly. As described earlier, energy (pumping) sources is used for excitation of lasing medium atoms [9]. Resonators are used for the feedback system to increase the stimulated emission. While typically two fine mirrors, one totally reflective and the other partially reflective are placed in the optical cavity to avoid escape of photons. Since, photon release elevates the medium

temperature and hence cooling is essential, thus a cooling system is used. Usually, water or chilled air is used as coolant.

2.6 Types of Lasers

Lasers are mainly classified based on the lasing material. There are many different types of lasers for material processing which may be classified by:

- Active medium (gas, liquid or solid and semi-conductor)
- Output power (*mW, W, kW*)
- Wavelength (infrared, visible and ultraviolet)
- Operating mode (Continuous wave (CW), pulsed or both)
- Application (macro-processing , micro and nano-machining)

The state of active medium determines the principal characteristics of a laser beam for laser material processing and commonly designates lasers [15]. The most commonly used lasers in material processing are CO_2, excimer and Nd: YAG lasers. A brief discussion on some of these lasers is given below.

2.6.1 Carbon Dioxide (CO_2) Laser

The amount of gaseous carbon dioxide (CO_2) as an active medium of commercial CO_2 lasers is in the range of 1 and 9%. The remaining part of the volume consists of helium (60-85%), nitrogen (13-35%) and small amounts of other gases. Design of the optical cavity, the gas flow rate and the output coupler are factors that are used for the exact composition of these gases. High gas purity is necessary, typically 99.995% for helium and nitrogen, and 99.990% for carbon dioxide [15]. CO_2 lasers emit an infrared invisible laser beam with a wavelength of 10.6 μm, with an efficiency of conversion of electrical energy into optical energy of 15%-30% and the beam power of up to 20 *kW*. The excitation of CO_2 lasers is normally through electrical methods either pure DC or high frequency AC.

Five basic configurations of the commercial CO_2 lasers are available: Sealed tube lasers, longitudinal flow lasers, transverse flow lasers, transversely excited atmospheric pressure (TEA) lasers and gas-dynamic lasers. These configurations of CO_2 laser designs are characterised on the factors like: composition of gas mixture (vol. %), gas flow rate (*m/s*), gas pressure (*mbar*), cooling (conduction or convection), and ergonomics (portable or fixed) [16]. CO_2 lasers are often used in Continuous Wave (CW) mode, but they may be pulsed by pulsing the electrical power supply. The beam quality of CO_2 laser is excellent at relatively low power, but as the output power increases, the beam divergence angle increases therefore limiting its desirability for material processing application with good focusing quality requirements. Another limitation of CO_2 lasers is that because of the wavelength the beam cannot be delivered by fibre optics.

2.6.2 Diode Lasers

Semiconductor lasers, also known as diode lasers, are based on the generation of photons when electrons in the conduction band of an appropriate semiconductor material recombine with holes in its valence band [15]. Diode lasers are based on semiconductor materials such as GaAs, GaAlAs or InGaAs and others [8]. Population inversion in the junction region occurs by providing an external voltage in forward bias [17]. When electrons in the conduction band recombine with the holes in the valence band above a certain current density threshold, spontaneous and stimulated emission occurs [18].

Normally, laser oscillation involves using two mirrors to form a cavity. In semiconductor lasers, this is achieved by cleaving two opposite facets of the semiconductor. Furthermore, since semiconductors have a very high index of refraction (about 3.6), the inherent reflectivity at the crystal–air interface is very high, about 35 %, making it unnecessary to use reflecting coatings [15].

The active region in the junction is confined to 1 ~ 5 μm so the emitted radiation is very low in power, equal to just a few *milliwatts*, and it also has a large divergence angle. Typically output of a single diode in a high power diode laser is 100mW. To increase the output power and intensity, the individual emitters are arranged in lines to form one or two-dimensional arrays, called bars. The output power of a bar depends upon the number of individual emitters in it and the power of the constituent emitters. The individual bars are then stacked on top of the others to form the laser diode stack as shown in Figure 2.4.

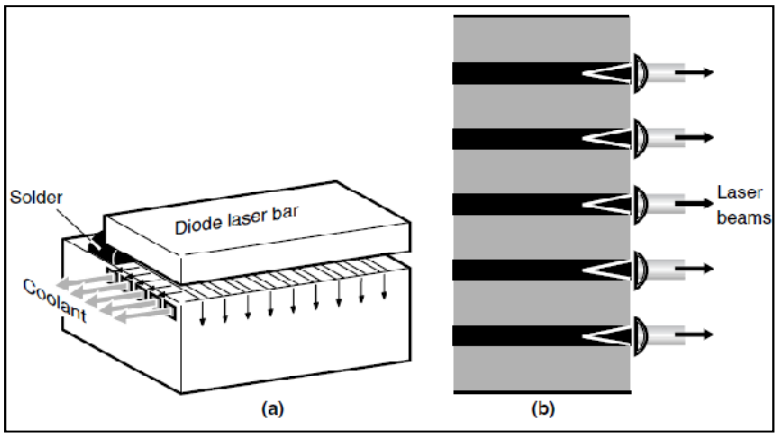

Figure 2.4: High-power diode laser construction. (a) Diode laser bar. (b) Stacked laser [16]

2.6.3 Excimer Laser

An excimer laser consists of a mixture of gases, a rare gas (1-9%), a halogen (0.05-0.3%) and an inert buffer gas (90-99%) as an active medium which is circulated at high velocity to maintain the desired composition. To maintain a stable beam mode, gas mixture is cooled in a heat exchanger and filtered. Electrical methods are normally used for the excitation of excimer lasers. In commercial excimer lasers, light is generated in the form of ultraviolet pulses, with a wavelength in the range of 0.15-0.35 μm. High speed electrical switch is normally used in excimer lasers to reduce the pulse length. The beam quality is relatively low (i.e. $M^2 \approx 100$) (see p-41for M^2) but can be

improved by using resonator optics, at the expense of a reduction in power. Light pulses generated by excimer lasers have energy in the range of *milli-joules to joules*, average power up to several hundred *watts*, peak power values up to 50 *MW*, repetition rates between 20 to 1000 *Hz* and pulse duration from few to a hundred *nanoseconds*. Ultraviolet light from the excimer lasers can be focused to a small spot size and used to process a wide range of materials, including metals, ceramics, and polymers [16].
Excimer lasers are useful in applications such as isotope separation where the ultraviolet output is very useful. XeCl excimer lasers have been used in laser-assisted chemical vapour deposition for semiconductor manufacture. Generally, excimer lasers are useful for removal processes such as photochemical reactions, or more specifically, photo-ablation, and are typically used for polymers, ceramics, and glass. In recent years, they have also been gaining increasing importance in materials processing [15].

2.6.4 Nd: YAG Laser

Solid-state lasers normally use an insulating crystal or glass as a host lattice in which the active medium is either doped or present as an impurity. The host crystal material has no direct participation in the lasing action. The dopant is the material which is directly responsible for the laser action. The host lattice for Nd: YAG is a crystal of yttrium aluminium garnet (YAG) with the chemical composition $Y_3Al_5O_{12}$, where the Nd^{3+} ions (about 0.1–2%) substitute for some of the Y^{3+} ions.
Light is generated through transitions between energy levels of the neodymium ions. The Nd: YAG laser is normally based on four level operations; a ground level, absorption bands, an upper laser level and a lower laser level. Flash lamps, arc lamps or semiconductor lasers are normally used for the excitation of Nd: YAG laser. The fundamental output wavelength is most commonly 1.064 μm, which is in the near infrared. The

active medium for lamp pumped excitation is normally in the form of Nd: YAG rod. These rods are typically 8-10 *mm* in diameter and up to 200 *mm* in length. A long rod produces low beam divergence while short rod possesses good mechanical stability. Similarly, rods with large diameter have high energy conversion efficiency while rods of small diameter have low beam divergence. The Nd: YAG laser is capable of transmission using a fibre optic cable, and can be used in either the pulsed or CW mode, with CW power levels up to 6 *kW*. In pulsed beam mode, pulse length of up to 10 *ms*, pulse repetition rates up to 50 *Hz* and pulse energy of about 150 *J* are obtained. The power level available from CW laser units can be used in welding application while short pulse duration and high peak power are suitable for drilling applications. Compared with CO_2 laser, the main disadvantages of the Nd: YAG laser are: limited output power, poorer beam quality and low wall plug efficiency i.e. 4%. However, the energy efficiency can be increased up to three times with diode pumped Nd:YAG laser [16].

2.7 Unique characteristics of Lasers

A laser beam possesses many distinctive characteristics that differentiate it from other sources of light. These distinctive characteristics/properties allow the laser beam to carry out various tasks that cannot be carried out using any other form of light [16].

2.7.1 Monochromaticity

A light beam is said to be monochromatic when it is composed of a single wavelength. Unlike conventional sources whose emission extends continuously over a broad band, distinguishing feature of lasers is its monochromaticity [15, 16]. This means that the laser light does not cover a wide range of frequencies as ordinary light does. Due to the monochromatic

property of laser beam, it can be more sharply focused than a beam of broad bandwidth.

2.7.2 Coherence

Waves that have a fixed- phase relationship over a long length of propagation or time are called coherent waves. Coherence phenomenon is both space (Spatial) and time (temporal) dependant. The term Spatial Coherence describes the constant phase relationship over a time between two points on a wave front of an electromagnetic field. While Temporal Coherence describes the constant phase relationship of any point "P" on a wave front at time "*T*" to be same at the same point "*P*" at time "*T*+*T*′′" [15].

2.7.3 Directionality

A conventional light source spreads out from the source in all directions equally. On the other hand, the directional nature of the laser beam allows the energy carried by it to be easily collected and focused to a small area [19] . A laser beam is very direct and can propagate over a long distance with little loss of beam intensity. Due to the low diffraction, laser beams have low divergence angles. This is the angle at which the beam spreads out as it leaves the laser invariably less than 10 *mrad*, typically in the order of 1 *mrad*. For a beam with wavelength of λ and beam waist diameter of d_w, the lower limit on beam divergence follows [19]:

$$\theta = \frac{2\lambda}{\pi d_w} \tag{2.4}$$

2.7.4 Brightness

One of the significant attributes of lasers is their high brightness (radiance). This quantity is defined as the power emitted per unit area per solid angle

for the light source. For a diffraction-limited beam with moderate divergence, the brightness of a laser beam is given by [20]:

$$B = \frac{P}{\pi w_o^{\,2}\theta^2} = \frac{P}{\pi w_o^{\,2}\left\{\frac{\lambda}{\pi w_o}\right\}^2} = \frac{P}{\lambda^2} \tag{2.5}$$

Where P is the laser power, w_o is the beam radius, θ is the beam divergence and λ is wavelength of the laser beam. This relationship shows that brightness depends upon power and wavelength of the laser beam.

Unlike the intensity of light (power per unit area) that can be increased by focusing, the brightness of a source is an invariant quantity, and cannot be altered by any lens or other optical system.

2.8 Important parameters for the selection of laser

The usefulness of lasers in materials processing and analysis is derived from the characteristics of laser light. Lasers are selected for a particular application based on some important parameters, which are briefly discussed below.

2.8.1 Wavelength

Industrial lasers can be divided into infrared, visible and ultraviolet lasers according to their output light wavelength. Wavelength affects the absorption, maximum resolution and focalization, the shorter the wavelength, the higher the resolution and better the focal property. Shorter wavelengths have higher photon energy [21].

The wavelength of the laser beam is not only dependent upon the energy level transitions that occur by stimulated emission but also on the lasing material, and the resonant wavelengths in the optical cavity. Although, the laser radiation is not entirely monochromatic, it has much narrower line

width at a considerably higher intensity than radiation obtained from most other sources. Frequently, the laser beam wavelength extends over one or more extremely narrow bands of wavelength corresponding to different laser transitions. Table 2.1 Output beam wavelengths for selected industrial lasers.

Table 2.1: Laser wavelengths and their applications [8, 21, 22]

Type of laser	Wavelength (μm)	Power	Applications
Carbon dioxide	10.6	1W-40KW	Material processing, medicine, isotope separation
Excimer	0.193- 0.3551	1KW-100MW	Micromachining, medicine, laser chemistry
He-Ne	0.632	1mW-1W	Holography, measurement
Argon Ion	0.515,0.458	1mw-150W	Medicine, printing technology
Nd:YAG	1.06	1W-3KW	Material processing, medicine, measurement
Diode	Infrared to visible	Up to 1.5KW	Material processing, pumping light source for solid-state lasers
Ruby	Red	Several MW	Measurement, pulse holography

2.8.2 Polarisation

As an electromagnetic wave, light consists of electric and magnetic fields that are oscillating orthogonally. In material processing, the electric field is more

important as it affects the amount of beam absorption by the material. Polarisation has a directional effect in machining due to reflectivity effects [8]. The angle of incidence is most commonly normal to the material surface. If the oscillation of electric field vector is perpendicular to the incidence plane it is known as *s*-polarised and if it lies in the plane of incidence it is considered as *p*-polarised. For other angles the electric field is configured by "*p*" and "*s*" components. A polarised beam can be achieved from an un-polarised beam by simply inserting suitable polarising optics into the laser beam path, but it results in the reduction in the intensity of light.

2.8.3 Laser beam modes

There are two spatial modes which are used to describe a laser beam. These are longitudinal and transverse modes. Longitudinal electromagnetic mode usually has very little influence on the beam performance and characteristics, while Transverse modes represent the beam intensity variation along a path perpendicular to the direction of propagation. They are of importance in laser material processing since they govern beam divergence, beam diameter, and energy distribution are governed by the transverse modes [23].

Electromagnetic field variations inside optical resonators are described by transverse electromagnetic modes as TEM_{mnq} where m is the number of radial zero fields, n is the number of angular zero fields, and q is the number of longitudinal fields. Usually, only the first two indices are used to specify a TEM mode where the first subscript indicates the number of rings and the second subscript indicates the number of bars across the pattern (see Figure 2.4). The higher the order of the mode the more difficult it is to focus the beam to a fine spot. The TEM_{00} (Gaussian) beam mode is usually the most desirable mode since, as compared to other modes; it can be focused to the smallest spot and has maximum intensity on the beam axis. The structure of

the TEM is affected by the geometry of the optical cavity, the alignment and spacing of internal cavity optics, propagation properties of active medium and the apertures in the optical cavity [24]. Various beam mode patterns are shown in Figure 2.5.

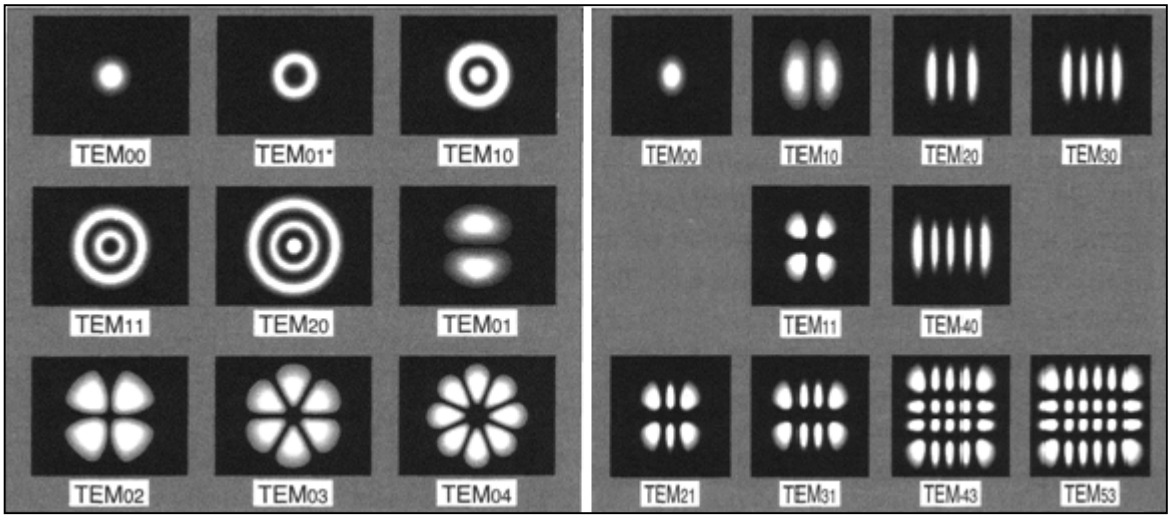

(a) (b)

Figure 2.5: TEM of beams with (a) circular symmetry and (b) rectangular symmetry [24]

2.8.4 Beam Waist

The beam waist is described as the location of minimum diameter of a laser beam. The laser beam starts to diverge after the beam waist. The location of the beam waist is dependent upon the characteristics of the optical cavity and its optics (i.e. length of optical cavity, radii of curvature of cavity optics etc). For flat mirrors in the optical cavity the beam waist is located at the mirror [23]. The beam waist cannot describe the beam radius accurately because it is dependent on the laser cavity and is independent of the beam mode.

2.8.5 Divergence

Divergence is the tendency of the beam to spread as it propagates from the laser. Low divergence is the property that enables a laser beam to retain high brightness over a long distance. Laser beam divergence is an important parameter as it can grow significantly over several metres inside the material and may affect the process mechanism The divergence θ of a Gaussian beam of wavelength λ, after it has passed through the beam waist of diameter d_b, is given by [23]:

$$\theta = \frac{2\lambda}{\pi d_b} \tag{2.6}$$

It means that larger beam waist diameter will exhibit smaller divergence.

2.8.6 Beam Quality

The beam quality is a measure of the focusability (spot size and focal length) of a laser beam. It shows that how closely a laser beam can be focused under certain conditions (e.g. with a limited beam divergence).A quantitative measure of the focusability or beam quality is M^2, which compares the divergence of the given beam with a pure Gaussian beam (i.e. M^2=1) with the same waist (i.e. minimum diameter of laser beam before any focusing optics) located at the same position [25]. For a TEM_{00} beam M^2 is given by:

$$\boldsymbol{M^2 = \frac{\pi d_b \Theta}{4\lambda}} \tag{2.7}$$

Where 'd_b' is the beam waist diameter, and 'Θ' is the full beam divergence angle. For a TEM_{00} (Gaussian) beam M^2 is 1. Therefore, a beam with M^2 value of 1.4 would have a focused waist diameter 40% larger than the Gaussian beam.

2.9 Summary

The invention of the LASER is a significant development in science and engineering. In order for a laser to function, a variety of necessary prerequisites must be in place. These working requirements include the presence of an active medium to support lasing, the accomplishment of stimulated emission and amplification, the attainment of population inversion, a non-equilibrium pumping mechanism, and in most lasers, a resonant cavity. In this chapter, the basic principles of laser operation, types and properties of laser have been discussed. Knowledge and understanding of these fundamentals is essential for carrying out any experimental work in laser materials processing.

Chapter 3. Laser Direct Metal Deposition

3.1 Introduction

In past few decades, there has been a rapid growth in the field of laser applications. A variety of laser processes have been introduced for different applications. Laser application has found great importance in industries like automotive, aerospace, bio medical and many others.

Among the applications of laser technology, the additive manufacturing technique also known as solid freeform fabrication has received significant attention in recent years. There are a wide range of commercial techniques including stereolithography, selective laser sintering, fused deposition modelling and 3D printing but only a small proportion can produce a full density metallic part like laser direct metal deposition. LDMD has a huge potential for material processing such as metallic coating, high value components repair, prototyping, and even low-volume manufacturing [26]. This chapter outlines the fundamental theory of laser direct metal deposition encompassing single layer cladding and multiple layer additive manufacturing. This chapter covers the Laser Direct Metal Deposition (LDMD) fundamentals as well as the applications.

3.2 Laser Direct Metal Deposition

Traditionally there are three methods for creating complex solid objects. They have been classified by Joseph *et al* [27] as follows,

a) Subtractive (material removal)

In this method a block or rod of material is taken and then the excess material is removed. E.g. turning, milling and grinding.

b) Shaping or forming

This technique is used to get the final shape by deformation. Examples are forging, extruding and molding.

c) **Additive**

Simple assemblies or subunits are joined together by a process like welding to create large assemblies or complex units.

With the advancement in technology, an alternative technique i.e. layered manufacturing (LM) has been developed and used for quite some time. Other terms used for layer manufacturing are rapid fabrication, solid free form fabrication, rapid prototyping and rapid manufacturing technologies. Layered manufacturing is not a totally new concept. Layered manufacturing has been in use (used in Egypt before 4000 B.C.) making pottery.

Laser Direct Metal Deposition (LDMD) is a technique that utilizes the concept of layered manufacturing to build 3D structures with the help of laser technology. The basic purpose of LDMD is to employ a laser to deposit a thin layer of any desired metal on top of another metal using a powder/wire mass delivery system to form a good interfacial bond with minimum dilution. Different deposition techniques exist apart from LDMD; for example Chemical Vapour Deposition (CVD), Plasma, Vacuum Furnace, Stereolithography, Fused Deposition Modelling, Solid Ground Curing, Laminated Object Manufacturing and TIG or Oxy-acetylene Flame. The particular advantage of the laser is its ability to heat and clad in specified areas alone [8]. So with this technique better coating, minimum dilution and less distortion of clad can be produced.

Varieties of names have been given to LDMD by several researchers and research groups. Mazumder *et al* [28] named their process as "direct metal deposition" which is based on laser cladding process with a feed back control system. Los Alamos National Laboratory in USA used the name

"directed light fabrication" [25, 26]. Laser Metal Deposition Shaping (LMDS)'' has been constructed and developed successfully by Chinese Academy of Sciences, Shenyang Institute of Automation [29].

Different manufacturers have commercialised these processes. Optomec has commercialised its research based on the LENS™ [30] while POM has been making their machines based on DMD technique [31].

In LDMD, a laser beam is directed onto the substrate that forms a melt pool due to absorbed power, and simultaneously build material (powdered metal) is delivered onto the melt pool by an inert gas that melts and forms a metallurgical bond with the substrate (see Fig. 3.1). The substrate is moved relative to the laser beam spot along a predetermined path, whilst powdered metal continues to be delivered onto the substrate. Due to the movement of the substrate, a trail of molten metal is formed which subsequently cools and solidifies. The predetermined path along which the substrate is moved is arranged such that the trail of solidified material builds a desired component through multiple layer depositions.

A typical LDMD system consists of a laser, a metal-powder delivery system, software and a computer-controlled multi-axis positioning system and stage. A solid model design of a desired component is first developed on a computer workstation using software like Pro/Engineer. The CAD model (data) is saved into a file and is sliced at a prescribed layer thickness and a motion path is produced for each layer. This path is translated to actual machine commands through a post-processor. The multi-axis positioning system controls the laser focal zone moving along the part cross-section defined by the part model and sliced layer thickness.

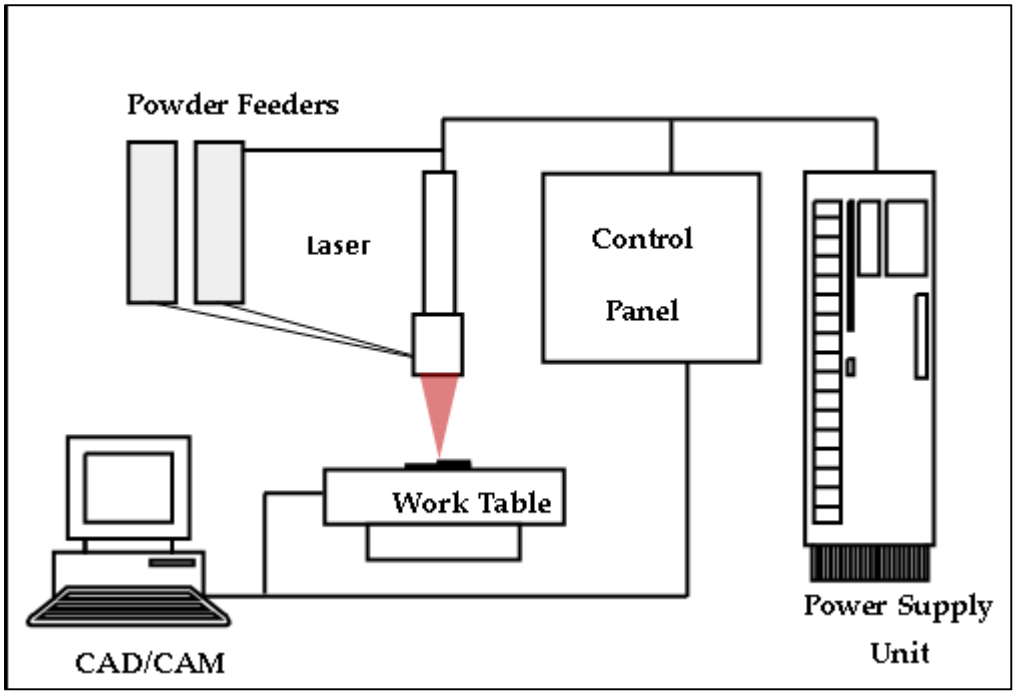

Figure 3.1: Schematic of a LDMD process

Laser Direct Metal Deposition (LDMD) is a very complex process and this is governed by different parameters including laser power, type of laser and its intensity and beam diameter, laser velocity, angle of the delivery nozzle, temperature of powder or wire. Similarly, the deposition process is affected by melting and solidification, melt circulation in the melt pool, the influence of shielding gas, surface tension gradients, thermal conduction and radiation effects and interaction time. Due to this complex nature of the process, it is difficult to obtain full understanding of all the parameter relationships and their effects on the deposition process.

3.3 Advantages and disadvantages of the LDMD process

One major challenge for all the manufacturers is the delivery of more economical, effective and better quality products. Therefore they must drastically reduce the time and costs to develop new products and introduce improvements to existing products and processes. As a consequence there is

a strong need to develop and implement new, flexible production processes, which have the potential to overcome the disadvantages of existing techniques in the design phase of product development as well as in the manufacturing and repair stages.

LDMD provides the manufacturers an ability to develop near net shape parts and also to employ this technique for repair purposes. This technique in combination with conventional manufacturing processes offers the possibility of advancement in current manufacturing cycles. The advantages can be summarised as:

- Localized heat input and consequently low distortion
- Minimum base metal dilution
- Near net shaped component built up
- Potential for automation
- Availability of a variety of materials

The current disadvantage is a rough surface finish and low dimensional accuracy acquired in LDMD parts. Typically LDMD parts must be polished or machine finished fitting required tolerances.

3.4 Types of lasers and materials used in Laser Direct Metal Deposition

CO_2 and Nd: YAG Lasers are most commonly used in LDMD process due to their extensive use in commercial systems like LENS^R, but the use of diode and fibre laser processing has been on the rise. LDMD process has been applied to a broad range of metals, intermetallic compounds and premixed combinations of materials. Those used or reported by some of the researchers are given in Table 3.1. Lasers and list of different types of materials is not exhaustive because of the large amount of work carried out

in the field of LDMD, but it intended to give readers a sense of the breadth of the field.

Table 3.1: Types of lasers and materials used in LDMD

Type of laser	Material	Investigated or reported by
CO_2	Hadfield Steel	Pelletier *et al* [32]
	StelliteX-40	Xiong *et al* [33]
	W-Ni	Zhong *et al* [34]
	H13	Choi, Han and Hua [35]
	WC-Co alloy	Yang and Man [36]
	Si	Fellowes, Steen and Saunders [37]
	Ti	Tan *et al* [38]
	316L	Tan *et al* [39]
	Cr3C2 + AISI316	Lin [40]
	Ni	Huang *et al* [41]
	Ti-50wt%Ni	Xu *et al* [42]
	Diamalloy 2002(nickel based alloy)	Davim, Oliveira and Cardoso [43]
	Ni20 alloy	Hua *et al* [44]
	Inconel718	Zhao *et al* [1]
	Ti alloy	Qu *et al* [45], Pashby *et al* [46]
	WC	Pantelis, Michaud and de Freitas [47]
	Ni, Ti, Si	Wang, Jiang and Liu [48]

	NiCrSiB alloy	Yang *et al* [49]
	Ni-Cr	de Damborenea, Vázquez, and Fernández [50]
	Ni base alloy	Hidouci *et al* [51]
	Co base alloy	Hidouci *et al* [51]
Nd YAG	Inconel625	Grujicic *et al* [52]
	Ti-6Al-4V	Kobryn, Moore and Semiatin [53]
	Ti-6Al-4V	Roberts *et al* [54]
	Co alloy	Lee [55]
	Stellite6	Wen *et al* [56]
	316L	Pinkerton and Li [57]
	H13	Foroozmehr, Lin and Kovacevic [58]
	316L	Yang [59]
	Co-Ti alloy	Alemohammad, Esmaeili and Toyserkani [60]
	Stainless Steel	Han, Phatak and Liou [61]
	WC-Co	Xiong, Smugeresky and Schoenung [62]
	NiCr based alloy	De Oliveira, Ocelik and De Hosson [63]
	Stellite	Doubenskaia, Bertrand and Smurov [64]
	NiCr alloy	De Oliveira, Ocelik and De Hosson [63]

	6H-SiC	Vreeling *et al* [65]
	Al-12Si	Anandkumar *et al* [66]
	SiC	Anandkumar *et al* [66]
	Hastelloy C	Sun and Brandt [67]
	Stellite21	Partes and Sepold [68]
Diode	316L	Pinkerton and Li [57]
	316L	Majumdar, Kumar and Li [69]
	SiC	Majumdar, Kumar and Li [69]
	H13	Zekovic, Dwivedi and Kovacevic [70]
	H13	Pinkerton, Wang and Li [71]
	316L	Syed, Pinkerton and Li [72]
	Cu 99%	Syed *et al* [73]
	316L	Syed, Pinkerton and Li[74]
	H13	Pinkerton, Wang and Li [71]
	Inconel625	Tuominen *et al* [75]
	Ti Alloy	Pashby *et al* [46]
Fibre	70% CrMo steel 20% Cu alloy 10% Ni	Furumoto *et al* [76]

3.5 Deposition methods

Deposition of the desired metal on the top of the substrate can be achieved by a number of methods. Some of the most popular methods are as follows:

1. Powder injection using inert carrier gas
2. Wire feed
3. Combined powder and wire feed
4. Preplaced powder and wire

3.5.1 Powder injection using inert carrier gas

In this method, powder is fed to the melt pool by using an inert gas. Inert gas flowing through the nozzle helps both in powder delivery and shielding the deposit from oxidation. Shielding strategy is a delicate balance between powder delivery without causing excessive disturbance at the melt pool and adequately driving away the ambient air. Argon is normally used, but the inert gas also protects the laser optics from damage.

A problem associated with this type of delivery method is that a significant proportion of powder which passes through the nozzle is not delivered to the melt pool and gets scattered off the substrate surface. This scattered un-melted powder does not contribute to building of the component. This scattered powder can be expensive, especially for applications using special alloys. Scattered powder can be collected and reused but there is always a risk of contamination. Apart from the above, another problem caused by the blown powder DLD technique is that un-melted or semi-melted powders can stick to the surface of a deposited track and cause the roughening of the component. A subsequent surface finishing process is thus normally required.

Two types of powder delivery nozzles are widely used in LDMD process; lateral and coaxial [77, 78]. Brief description of each nozzle is given below.

3.5.1.1 Lateral nozzle

This is the simplest way to carry powder to the melt pool created by the laser. In more advanced designs, there are two concentric nozzles. The central nozzle feeds the powder through carrier gas, while the outermost nozzle carries the shielding gas, which in addition focuses the powder stream when entering the melt pool [79]. In lateral nozzle, there is a directional effect on the clad bead shape and alignment of the powder stream with the melt pool is critical. Angle of inclination of nozzle plays an important role. Temperature distribution varies with the changed angle resulting in more attenuation of laser beam [80]. A view of lateral nozzle is shown in Figure 3.2.

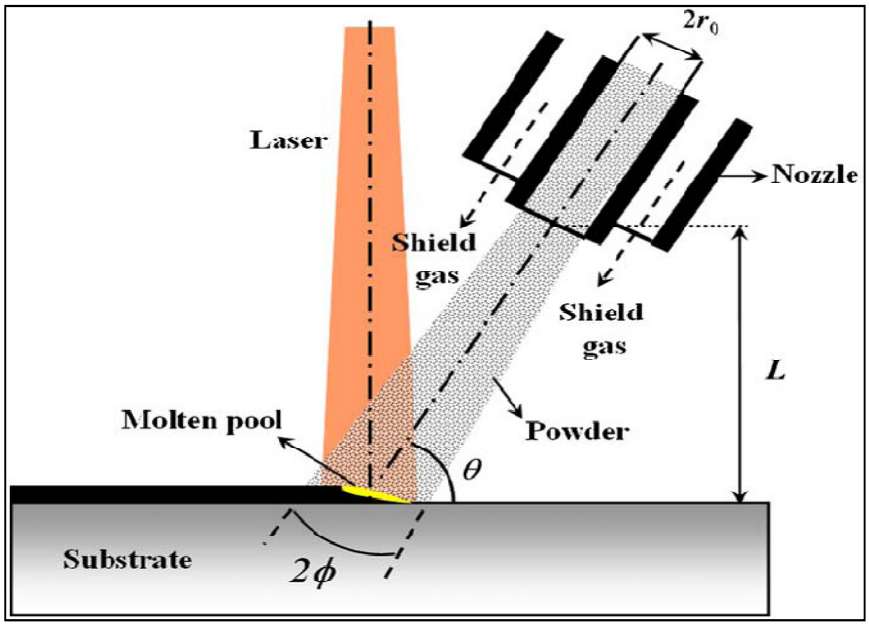

Figure 3.2: View of a lateral nozzle [38]

3.5.1.2 Coaxial nozzle

A coaxial powder nozzle provides metal powder from all radial directions. The advantage of the coaxial nozzle is its independence from the direction of motion. Lin [81] concluded from his experimental work that the powder

efficiency of the coaxial nozzle, which is the ratio between the deposited powder on the substrate and the delivered powder by the powder feeder in a specified period, is significantly less than that of the lateral nozzle. The catchment efficiency which is the ratio of powder deposited to the powder delivered is less than that of lateral nozzle. It can be increased with increase in surface tension of melt pool and by decreasing powder particle size and impact velocity [82]. In coaxial nozzle, the inclination angle does not affect powder stream thus allowing work in three dimensional space without any effect on the powder flow [83]. Pinkerton and Li [84] found in their work that the standoff distance between the nozzle and substrate, good layer consistency can be achieved without changing the standoff distance for 10*mm* high walls. Figure 3.3 gives a coaxial nozzle view.

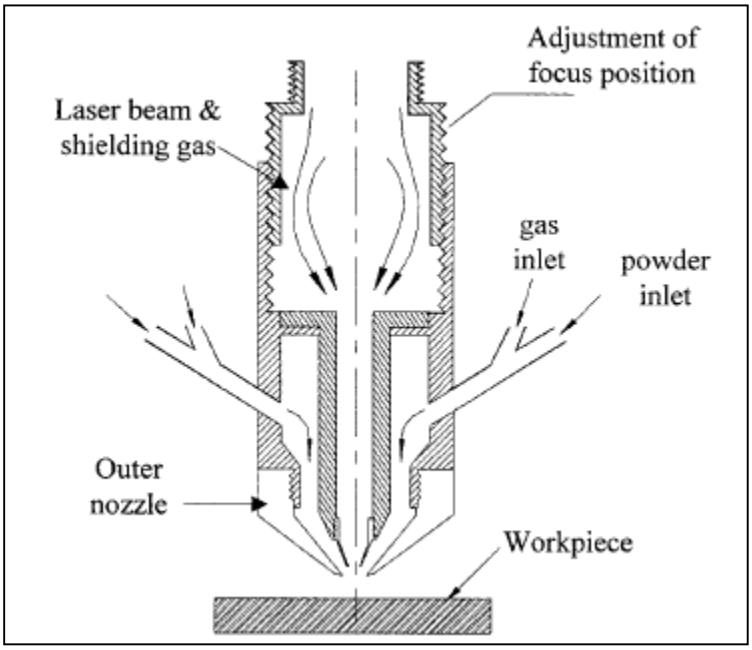

Figure 3.3: View of a coaxial nozzle [85]

3.5.2 Wire feeding

In the wire feed method, a metal wire is fed to the melt pool from the side of laser of the laser head. LDMD using wire rather than powder was first

proposed by Schneebeli *et al* [86]. More recently this approach has been exploited by various researchers using high power fibre and diode lasers [87, 88].

Wire feeding method appears to solve the wastage of powder as noticed in the blown powder delivery method. The surface finish of the final part is much better than the blown powder LDMD. The disadvantages of wire feeding are its feeding direction and the availability of the desired material in wire form.

Effects of wire feed direction were first studied in detail by Kim and Peng [89] that revealed the importance of wire feeding direction and position in a wire laser cladding process. It was found that wire-feeding is disturbed at low angles between the wire and the base material and wire cannot be completely melted by the laser beam if the wire feeding speed is high. Moreover non-symmetric tracks were observed when the wire feeding position was not exactly in the middle of melt pool. Front feeding was found to be better amongst all other directions that were tested during the experiment. Breinan and Kear [90] found that the satisfactory transfer occurred when the fed wire is adapted to an impingement angle of 30° and positioned to the exact edge of the molten pool. A later study by Nurminen *et al* [91] showed that heating the wire can increase the productivity by three times as compared to without heating or powder deposition method.

According to Syed *et al* [92], in case of front feeding, surface roughness of the clad increases with the increase in feeding angle. This is shown in the Figure 3.4.

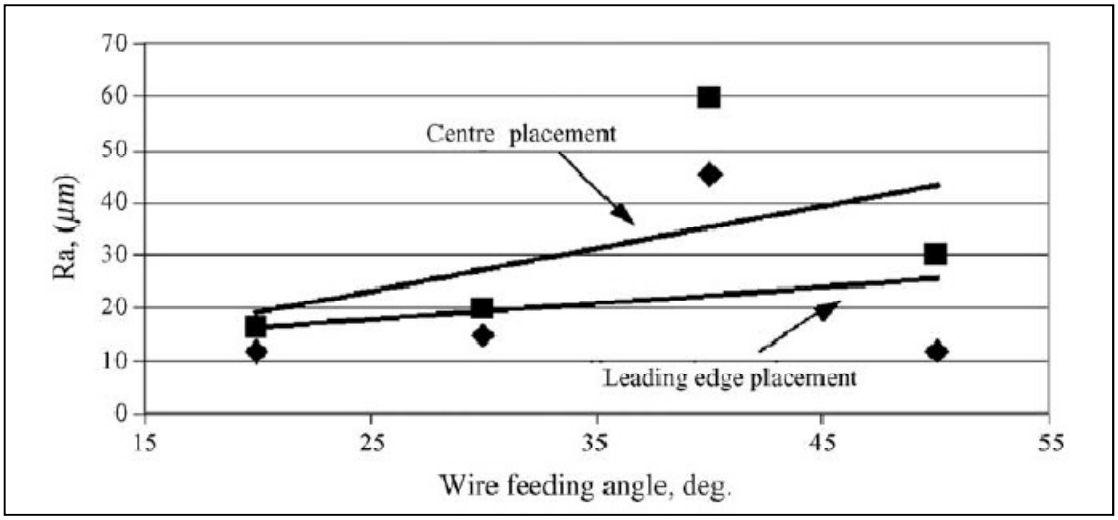

Figure 3.4: Surface roughness Ra vs. wire feeding angles for the wire placed at the leading edge and at the centre of the melt pool (front feeding) [92]

Positioning the wire at the leading edge of the melt pool in front feeding gave the best results in terms of surface finish which suggested that the melt pool was the least disturbed in this case.

Syed *et al* [92] also reported that in rear feeding, the surface roughness dependence on wire feeding angle was the opposite to that with front feeding. Surface roughness decreased by increasing the feeding angles, when the wire was placed in the centre and at the trailing edge of the melt pool. It is shown in the Figure 3.5.

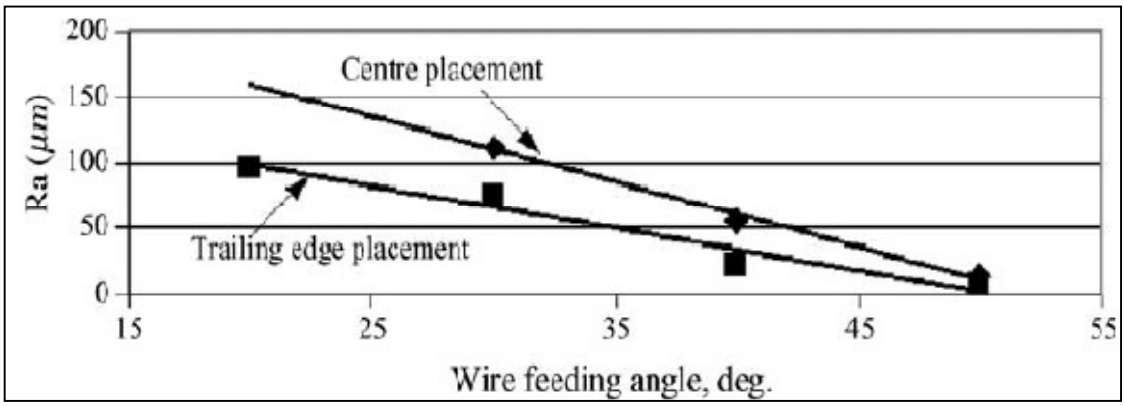

Figure 3.5: Surface roughness Ra vs. wire feeding angles for the wire placed at the centre and at the trailing edge of the melt pool (rear feeding) [92]

Sun *et al* [93] used the wire feeding technique for laser welding and investigated the mechanical and metallurgical characteristics of the weld pool. Kim *et al* [89] found out that with an increase in cladding time or decrease of the cladding speed, the dilution of clad layer increases. They also found out that an increase in cladding speed, the hardness of clad increases as shown in Figure 3.6.

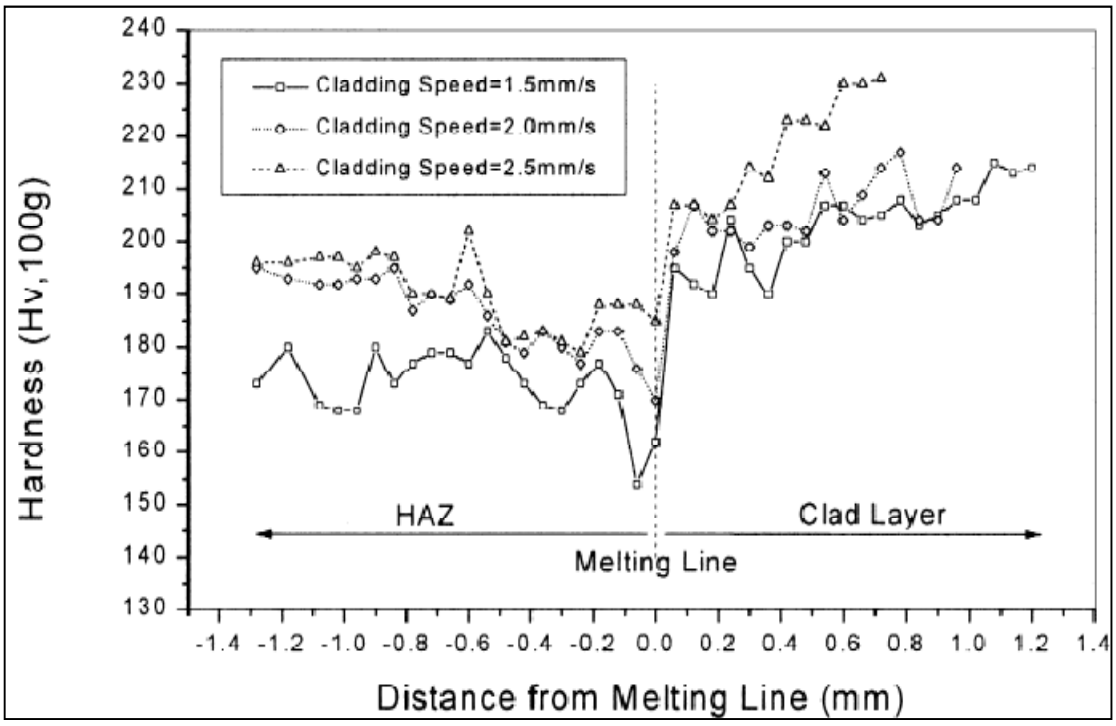

Figure 3.6: Hardness distribution of clad layer and HAZ [89]

Studies comparing wire feed with pneumatic powder delivery LDMD [94, 95] have highlighted the higher material efficiency achievable with wire (theoretically up to 100%), although energy efficiency is lower.
Cheap metal wires and less material wastage are generally regarded as advantages of wire feeding as compared to metal powders. In contrast, pool agitation, track perturbations, ripples or serrations and laser reflections are considered as the potential problems wire feeding method [96]. In addition,

specialist equipments are required to prevent wire bending and to deliver it to the melt pool.

3.5.3 Combined wire and powder feed

The combined wire and powder method utilises both wire and powder for the deposition of layers on the substrate. Wire and powder are simultaneously injected from the lateral and coaxial nozzles into a laser generated melt pool. In another study Syed *et al* [74] utilized this idea of combining two separate processes of powder and wire to produce multilayer parts. They concluded that the energy absorbed by the melt pool increases compared to having wire or powder deposition process only. They noted the increased deposition efficiency of the process and improvement of the surface finish in the deposited parts. Figure 3.7 shows a schematic view of combined wire and powder metal deposition.

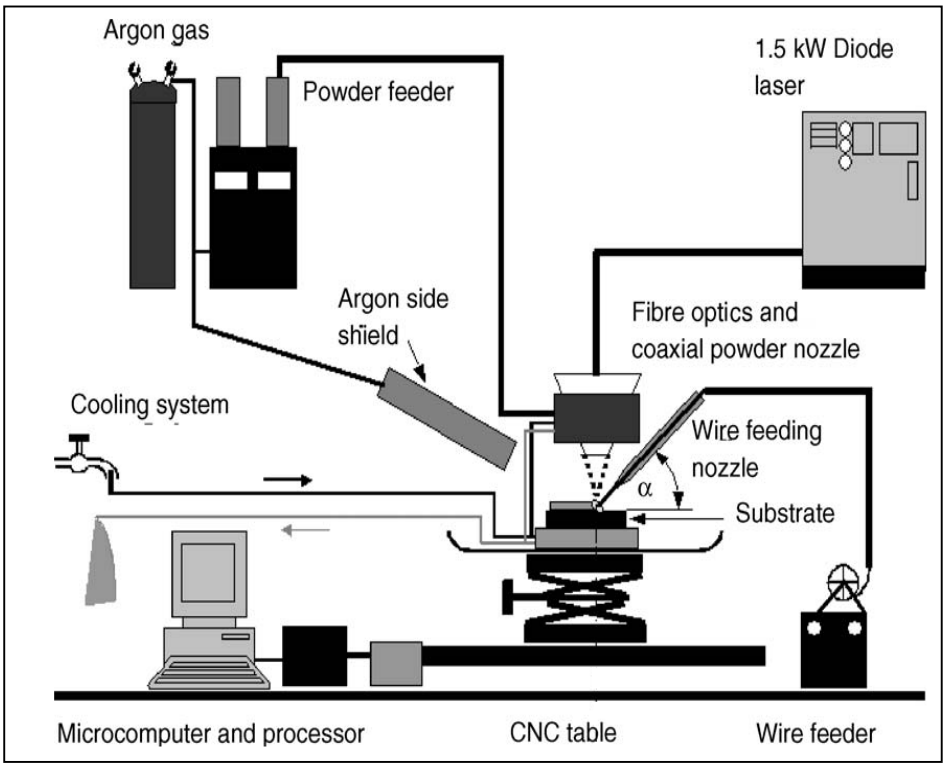

Figure 3.7: A schematic view of combined wire and powder metal deposition [74]

3.5.4 Pre-placed powder and wire

This method is simple compared to mass delivery through an inert gas carrier. Powder is placed on a surface and a defocused laser is scanned across the powder. Laser power is easily transmitted through the powder and therefore melts both the surface of the substrate and powder [97]. But as a result of evaporation with intense laser heat, porosity develops in the powder. In addition, high dilution also occurs with the increased exposure time [98]. Preplaced wire has also been used by Cheng *et al* [99] and they found that it is feasible to get thick and homogeneous clad layer. In terms of the ability to produce solid structures using lasers, the pre-placed powder method is limited to one layer normally.

3.6 Final Characteristics of Direct Laser Metal Deposition (LDMD)

3.6.1 Accuracy and surface finish

Accuracy and surface finish are the major issues for parts fabricated via direct laser metal deposition process. Deposited layers by the LDMD process have an average surface roughness of 10 μm making a secondary finishing operation necessary for some applications to achieve high accuracy and polished surface texture.

Weerasinghe and Steen [100] found that the surface finish of the clad layer is governed by the degree of overlap of adjacent tracks and track section profiles. In another study [101], they concluded that surface finish is also a function of viscosity of the cladding material. While, Resch *et al* [102] categorized surface roughness into three process modes by low, medium and high based on the powder feeding rate.

Adaptive slicing algorithms and techniques have been applied by many researchers [103-106] to obtain an accurate and smooth part surface in a rapid prototyping process. An in-time motion adjustment in laser cladding process has been adapted by Liu and Li [107] that has resulted in improved dimensional accuracy and surface finish. Experiments were conducted on Steel 45 and by adjusting process parameters in a closed-loop control system; they were able to obtain dimensional accuracy within ±0.05 *mm* and an improved surface finish.

3.6.2 Porosity

Porosity and void formation are the inherent problems of the gas fed LDMD process. Porosity can be generated due to multiple factors depending upon processing conditions and the deposition of material itself. Due to complex combination of factors in creation of porosity, it is difficult to provide a solution to achieve fully dense porosity free material.

Porosity in LDMD can be classified into two types i.e. lack of fusion and gas porosity. The former is caused by the insufficient melting along the layer boundaries also called as interlayer porosity; the latter is caused by the entrapment of gas in metal powder and /or release of the gas from powder particles.

A microstructure examination of Stainless Steel 316L by Lewis and Schlienger [108] using DLF process revealed pores in the fabricated part shown in Figure 3.8. The porous microstructure was reported to be a result of gas evolution during solidification and due to lack of fusion between layers or adjacent passes of the molten pool.

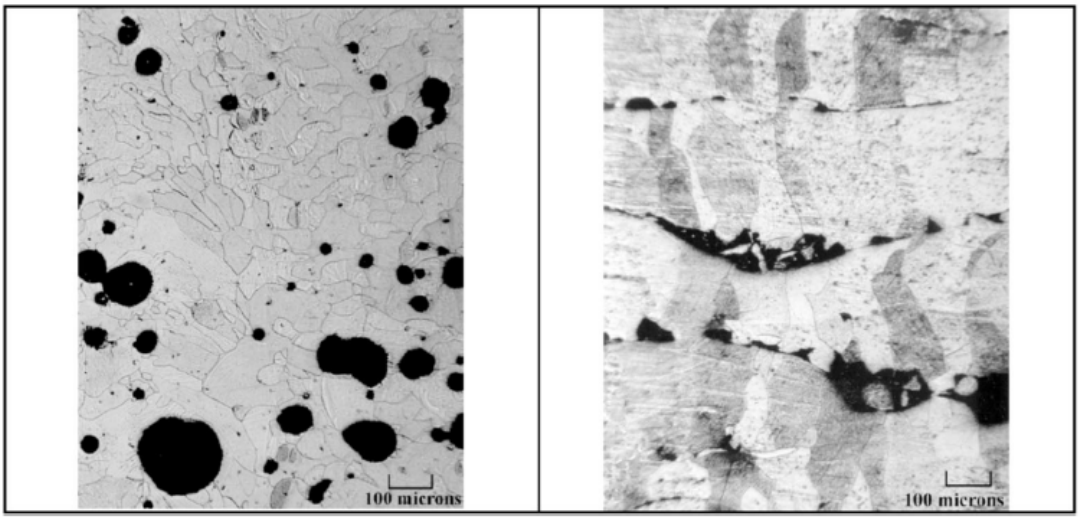

Figure 3.8: Porosity observed in DLF deposits due to residual gas contents and lack of fusion between layer boundaries [108]

In order to minimise the formation of porosity, Li [109] suggested that one way to control the formation of porosity is to bake the powder immediately before depositing it. Nurminen *et al* [91] proposed that by increasing the heat input to the process, gas porosity can be decreased. In this way, the solidification rate can be reduced thus allowing the gas bubbles to escape into the environment before the melt pool solidifies. The lack of fusion porosity occurred more in a thin substrate because of more heat dissipation compared to a thick substrate [110].

It was reported [110, 111] that both lack of fusion and gas porosity tends to decrease with decreasing speed and increasing power, as this provides more energy to melt the powder and therefore reduces the likelihood of porosity. However, in their work, only the effects of laser power and speed were investigated, even though the process involves other variables such as powder feed rate and gas settings which also influences the occurrence of porosity. It has been reported by Morgan *et al* [112] that a re-melting scan, where the laser beam scans the previously deposited layer without delivering any powder, can be used to reduce porosity through releasing of any entrapped gas. Goswami *et al* [113] discovered that porosity can be

avoided by the proper selection of scanning speed. They noted that at high scanning speed the gas bubbles do not have enough time to come out from the surface of melt pool and at low scanning speed the amount of dissolved gases increases substantially.

Steen *et al* [114] showed that lack of fusion porosity would develop if the track aspect ratio (width/height) becomes less than five, while Susan *et al* [115] showed that powder with high porosity contents results in deposits with increased porosity. They also found that powder with large void/particle size ratios may result in less deposit porosity compared to powder with lower void/particle ratios and this was attributed to escape of the gas from the melt pool due to significant increase in the buoyancy with larger voids. Hua and Choi [116] found that porosity formation in the LDMD process is related to the dynamics of the melt pool, and irregular shaped voids are caused by insufficient laser power. Choi and Chang [117] found that high powder feed rate results in higher porosity, while higher laser power results in low porosity level regardless of powder feed rate. Wang and Felicelli [118] found that higher traverse speed can cause lack of fusion porosity, particularly in layers close to the substrate and that more laser power is required at higher traverse speeds in order to get a dense part.

Ng *et al* [119] found in their work on Inconel 718 LDMD that Marangoni flow will tend to retain the gas bubbles resulting in coalescence and creation of larger pores.

LDMD process has also been used to intentionally generate porous structures as reported by Ahsan *et al*[120]. Such porous LDMD structures have their use in catalysts, sensors and biomedical implants where a certain degree of porosity is crucial. One of such porous structure is shown in Figure 3.9.

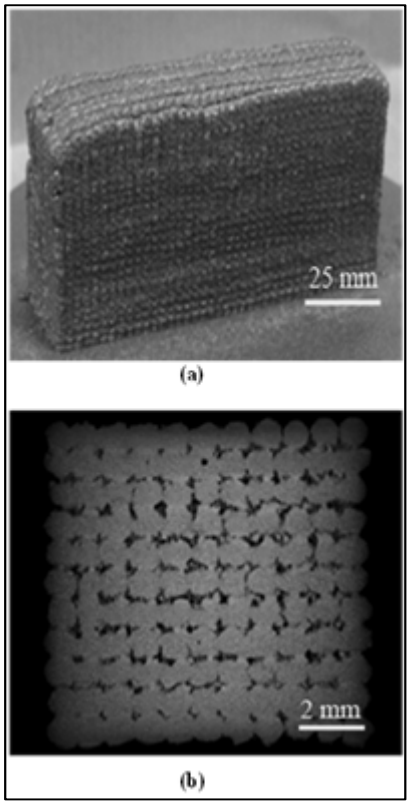

Figure 3.9: A typical porous structure of Stainless Steel 316L fabricated by LDMD at 1.6kW laser power, 250ms pulse duration and 0.133g/s powder flow rate:(a) sample; (b)MicroCT image [120]

3.6.3 Surface hardness

The hardness of a material is determined by its intrinsic hardness which is the hardness of the material in single crystal form and by its microstructural nature that affects the deformation mechanisms [121]. As indicated by the Hall-Petch relationship, the hardness is a function of the grain size [122] as given below:

$$H = H_o + kd^{-\frac{1}{2}} \tag{3.1}$$

Where H, d are hardness and grain size respectively and H_o and k are constants. Hardness varies with the reciprocal square root of the grain size. According to Takaki *et al* [123], the Hall-Petch relationship can only be applied for the grain size above $0.1\mu m$. Below this grain size the experimental results of hardness deviates from the relation. In LDMD

processed structures, average grain size is above $0.1\mu m$ so the above relationship is valid.

Wang *et al* [124] reported that grain size decreases with increasing cooling rate, thus according to the Hall-Petch relationship the hardness will increase with increasing cooling rate during solidification. In addition, Wang and Felicelli [118] observed that hardness of deposited layers increases with increases in traverse speed which is consistent with the earlier finding of Griffith *et al* [125]. Hardness in the LDMD processed materials is often position dependent. High hardness values are observed near the substrate because of the three dimensional heat flow, but re-heating of the subsequent layer deposition eventually leads to low values [126].

3.6.4 Mechanical properties

The mechanical properties of laser direct deposited parts are determined by the solidification microstructure. The solidification microstructure depends essentially on the local solidification conditions e.g., solidification rate, temperature gradients at solid/liquid interface etc, which in turn depend on the heat and mass transfer of the system. The process variables, such as laser power, traverse speed and powder feed rate also play an important role in producing components with different mechanical properties. Tensile and yield strengths of the deposited material generally increase with traverse speed and decrease with laser power [127] due to the increased cooling rates that these parameter changes induce.

Mechanical tests conducted by Zhang and Shi [128, 129] revealed mechanical properties of laser direct deposited materials that exceeded conventionally processed wrought materials. The properties were observed for 633 copper alloy, 316L Stainless Steel and Rene'95 nickel super alloy. A similar comparison for Stainless Steel 316L, Inconel 690 and Titanium alloy was done by Lewis and Schlienger [108]. Laser direct deposited parts are

generally anisotropic due to the layered construction method, i.e., the properties are different in the vertical (across the track) and in the horizontal direction (along the track). This is due to the residual stresses generated during the process and directional solidification of the part. In most cases, yield and ultimate tensile strengths are greater in the horizontal direction, but ductility is lower than in the vertical direction [130]. Resch *et al* [102] examined the properties of 45C-NS in both directions in a blown powder deposition process. A comparison of mechanical properties for various laser deposited materials is given in Table 3.2.

Table 3.2: Mechanical properties comparison of laser direct deposited materials [102, 108, 129]

Material	Test direction	UTS *(MPa)*	Elongation (%)
45C-NS	Horizontal	1046	11.4
45C-NS	Vertical	864.7	2.4
Stainless Steel 316	Vertical	579	41
Stainless Steel 316L	Vertical	626	43
Inconel 690	Vertical	666	48.8
Ti-6Al-4V	Vertical	1027	6.2
663 Copper alloy	Vertical	260	26

3.6.5 Deposition microstructure

Solidification microstructures largely depend upon properties of phases of the alloy, local solidification processing conditions such as thermal gradient, solidification velocity and stresses [131]. The LDMD process can produce much finer and controlled microstructure than conventional methods, due to

its rapid solidification and several solid-state phase transformations occurring as the part is cooled to room temperature.

The thermal gradient, solidification cooling rate and solidification velocity are related by the following equation [132]:

$$R = \frac{1}{G}\frac{\partial T}{\partial t} \tag{3.2}$$

Where R is solidification velocity, G is thermal gradient and $\frac{\partial T}{\partial t}$ is solidification cooling rate.

Key theory for directional solidification was initially developed by Fisher and Kurz [133, 134]. In another study by Kurz and Trivedi [135], they classified rapid solidification processes into three groups and found that rapid solidification covers the interface growth velocities from 10^{-2} to 10^{3} m/s. They illustrated that solidification velocity and cooling rate are more important variables than the temperature gradient in the liquid ahead of the solid-liquid interface, G.

Results for solidification on cooling rate and thermal gradient can be interpreted in the context of a solidification map to predict trends in grain size and morphology. Building on the Fisher and Kurz work [133, 134], Gaumann *et al* [136] carried out analytical modelling and developed process maps that relate the expected solidification microstructures and growth morphologies to the processing conditions for single crystal LDMD as shown in Figure 3.10.

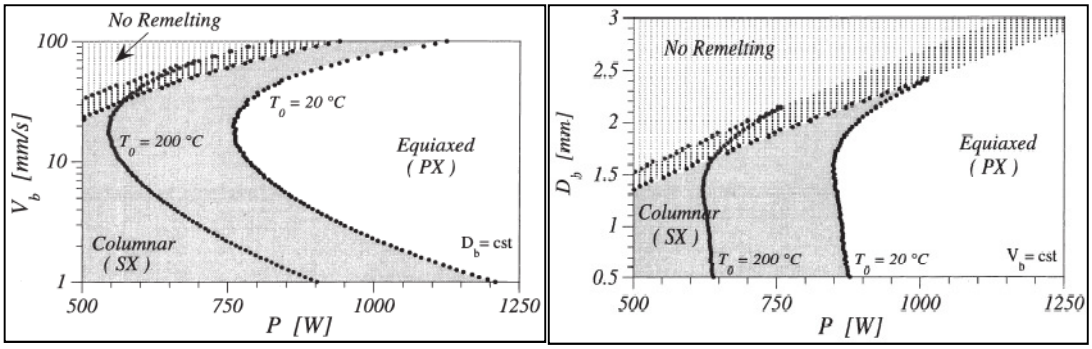

(a) (b)

Figure 3.10: Processing map showing the dominant microstructure as a function of the laser power Q: and (a) laser scanning speed V_b; and (b) laser beam diameter D_b; for two preheating temperatures T_0 [136]

Bontha *et al* [132] utilised both analytical and finite element modelling to determine the relationship between the dendrite morphology, the temperature gradient and solidification velocity during the LENS deposition of Ti-6Al-4V by plotting points in G vs. R space. The authors found that the resulting grain morphology can be predicted as columnar, equiaxed or mixed. The conditions of laser power and laser travel speed for a fully columnar dendritic structure are also obtained in LENS-deposited Ti–6Al–4V thin walls as shown in Figure 3.11.

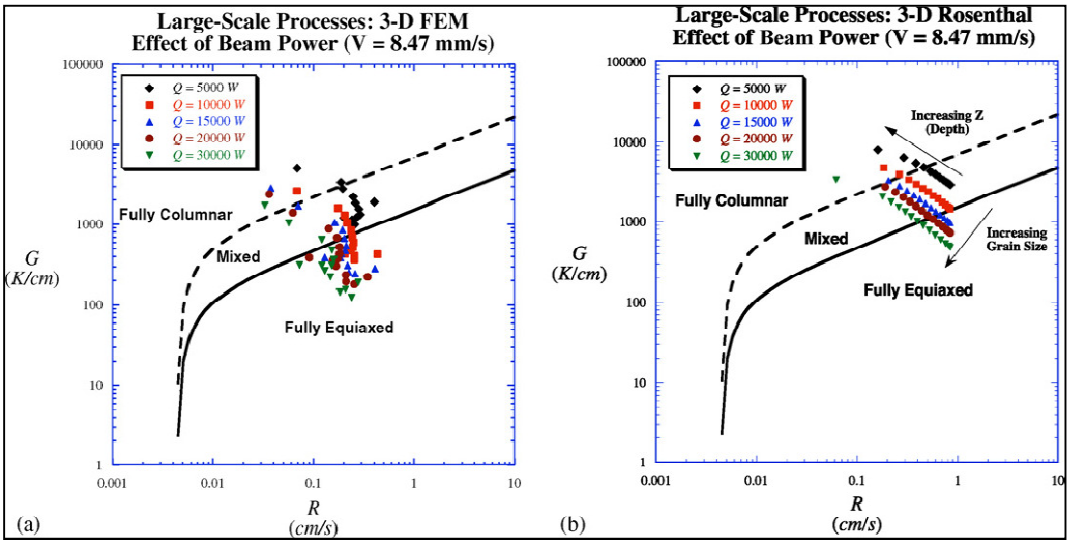

Figure 3.11: Comparison of trends in grain size and morphology in large-scale (higher power) deposition of Ti–6Al–4V from (a) 3D FEM and (b) 3D Rosenthal [132]

The relationship between dendrite arm spacing (DAS) and cooling rate provides a useful approach to establish the effect of thermal conditions on microstructure. The general relationship between cooling rate and DAS is [137]:

$$DAS = A\left(\dot{T}\right)^{b} \tag{3.3}$$

Where A and b are constants and $\dot{T}$ is cooling rate.

Hofmeister *et al* [138] utilised thermal imaging and metallographic analysis techniques to investigate the thermal behaviour during the LENS process, and in particular, the cooling rate. They showed that cooling rates during solidification depend on melt pool length, so by controlling the laser power a desired melt pool length and hence microstructure can be achieved. Another study carried out by Hofmeister *et al* [139] investigated the solidification microstructure of LENS processed Stainless Steel 316 and showed that microstructure near the melt pool interface has a columnar structure while the other regions have cellular morphology. They also found that the dendrites and cells have a finer structure at lower laser power. Zheng *et al* [140] established cooling rates based on the DAS during LENS deposition of Stainless Steel 316L.

Guo and Kar [141] used a one-dimensional mathematical model to investigate the evolution of microstructure due to rapid solidification in laser material processing. They also conducted laser cladding experiments [142] with Stainless Steel 316 on plain carbon steel substrate to verify the theoretical predictions.

Pinkerton *et al* [143] found that different grain morphologies were obtained by varying laser power and powder flow values. They proposed that although the commonly used thermal gradient and solidification velocity diagrams can be used to predict the columnar-equiaxed nature of the microstructure; intramelt pool factors such as Marangoni flow and changes

in nucleation density caused by injected powder should also be accounted for in a realistic model.

Grujicic *et al* [144] used Cellular Automation and Finite Difference methods to simulate solidification of the melt pool and the effect of LENS process parameters on the resulting solidification microstructure of Al-7wt% Si. They noted that an increase in the laser power promotes the formation of equiaxed grains and gives rise to a coarser columnar microstructure.

While, Yin and Felicelli [145] simulated dendritic structure using Finite element and Cellular Automation during solidification of Fe-C alloy in the molten pool of the LENS process. They analysed the effects of several process conditions such as laser power, cooling rate, and laser traverse speed and layer thickness on the solidification microstructure. Figure 3.12 shows that deposited layer increases from 0.25 to 0.5 *mm* (greater amount of powder metal) for a single pass, the corresponding laser power is also increased, and thus a larger molten pool is formed. A thicker layer needs higher laser power, which results in more latent heat being removed from the molten pool, thus producing a lower cooling rate.

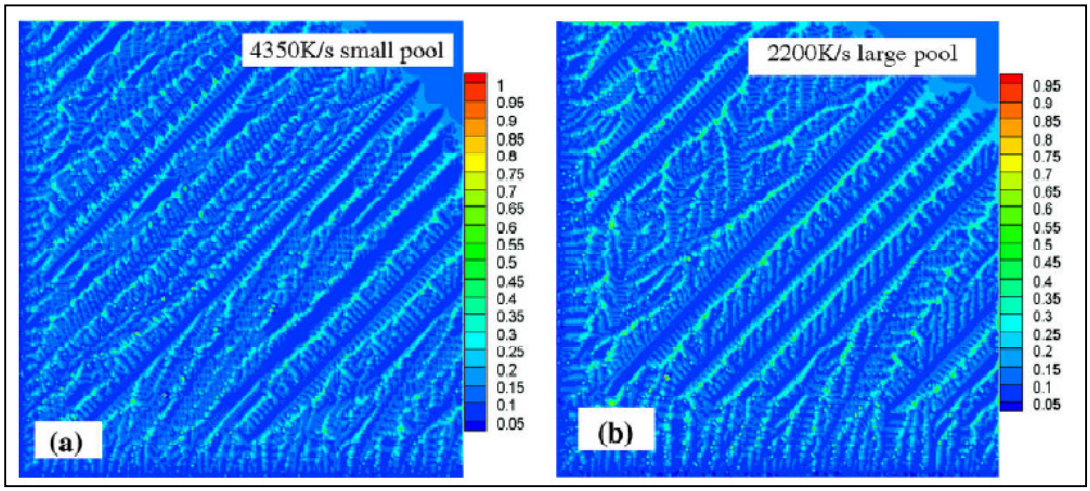

Figure 3.12: Dendrite structure with deposition layer thickness of (a) 0.25 mm and (b) 0.5 mm at a laser moving speed of 10 mm s^{-1}. The colour bar indicates solute concentration of C (wt %) [145]

3.6.6 Residual stresses and distortion

Residual stresses usually obtained in LDMD process can produce cracking or limit the practical use of these deposits. Moreover, residual stress-induced warping is a major concern in a LDMD process which can lead to unacceptable losses in dimensional tolerance. Stresses are caused by the differences in the thermal expansion/contraction of the deposit and substrate and most importantly due to the thermal load that induces the residual stresses during deposition process.

There is a desire to control the formation of the residual stresses and many researchers have tried to minimise the effects of residual stresses during deposition process. The effects of different parameters such as substrate preheating [146, 147] , heat treatment of the deposited material [148] and deposition pattern [149, 150] on the magnitude of residual stresses have been extensively studied.

Dai and Shaw *et al* [151] demonstrated that the distortion in laser processed components is mainly caused by the transient thermal stresses rather than residual thermal stresses. They also noted that distortion can be decreased by increased laser scanning rate. In another work by Dai and Shaw [152], it was found that variation in the laser scanning pattern could lead to a reduction in the residual stress levels as shown in Figures 3.13 and 3.14.

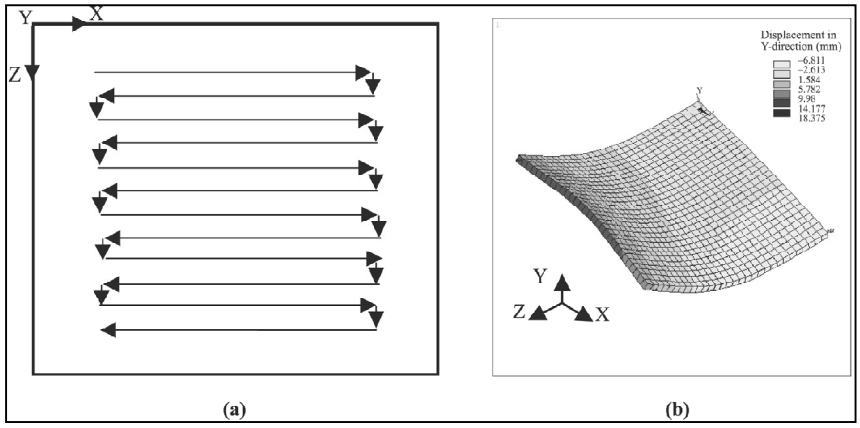

Figure 3.13: (a) Schematic of laser scanning pattern I and (b) the final shape of the nickel plate after the laser scan using the scanning pattern I [152]

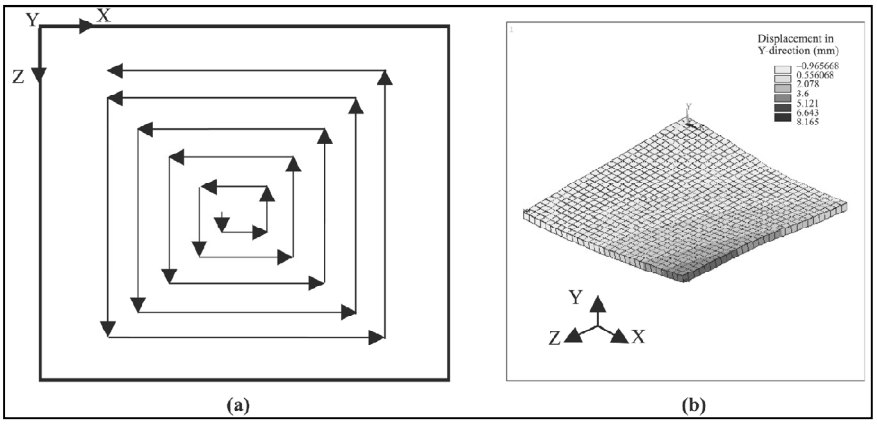

Figure 3.14: Laser scanning pattern II and (b) the final shape of the nickel plate after the laser scan using the scanning pattern II [152]

Beuth and Klingbeil [153] showed that substrate preheating and laser power and velocity adjustment are possible strategies of controlling thermal gradient and melt pool size and hence a means to influence the residual stress fields generated during LDMD.

Grum and Žnidaršič [154] found that along with deposition pattern, different alloy powders have different effects on the residual stress fields. Multilayer clads of austenitic Stainless Steel as an intermediate layer and stellite 6 as the surfacing layer were produced by Frenk *et al* [155] to investigate the potential of controlling residual stresses in a laser cladding process with an intermediate layer, however their technique does not

seemed to be very promising in solving the problem of residual stresses. On the contrary, pre-heating the base before cladding and thermal retardation after the process are reported by Tian *et al* [156] to relieve the residual stresses.

Griffith *et al* [156] used a holographic-hole drilling technique to determine the residual stress state in the H13 tool steel samples. It was conceived that the transformation that occurs during the deposition process may act to reduce the residual stress level. Rangaswamy *et al* [157, 158] undertook detailed studies of residual stresses in thin wall and pillar structures using neutron diffraction and contour methods. They noted that in the first few *millimetres* of the thin wall, compressive stresses in the direction of growth have been found to dominate. While higher in the deposit, near the top surface, tensile stresses in the longitudinal direction were observed. Moat *et al* [159] employed pulsed beam diode laser deposition parameters to influence residual stress fields. They noted that pulsed parameters appeared to have little effect on the stresses close to the top of the wall, while close to the bottom of the wall the magnitude of stresses appeared to be affected by the sample height produced during the laser deposition process.

A recent study by Pratt *et al* [160] concluded that component of the stress in the vertical direction (i.e., perpendicular to the deposition direction) is dominant, and relatively insensitive to variations in laser power and travel speed. The results shown in their work compared well with those of Rangaswamy *et al* [158].

3.7 The effects of process parameters on part geometry

The characteristics of net-shape or final part obtained by LDMD process are mainly affected by process parameters, therefore optimal processing parameters are the key to get good results. Experimental investigations were

carried out by many researchers to understand the influence of process parameters on part characteristics, a selection of these studies with a major dependent process variable is given below:

3.7.1 Powder-feeding rate and scanning velocity

Since powder-feeding rate and scanning velocity obviously determine the quantity of powder fed into molten pool and the intensity of the laser energy absorbed by substrate and powder in unit time, to a great extent, they dominate the height of layer in LDMD process. Consequently, they must be restricted in a certain range so as to make the height of individual layers formed by the fused metallic powder matching the thickness of sliced CAD model. Otherwise, the accumulative multi-layer errors in height direction can lead to the component distortion resulting in a mismatch between the final geometry and the designed geometry.

The effects of various process parameters such as powder injection point, laser power, scanning velocity, spot size and quality of the clad were investigated by Li *et al* [161]. It was found that the height of the clad was affected by almost all the processing parameters while width of the clad was affected by laser power, scanning velocity and spot size in such a manner that it increases with the increase in laser power and spot size and decreases with increase in scanning speed. A study conducted by Kumar and Roy [162] investigated the relationship between laser power and scanning speed on process parameters namely build-up height and average dilution. It was suggested that in order to achieve the desired clad height, laser power should be controlled.

A study by Resch *et al* [102] has shown that the layer width, height and roughness of the clad surface decreases with a decrease in powder feeding rate. Li *et al* [161] on the other hand reported a linear relationship between scanning velocity (V), powder feeding rate (M) and the height of the single

clad layer (H) using Stainless Steel 316L and nickel base alloy. The influence of these parameters on clad height (H) was found to be same for both materials and is shown graphically in Figure 3.15.

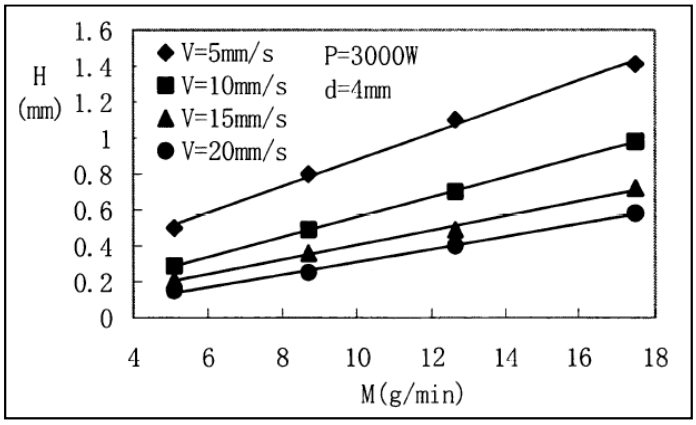

Figure 3.15: The variation of the height of single cladding layer under varying feeding rate and scanning velocity for nickel-base alloy [161]

3.7.2 Laser power and spot diameter

Laser power (P) and spot diameter (d) mainly affect the width of the clad as investigated by Li *et al* [161], in addition to scanning velocity (V) that was also found to affect track width. Figure 3.16 shows the width of single clad increases with increasing of laser power and decreases with increasing of the scanning velocity. While, increasing spot diameter results in the increase of the width of single clad when laser power is high enough and decreases when it is not high enough.

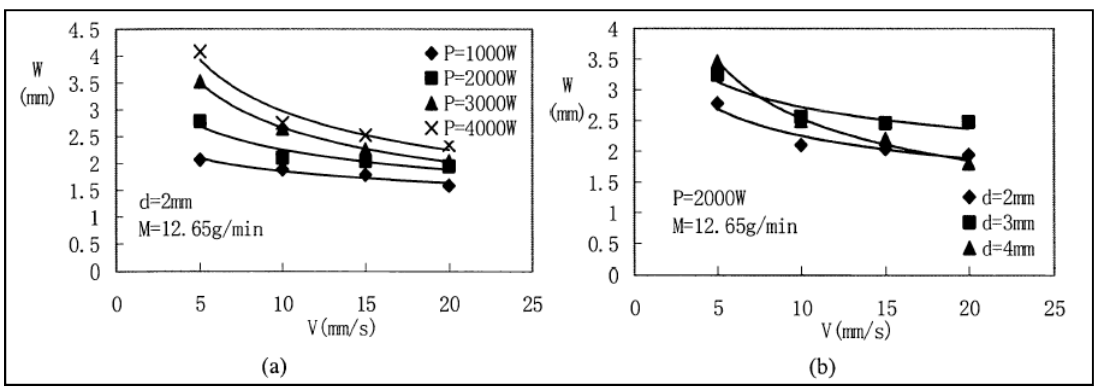

Figure 3.16: Width of the laser clad under different parameters [161]

Another important factor in this research concerning dilution was found to be the temperature of the base material. A relationship was established that showed an increase in dilution with the increase of preheating temperature. Kim and Peng [163] suggested that for multi-path cladding, a lower laser power should be selected for the second cladding layer in order to avoid the influence of dilution with the first cladding layer.

Research done by Smugeresky *et al* [164] showed that the surface hardness is a function of laser power, traverse speed and particle size. Hardness was found to increase with the increase in traverse speed, whereas the inverse was true for increasing powder particle size and laser power. The effect of laser power on metal clad were also investigated by Utsumi *et al* [165] using a new cladding technique that combines CO_2 laser and a tungsten inert gas (TIG) arc for cladding at high speeds. It was observed that the degree of dilution improved using laser-TIG combined cladding. By applying the results to subsequent cladding in layered fashion, high quality clads were obtained with a very low dilution into the base material.

3.7.3 Cooling rate

The cooling rate during the deposition can be affected by several parameters including laser input energy, substrate temperature, material properties, substrate geometry and beam shape. Microstructure is related to the cooling rate during solidification by the Kurz and Fischer [166] relationship, that defines microstructure as being proportional to the reciprocal cube root of cooling rate during solidification.

Effects of cooling rate on microstructure have been studied in great detail by Pryds and Huang [167] on a low carbon steel. The dependence of microstructure on cooling rate was determined by X-ray diffraction (XRD) and transmission electron microscopy (TEM) and, in general, surface hardness was found to increase with the increasing cooling rate. Apart from

its direct relation with microstructure, rapid cooling rates can lead to higher tensile and yield strengths [168, 169]. Mazumder *et al* [28] studied the effects of specific energy and deposition layer thickness on the cooling rate as shown in Figure 3.17.

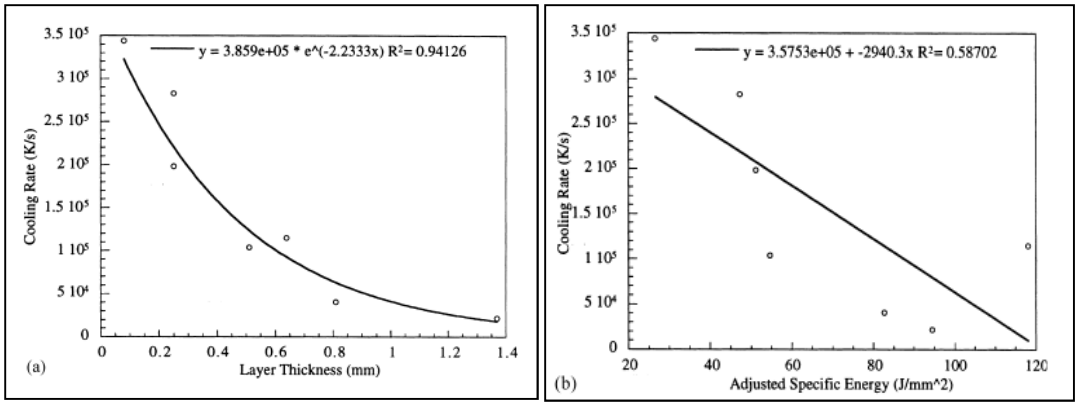

Figure 3.17: (a) Influence of layer thickness on cooling rate (b) inverse relationship between specific energy and cooling rate [28]

3.7.4 Powder flux and specific energy

Work carried out by Pelletier *et al* [170] proved that dilution is highly dependent on injected powder flux. Dilution was found to increase for a lower powder flux and decrease with a high powder flux, whereas the inverse occurred for variation in deposited mass of the clad layer.

Earlier in 1983, Weerasinghe and Steen [100] described the process of laser cladding using Argon blown powder delivery in which they observed that for a given specific energy, dilution of a single cladding layer is independent of laser intensity and traverse speed. An increase in dilution effects with an increase in specific laser energy was also seen by Sun *et al* [171] in a titanium alloy substrate using TiC powder, where the dilution was enhanced as a result of increased specific energy. However, a decrease in micro-hardness was observed in both the clad and the dilution zones.

Choi *et al* [172] found that an increase in specific energy reduces the surface hardness of Fe-Cr-C-W alloy deposit on AISI 1016 steel. They argued that

increasing the specific energy input can significantly reduce the cooling rate of the melt zone, which therefore resulted in a reduction in the hardness of the deposited sample.

3.8 Melt pool dynamics

During the LDMD process, a melt pool is generated because of laser irradiation. There are lot of factors which determine the size of the melt pool, and hence also the mechanical and microstructural properties in the final deposit or part. These factors involve thermal conduction, Marangoni / thermocapillary flow, powder and shield gas forces on melt pool, mass transport, laser / powder interaction, melt pool / powder interaction, and laser / substrate interaction in the process zone [26].

The effect of Marangoni convection, also known as surface-tension-driven convection, causes the melt pool to circulate. This is generated by a local change in any variable affecting the surface tension including composition and temperature [173]. Limmaneevichitr and Kou [174] showed that a surface tension gradient is induced by the temperature gradient along the pool surface and the temperature dependence of surface tension. As surface tension and temperature are inversely proportional [175], the fluid will flow along the surface from the centre (where temperature is high and surface tension is low), to the edge (where temperature is low and surface tension is high).

Mathematically it is given as:

$$\frac{\partial \gamma}{\partial \mathrm{s}} = \frac{\partial \mathrm{T}}{\partial \mathrm{s}} \times \frac{\partial \gamma}{\partial \mathrm{T}} \tag{3.4}$$

Where γ is the surface tension, T is the temperature and s is the distance along the pool surface, outward from the centre of the pool. The melt pool has its highest temperature under the laser beam, where the surface tension has the lowest value. Away from centre of the laser beam, the surface

temperature decreases and surface tension increases. Due to this effect, liquid is pulled towards the boundary of the melt pool, creating a small depression in the centre. This depression can be clearly seen in Figure 3.18 [176] where a CO_2 laser was used to create a melt pool on a steel substrate.

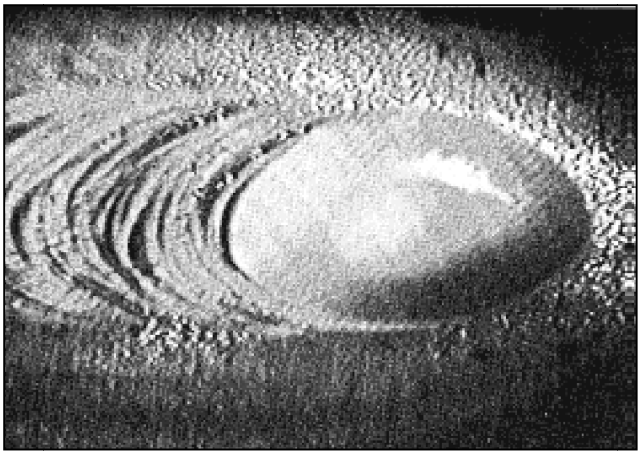

Figure 3.18: A melt pool created by CO_2 laser [176]

To make up for the depression caused in the centre of the melt pool, any internal pressure differential coupled with gravitational force will induce a counter flow to try to fill this depression [177]. The resultant circulation and consequent mixing in the melt pool with thermocapillary effect is termed as Marangoni-Benard convection [178].

The Marangoni number, which is a measure of the extent of Marangoni convection, is defined as [179]:

$$Ma = \frac{\partial \gamma}{\partial T} \frac{1}{\mu \alpha} L \Delta T \tag{3.5}$$

Where, $\frac{\partial \gamma}{\partial T}$ is the surface tension temperature coefficient, ΔT is the temperature difference between the centre and edge of the pool surface, L is the radius of the pool surface, μ is the dynamic viscosity and α is the thermal diffusivity.

Kumar and Roy [178] numerically modelled the effects of scanning speed and Marangoni number. They noted that maximum and average melt pool temperature reduces due to convective heat transfer at low scanning speed,

where as small reduction is observed at higher scanning speed. In another study, Limmaneevichitr and Kou [179] experimentally evaluated that by increasing power, Marangoni convection and hence pool size increases. Chan *et al* [180] confirmed this finding by numerically modelling the process and found that the presence of the thermocapillary convection changes the physics of the process from conduction to convection dominated, resulting in an increase in aspect ratio as compared to pure conduction case.

Lie *et al* [181] showed the spatial variations in Marangoni forces on a melt pool surface by numerical analysis. They showed that with a negative surface tension temperature coefficient, flow is outward from the pool centre to the pool periphery and results in a shallow and wide pool. In contrast, with a positive surface tension temperature coefficient the flow is inward from the pool periphery to the pool centre causing a deep and narrow pool. Figure 3.19 (a, b) shows the positive and negative surface tension temperature coefficient effect on the Marangoni flow in the melt pool.

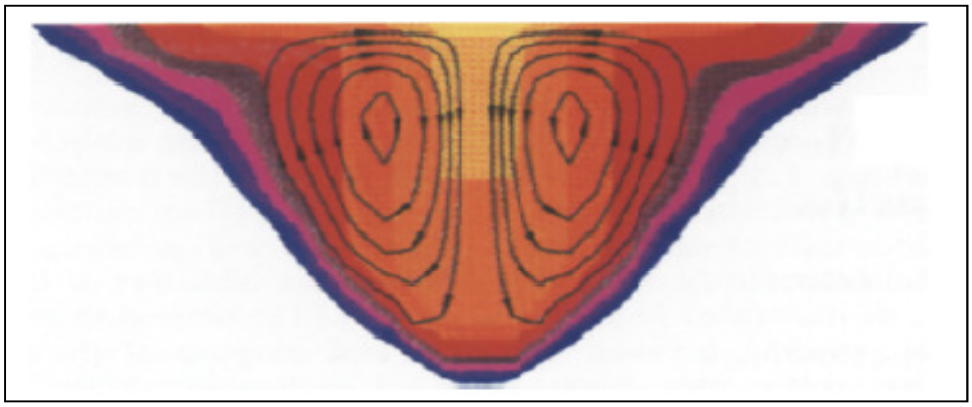

(a)

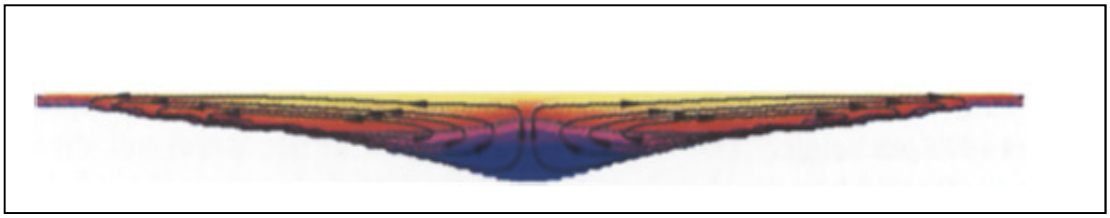

(b)

Figure 3.19: Melt pool shape (a) Inward flow (b) Outward flow [182]

The surface tension is known to be markedly dependent upon the concentration of surface active elements such as oxygen and sulphur in the metal [179, 183]. Such elements are responsible for a positive surface tension temperature coefficient, increasing temperature and decreasing surface tension in the melt pool [182, 183] .

Kreutz and Pirch [184] solved numerically the surface-tension driven melt dynamics in order to determine the geometry of the molten pool, the temperature field, the flow field and the surface deformation as a function of processing variables. Their results showed that the thermocapillary flow became suppressed above a critical laser scanning velocity. Anthony and Cline [185] showed that Marangoni flow rippling can be avoided by operating above a critical scanning speed at which the interaction time would be too short to activate Marangoni flow.

3.9 Measurement techniques and control of LDMD process

In addition to the need to control the high temperatures that are encountered in a LDMD process , residual stress measurement and its control is also required to avoid distortion of the deposited components. Moreover, motion path and control code need to be optimized to reduce overall process time from the CAD model to the finished part. This section lists some of the monitoring techniques adopted by researchers to improve part properties and gain better control of the LDMD process.

An image processing system developed by Meriaudeau *et al* [186] used two CCD matrix cameras to control parameters during the process. One camera was used to give a surface temperature reading that in turn enabled calculation of variations in mass feed rate during the process. The other camera provided information on powder distribution and powder speed.

Using this open-loop system and by analysing the acquired results, they were able to increase the efficiency of the laser cladding process.

Yu *et al* [187] utilized high temperature thermocouples to measure the thermal cycle and temperature distributions for laser cladding process. They used an optimum set of process parameters with various cladding materials in their experiments and measured the clad zone temperatures under various conditions. The recorded temperatures were found to be in the range of 1650 to 1800 °C that were in good agreement with those measured by an optical pyrometer.

Work has been carried out by Koch and Mazumder [188] to improve the accuracy of a DMD process. They used a closed loop feedback controller system as shown in Figure 3.20, where an optical sensor measures the layer height and controls the laser duty cycle. The duty cycle is used to control powder flow rate.

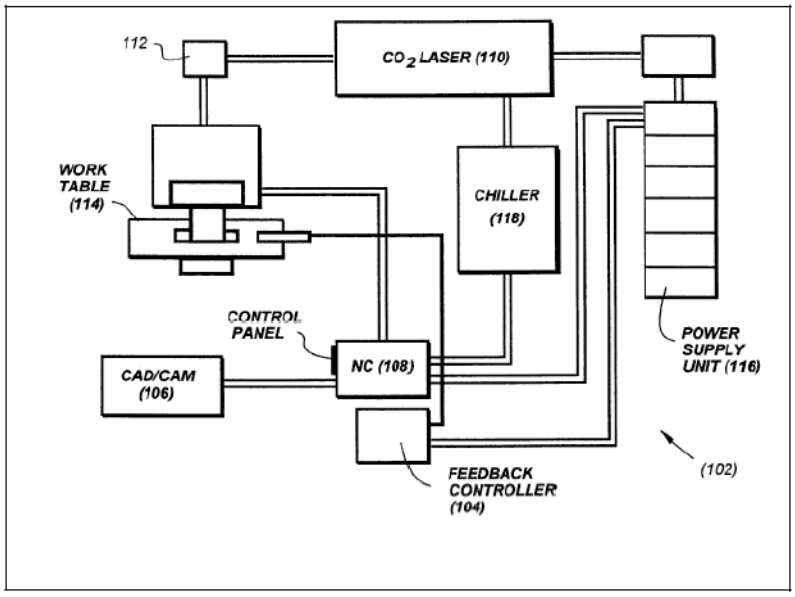

Figure 3.20: Closed loop DLD system with feedback controller [188]

Using optical sensors for the control of the laser welding process, Dilthey [189] was able to control the filler wire speed that can fill up joint gaps and

thus prevents welding faults. A seam tracking sensor was used to measure the joint gap width in the laser welding process; the data was then transmitted on-line to an adaptive wire feeding system and converted into the required wire-feeding speed. Moreover, additional power and weld speed adaptation allowed the filler wire to be fed safely and reliably into the process.

Control of deposit thickness and height is a critical issue in a LDMD process since it impacts on the quality of the product and a better control will result in substantial savings in post process machining cost for surface finish. Mazumder *et al* [126] used a series of sensors to measure the deformation of melt pool by a Reflective Topography technique, which was operated in a feed-back loop to control the process parameters to limit the maximum height of the metal deposition. The sample produced without any height control was found with excess cladding build-up where the track overlapped as shown in Figure 3.21.

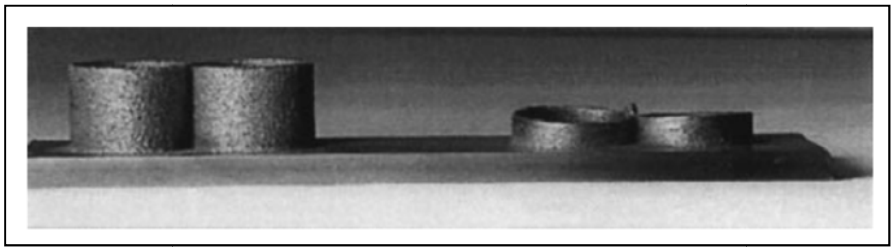

Figure 3.21: Fabricated samples. Left: with height controller, Right: no height controller [126]

The control of the melt pool is also important to keep the process stationary and to compensate the different fluctuations. Demure *et al* [190] used a PID controller to control the size of the molten pool. The closed loop controller regulated the laser power based on the light of the molten pool. This in turn controlled the temperature of the process, by keeping the temperature constant and varying the laser power to compensate for the variation in

temperature of the melt pool. The layer thickness using this PID controller was found to be more regular than without the controller as shown in Figure 3.22.

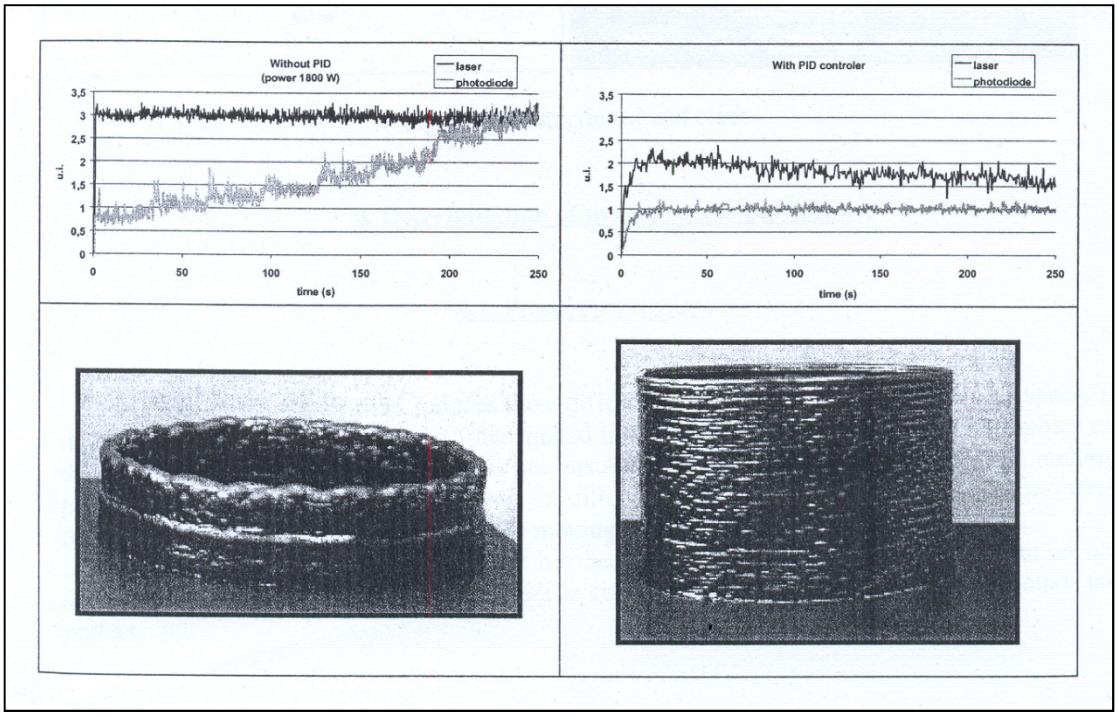

Figure 3.22: DLD process with and without PID control [190]

Grant *et al* [191] disclosed a fuzzy logic controller for manipulating the laser processing variables such as laser power, laser intensity and laser beam velocity to control the penetration depth of welding.

3.10 Summary

Direct laser deposition is a promising manufacturing technique, which combines the technologies of computer-aided design, laser cladding and rapid prototyping. In this chapter different material delivery methods involved in LDMD have been discussed. The literature has shown that the macro and micro structures of LDMD processed materials are dependent on a complex combination of the process parameters. The phenomenon of Marangoni flow in the LDMD process which plays an important role in the

final characteristics of a part has also been discussed. The process characteristics of LDMD and closed loop control system by various authors have also been detailed.

Chapter 4. Materials and Equipments Used In the Experiments

4.1 Introduction

This chapter describes in detail the materials and experimental equipments used in this project to fabricate samples and characterise the microstructure and residual stresses generated during LDMD process.

4.2 Materials

The outline of the project proposed for this study, was to investigate three alloys, namely Inconel 718, Ti-6Al-4V and Stainless Steel 316L. These three alloys are widely used in automotive, aerospace, electronics, ornaments and medical instruments applications. They are briefly discussed in the following section.

4.2.1 Nickel based super alloys

The wrought and cast forms of nickel are of particular value in the chemical industry because of their resistance to corrosion in alkaline and other media. Similarly nickel alloys with additions of manganese, silicon and zirconium are used for the electrodes of internal-combustion engines spark plugs [192]. Nickel-based alloys have emerged as a key candidate material for use in aerospace industry because of their high operating temperature capabilities. They have good mechanical properties and good corrosion resistance at high temperatures. Ni alloys are grouped into binary Ni alloy (i.e. Ni-Cr alloy and Ni-Cu alloy) and ternary Ni alloy systems. The Ni-Fe-base super alloy is widely used in comparison with other ternary Ni alloys.

All nickel based super alloys have a face-centred cubic (FCC) structure and this is conventionally termed as "γ" or gamma phase. To improve the oxidation resistance and increase the strength, Cr and Mo are usually added to nickel based alloys. Unique intermetallic phases can form between nickel and nickel alloying elements. Aluminium and titanium are usually added together for the age hardening γ' precipitate Ni_3 (Al, Ti). The Ni_3Nb γ'' precipitate generally forms preferentially in alloys with Nb contents above 4wt% [193].

Inconel 718 is probably the most commonly used nickel based super alloy. Unlike the γ' strengthened nickel super alloys, Inconel 718 is strengthened by a metastable Body Centred Tetragonal (BCT) intermetallic phase γ''. Compared to γ' strengthened alloys the precipitation kinetics of Inconel 718 are considerably slower with ageing heat treatments commonly lasting 17 hrs before optimal hardness is reached [194].

Normally, in LDMD processes two types of powders are used i.e. Gas Atomised (GA) and Water Atomised (WA). But recently, Plasma Rotation Electrode Preparation (PREP) Inconel 718 powder has also been used and has showed improved tensile properties as compared to GA powders, as indicated in Table 4.1 [1].

Table 4.1: Tensile testing results of LRF PREP IN718 [1]

Material condition (25 °C)	UTS (MPa)	0.2% YS (MPa)	EL (%)
LRF + heat treatment	1360	1170	18
Wrought IN718	1340	1100	12

This alloy is one of the most widely used superalloys, having found numerous applications in the aeroengine, e.g. as a turbine disk material, for shafts and as compressor blades [195]. It is also used in cryogenic

applications [196]. Temperature dependent thermal and mechanical properties of Inconel 718 are shown in Table 4.2 [197, 198]

Table 4.2: Thermal and Mechanical Properties of Inconel 718 [197, 198].

Temperature, (K)	**293**	**500**	**700**	**1000**	**1200**	**1400**	**1533†**	**1617††**	**1800**	**2100**
Density, ϱ (kg/m^3)	8220	8120	8048	7961	7874	7786	7733	7579	7487	7341
Enthalpy, H x 10^9 (J/m^3)	0.044	0.66	1.44	2.65	3.65	4.62	5.23	7.34	8.36	9.9
Thermal conductivity, k ($W/m\ K$)	11.4	18.7	20.2	22.2	25.7	29.0	31.1	26.8	29.4	33.5
Temperature (K)	**293**	**700**	**811**	**922**	**1033**	**1144**	**1306**	**1400**		
Thermal expansion coefficient, α x 10^{-6}	12.2	14.4	14.9	15.43	-	17.45	18.34			
Modulus of elasticity, E (GPa)	200	178	-	-	-	139	99	81		
Poisson's ratio, υ	0.30	0.277	-	-	-	0.336	-	-		
Yield stress, σ_y (MPa)	1125		1020	965	800	32	-	-		

4.2.2 Titanium alloys

Pure titanium, as well as the majority of its alloys, crystallizes at low temperatures in a modified Hexagonal Close Packed (HCP) structure, called

"α" titanium. At high temperatures, however, the Body-Centred Cubic structure (BCC) is stable and is referred to as "β" titanium. The β-transus temperature for pure titanium is 882±2°C [199]. The atomic unit cells of the HCP "α" titanium and the BCC "β" titanium are schematically shown in Figure. 4.1 with their most densely packed planes and directions highlighted.

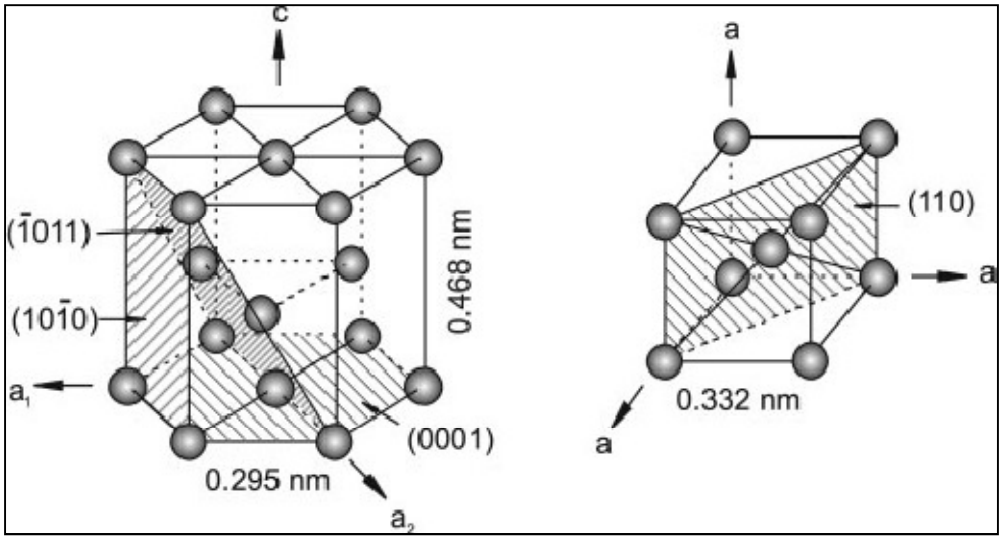

Figure 4.1: Crystal structure of " α" and" β" phase [199]

Titanium is a low density element, and it has one of the highest strength-to-weight ratios and corrosion resistance of the metals [200]. These two properties explain its extensive use in the aerospace sector, the chemical industry, medical engineering, and the leisure sector. However, Ti alloys have an affinity with oxygen, hydrogen and nitrogen, which readily generates embrittlements when welding them without properly using an inert gas protection [201, 202].

The titanium alloys are generally categorised into four types according to their phases [200]:

- Alpha "α"
- Near- alpha
- Alpha+beta "α+β"
- Beta "β"

Most α+β alloys have high-strength and formability, and contain 4-6 wt% of β-stabilisers which allow substantial amounts of β to be retained on quenching from the β→ α+β phase fields, e.g. Ti-6Al-4V. Aluminium reduces density, stabilises and strengthens α phase, while vanadium provides a greater amount of the more ductile β phase for hot-working. This alloy, which accounts for about half of all the titanium that is produced, is popular because of its strength (1100 *MPa*), creep resistance at 300°C, fatigue resistance and castability [203]. Some of temperature dependent thermal and mechanical properties of Ti-6Al-4V are shown in Table 4.3 [2, 3].

Table 4.3: Thermal and Mechanical Properties of Ti-6Al-4V [2, 3].

Temperature, T (K)	**293**	**400**	**600**	**800**	**1000**	**1200**	**1400**	**1878†**	**1928††**	**2100**
Density, ϱ (kg/m³)	4430	-	-	-	4390	4370	4400	4140	4130	-
Enthalpy, H x 10^9 (J/m³)	0.044	0.66	1.44	2.65	3.65	4.62	5.23	4.934	6.56	-
Thermal conductivity, k (W/m K)	6.6	6	7.6	11	12.6	15	20.12	25.96	27.5	31.5
Temperature (K)	**293**	**473**	**673**	**873**	**1073**	**1878**	**1928**	**2100**	-	-
Thermal expansion coefficient, α x 10^{-6}	8.6	9	9.4	9.7	11	11	11	-	-	-
Modulus of elasticity, E *(GPa)*	113.8	94.7	84.1	74.2	62.8	10	-	-	-	-
Poisson's ratio, υ	0.342	0.23	0.23	0.24	0.24	0.5	-	-		
Yield stress, σ_y *(MPa)*	828	270	-	-	80		-	-	-	-

Most titanium alloys exhibit poor resistance to sliding wear and are susceptible to galling and seizing [204, 205]. In order to improve the wear resistance of titanium alloys, laser cladding of carbide and ceramic particles with titanium has been studied [206, 207].

4.2.3 Stainless Steel alloys

The stainless steels are highly corrosion resistant in a variety of environments, especially at ambient atmosphere [208]. Due to the passivity of chromium [209], all stainless steels contain at least 11wt % Cr which creates a thin protective layer of chromium oxide when steel is exposed to oxygen. This is especially useful when the metal is scratched, as the oxide layer re-forms quickly, hence protecting it from corrosion.
Stainless steels are divided into three main classes based on the strengthening mechanism and predominant phase constituents of the microstructure i.e. austenite, ferrite and martensite. The austenite phase (gamma phase) of stainless steel has a Face Centred Cubic (FCC) crystalline structure, while the ferrite phase (alpha or delta phase) has BCC crystalline structure and martensite has BCT crystal structure. The austenitic grades are the most commonly used grades of stainless steel mainly because, in many instances, they provide very predictable levels of corrosion resistance with excellent mechanical properties [210]. Austenitic stainless steels are the most creep resistant types of the stainless steels. Alloying with carbon, nitrogen, and niobium produces the greatest strength at elevated temperatures. The austenitic steel family tree is shown in Figure 4.2.

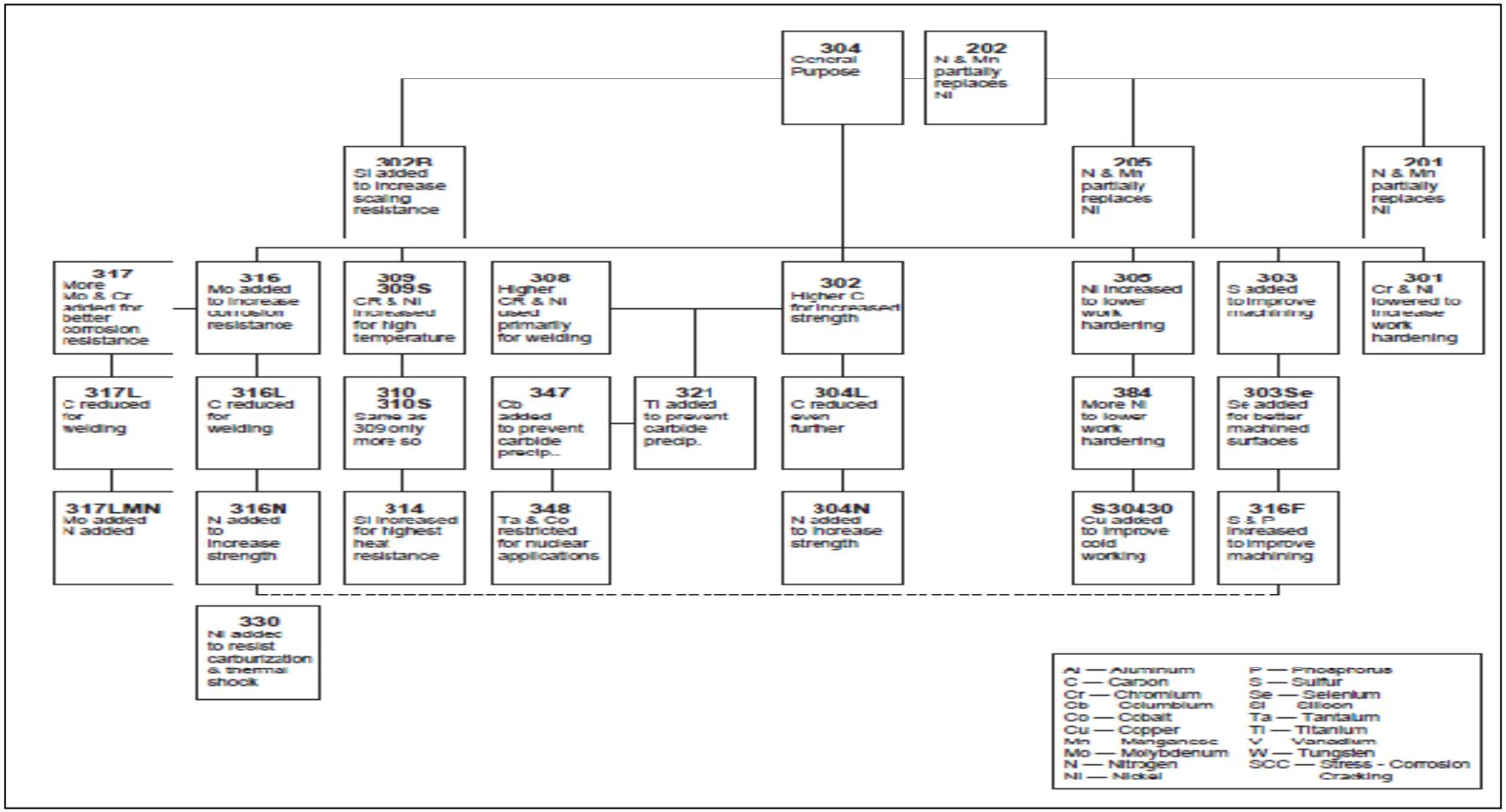

Figure 4.2: The austenitic steel family [211]

Type 316 stainless steel has the highest stress-rupture strength of the 300 series alloys [212] and has a wide range of applications in oil and gas industry, refineries, chemical and petrochemical plants and as biomaterials because of its excellent corrosion properties and bio compatibility [213]. Type 304 and 316 series stainless steels have extensively been used both as the deposition powder and as the substrate in the laser deposition process. Normally, gas atomised powder is considered superior to water atomised powder in terms of surface finish, microstructure, hardness and tensile strength of the final part [214].

4.3 Experimental equipment used for LDMD process

4.3.1 Laserline LDL 160-1500 Diode laser

All the experiments carried out throughout this project were performed using a Laserline LDL160-1500 diode laser manufactured by Laserline GmbH, Germany as shown in Figure 4.4. It operates in the near infrared wavelength range with approximately equal intensities of 808 *nm* and 940 *nm* radiation with a maximum power of 1500 *W*. The output beam of the diode laser has a rectangular transverse beam intensity profile with an approximately "top hat" intensity distribution and was fitted with optics with a focal length of 300 *mm*. This type of laser has a wide range of applications and can be used for cutting, welding, cladding and surface processing [215].

Figure 4.3: Laserline LDL160-1500 diode laser

4.3.2 Powder delivery system

An FST PF-2/2 powder feeder manufactured by Flame Spray Technologies Ltd, UK was used in the experiments. Powder feed contains two canisters of 1.5 litres each capacity and a mixing motor to distribute the powder evenly on the rotating disks. The disks and mixing motors are controlled electronically using a Siemens controller [216]. Argon gas was used as a carrier gas for powder feeding.

The powder feeder had to be calibrated for the delivery of Stainless Steel 316L powder. As powder feeder shows its output in rpm, so to get the delivery rate of powder in *g/s*, a calibration was needed. For calibration purpose, powder was collected in a container at different *rpms* for known time periods. The weights of empty and full containers were measured using a Sartorius electronic precision scale. Powder was carried through piping to

the coaxial deposition head shown in Figure 4.4. The deposition head comprises Laserline collimating and focusing optics and a nozzle assembly made by DeBe Lasers Ltd. The nozzle consists of a central laser passage with a gas stream to protect the optics, a single powder outlet annulus, with no second outlet for a focusing gas stream, and an annular water cooling passage.

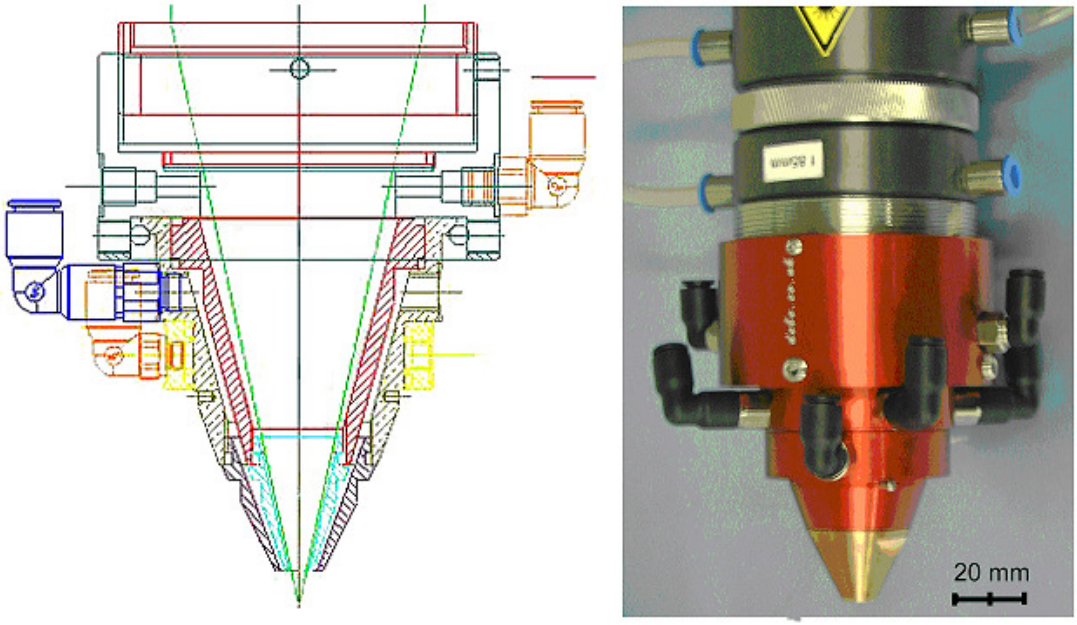

Figure 4.4: Deposition head used during the experiments

4.3.3 Scanning electron and optical microscopy

Scanning electron microscopy (SEM) is a common method used for microstructural analysis for LDMD. In optical microscopy, visible light and a system of lenses are used to magnify the images or micrographs. But optical microscopy is limited by the inherent resolution defined by the wavelength of light. As compared to the optical microscope, electron microscopy can be used to gain resolution, by using electrons as its illumination radiation rather than visible light.

SEM does not directly image the surface of a sample, but rather maps the electron emissions from regions by continuously sweeping an electron beam across a sample surface. The signal collected from the sample can be formed from different types of emitted electrons.

During this project, a PolyVar-MET optical microscope manufactured by Reichert/Leica, Austria, along with iSolution DT software was used for optical imaging as shown in Figure 4.5. The microscope had bright field - dark field and Nomarski (Differential Interference Contrast) imaging modes and a 3 *MP* digital camera with 2x, 5x, 10x, 20x, 50x, and 100x objective lenses to capture high quality images. Illumination was by a tungsten-halogen bulb or high power arc lamp. For scanning electron microscopy, a Hitachi-S3400N scanning electron microscope manufactured by Hitachi High Technologies, Japan, was used as shown in Figure 4.6. The filament of the system is tungsten and featuring magnification from 5 to 300,000x. The acceleration voltage range of the system is 0.3-30 kV.

Figure 4.5: PolyVar – MET optical microscope

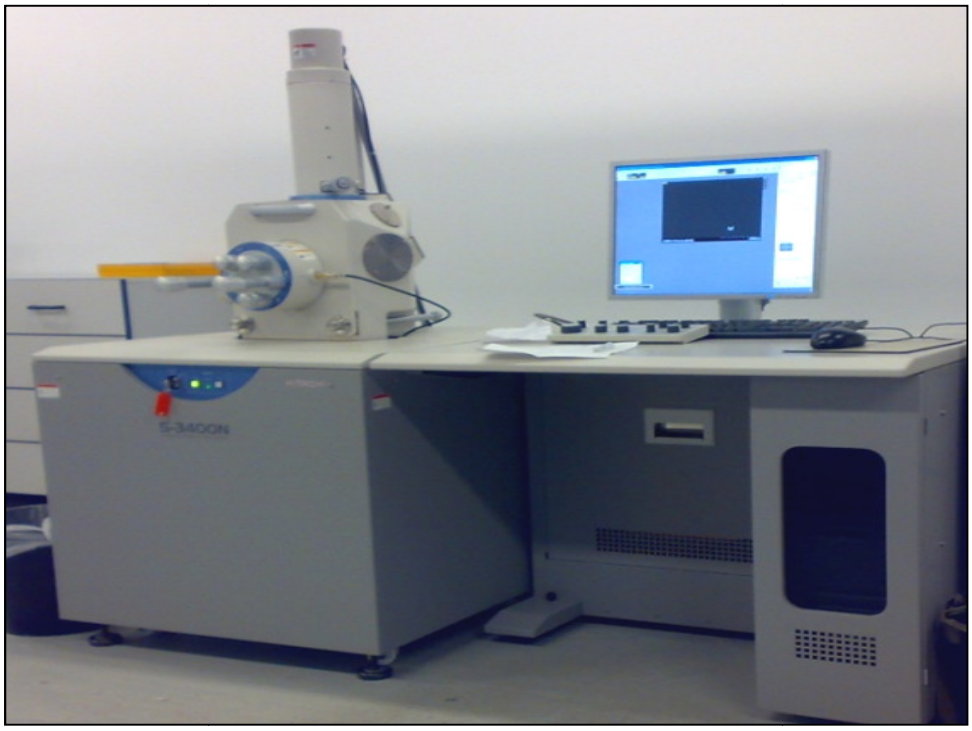

Figure 4.6: Hitachi S-3400N scanning electron microscope

•

4.4 Mechanical testing

4.4.1 Vickers indentation hardness test

Indentation tests are perhaps the most commonly applied methods of testing the mechanical properties of materials. The hardness tester forces a small sphere, pyramid or cone into the surface of the metals by means of a known applied load, and the hardness number (Vickers or Brinell) is then obtained from the diameter of the impression. The hardness may be related to the yield or tensile strength of the metal, since during the indentation, the material around the impression is plastically deformed to a certain percentage strain [217].

In a micro-hardness test, a hard tip (typically diamond) is pressed into the sample with a known load. After some time, the load is removed and the mean value of a diagonal is measured in *millimetres*.

The Vicker hardness number is then calculated based on the following equation [218]:

$$HV = \frac{1.8544W}{d^2} \tag{4.1}$$

Where d is the mean value of a diagonal in *millimetres* and W is the imposed load in *kilogram*,

Vicker hardness measurements were used in this work to obtain information on the mechanical properties of the LDMD structure. Vickers hardness testing was undertaken using a MICROMET® 5114 micro-indentation hardness tester manufactured by BUEHLER Instruments, as shown in Figure 4.7. The measurements were performed in cross sections of the materials that had been ground and polished to eliminate the macro- roughness. The depth of the work hardened zone is negligibly small compared to the depth of the indentation so that it does not influence the measurement. The test samples were forced with a diamond indenter. The loading force of this machine

ranges from 1 *gf* to 2000 *gf* for the duration of 10 *seconds* for each measurement. Diagonal lengths of indentations were measured under the magnification of 10X.

Figure 4.7: MICROMET® 5114 microhardness test machine

4.4.2 Dry sliding wear test

Wear has been defined as the removal of material by mechanical action. A number of possible wear mechanisms may operate simultaneously. Types of wear mechanisms can be split into five main categories which are abrasive, adhesive, erosion, fatigue and fretting wear.

In this work, only abrasive wear has been calculated on the laser deposited functionally graded Ni-Steel structures. In Abrasive wear, that is defined as the removal of a material from a surface by harder material moving along the surface under load, a harder material indents the surface and removes the material. A Teer Coatings (POD-2) pin on disk wear tester, Figure 4.8, was used in this work to evaluate the wear properties of functionally graded LDMD structures. The machine is a computer controlled pin on disc type. The wear pin used in this study was an Ø 5 *mm* WC-6%Co ball (Ra= 0.02

μm). The wear pin creates a circular wear track on the sample. The sliding motion of the sample under the wear pin provides a frictional force proportional to the applied load. The friction force is detected by a load cell and recorded by the computer. The load can be varied by adjusting the mass of dead weight hung at the end of the loading beam.

Wear coefficients for the sample were calculated from the volume of the material lost during a specific friction run. The wear rate (W) and specific wear rate (SWR) of the deposited tracks were calculated from the wear track cross-section geometry, using the following equations:

$$W = \frac{w \times w_d \times \pi d_t}{2 \times n \times t \times \pi d_t} \tag{4.2}$$

$$SWR = \frac{w \times w_d \times \pi d_t}{2 \times L \times n \times t \times \pi d_t} \tag{4.3}$$

Here, w is the wear track width, w_d is the wear track depth, d_t is the track diameter, n is the sample rotating speed (rpm), t is the test time in minutes and L is the applied load.

The wear track width was measured by high magnification optical microscopy. The wear track depth was measured by using Veeco Wyko NT1000 optical surface profiling system as shown in Figure 4.9.

Figure 4.8: Teer Coatings POD-2 wear testing equipment

Figure 4.9: Veeco Wyko NT1000 optical profiling system

4.4.3 Tensile Testing

Tensile tests were carried out horizontally to the deposition direction at room temperature using an INSTRON 4507 universal tensile testing machine operating with a crosshead speed of 1 *mm/s* shown in Figure 4.10. As no international standard exists for evaluating tensile strength properties for functionally graded materials, a comparative study was undertaken for tensile strength evaluation. All the samples were tested on as-deposited basis

and effective tensile strength was calculated for each sample. After tensile testing, the fracture surface was observed using a Hitachi S-3400N SEM.

Figure 4.10: INSTRON 4507 universal testing machine

4.5 Chemical composition analysis

Chemical composition analysis using line scanning, was carried out using a Zeiss EVO 50 scanning electron microscope equipped with an energy dispersive spectrometer (EDX) manufactured by OXFORD Instruments, as shown in Figure 4.11. The specification of the Zeiss EVO 50 SEM is listed in Table 4.4.

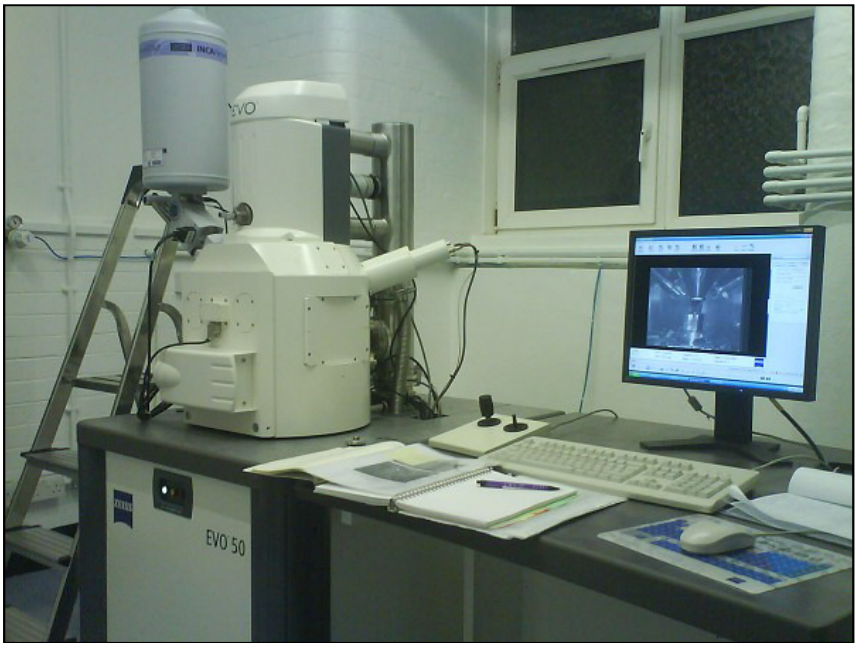

Figure 4.11: Zeiss EVO 50 scanning electron microscope equipped with an Oxford instruments EDX detector

Table 4.4: Specification of Zeiss Evo 50 scanning electron microscope

Item	Value
Resolution	3.0*nm* at 30*kV*
Resolution BSE	4.5nm at 3.0*kV*
Magnification	5X to 1,000,000X

4.6 High speed Camera and illumination

A Photron ultima APX-RS [219], high speed camera was used to observe the LDMD process, shown in Figure 4.12. It can operate at 250,000 *fps* and records frames in AVI format data. Illumination of the melt pool was provided by an Oxford Lasers copper vapour laser [220], giving 511 *nm* and 578 *nm* wavelength light. A narrow pass filter in front of the camera, blocks all other wavelengths and the camera and copper vapour laser were synchronized for maximum illumination during the Laser DMD process.

Figure 4.12: Photron Ultima APX-RS high speed camera

4.7 Xray Diffraction

X-ray diffraction (XRD) is a powerful technique used to uniquely identify the crystalline phases present in materials and to measure the structural properties such as strain state, grain size, phase composition and preferred orientation of these phases.

The identification is done by Bragg's Law, given by Equation.4.4, where n is an integer, λ is the wavelength of the incident X-ray beam and θ is the Bragg diffraction angle. The phase analysis was carried out using a Phillips PW3710 machine with an X-ray diffractometer using CuK_{α} radiation.

$$n\lambda = 2\mathrm{d}\sin\theta \tag{4.4}$$

Laboratory based X-ray diffraction systems use relatively large wavelength radiation, commonly using Cu radiation of ~1.54Å. This method gives low penetration in metallic materials, typically 10s of microns. A method to overcome the low penetration, known as the $\sin^2\Psi$ method has been used to calculate stresses. In this method, the sample is tilted at an angle Ψ to get the principal stress according to Equation 4.5:

(4.5)

Where

= Stress in direction E = Young's modulus *(GPa)*

ν = Poisson's ratio Ψ = Tilt angle *(degrees)*

= d-spacing measured at tilt angle, Ψ (Å)

= The "stress free d-spacing" from approximation measured at $\Psi = 0$ (Å)

Residual stresses were measured using a Bruker AXS D8 Discover laboratory X-ray diffractometer. This equipment has a polycappilary optics X-ray beam and General Area Detector Diffraction (GADDS) detector collecting backscattered X-ray Debye-Scherrer cones. Diffraction peaks were recorded at a 2θ angle of about 128°. 10 Ψ values, from 0 to 45 degrees, were used for each data point, giving a data collection time of 200 *seconds* for each θ value. A Young's modulus of 203 *GPa* and Poisson's ration of 0.32 were used to derive stresses. The equipment is shown for stress measurement is shown in Figure 4.13.

Figure 4.13: The Bruker AXS D8 Discover laboratory X-ray diffractometer configured for stress measurement

Chapter 5. Stress Formation and Cracking During Deposition of Inconel 718 on Ti-6Al-4V

5.1 Introduction

There has been a growing interest in the use of multi- functional materials with significant physical properties difference in a past few decades. The functionally graded materials (FGM) concept has been extended to a variety of materials in various applications [221]. In FGM, the composition and properties are customised to suit specific engineering applications [222]. The development of FGMs by laser direct metal deposition has received much attention [223, 224]. The freedom to selectively deposit different elemental powders at discrete locations using multiple powder feeders makes LDMD well suited for the fabrication of FGMs.

Deposition of dissimilar materials is different from similar materials deposition for the following reasons: (1) the thermo-physical properties of the substrate and clad materials are, in general, different, and this difference can influence the heat transfer during deposition; (2) the magnitude of stress differs due to the difference in thermal expansion/contraction properties of the two or more materials; (3) composition becomes a parameter that can vary over a wide range across the melt pool and consequently, there does not exist a single liquidus isotherm that defines the solid-liquid interface. All layered fabrication processes based on melt deposition, such as the laser

deposition process, suffer from residual stresses in the final part, due to the large temperature gradients between the hot melt zone and the cold substrate [225].

This chapter describes a study on LDMD of two dissimilar aerospace alloys i.e. Inconel 718 and Ti-6Al-4V and the results obtained. Instead of gradual change in the composition, normally observed in various FGMs, the deposition of pure Inconel 718 on top of Ti-6Al-4V substrate has been carried out. Laser pulse parameters and the powder mass flow rates have been utilised to investigate their effect on the cracking susceptibility of the final deposited structures.

5.2 Previous Work

There is rather limited work on the deposition of Inconel 718 and Ti-6Al-4V. Domack and Baughman [226] utilised the flexibility of a Laser Engineered Nest Shape (LENS) system to deposit a functionally graded structure of Ti-6Al-4V and Inconel 718. They used a premixed powder blend, with the composition adjusted in steps of 10 percent by volume from 100 percent Ti-6Al-4V to 100 percent Inconel 718. Macroscopic cracks formed before the full transition from Ti-6Al-4V to Inconel 718 was achieved, but the cause of these was not investigated in any detail in the reported work. In another detailed study of a Titanium and Nickel graded structure by laser deposition, Lin *et al* [227] investigated the solidification behaviour and phase evolution of Ti-6Al-4V and Rene 88 DT. All proportions of the constituent alloys were not investigated; the compositional gradient tested ranged from 100 percent Ti-6Al-4V to Ti-6Al-4V with 38 percent Rene 88 DT. In their work, they did not discuss any cracking observed during their experiment. There have been a few reports [228-230]on the laser welding of titanium and nickel alloys but

the work was not particularly successful. In spite of this, less work has been reported in this field related to laser deposition of dissimilar materials.

5.3 Experimental Procedure

A series of experiments were performed to investigate single layer laser deposition of Inconel 718 onto a Ti-6Al-4V substrate in a setup shown in Figure 5.1. Two sets of samples for each parameters combination were used in order to analyse the effect of diode laser pulse parameters and powder flow rate, with varying pulse length and period. Pulse length and period has been shown schematically in Figure 5.2, with pulse length and period ranging from 20 *ms* to 50 *ms*.

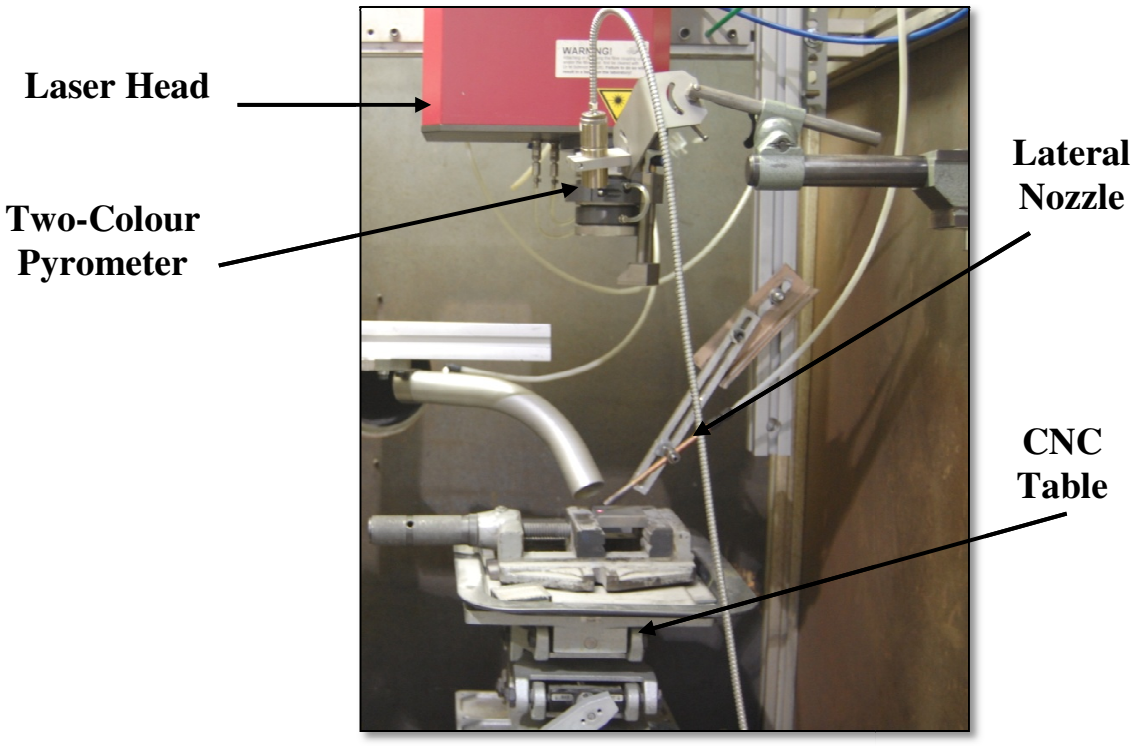

Figure 5.1: Experimental setup

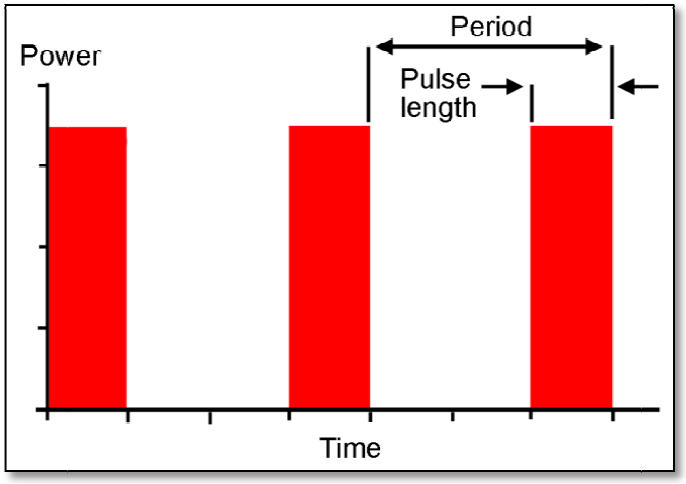

Figure 5.2: Wave definition

Inconel 718 powder (nominal composition of powder given in Table 5.1) was deposited on a Ti-6Al-4V substrate. The substrates were machined into 48 ×50 × 11 *mm* rectangular coupons. These substrates were first sand blasted in a Guyson sand blaster and then degreased using ethanol to aid deposit adhesion. In this study, 9 samples were produced using the set up shown in Figure 4.1. A 1.5 *kW* Laserline LDL 160-1500 diode laser, producing approximately equal amounts of 808 and 940 *nm* laser radiation operated in either continuous and pulsed mode, was used to carry out the experiments. The beam size was experimentally measured by exposing an infrared detector card with a sensitivity of 1.75×10^{-9} W/mm^2, to the pilot beam (20 *mW*) of the diode laser and was found to be 2.5 *mm* (slow axis) × 3.5 *mm* (fast axis) with top hat (approximately uniform) power distribution.

Table 5.1: Nominal composition of Inconel 718 [231]

Ni	Cr	Cb	Mo	Ti	Al	Co	Si	Mn	Cu	C	P	Fe
53.4	18.8	5.27	2.99	1.02	0.5	0.17	0.12	0.07	0.07	0.03	0.01	Bal

The absorptivity of diode laser wavelengths (808 and 940*nm*), was measured using a SD2000 fibre optic spectrometer was 45 ~ 51 %. The substrate was tightly secured on a clamp, and then mounted onto a 3 axis position and

motion control system. The Inconel 718 powder used was gas atomised, giving particles with approximately spherical morphology, and a powder size distribution of 53–150 μm. A disc-type powder feeder was used to deliver them to the nozzle. The deposition area was also shrouded by an Argon gas flow from a side nozzle directed at the melt pool. The gas pressure for all the experiments was set at 5 *bars*. The temperature of the melt pool was measured every 0.01 seconds by using a two colour pyrometer with a measurement range from 772 *K* to 2272 *K*. The pyrometer was fixed close to the laser head such that it always recorded the temperature of melt pool created by the laser. The experimental arrangement was such that the pyrometer could not be placed directly above the measured point and hence was fixed at an angle. This arrangement made the pyrometer spot elliptical. For an accurate measurement of the maximum temperature, the spot size of the pyrometer should be smaller or at least equal to the laser beam spot size [232, 233]. In this case, however, as the pyrometer spot was at its focal position, its spot size was significantly less than that of the laser beam spot size. A velocity of 4 *mm/s* was maintained during the deposition of all the samples.

During the deposition process, the sample moved parallel to the fast axis of the beam. A side feed powder nozzle was positioned at 45° angle to the vertical and in line with the direction of motion. Front feeding was maintained throughout for all the samples.

Parameters were varied specifically to enable the study of the effect of powder flow rate and the duty cycle. A mean power of 600 *W* was used as established from previous experiments. This provided a specific energy appropriate for the deposition of both Inconel 718 and Ti-6Al-4V at the chosen traverse speed and beam area and was kept constant throughout. The experimental parameters used are shown in Table 5.2.

Table 5.2: Experimental Parameters used in the experiments

Sample No.	Peak Power (W) [A]	Pulse length (ms)	Period (ms)	Duty Cycle [B]	Powder mass flow rate (g/s)
1	1500	20	50	0.4	0.358
2	857	35	50	0.7	0.358
3	600	-	-	1	0.358
4	1500	20	50	0.4	0.586
5	857	35	50	0.7	0.586
6	600	-	-	0.1	0.586
7	1500	20	50	0.4	0.674
8	857	35	50	0.7	0.674
9	600	-	-	1	0.674

[A] Mean power = 600 *W* in all cases

[B] Duty cycle = pulse length / period

After the experiments, un-cracked samples were held in a fixture on HURCO 425 Mark 2 sink type spark erosion Electric Discharge Machine (EDM). Samples were longitudinally machined till they reached the middle of the clad by using Copper as a tool electrode.

After machining the samples, residual stresses on one set of un-cracked deposited tracks (S1-S3) were measured using a Bruker AXS D8 Discover laboratory X-ray diffractometer. An iron anode X-ray tube (λ = 1.9360 Å) at 30*kV* and 20*mA* was used and the 311 diffraction peak was recorded at a

"2θ" angle of about 128°. 10 ψ values, from 0 to 45 degrees, were used for each point, giving a data collection time of 200 *seconds* for each θ value. A Young's Modulus value of 200 *GPa* and Poisson's ratio value of 0.30 [234] were used to calculate residual stresses.

X-ray diffraction phase analysis was carried out using a Philips X'Pert MPD X-ray diffractometer with a Cu anode to provide radiation of 1.5405 Å wavelength. For each sample, the deposited tracks were separated from the substrate and the interface was scanned between 2θ angles of 0 and 85 degrees with a 30 second scan step time. To perform the X-ray diffraction phase analysis, samples 1, 2 and 3 were broken from the substrates, forcefully if necessary. X-ray diffraction phase analysis was then carried out on the bottom side of the clad and on the top of the substrate where individual tracks were deposited.

After stress analysis, another set of un-cracked samples was transversely sectioned and mounted in Struers epoxy resin. All samples were polished to Ra=1μm using standard metallographic techniques. The samples were electrolytically etched in 10% Oxalic acid to reveal the microstructure. These microstructures were then evaluated using a Hitachi SEM. Grain or interdendritic spacing was measured by the linear-intercept method.

5.4 Results

5.4.1 Microstructure and Visible Cracking

Examination of the final Ti-6Al-4V and Inconel 718 structures showed that only three out of the nine samples were crack-free. Sample 1 (0.4 duty cycle, low powder mass flow rate), sample 2(0.7 duty cycle, low powder mass flow rate) and sample 3(continuous wave, low powder mass flow rate) showed no signs of cracking. The cross-section of sample 1 is shown in Figure 5.3.

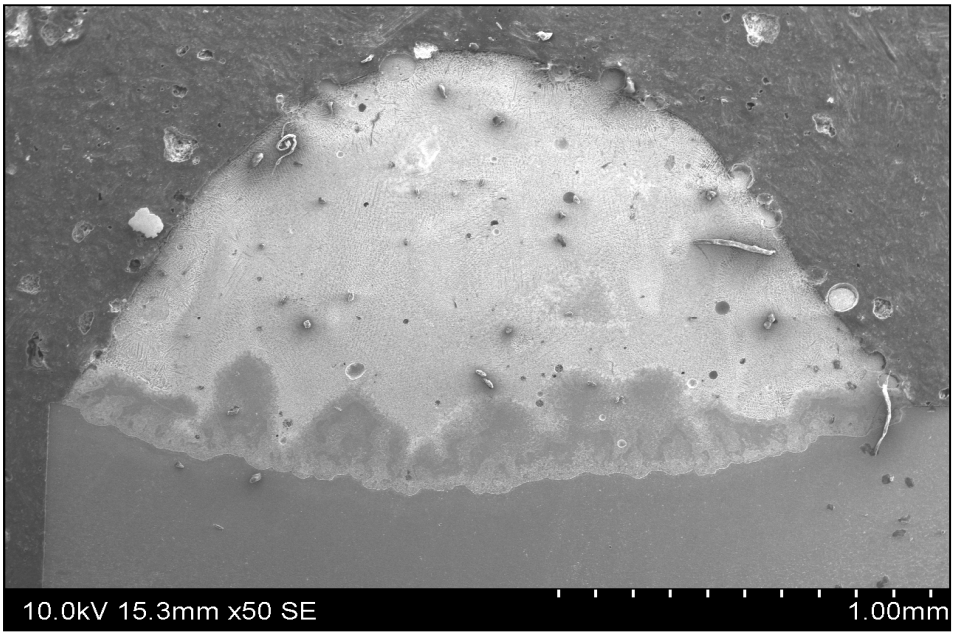

Figure 5.3: Micrograph of Crack free sample at 0.4 duty cycle and powder flow rate of 0.358 g/s

All other samples developed severe cracks, initiated at the interface of the clad and the substrate. A cross section of the cracked interface of sample 4 is shown in Figure 5.4.

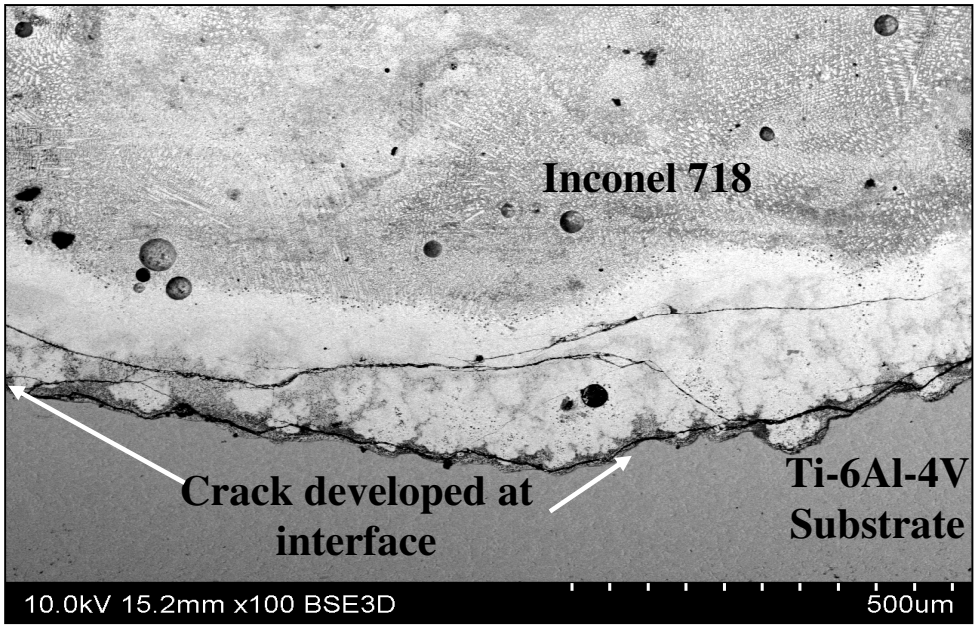

Figure 5.4: Cracked interface between Ti-6Al-4V and Inconel 718 in sample 4

SEM of samples, as shown in Figure 5.5, reveal a dendritic structure found in the clad region. Variation of the grain size is plotted against the duty cycle in Figure 5.6. It must be noted that with an increase of duty cycle, the grain size is reduced. This behaviour is also shown for an increase in the powder flow rate. It is likely that smaller grains resulted due to fast cooling experienced during the continuous wave deposition process in which low power values were used as compared to the pulsed deposition process. Pulsed laser deposition, due to its high instantaneous power has a slow cooling rate, thereby resulting in larger grains. Similar conclusions were drawn by Xinhua *et al* [235], and Kelly and Kampe [236] in their work on the Ti-6Al-4V deposition process.

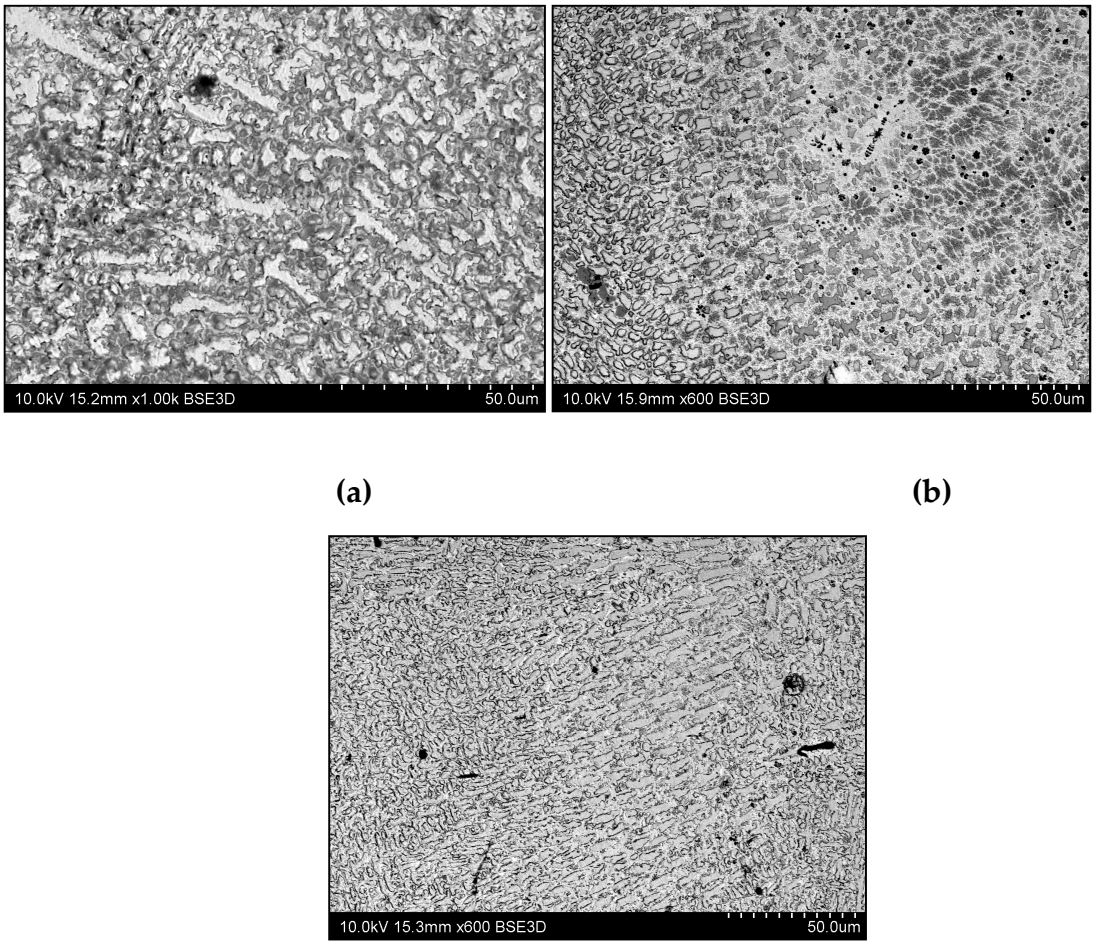

Figure 5.5: Dendritic structures in Samples 1-3(a-c)

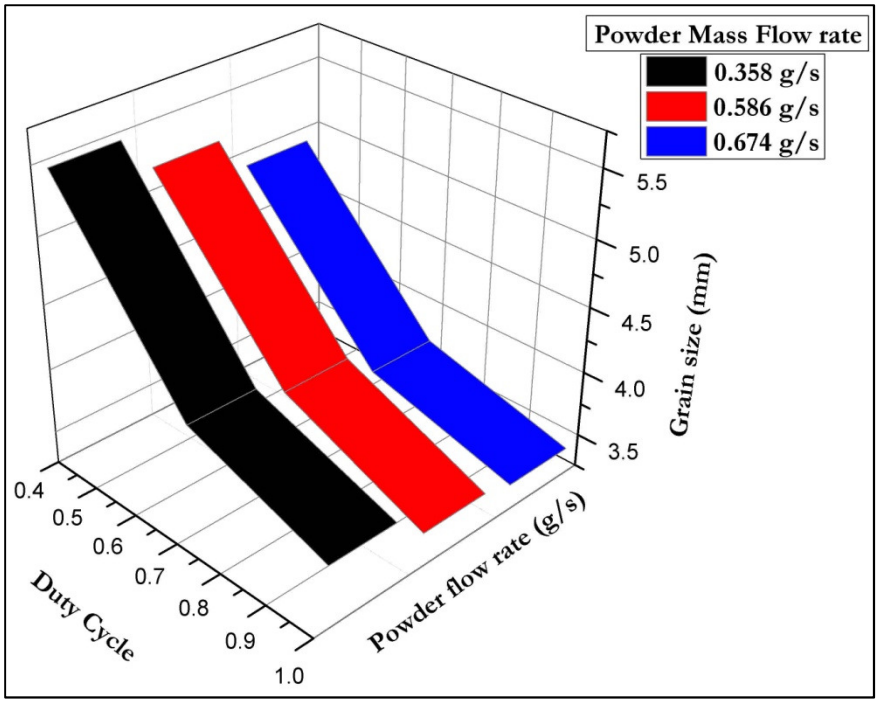

Figure 5.6: Grain size variation with duty cycle and powder mass flow rate

5.4.2 Phase Analysis using X-ray Diffraction

Different phases constitute the microstructure of the melt pool and these are identified from the composition analysis using X-ray diffraction. In this work, despite the small size of the samples, clear spectra with well defined diffraction peaks were obtained. Figures 5.7 and 5.8 show X-ray diffraction spectra for the bottom of clad and the top of substrate of all the samples. The XRD patterns for all the samples look very similar except in sample 6 which reveals the presence of $TiNi_3$: All these results indicate the presence of Ti_2Ni and Ti in all of the samples. Quantification of the phases present was not possible.

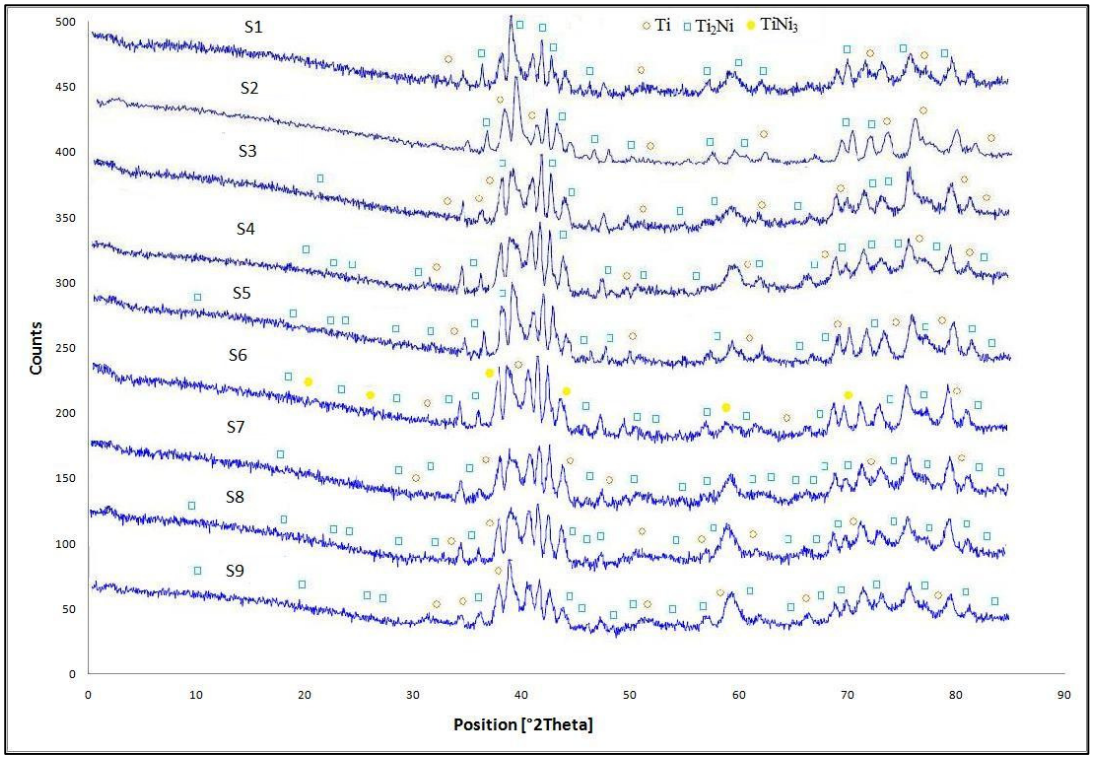

Figure 5.7: XRD diffraction patterns showing the presence of various phases at the bottom of clad

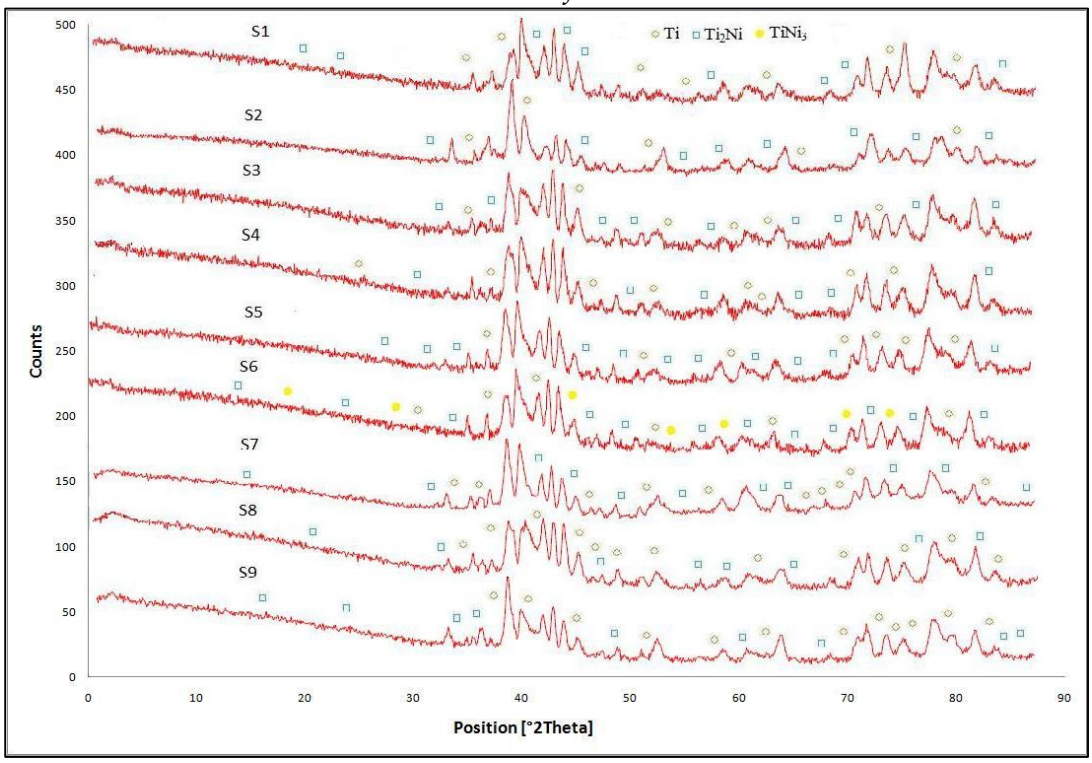

Figure 5.8: XRD diffraction patterns showing the presence of various phases at the top of the substrate

5.4.3 Effect of duty cycle on temperature

Figure 5.9 shows a 3D graph for the variation of maximum temperatures attained during the deposition with duty cycle and for three powder mass flow rates used. It is evident that an increase in the duty cycle has an inverse effect on the maximum temperature attained during deposition. This can be attributed to the high instantaneous power used in low duty cycle laser deposition process. Moreover, an inverse relation between the temperature and powder mass flow rate has also been observed. Temperature variations during high duty laser deposition are more drastic as compared to those with a low duty cycle.

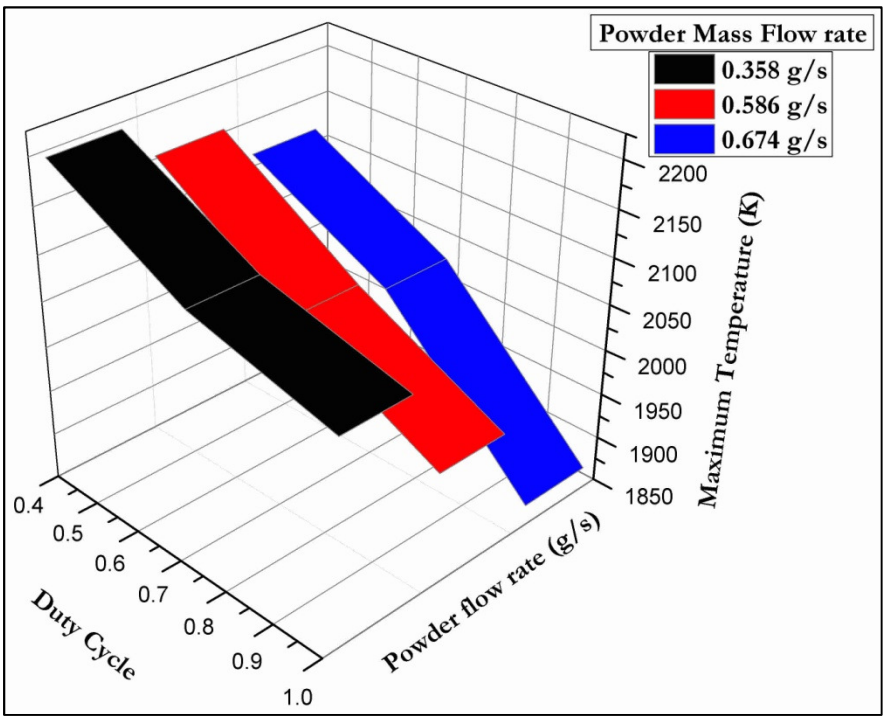

Figure 5.9: Effect of duty cycle on temperature for different powder mass flow rates

5.4.4 Effect of duty cycle on clad dimensions

Clad heights ranging from 0.78 *mm* to 1.19 *mm* were observed across the range of parameters used in the experiments, with maximum clad height observed at 0.7 duty cycle (Figure 5.10). An inverse trend was observed for the clad width, as shown in the Figure 5.11; with lowest clad width of 2.1*mm*

at the high powder flow rate, continuous wave deposition sample, and 2.23 *mm* at low powder flow rate, 0.4 Duty cycle deposition sample. In comparison to the clad height, the effect of duty cycle on clad width is more subtle.

It can be concluded from these results that the clad dimensions are determined by instantaneous power and hence the maximum temperatures attained during different duty cycles.

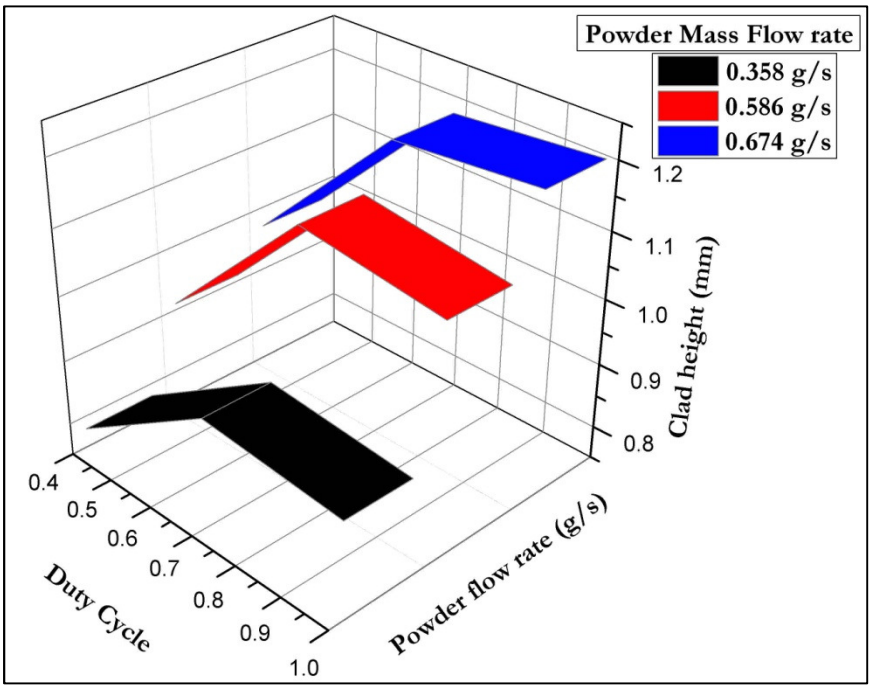

Figure 5.10: Effect of duty cycle on clad height for various powder mass flow rates

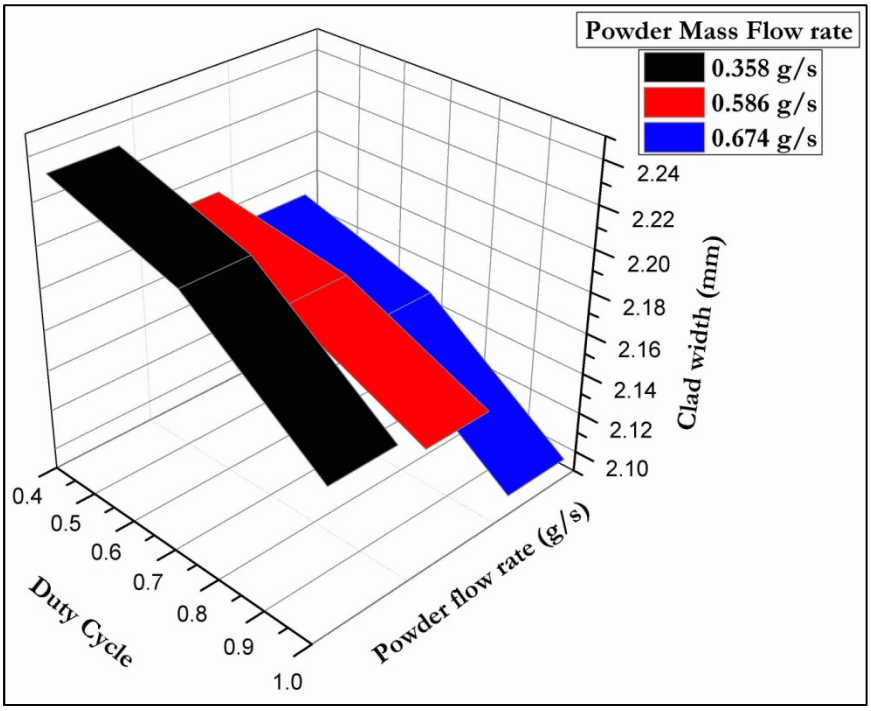

Figure 5.11: Effect of duty cycle on clad width for different powder mass flow rates

5.5 Residual Stress Results

Un-cracked samples were machined in a y-z plane as shown in Figure 5.12. Line scans were carried out to measure vertical "σ_{yy}" and longitudinal "σ_{zz}" residual stresses in the middle of the clad and along the track length of un-cracked samples 1-3. The measured distributions are plotted for three different duty cycle depositions in Figures 5.14, 5.16 and 5.17 respectively.

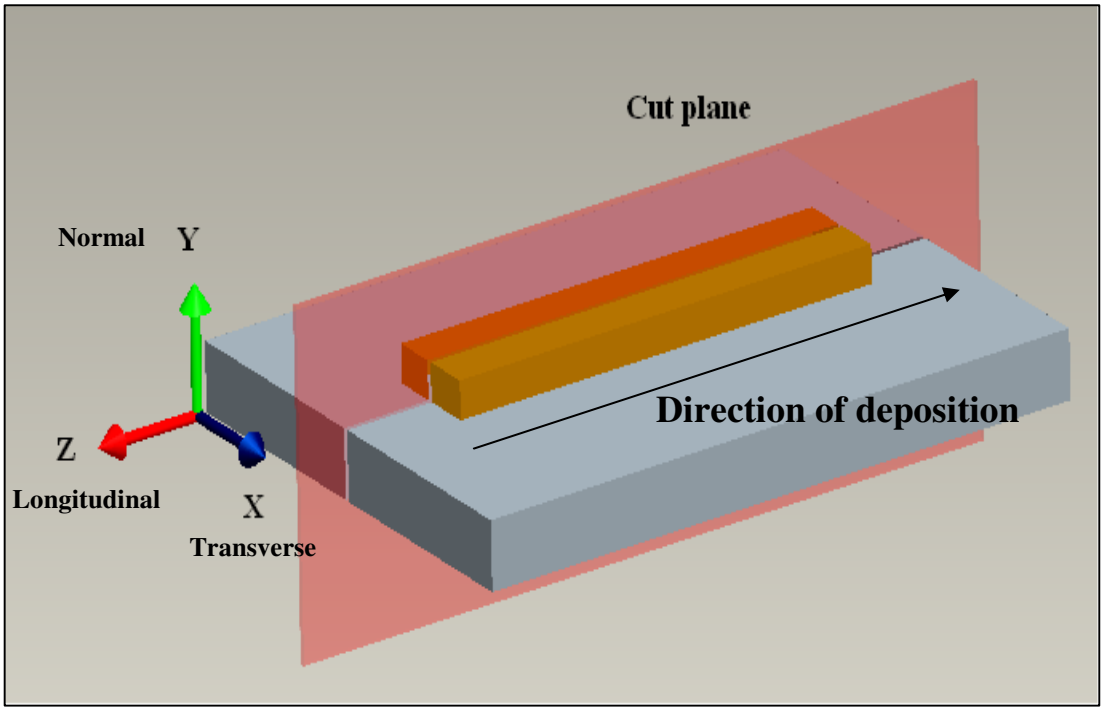

Figure 5.12: Substrate and clad geometry

Figures 5.13 -5.15 show an approximately parabolic distribution of residual stresses in the z-direction with a maximum calculated stress close to the centre position. An increase in tensile stresses in the longitudinal direction with increasing duty cycle is also noted. The maximum longitudinal tensile stress "σ_{zz}" value of 378 *MPa* is observed in the continuous wave deposition case midway along the clad and the residual stress decreases at the edges of the deposited tracks, in agreement with stress balance at a free surface.
For the samples 1, 2 and 3, the normal residual stress "σ_{yy}" appears to be tensile at the limits of the clad and then changes to compressive towards

interior of the wall.

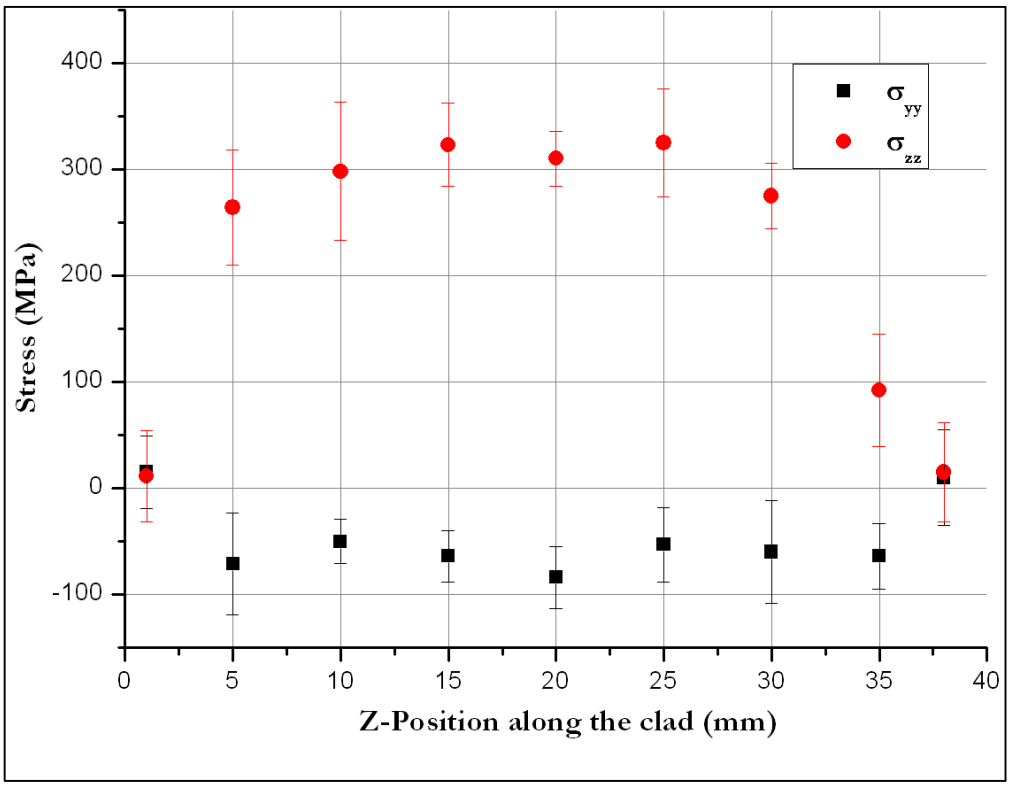

Figure 5.13: Stress result in sample 1, 0.4DC Pulsed Laser Deposition

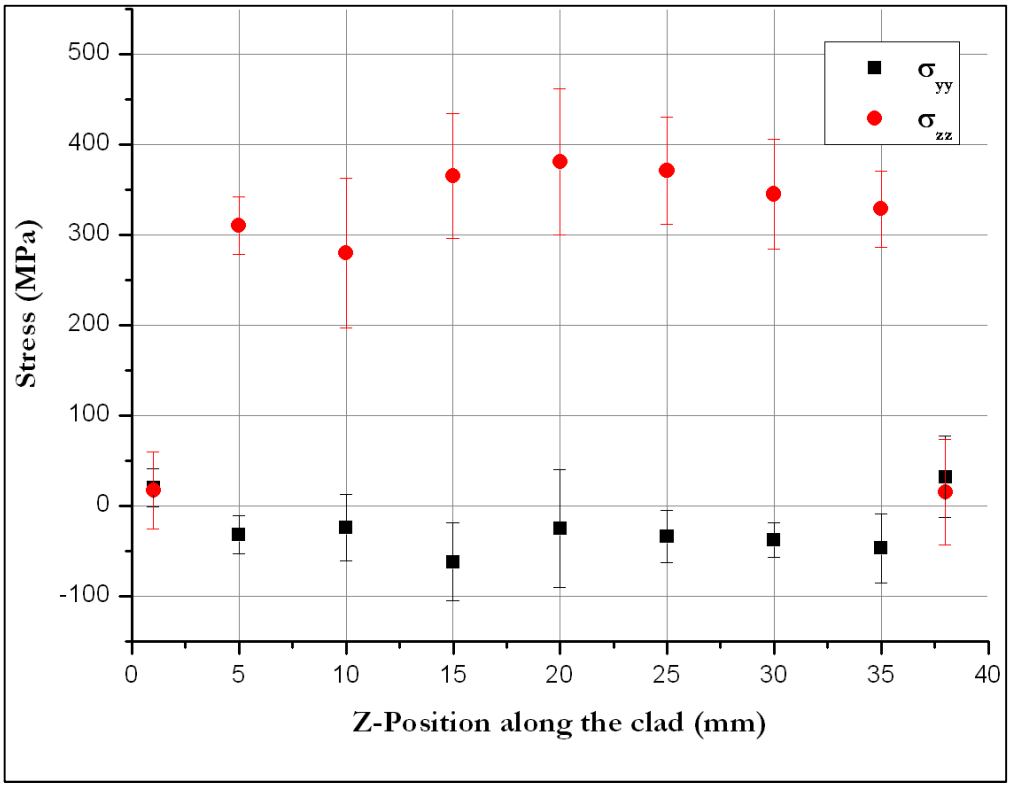

Figure 5.14: Stress result in sample 2, 0.7DC Pulsed Laser Deposition

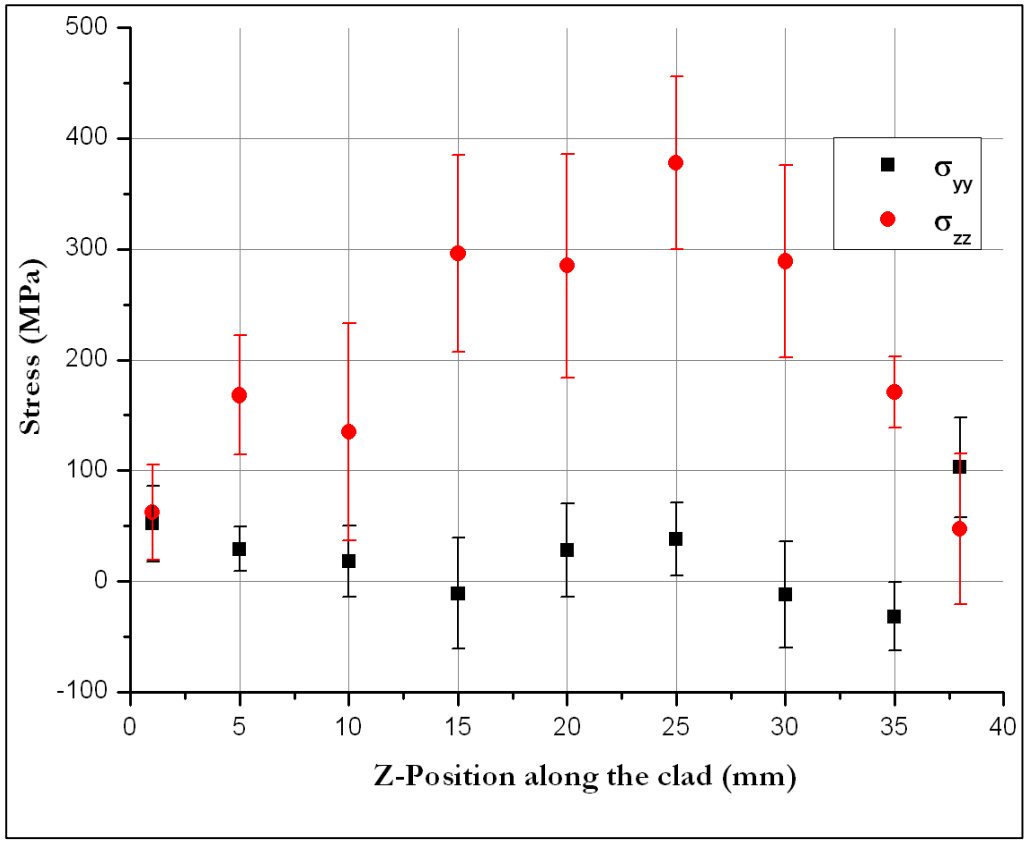

Figure 5.15: Stress result in sample 3, Continuous Wave Laser Deposition

5.6 Discussion

A study of laser pulse parameters has shown that by varying pulse length and duty cycle, considerable control over clad and grain morphology can be achieved. Varying duty cycle has shown some scope for controlling high power diode laser deposition microstructures. At constant specific energy, continuous wave deposition is found to produce the finest grain structure. However these changes in microstructure come at the expense of variations in clad height and more significantly clad width.

Factors which can cause deposited clads to crack can be divided into metallurgical and mechanical factors. Metallurgical factors mainly concern phase relationships, while mechanical factors are related to stress behaviour.

Considering metallurgical factors; XRD results show the presence of Ti_2Ni and $TiNi_3$ in all of samples whether cracked or un-cracked. Ti_2Ni and $TiNi_3$ are recognised as one of the brittle phases responsible for cracking in welding and their presence in all samples suggest that an appropriate selection of laser parameters may not be sufficient to avoid the production of such intermetallics.

Taking into account the mechanical factors; stresses can be generated by constrained elastic expansion or contraction due to transient temperature gradients, and thermal expansion coefficient mismatch, and changes in specific density due to solid phase transformations. The amount of heat input determines the cooling rate, which is inversely proportional to the square of the melt pool length [237]. Thermal strains caused by high cooling rates can increase the crack initiation rate, but higher thermal gradients results in a rapid cooling rate which has been shown previously in case of a weld, can also reduce the grain size to increase solidification and crack resistance [238].

The residual stress profiles have been found to be weakly dependent on the laser pulse parameters, most notably an increase in tensile stress gradient with increasing duty cycle, but the maximum residual stresses are largely unaffected. This can be explained by the fact that the cooling rate for the continuous wave deposition samples are higher as shown by the clad width. Consequently, a larger proportion of residual stress in the longitudinal direction is observed as compared to the shorter pulse length or low duty cycle samples. This kind of conclusion is also reported by Moat *et al* [239] who found large tensile longitudinal stresses at the mid position of the wall. The vertical stresses "σ_{yy}" are tensile near the vertical free surfaces which are balanced by the compressive stresses in the interior of the track.

It is observed that the stresses developed during low powder feed rate deposition (continuous and pulsed) are less than the yield strength of either

of the two materials (Inconel 718 and Ti-6Al-4V) and the phases which are present in the samples are also similar. The measurement of residual stresses in this work is limited only to low powder mass flow rate deposition. It is necessary, however to establish the residual stress behaviour generated during the medium and high powder mass flow rate deposition. Numerical modelling of the deposition process may provide the best means of estimating these stresses. The next chapter will cover the numerical modelling aspects of the deposition process.

5.7 Conclusions

Various pulse parameters for a diode laser have been used to exploit the effects of direct laser metal deposition of Inconel 718 on Ti-6Al-4V substrate. The driver for this study is to understand and analyse the deposition of Inconel 718 and Ti-6Al-4V by examining the stress fields and phases evolved during LDMD. XRD techniques have been utilised for the residual stresses and phases generated during the deposition process. It has been found that two brittle phases i.e. Ti_2Ni and $TiNi_3$ are produced during the deposition of all of the samples. It has also been observed that high longitudinal tensile stresses are developed along the tracks during the deposition process that increased with the increase in duty cycle.

Chapter 6. Finite Element Analysis of Dissimilar Material Deposition and Stress Formation

6.1 Introduction

Engineering problems in various applications have been addressed by deriving the appropriate differential equations which relate the variables for the problem through basic physical principles such as equilibrium, conservation of mass, conservation of energy etc. However, once formulated, solving the resulting set of mathematical equations is often impossible, especially when the resulting systems are non-linear. To tackle such problems, numerical methods offer a viable alternative thereby producing an approximate solution for the given problem. Various numerical techniques such as the finite element method have been developed over many years.

The Finite Element Method (FEM) is the most common and powerful technique used in structural mechanics. In FEM, a complex region defining a continuum is discretised into simple geometric shapes called elements. Depending upon the problem, each element can be 1D, 2D or 3-dimensional. The properties and the governing relationships are assumed over these elements and expressed mathematically in terms of unknown values at specific points in the elements called nodes.

The solution of a typical stress problem through FEM is usually achieved in a series of steps as follows:

a) Dividing the structure into sub-regions or elements by creating a mesh that represents the physical problem

b) Finding the stiffness of each element

c) Assembling the individual element stiffness matrices into a global stiffness matrix for the whole system

d) Using stiffness to calculate the displacement field in a response to the specified loading

e) Using the displacement field to calculate stresses and strains for the whole system

Depending upon the nature of the given problem, various types of finite element analyses, namely; thermal, structural, fluid flow, coupled-field such as thermo-mechanical, etc are possible. Attention is focussed on thermo-mechanical analysis in this chapter.

As a result of the wide application capabilities, several finite element software packages such as ANSYS, ABAQUS, ADINA, ALGOR, FLUENT, MARC, NASTRAN, etc are available. The choice between different packages is based on the capability of the package for performing the intended type of analysis successfully with the availability of necessary options and functions in the software.

There have been several studies based on numerical modelling of the laser cladding/deposition process. Earlier work on laser cladding was focussed on thermal or heat transfer aspects of the laser process. Weerasinghe and Steen [240] used a circular bead section in a 3D finite difference model to calculate thermal fields. Kar and Mazumder [241] considered the dissolution of powder and the effect of process parameters on the composition of the clad in a one-dimensional discretisation study. Picasso and Rapaz [242] used a 2D approach to find the shape of the melt pool and interaction between the laser and the material. There have been several studies that have investigated the

transport phenomena in and around the molten pool, including solidification, microstructure formation, and the effects of powder injection. Toyerskani *et al* [243, 244] proposed a model to predict the clad geometry as a function of time and process parameters including laser pulse shaping, velocity of the beam and laser pulse energy. Qi and Mazumder [245] used a finite volume model to simulate heat transfer, phase changes, and fluid flow in the molten pool during the deposition process. Bontha *et al* [246] calculated cooling rates and thermal gradients at the onset of solidification which were numerically extracted from the 2D Rosenthal solution; thus developing dimensionless process maps for the prediction of solidification microstructure. Kelly and Kampe [247] developed micro-structural evolution maps using the results of their thermal model to qualitatively determine the equilibrium and non-equilibrium transformations during deposition of Ti-6Al-4V. Wang and Felicelli [248] developed a model to predict the temperature distribution and phase transformation in deposited stainless steel 410 (SS410) during the Laser Engineered Net Shaping (LENS™) rapid fabrication process.

LDMD manufactured products have complex residual stress fields that are often unwanted. Especially, tensile residual stresses have a adverse effect on the performance of a component as they reduce the effective fatigue and tensile properties of the structure [249]. In addition, residual stresses can cause distortion in the component resulting in a mismatch between the final geometry and the designed geometry.

Several studies have been carried out by various researchers to model the residual stress fields in the deposition process. First calculations of the thermo-mechanical history of the parts deposited by laser cladding were published in late 1990s [250, 251]. Authors used one- dimensional models for calculating the residual stress after the deposition of layers. Dai and Shaw [151] calculated stresses in multi material (Porcelain and Nickel) parts

without considering the influence of phase transformations on residual stresses. The first three-dimensional simulation of the deposition process with phase transformation and transformation plasticity considerations was carried out by Ghosh and Choi [252, 253]. Bruckner *et al* [254] evaluated the pre and post weld heating effects on the development of residual stresses in a single layer deposition process.

Despite considerable progress over the past 15 years, there is still room for refining the simulation tools that can predict the required results and the effects of changing the process parameters. Moreover, each numerical model is process specific due to the boundary conditions, work piece geometry, availability of material properties and loading involved. Any change in the boundary conditions, loading or geometry requires the development of a new model which is sometimes considered a limitation. However, the accuracy of results, the ability to incorporate complex boundary conditions and the ability to carry out extensive post processing analysis on results counterbalance this limitation.

6.2 Finite element model description

Due to the intrinsic three-dimensional nature of loads, boundary conditions and geometry usually involved in the deposition processes, a sequentially coupled, three-dimensional thermo-mechanical FEM model was built using a commercial FE programme, ANSYS. The geometry was first created for the substrate and then for the moving beam. An elemental heat input method was used to model the moving laser beam, which is modelled as a moving heat flux which traverses step wise in the scanning direction, changing its spatial position in small time steps. Each beam area on the substrate surface is subjected to a heat load for a time period equal to the interaction time dictated by the processing speed and the duty cycle. As a rectangular beam

shape was used to replicate the laser output. Based on the experimentally determined height of the clad, a clad geometry was generated on top of the substrate.

Owing to the potential difficulty in formulating a model for the LDMD process, particularly if all the processing parameters are to be taken into account, the following assumptions were made to simplify the analysis.

a) Mass transfer, fluid flow and phase transformation are uncoupled from the analysis by assuming that the residual stress generation in laser direct metal deposition process is primarily a thermal driven process [151, 255, 256]. This assumption reduces the model to a heat transfer and structural problem.
b) Powder particles do not become molten until they are injected into the molten pool in the deposition region; an assumption used previously by various authors [257, 258]
c) The work piece is initially at 293K. Both the work piece and the coordinate system are fixed and the laser beam moves in the negative z-direction with a constant velocity, of 4 *mm*/*sec*, as shown in Figure 6.1.
d) Heat losses due to radiation are assumed insignificant since high temperatures occur only for very short time periods [259].
e) Heat losses from melt pool due to convection are ignored.

With the above assumptions, a sequential thermo-mechanical analysis was carried out. Transient temperature distribution results from the thermal analysis were applied as the body loads to the structural or mechanical model.

Owing to the phenomena of melting and solidification, which are associated with the laser deposition process, solutions to modelling simulation problems with the process are often path dependent and thus require the use

of temperature-dependent material properties in their analysis. In that respect, the specific temperature dependent thermal and mechanical properties (see Table 4.2 and Table 4.3) are used in the analysis.

6.2.1 Thermal Analysis

Using the commercial software package, ANSYS 11.0, the simulation considered a transient thermal analysis on a 3D model of the geometry shown in Fig. 6.1. The geometry is a representation of the physical mapping of the clad and substrate assembly under investigation, which represents the individual experimental sample. Simulation has been carried out for each individual experimental run as defined in Chapter 5 Table 5.2. A 3D thermal model was developed using a top hat (approximately uniform) power distribution heat source and three dimensional 'Solid70' element. The clad region, where fusion takes place and temperature gradients are expected to be most severe, was assigned the finest mesh and regions remote from the clad were assigned a relatively coarse mesh. Simulation of the heat source, from the moving laser beam was achieved using the ANSYS Parametric Design Language (APDL) (see Appendix A). This was such that along the beam's path of scanning the heat source is moved from each surface area element (within its size of 2.5 x 3.5 mm^2) to the next at a scanning speed of 4 mm/s.

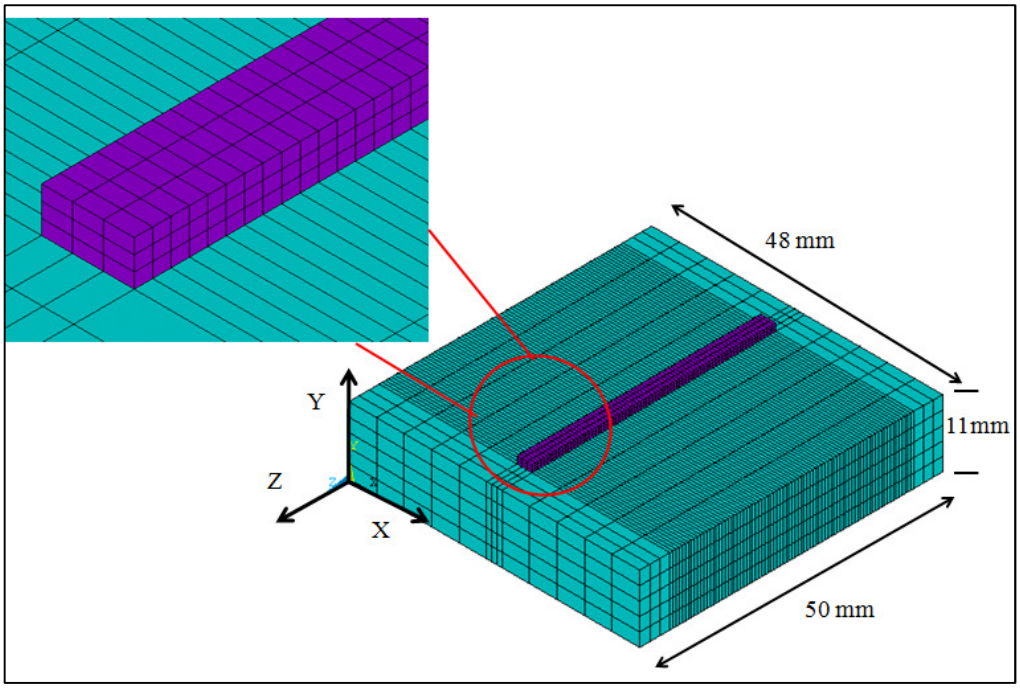

Figure 6.1: Three dimensional FE mesh for the substrate and clad

A FE solution for a transient thermal problem is obtained by solving numerically the 3D heat conduction equation [260]:

$$\frac{\partial}{\partial x}\left[k_{xx}\frac{\partial T}{\partial x}\right]+\frac{\partial}{\partial y}\left[k_{yy}\frac{\partial T}{\partial y}\right]+\frac{\partial}{\partial z}\left[k_{zz}\frac{\partial T}{\partial z}\right]+\beta q'=\rho C_p\frac{dT}{dt} \tag{6.1}$$

Where T is the temperature field variable, t is time, x, y and z are the spatial coordinates; k is thermal conductivity, ρ is density, C_p is the specific heat and q' is the initial laser power. Some of the initial laser power q' is reflected from powder in the powder stream, absorbed by lost powder and reflected from the surface; β represents the proportion actually transferred to the substrate. Numerically the value of β was taken as 0.45. this value was reported for the same laser setup by Pinkerton and Li [261].

The initial conditions are:

$$T(x,y,z,0)=T_0 \tag{6.2}$$

$$T(x,y,z,\infty)=T_0 \tag{6.3}$$

Where $T_0(K)$ is the ambient temperature. The convection boundary conditions can be considered as:

$$K(\nabla T.n)|_\Omega = [-h(T - T_{0)}]\,|_\Omega \qquad \text{if } \Omega \notin \Lambda \tag{6.4}$$

Where n is the normal vector of the surface, h is the heat convection coefficient ($Wm^{-2}K^{-1}$), Λ is the area of the laser beam on the substrate (m^2) and Ω is the substrate surface area (m^2).

Thermal boundary conditions were such that all the surfaces exposed to the environment were assumed to be under heat losses by free convection which follow Newton's cooling law with a heat transfer coefficient, h= 20 $Wm^{-2}K^{-1}$ to ambient air.

The effect of the moving laser beam can also be considered as a surface heat source with the boundary conditions as follows:

$$K(\nabla T.n)|_\Omega = \beta\,[I(x,y,z,v,t)[-h(T - T_0)]\,|_\Omega \qquad \text{if } \Omega \in \Lambda \tag{6.5}$$

Where I (Wm^{-2}) is the laser energy distribution on the work piece, v (ms^{-1}) is the velocity of the substrate.

The heat input from the laser beam was set such that a constant specific energy E_a= 17.14 Jmm^{-2} was maintained. Whereas:

$$E_a = \frac{I}{vd_b} \tag{6.6}$$

Where v and d_b are substrate traverse speed and laser beam spot size (diameter) respectively.

Numerical modelling of the powder deposition process involves the element birth and death technique [262]. This technique enables successive discrete addition of new elements to the computational domain. Element birth and death technique was implemented such that before the start of the

simulation, the part of the structure that has not been laid as yet (i.e. clad) is included in the initial computational domain. However, these elements are made passive or killed by assigning them with material properties so that they do not affect the rest of the model. These dead elements remain inactive until they are active or made alive at the proper time step and temperature.

6.2.2 Structural analysis

In a sequentially coupled analysis, the mechanical fields are analyzed following from the already known temperature fields. Extreme ranges of temperatures, high temperature gradients, and a large variation in the temperature rates, all affect the mechanical behaviour. In processes incorporating phase transformation, such as LDMD and laser welding, the change of material structure is affected by phase transformations. Although uni-axial tensile data is available for a large variety of alloys tested over a wide range of temperatures under steady conditions, there is little information on the effect of thermal transients and thermal gradients on the mechanical response, especially for the combination of alloys used in this study. The traditional decomposition of the mechanical response into uncoupled thermal and mechanical components is a first approximation at best.

The structural model considered for the deposition process employed the same geometry as the thermal model. A Solid 185 element with large deflection capabilities was used. The mesh size and time step scheme for structural analysis was similar to that used for thermal analysis.

The method of element birth and death used in the structural analysis was similar to the thermal analysis. At the start of the analysis, all the clad elements were 'killed' and these were reactivated or made 'alive' on reaching the melting temperature. APDL for the structural modelling used during the

simulation is shown in Appendix B. Creep effects were neglected since the time spent by the scanned material at high temperature was very short. During the deposition process, the thermal cycles experienced by the material will give rise to thermal expansion and contraction. Since the thermal history varies from point to point in the work piece, the thermal expansion gradient will originate thermal stresses in the material. In fact, the clad and substrate materials have different coefficients of thermal expansion (CTE) and the substrate un-deformed state is defined at room temperature, whereas the clad comes in contact with the substrate as it solidifies, thus at the clad melting temperature. If the stress state brings a certain material point above the yield strength, plastic strain develops.

The total strains can be mathematically broken down into following major components as [262]:

$$\{\varepsilon\} = \{\varepsilon^{el}\} + \{\varepsilon^{pl}\} + \{\varepsilon^{th}\} \tag{6.7}$$

Where $\{\varepsilon\}$ is total strain vector, $\{\varepsilon^{el}\}$ is elastic strain vector, $\{\varepsilon^{pl}\}$ is plastic strain vector and $\{\varepsilon^{th}\}$ is thermal strain vector.

The mechanical analysis was performed using formulation with kinematic hardening rule and Von Mises yield criterion. No external loading is considered, and constraints are applied on the sides of the substrate so as to prevent rigid body motion, where condition $u_x = uy = u_z = 0$ was prescribed as shown in Figure 6.2.

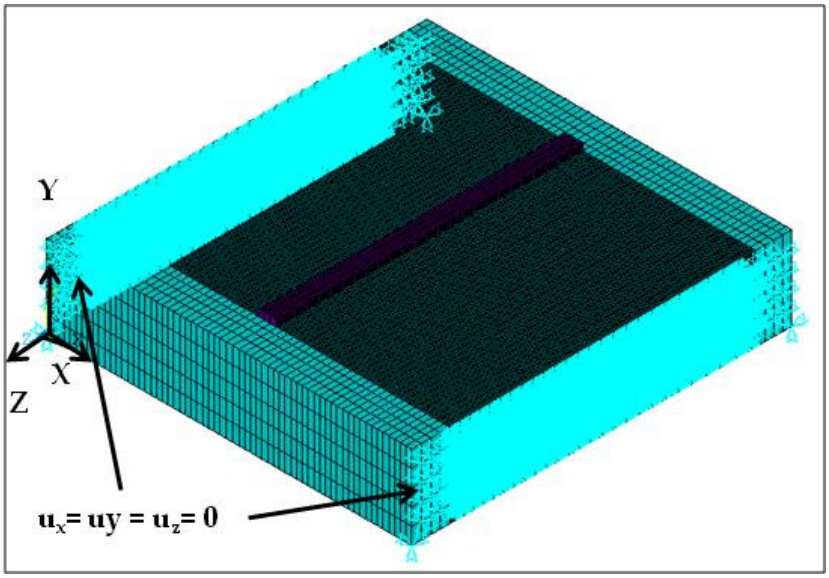

Figure 6.2: FE model with the constraints and coordinate system

6.3 Finite Element Simulation Results and Experimental validation

6.3.1 Temperature Results

A global coordinate system for the model, as shown earlier in Figure 6.1, has x-axis representing the transverse direction, z-axis the laser traverse direction and y-axis the depth. The temperature variation with time in the melt pool was obtained through the model.

During the deposition process, Inconel 718 is progressively evolving and the whole process along with the temperature profiles are shown in Figure 6.3.

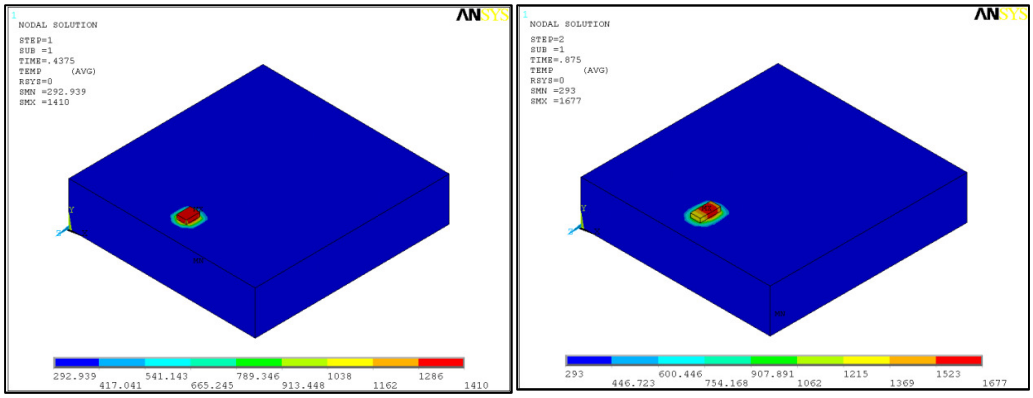

(a) (b)

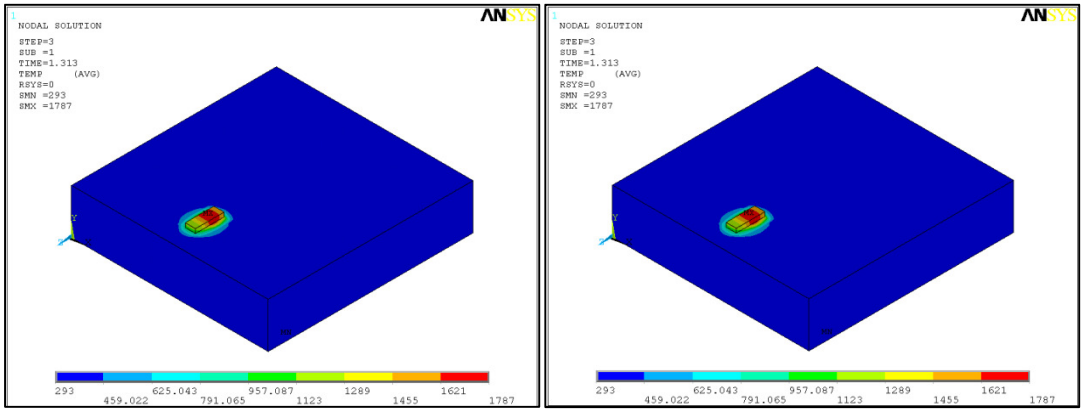

(c) (d)

Figure 6.3:(a-d) Clad evolution and temperature distribution during FEM

A comparison of the finite element results for all the samples showed close agreement with the experimental results shown in chapter 5. Figure 6.4 shows the simulated results with those measured for sample 3 (Chapter 5, Table 5.2).

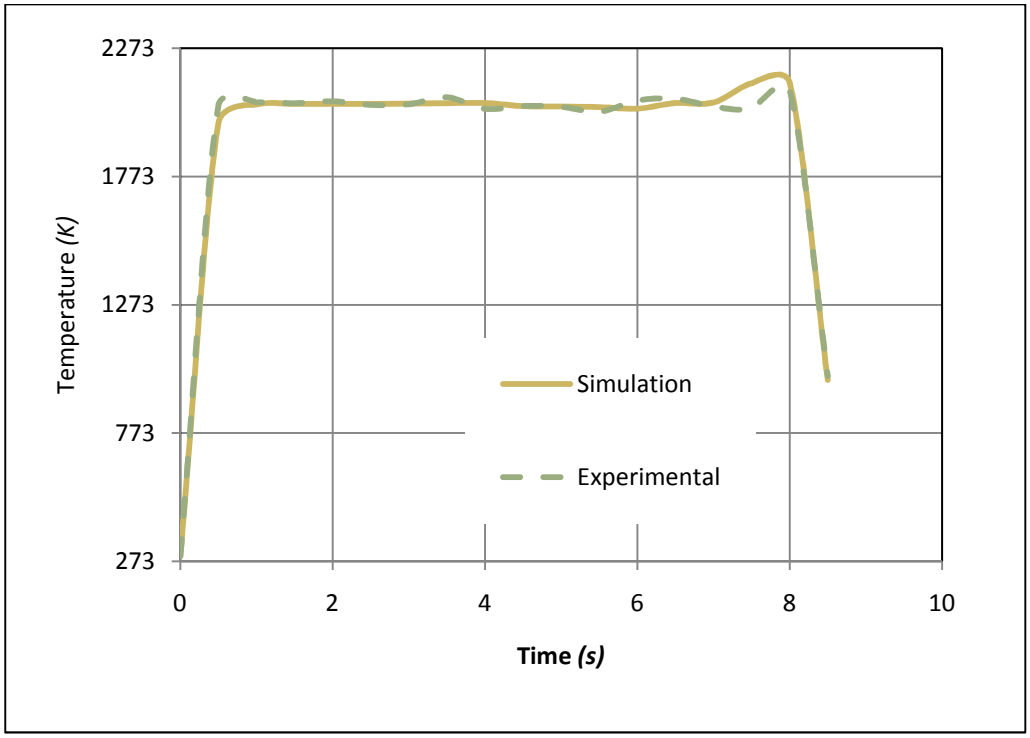

Figure 6.4: Temperature vs. Time-comparison of simulation results with experiments (sample 3) at the melt pool using CW

6.3.2 Residual Stress Results

6.3.2.1 Residual Stress calculation in the clad

Comparison of the finite element modelling results with the experimental measurement has been shown in Figures 6.5-6.7. Residual stress distributions of normal and longitudinal stresses are taken in the middle of the clad and along the track length of the deposited clad for sample 1, 2 and 3 (Chapter 5, Table 5.2). The corresponding data points from the experimental measurement presented in Chapter 5 are superimposed in the plot. Finite element model results are in a fairly good agreement with the experimental results. The normal stress component, 'σ_{yy}' is compressive in the interior of the wall along the z-direction, while tensile stresses are observed at the edges of the clad. From the simulation, a maximum 'σ_{yy}' value of 69.474 *MPa* at the start of clad and 38.644 *MPa* at the end of the clad

is obtained in sample 1. The stress component, 'σ_{zz}' is tensile and its maximum value in 0.4DC pulsed wave deposition is 349.94 *MPa*.

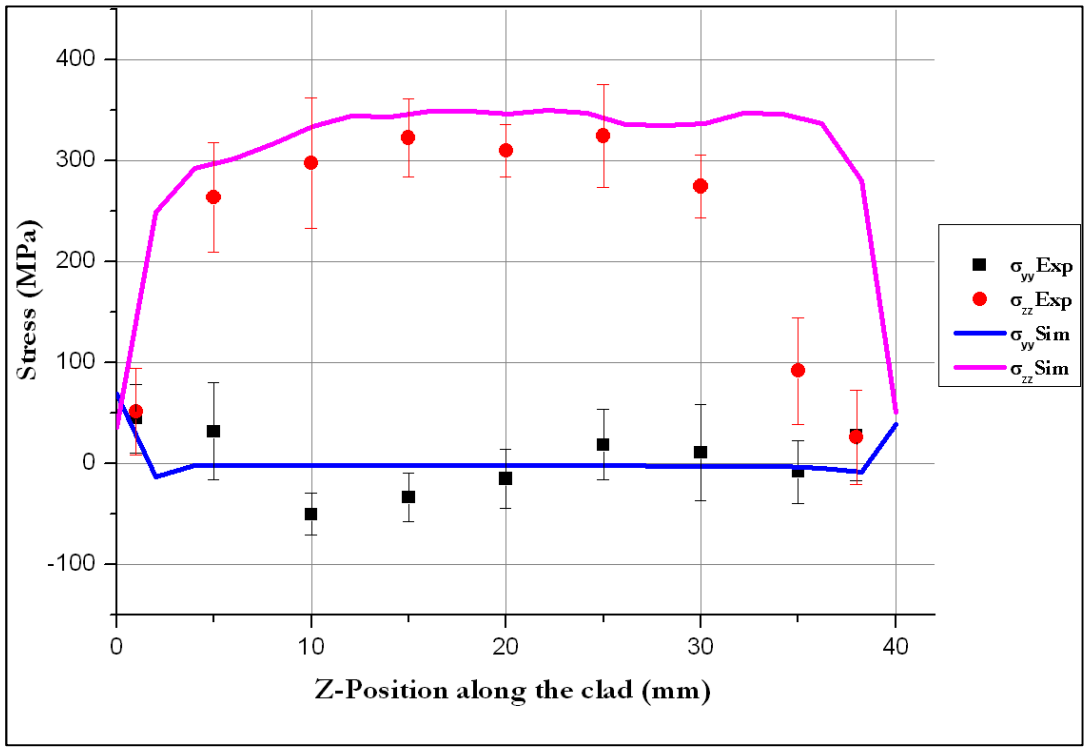

Figure 6.5: Stress distribution along the clad with 0.4 DC Pulsed Wave deposition (Sample 1)

Figures 6.6 and 6.7 give a comparison of experimental and numerical results for the residual stresses in samples 2 and 3. Maximum tensile stress 'σ_{yy}' values of, 96 and 134 MPa are obtained for 0.7DC pulsed and CW deposited samples at the start of the clad. Whereas, normal tensile stresses of 78 and 109 *MPa* magnitude for 0.7DC and continuous wave deposition are observed at the cladding finish end. Qualitatively, the trend of normal stress 'σ_{yy}' and longitudinal stress 'σ_{zz}' in the 0.7DC pulsed laser deposition and continuous wave laser deposition processes is similar. However, the values of longitudinal stress 'σ_{zz}' and normal stress 'σ_{yy}' in continuous wave deposition process are comparatively higher than the 0.4DC and 0.7DC deposition process.

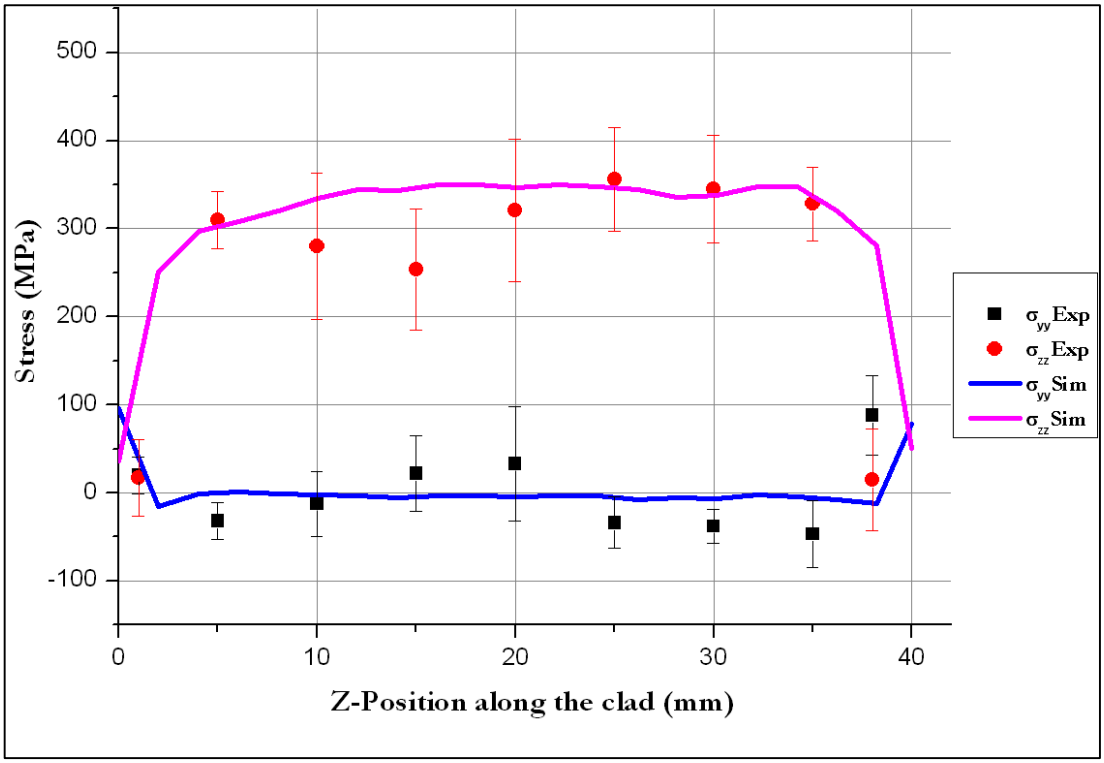

Figure 6.6: Stress distribution along the clad with 0.7 DC Pulsed Wave deposition (Sample 2)

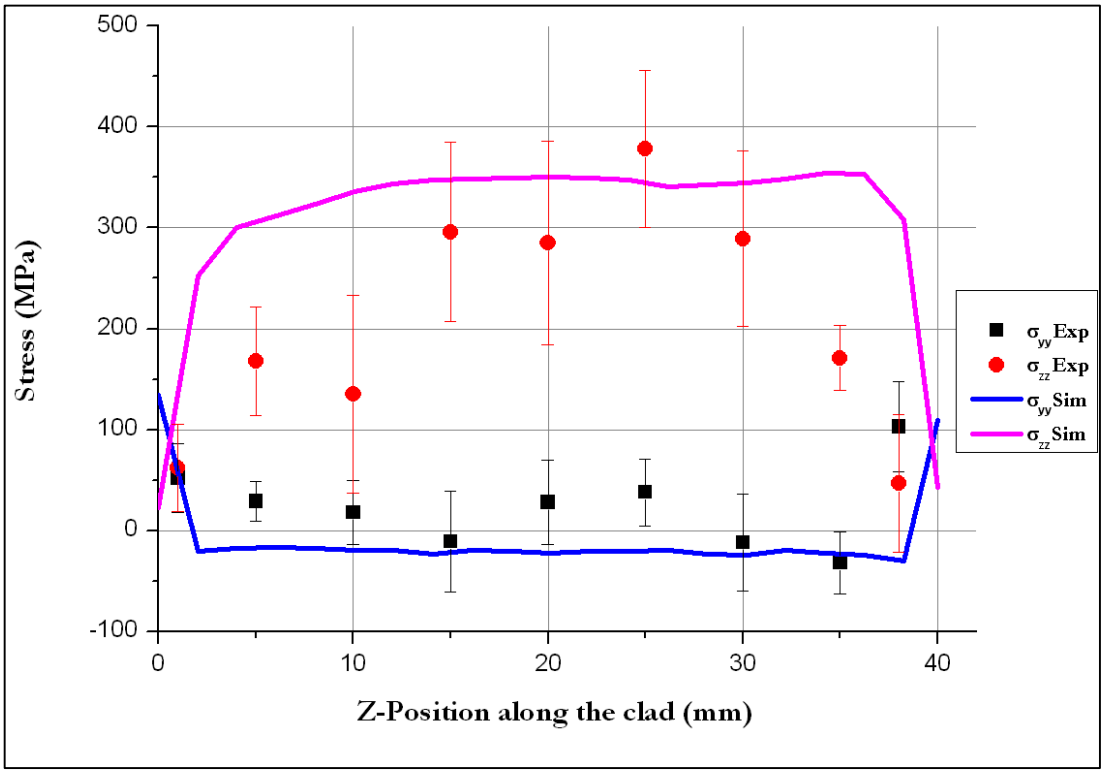

Figure 6.7: Stress distribution along the clad with Continuous Wave deposition (Sample 3)

6.3.2.2 Residual Stresses at the interface of clad and substrate

As shown in Figure 6.8, it was observed that cracks initiated at the start of the deposited track and at the interface between the clad and substrate in the medium and high powder flow rate deposition processes. Cracks extended to approximately mid length of the whole track. In order to fully understand the effect of residual stresses on the crack initiation and propagation, residual stresses at the interface for each all duty cycle are calculated.

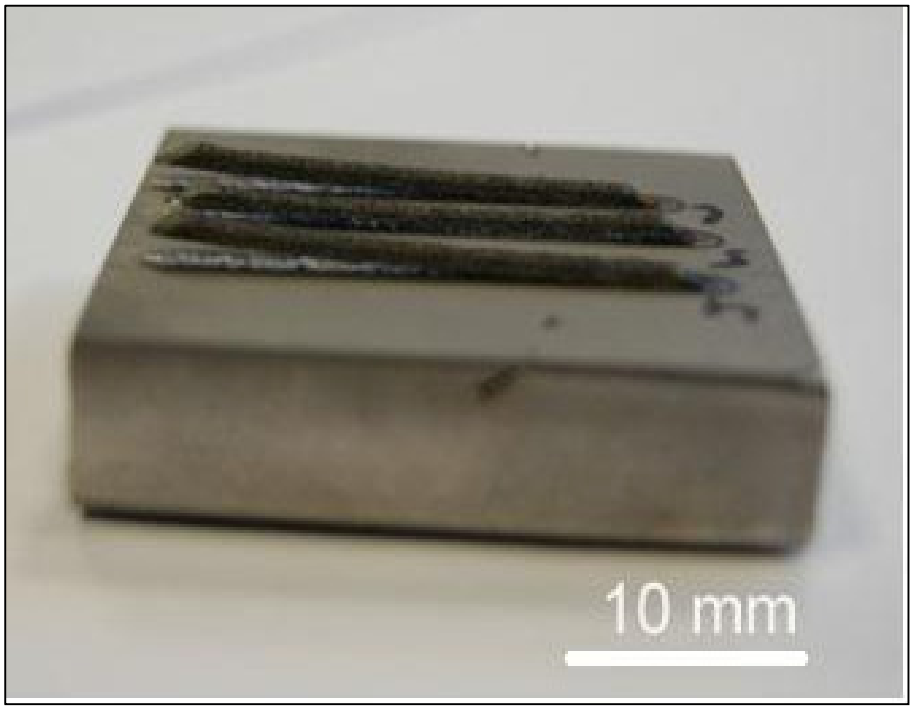

Figure 6.8: Observed cracks in the samples during experiments

6.3.3 0.4 DC Pulsed wave deposition results at the interface

Figure 6.9 shows the variation of longitudinal and normal stress components at the interface for 0.4DC Pulsed wave deposition at different powder mass flow rates.

At the interface of the clad and substrate, an approximate parabolic distribution of tensile stress is observed in the y-direction (normal) at the edges, while stresses in the z-direction (longitudinal) appear to be at

maximum at the mid length of the clad and then decreases towards the edges. With the increase in powder flow rate, an increase in the normal and longitudinal stresses is observed. Maximum normal tensile stress 'σ_{yy}' values of 170.58, 185.95 and 191.41 *MPa* are obtained at the starting edge of the clad for low, medium and high powder flow rate deposition respectively. Similarly, stress 'σ_{yy}' values of 145, 170.34 and 179.25 *MPa* are obtained at the finishing edge of the clad for low, medium and high powder flow rate deposition respectively.

Whereas, maximum longitudinal stress 'σ_{zz}' values of 251.33, 311.88 and 316.34 *MPa* are obtained at the approximately midlength of the clad for low, medium and high powder flow rate deposition respectively.

.

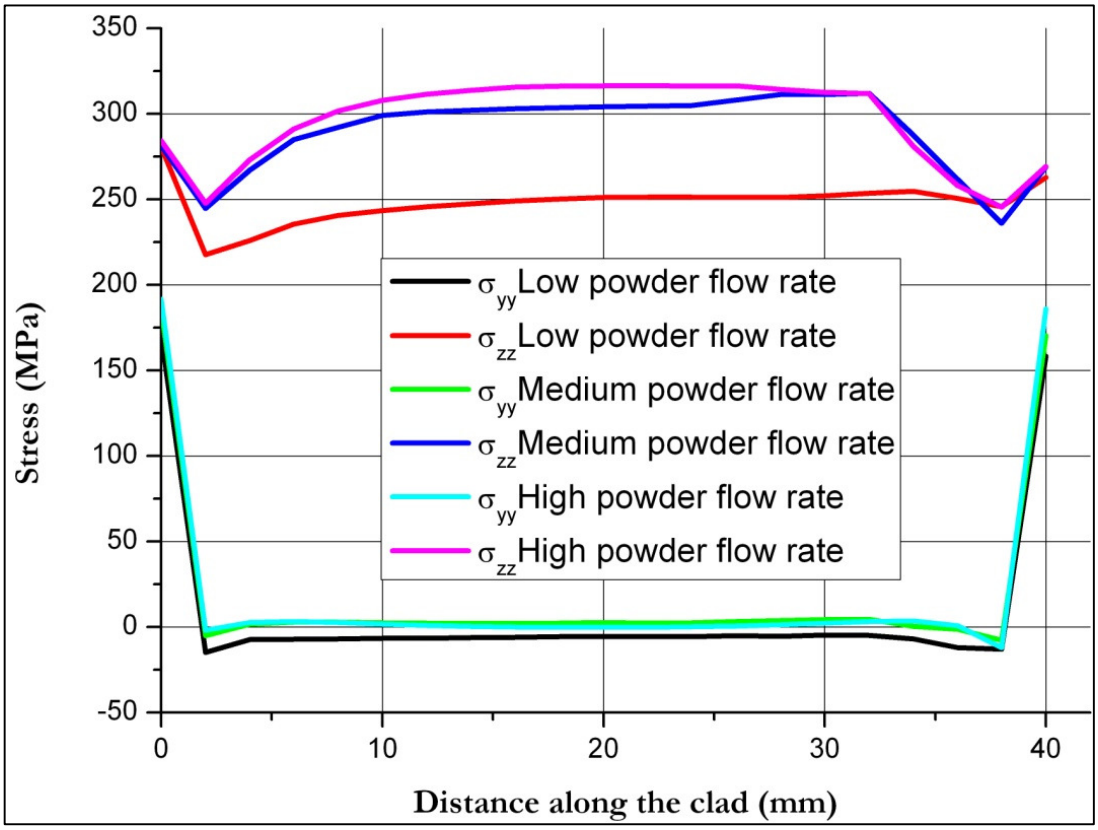

Figure 6.9: 0.4DC Pulsed wave laser deposition results at the interface

6.3.4 0.7 DC pulsed wave deposition results at the interface

Variation of longitudinal and normal stress components at the interface for 0.7DC Pulsed wave deposition at different powder mass flow rates is shown in Figure 6.10. Similar to 0.4DC pulsed wave deposition, an approximate parabolic distribution of tensile stress is observed in the y-direction (normal) at the edges, while stresses in the z-direction (longitudinal) appear to be at maximum at the mid length of the clad and then decreases towards the edges. Increase in powder flow rate, seems to raise the normal and longitudinal stress values. Maximum normal tensile stress 'σ_{yy}' values of 170.42, 184.77 and 193.35 *MPa* are obtained at the starting edge of the clad for low, medium and high powder flow rate deposition respectively. Similarly, stress 'σ_{yy}' values of 158.24, 170.86 and 185.85 *MPa* are obtained at the finishing edge of the clad for low, medium and high powder flow rate deposition respectively.

Whereas, maximum longitudinal stress 'σ_{zz}' values of 251.57, 311.91 and 317.67 *MPa* are obtained at the approximately midlength of the clad for low, medium and high powder flow rate deposition respectively.

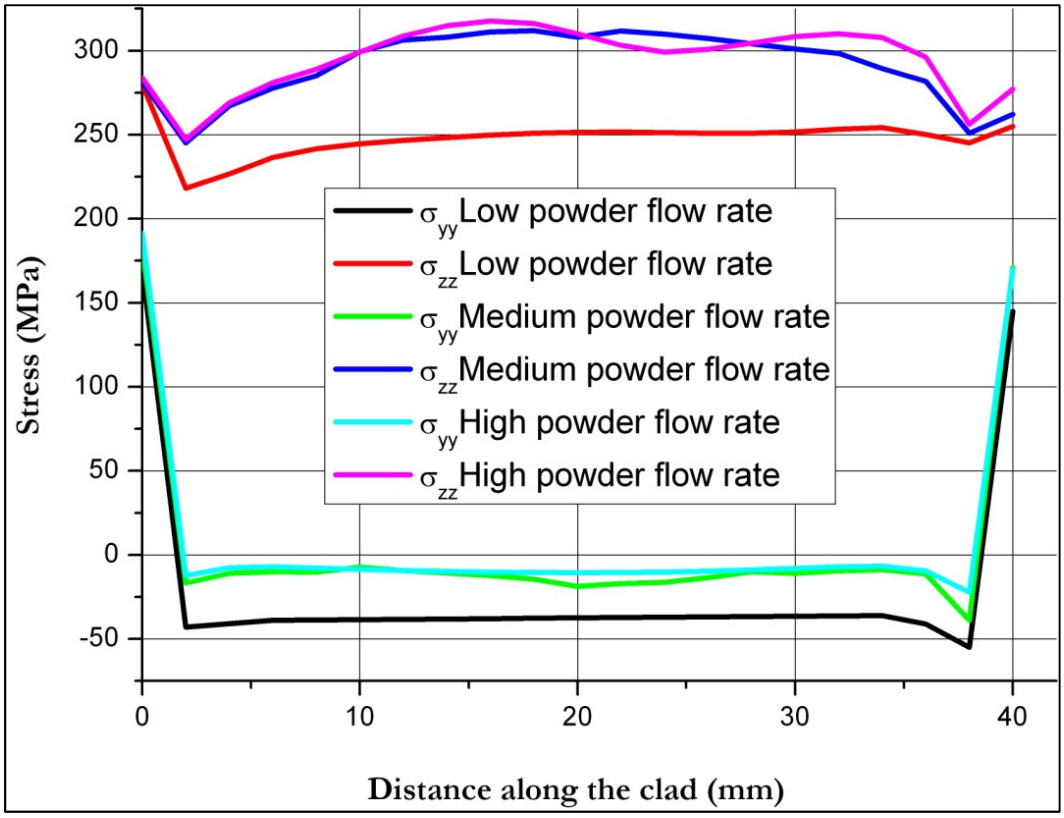

Figure 6.10: 0.7DC Pulsed wave laser deposition results at the interface

6.3.5 Continuous wave deposition results at the interface

Residual stress distributions at the interface comparing continuous wave deposition at different powder flow rates are plotted in Figure 6.11. It can be seen that similar to the 0.4DC and 0.7DC pulsed wave deposition, the residual stress in the vertical direction (y), is compressive at the mid-length along the clad and tensile at the edges. From the Figure 6.11, it can be seen that increase in powder flow rate results in the increase of the normal and longitudinal stress values. Maximum normal tensile stress 'σ_{yy}' values of 170.99, 186.67 and 195.25 *MPa* are obtained at the starting edge of the clad for low, medium and high powder flow rate deposition respectively. Similarly, stress 'σ_{yy}' values of 161.15, 176.65 and 187.84 *MPa* are obtained at the finishing edge of the clad for low, medium and high powder flow rate deposition respectively.

Whereas, maximum longitudinal stress 'σ_{zz}' values of 252.68, 312.5 and 320.21 *MPa* are obtained at the approximately midlength of the clad for low, medium and high powder flow rate deposition respectively.

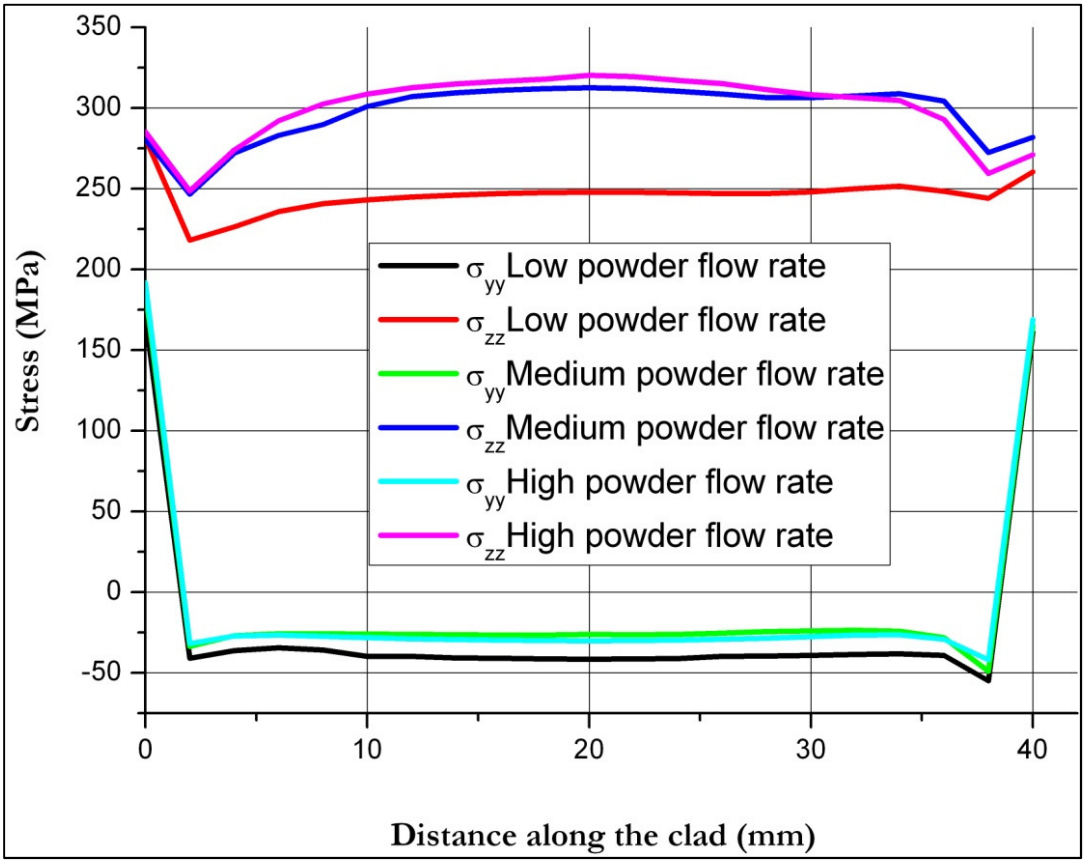

Figure 6.11: Continuous wave laser deposition results at the interface

6.4 Discussion

The aim of the finite element modelling presented in this chapter is to assess the influence of residual stresses developed during the deposition of Inconel 718 powder on Ti-6Al-4V substrate.

In all cases, in the middle of the deposited clad models show that the longitudinal stresses are tensile towards the mid-length of the clad which decreases to almost zero at the edges of the clad, while the stresses perpendicular to the substrate are tensile towards the end and compressive at the centre. Whereas, at the clad-substrate interface, tests on deposited samples show that the stresses along the direction of deposition remain tensile along the length of the clad, while the stresses perpendicular to the substrate are compressive at the centre and tensile towards the ends

With the distribution of the normal and longitudinal direction stresses qualitatively being similar, the amount of residual stress generation in continuous wave deposition seems to be higher as compared to 0.4DC and 0.7DC pulsed wave deposition parameters. Pinkerton and Li [263] have reported lower cooling rates for shorter pulse lengths. Therefore, the structures produced with long pulse lengths or increased duty cycle will have cooled faster. Consequently, high residual stresses are observed in continuous wave deposition (duty cycle=1) as compared to the other duty cycle pulse length samples.

Modelling results are dominantly tensile along the z direction. This kind of behaviour could be explained in terms of thermal shrinkage arising from localised thermal contraction as melt pool cools down. This contraction would also set up a bending moment in the substrate. This will induce tensile stress at the edges and a balancing compressive stress in the inner portions of the sample.

An increase in the powder flow rate results in an increase in the size of the area which is being subjected to high tensile stresses at the edges. From the results in previous chapter, it can be suggested that the intermetallic compounds form first, mostly close to the substrate where their main contributing element comes up through the Ti-Ni mixture. This has been confirmed by the XRD analysis, where brittle intermetallics like Ti_2Ni, $TiNi_3$ were found at the interface. This also means that the formation of intermetallics mostly increases the brittleness of the interface rather than that of the whole clad section, thereby weakening the metallurgical bonding between the substrate and clad.

Thus, results suggest that the combined effect of increased clad thickness along with the brittle intermetallics increase the susceptibility of the clad to peel off from the substrate.

6.5 Conclusions

An investigation has been carried out to understand and analyze the effects of powder mass flow rate and duty cycle of the laser beam on direct laser deposition of Inconel 718 on Ti-6Al-4V. A commercial FE package ANSYS was used to predict the stress distribution in the clad and at the interface. It has been established that the thickness of clad plays an important role in cracking and/or debonding. Increasing laser pulse length and duty cycle has been found to increase the residual stress and size of the region of maximum stress for z-direction tensile stresses. The effect of high powder flow rate results in high normal tensile stresses at the edges of the clad especially, at the starting edge. The combined effect of intermetallics and the higher stresses due to high powder flow rate will increase the susceptibility of the clad to debond from the substrate. It can be concluded that in order to successfully

deposit multiple tracks of Inconel 718 on Ti-6Al-4V, powder mass flow rate should be kept to a low value.

Chapter 7. Melt pool Stability During Deposition of Inconel 718 on Ti-6Al-4V

7.1 Introduction

In this chapter, LDMD of Inconel 718 and Ti-6Al-4V has been further investigated in terms of melt pool stability and final deposit characteristics. Despite considerable advances in laser direct metal deposition (LDMD) process optimisation, there is rather limited work reported on the effects of melt pool variables on the final deposit characteristics. This chapter considers the effects of process parameters and melt-pool characteristics on the deposition of Inconel 718 powder on a Ti-6Al-4V thin wall. A 1.5 *kW* diode laser and LDMD system is used to produce a series of deposits. Images of the process are captured using Cu-vapor laser illumination and a high speed camera with long range microscopy optics and quantitative results are extracted via image analysis. Process parameters such as carrier gas flow rate, powder mass flow rate and laser operating mode (CW and pulsed) and in process variables such as quantified melt pool disturbance, and final part characteristics are correlated and discussed. Scanning electron microscopy (SEM), electron backscatter diffraction (EBSD) and energy dispersive X-ray spectroscopy (EDS) are used to analyse deposited clads in terms of elemental composition and flow characteristics in the deposition melt pool. Melt pool disturbance is found to be a vital parameter in determining the surface roughness of the final part. An inverse relation between the mean surface disturbance of the melt pool and the surface roughness of the part is observed and carrier gas flow rate and powder mass flow rate both affect the overall melt pool size. The work has implications for the selection of process

parameters for commercial laser deposition processes – the speed with which powder is delivered to the melt pool as well as the mass flow rate may need to be taken into account when calculating build rate and for a good surface finish requiring minimum post process finishing a stable melt pool may actually be the worst situation.

7.2 Previous Work

Laser direct metal deposition being a very complex process involves a large number of parameters that can affect the final characteristics of the deposited part. These final characteristics include deposition dimension, microstructure, mechanical properties and the surface roughness [264]. Control of these properties requires good understanding of the relationship between the independent process variables (such as laser power, beam parameters, transverse speed, powder feeding rate, and shielding gas speed) and deposit properties such as geometry, microstructure and phases.
Accuracy and surface finish are one of the major issues for parts fabricated via laser direct metal deposition [265]. In LDMD there are two main process variables; energy input and mass input. These two can be controlled by the combination of laser power, traverse velocity and powder feed rate. Resch et al [102] investigated layer cross section and surface roughness as a function of processing speed in a blown powder process involving continuous wave laser deposition. But in their study, they did not consider the effects of the velocity of the blown powder on the final part or make a comparison between continuous and pulsed wave deposition.

The effect of absorptivity of metal powder under long and short time irradiation in laser cladding was reported by Kizaki *et al* [266]. The effects of various process parameters such as powder injection point, laser power, scanning velocity, spot size and quality of the clad were investigated by Li *et*

al [161]. They concluded that high quality clad surfaces can be achieved through having both narrow powder stream and high enough laser power to form a stable melt pool.

There has been much emphasis on the control of power and traverse velocity of substrate/ laser head in order to control the dimensional accuracy of the deposited tracks. Hua and Choi [267] employed a closed loop real time optical height control system to effectively control the power of the laser beam to reduce surface roughness and dimensional accuracy. In their work, feedback control had little effect on the surface roughness of the parts. Mazumder *et al* [28] employed a three sensors system to reduce the surface roughness of the fabricated parts. Liu and Li [268] used an in-time motion strategy to improve the dimensional accuracy and surface finish in the laser cladding process. They did not consider the effect of laser pulsing or carrier gas flow rate in their work.

There have been number of reports published on the CW and pulsed wave laser deposition processes [269-273] but there has been a very few on comparison between the two. In such a piece of work by Sun *et al* [274, 275] the comparison between pulsed and continuous wave laser deposition was based mainly on fixed powder mass flow rates and average laser power. Pinkerton and Li [263, 272] correlated the pulse width, frequency and the surface roughness of the samples. However, the work did not provide conclusive evidence of the effect of laser pulses on the surface roughness of the deposited part. There has been no comparative study of pulse and CW laser deposition that considers the effect of powder mass flow rate and powder carrying gas flow rates.

7.3 Experimental procedure

A series of experiments was performed, using various combinations of parameters to deposit Inconel 718 powder on a Ti-6Al-4V wall. A 1.5 *kW* Laserline LDL 160-1500 diode laser, operated in both continuous and pulsed modes was used. In the pulsed mode the output was approximately a square wave defined by the period and pulse length (Chapter 5, Figure 5.2).
The beam profile was measured using a Prometec Laserscope UFF100 rotating hollow needle type diagnostic equipment. The beam intensity distribution in the focal plane was found to be top-hat in shape with a beam diameter of 1.59 *mm*. The substrates were 50 ×30 × 10 mm^3 blocks of Ti-6Al-4V, sandblasted in a Guyson sand blaster and then degreased using ethanol. The work piece was tightly clamped and then mounted on a 3 axis CNC motion system.
The build materials were Ti-6Al-4V (5.5-6.75% Al, 3.5-4.5% V, 0.4 % Fe, 0.2% O, and balance Ti) and Inconel718 (50-55% Ni, 17.2-21.0% Cr, 18.5% Fe, 3% Mo, 5.1% Nb and 0.20-0.80%Al). The powders were both gas atomised, giving particles with approximately spherical morphology and size distribution of 53 – 150 μm. A FST PF-2/2 disk type powder feeder manufactured by Flame Spray Technologies Ltd was used in the experiments. An in-house built coaxial powder delivery nozzle, fixed vertically above the motion system, was used to deliver the powder. The deposition area was shrouded by an Argon gas flow from the nozzle. The gas pressure for all experiments was set to 5 *bars* with flow-rates between 0.067-0.134 *l*/*m*. A constant deposition scanning velocity of 5 *mm*/*s* was maintained during the deposition of all the samples. The length of each of the deposited layers was kept at 40 *mm*. Parameters used in the experiment are shown in Table 7.1.

Table.7.1: Experimental Parameters used during the experiment

Sample No.	Peak Power (W) [A]	Pulse length (*ms*)	Period (*ms*)	Duty Cycle [B]	Powder mass flow rate (*g/s*)	Carrier Gas flow rate (*l/s*)
1	600	-	-	1	0.179	0.067
2	600	-	-	1	0.358	0.067
3	600	-	-	1	0.537	0.067
4	600	-	-	1	0.179	0.134
5	600	-	-	1	0.358	0.134
6	600	-	-	1	0.537	0.134
7	1500	20	50	0.4	0.179	0.134
8	1500	20	50	0.4	0.358	0.134
9	1500	20	50	0.4	0.537	0.134
10	1500	20	50	0.4	0.179	0.067
11	1500	20	50	0.4	0.358	0.067
12	1500	20	50	0.4	0.537	0.067
[A] Mean power = 600 *W* in all cases [B] Duty cycle = pulse length / period						

Firstly, 8 *mm* high Ti-6Al-4V walls were initially built on a Ti-6Al-4V substrate. On top of each wall, Inconel 718 layers were then deposited as shown in Figure 7.1. Deposition of Inconel 718 on top of Ti-6Al-4V was captured at 10,000 frames per second (fps) as AVI format data by a Photron Ultima APX high speed camera. Illumination of the melt pool was provided by an Oxford Lasers copper vapor laser providing 511 and 578 *nm*

wavelength light. A narrow band filter in front of the camera was used to block all other wavelengths and the camera and the copper vapor laser were synchronized for maximum illumination during the process. A schematic of the experimental setup is shown in Figure 7.2. The recorded AVI files were analyzed using a purpose written routine in MATLAB to extract quantitative data on the surface disturbance of the melt pool.

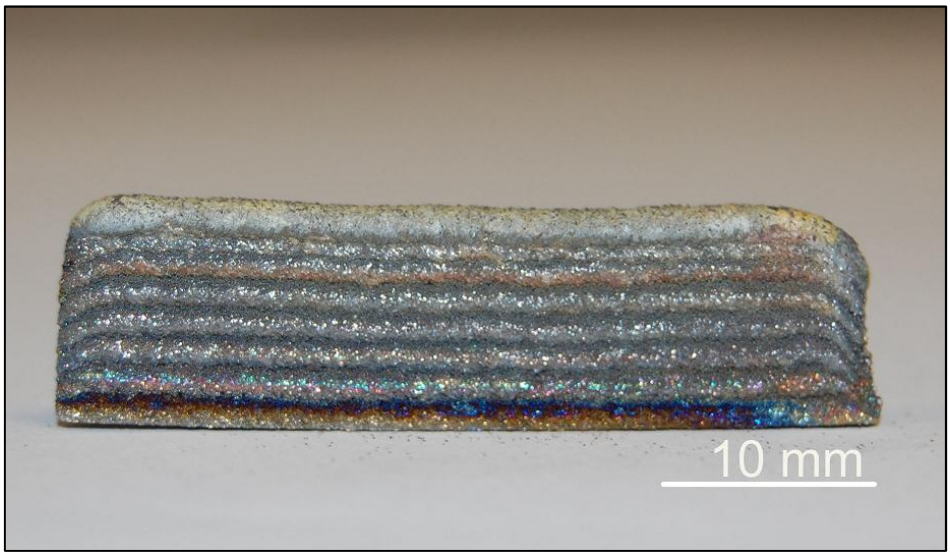

Figure.7.1: Ti-6Al-4V and Inconel 718 wall

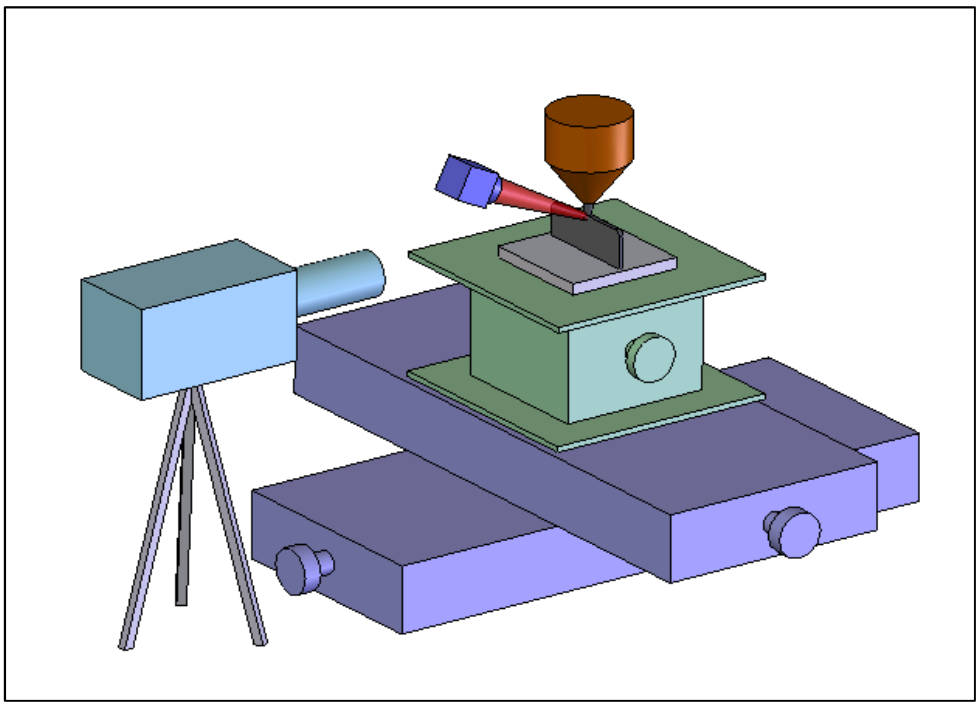

Figure.7.2: Schematic of the experimental setup

Five frames at 0.1sec intervals were first extracted in bitmap format from each of the motion pictures taken by the high speed camera. Each frame of the melt pool was closely cropped to select the area of interest and eliminate redundant noise in the image. These images were then converted to grayscale and underwent histogram equalization to increase the contrast. The aim was to allow the surface of the pool to be clearly discriminated from the rest of the image. The next step was edge detection of the melt pool. Edges were detected using the Canny method [276] which finds the edges in the image by looking for the local maxima of the image gradient. The gradient was calculated using the derivative of the Gaussian filter; this method uses thresholds to detect strong and weak edges. Weak edges are included only when they are connected to the strong edges. The advantage of using this technique is its robustness against noise [276]. After edge detection, the next step was to find the longest line segment, which corresponds to the surface of the metal pool in the images. To avoid discontinuities due to salt-n-pepper noise, it was necessary to dilate the image. The Standard Hough Transform [277] was then used to extract the line segments. A straight line was then fitted to the longest line segment, starting and finishing at the limits of the pool (as if the surface had zero disturbance). Total melt pool disturbance was calculated by measuring the white pixels nearest to this line segment. All pixels related to the melt pool surface above or below the straight line were assumed to be the disturbance created by the injected powder. The system was initially calibrated to obtain the relation between dimensions within the image and number of pixels so the length of the pool and melt pool disturbance could be translated to SI units. MATLAB code for the whole procedure is shown in Appendix C. A flow chart illustrating the above procedure is shown in Figure 7.3 (a-f). After the image analysis on each of the five frames, the average surface disturbance in the melt pool over time was calculated.

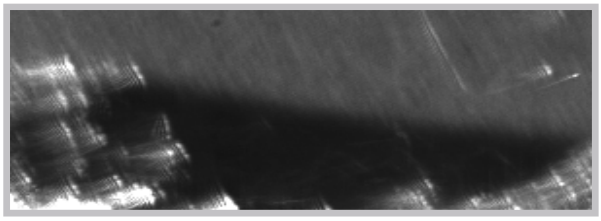

a: Original Image of the melt pool

b: Grey scale image

c: Image with increased contrast using histogram equalization

d: Melt pool extraction using thresholding

e: Edge detection

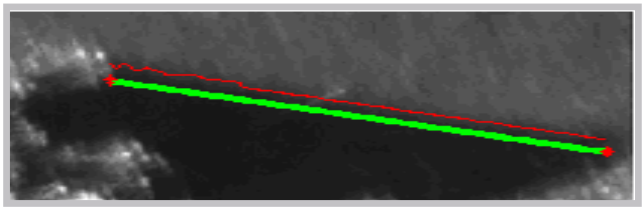

f: Disturbance calculation (red) with reference to the pool surface along with longest line segment (green)

Figure.7.3: (a-f): Flow chart of image analysis done on the melt pool

Surface roughness of the final samples was measured parallel to the deposition direction, on the top surface of the deposited wall. These were measured by an in-house laser based scanning/profiling system with a resolution of $1\mu m$. Scanning electron microscopy and electron backscatter diffraction (EBSD) analysis were performed on the top surface of each sample. The samples were then cross-sectioned across the deposit, polished to $1\mu m$ finish, and separately etched using Kroll's reagent for Ti-6Al-4V and 10% oxalic acid solution for electrolytic etching using $6V$ DC for the Inconel 718 part of the wall. Energy dispersive x-ray spectroscopy (EDX) analysis was performed for investigation of elemental distribution in the samples.

7.4 Results

The mean melt pool surface disturbances with the laser in both continuous wave and pulsed wave mode are shown in the Figure 7.4. This clearly shows a positive relationship between mass flow rate and mean surface disturbance. However, the magnitude of mean surface disturbance in the case of pulsed deposition is higher than continuous wave deposition. Values of the mean surface disturbance in the case of high carrier gas flow rate are almost double the values obtained in the case of low carrier gas flow rate for both modes of laser operation.

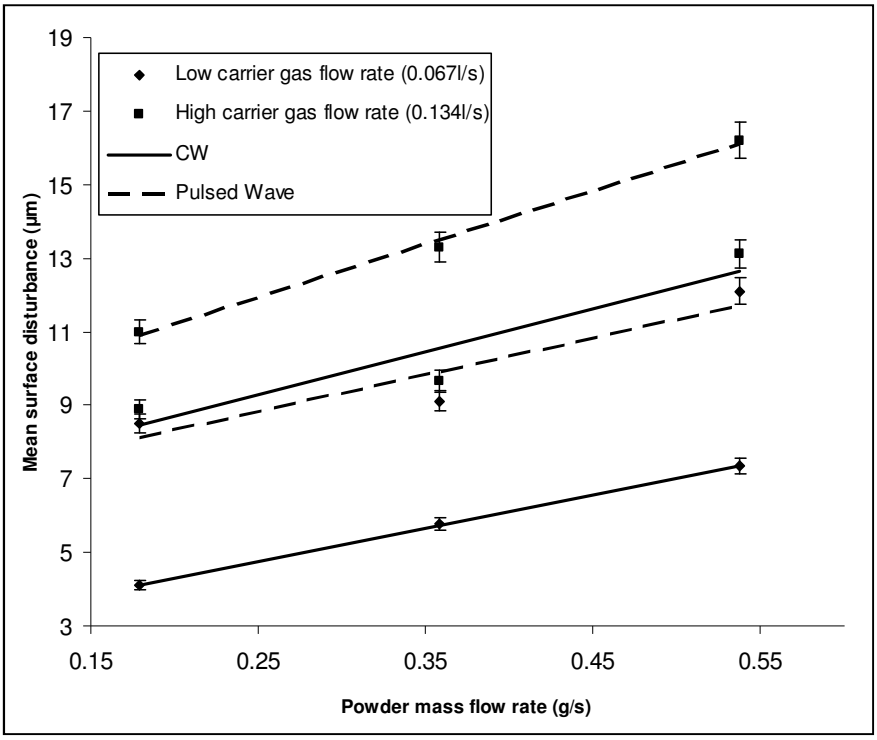

Figure.7.4: Mass flow rate vs. Mean surface disturbance

The overall roughness of the top surface depends partly on the partially assimilated powder particles. These partially assimilated powder particles on the top surface of the wall are shown in Figure 7.5.

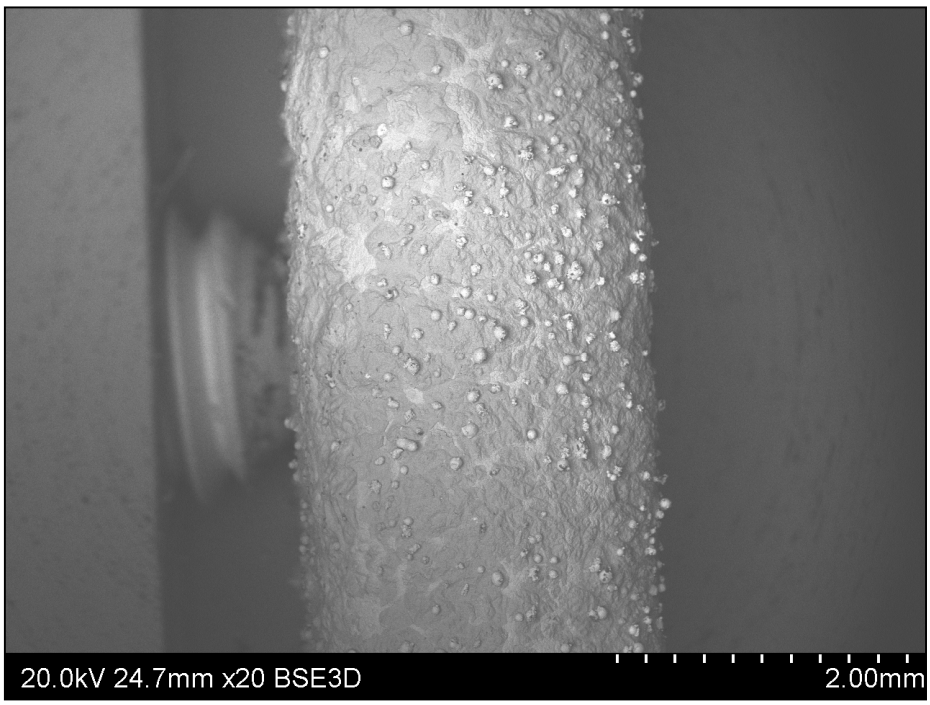

Figure 7.5: Partially assimilated powder particles on top surface of the sample

Figure 7.6 shows the mean surface roughness of the samples produced by the continuous and pulsed wave deposition. This graph demonstrates that in both cases mean surface roughness decreases with an increase in powder flow rate for both continuous and pulsed wave deposition. The mean surface roughness is higher with a low velocity of carrier gas flow than with a high velocity of carrier gas flow. Overall, lower mean surface roughness is produced by pulsed wave mode deposition. The differences in surface roughness caused by carrier gas flow are smaller in pulsed wave deposition than continuous mode deposition.

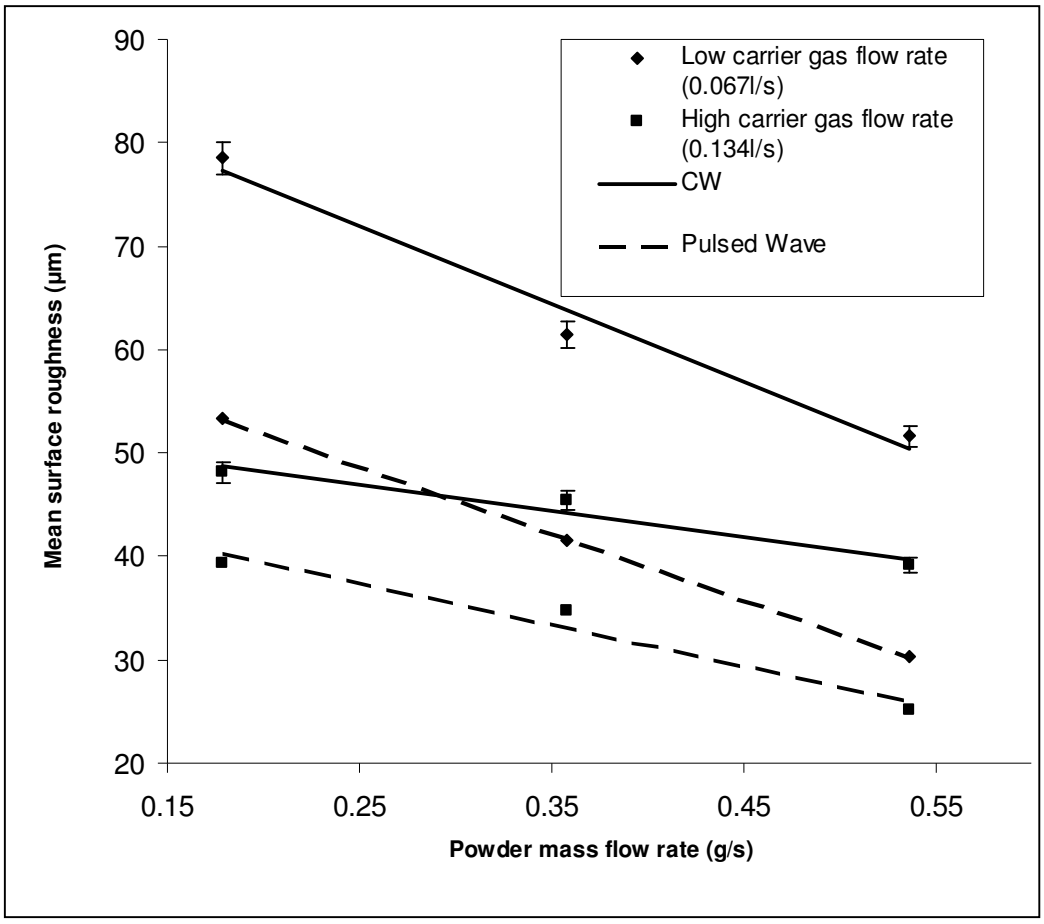

Figure.7.6: Mass flow rate vs. mean surface roughness

Figure 7.7 depicts the effect of powder mass flow rate on the length of the melt pool in continuous and pulsed wave deposition. It is noted that length of the pool increases with powder mass flow rate during both pulsed and

continuous wave deposition. The pool is longer with the low carrier gas flow rate than with the high carrier gas flow rate. This trend is observed during both continuous and pulsed wave deposition. At the same parameters, the mean pool length is longer during pulsed wave deposition than continuous wave deposition.

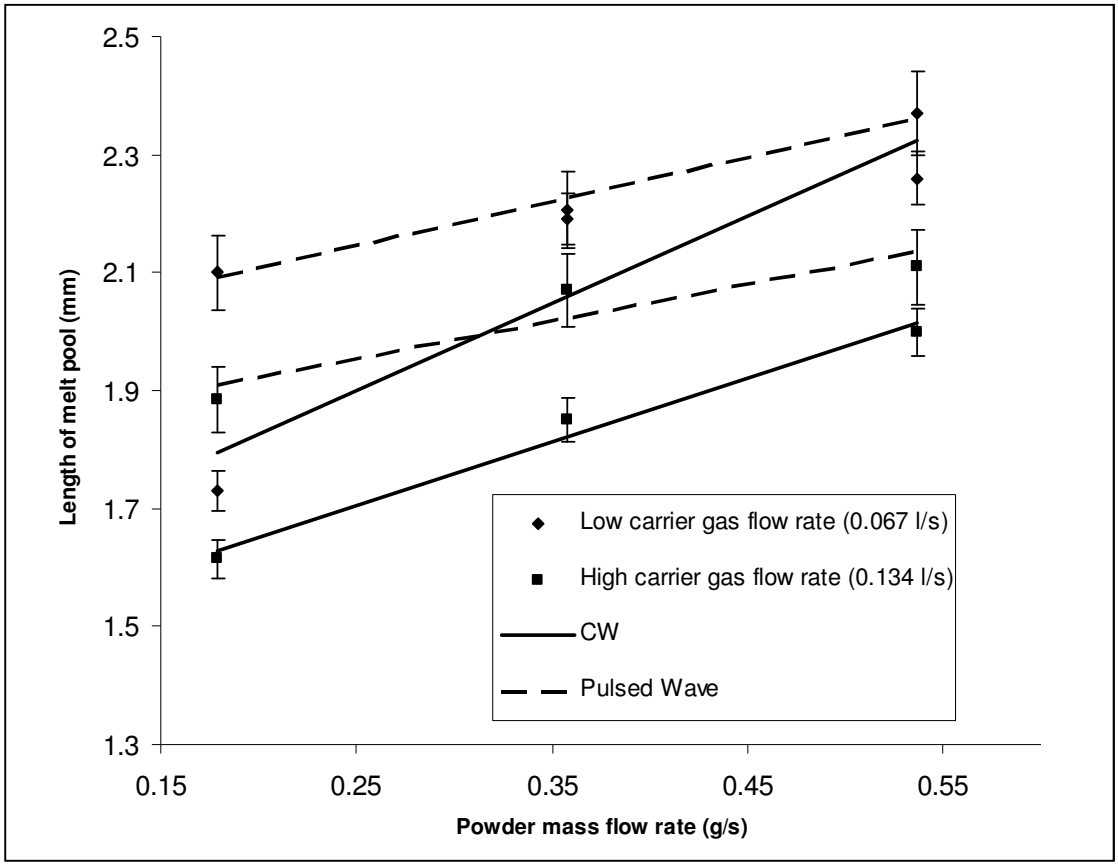

Figure.7.7: Mass flow rate vs. Length of the melt pool

In Figure 7.8, variation of the depth of the melt pool during pulsed and continuous wave deposition is shown. It is noted that the depth of the melt pool decreases with an increase of the powder mass flow rate. A high carrier gas flow rate has the effect of increasing the overall depth of the pool, compared to a low flow rate during both pulsed and continuous wave deposition.

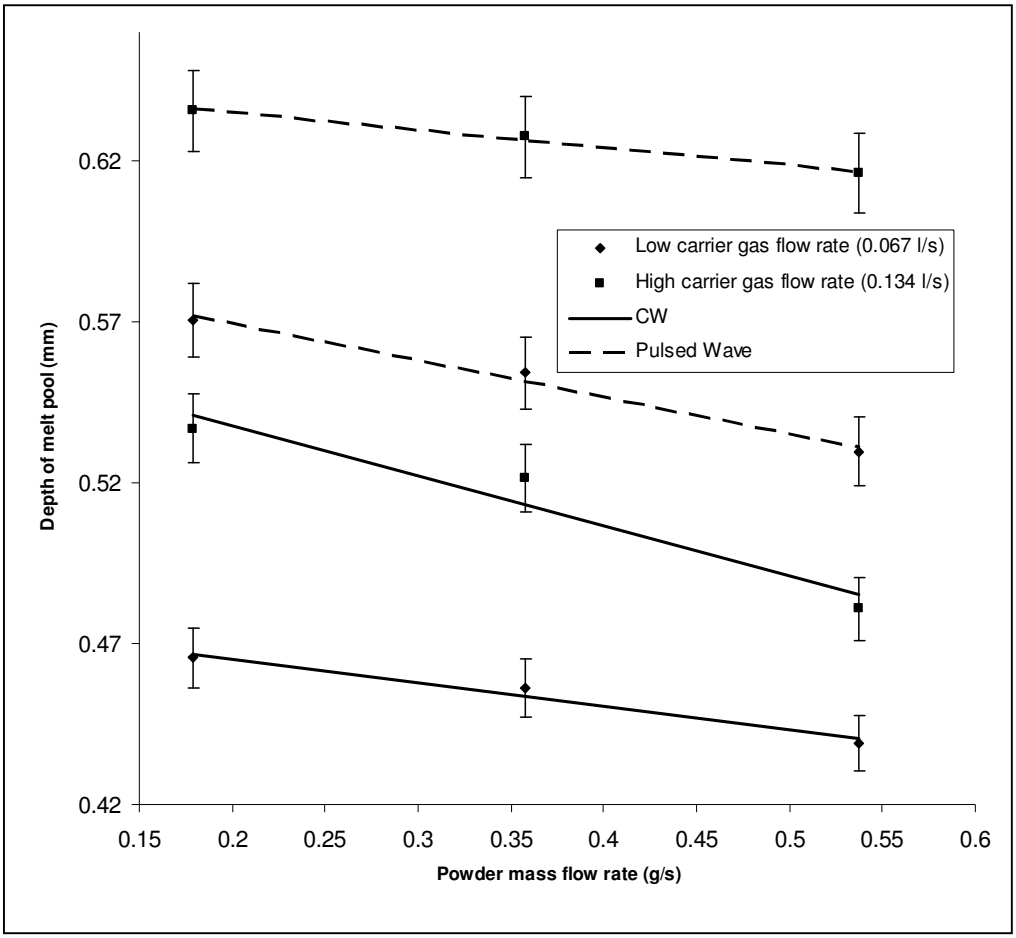

Figure.7.8: Mass flow rate vs. Depth of the melt pool

Figure 7.9 shows the melt pool area variation during both continuous and pulsed wave deposition. It can be seen that in continuous wave deposition the area of the melt pool produced with a high carrier gas flow rate is larger than the area produced with a low gas flow rate. The area of the melt pool increases with increasing powder mass flow rate during the deposition process. The same is true of deposition in pulsed wave mode. Figure 7.9 illustrates melt pool area increases with increasing powder mass flow rate under conditions of high and low velocity of carrier gas. It is also noted that the melt pool area during pulsed wave deposition is higher than the melt area during the continuous wave deposition. This trend is observed under both low and high carrier flow rate conditions.

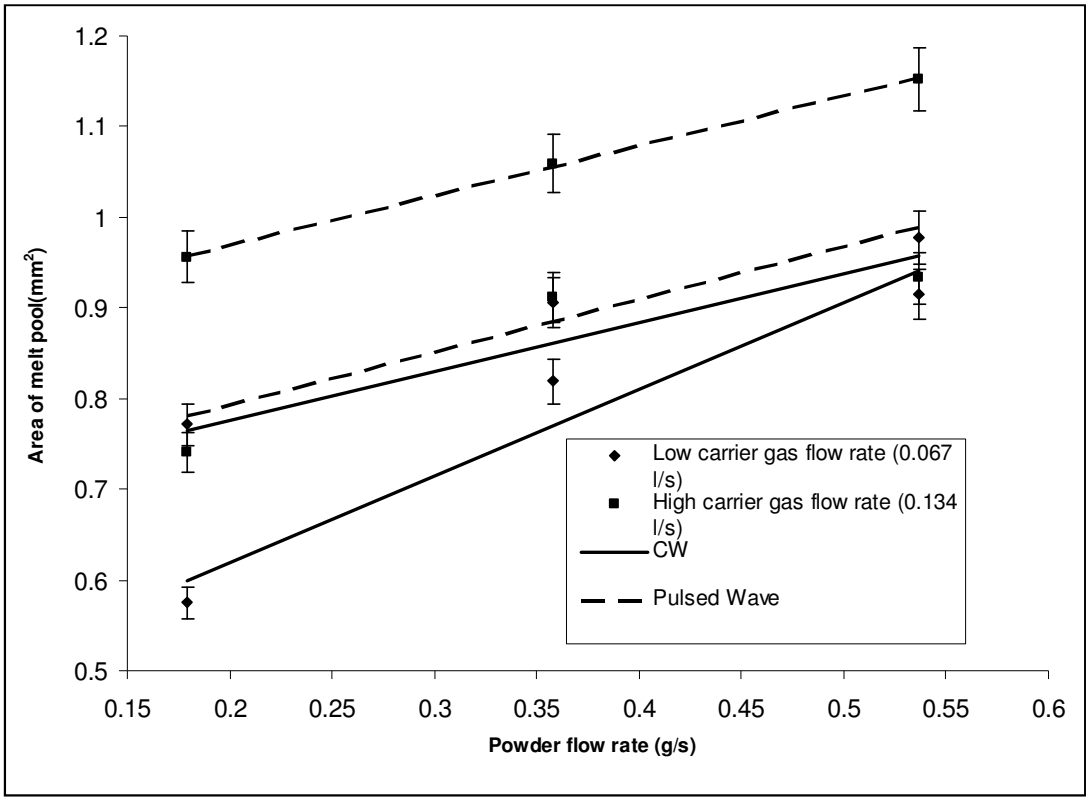

Figure.7.9: Mass flow rate vs. Area of the melt pool

Trends in EDX line scans suggest more mixing of Ti and Ni in the case of pulsed deposition as compared to continuous deposition. However, as shown in the Figure 7.10 (a-b), the gradient in elemental composition at the clad-substrate interface is not very different for the different laser modes.

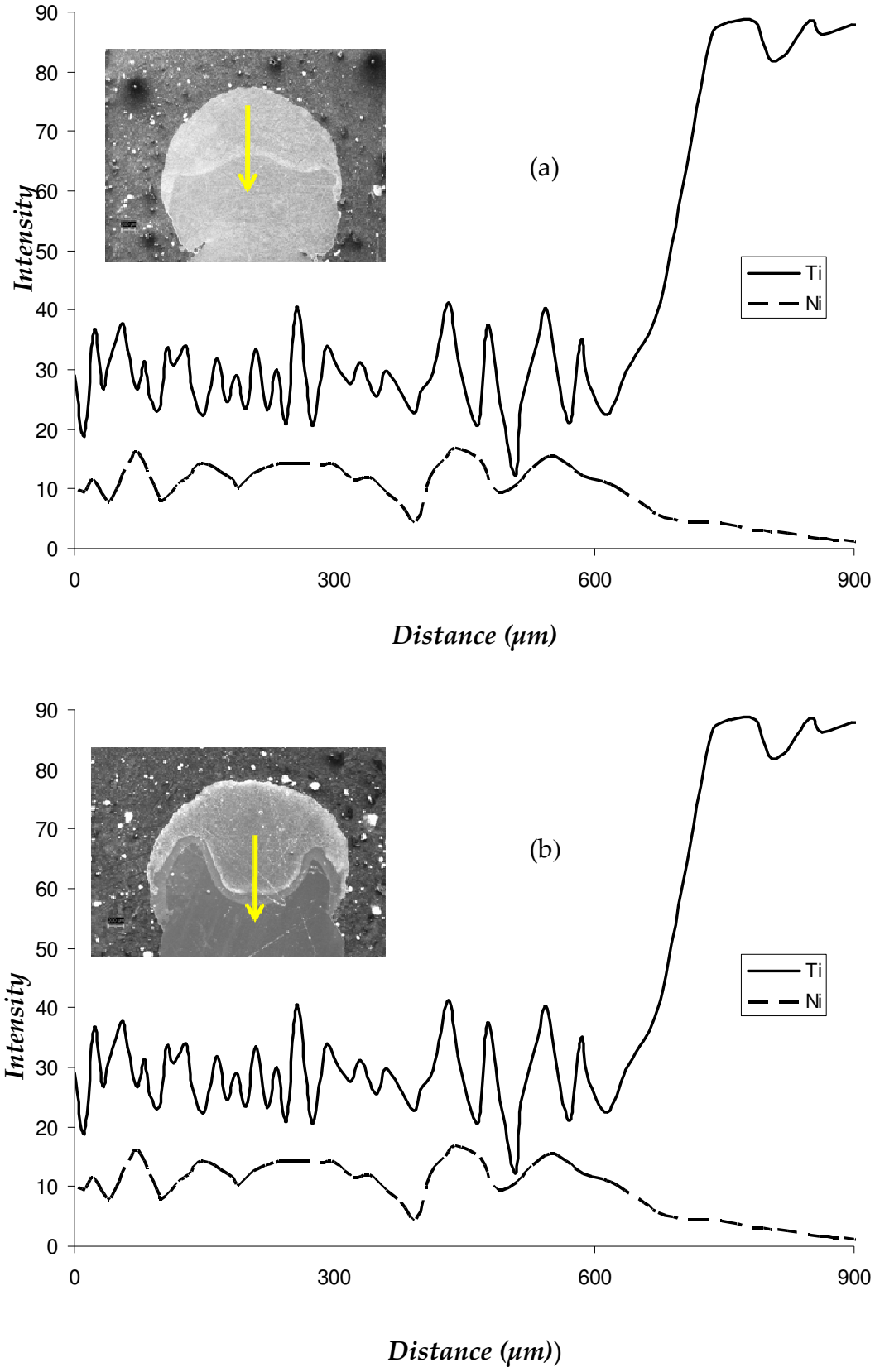

Figure 7.10: EDX line scan, change in gradient (a) Continuous wave deposition (b) Pulsed wave deposition

7.5 Discussion

7.5.1 Melt pool surface disturbance

Surface disturbance in the melt pool and deviation from ideal quasi-stationary conditions can be caused by a variety of factors like Marangoni convection, powder flow impinging on the melt pool surface, turbulence in powder conveyance and shielding gases, and variable input power when the laser is in pulsed mode.

Experimental results suggest that the surface disturbance produced during the continuous and pulsed wave deposition plays an important role in determining the surface roughness of the final part. The mean surface disturbance obtained during pulsed deposition is high compared to that during continuous wave deposition which effectively decreases the mean surface roughness of the final part. This is not the intuitive effect but, a higher surface disturbance of the melt pool may effectively enhance mixing and melting of the powder particles in the melt pool, preventing partially assimilated particles which are a common cause of increased roughness in LDMD. In addition the melt pool during the pulsed deposition periodically experiences high temperature as compared to the continuous wave deposition [275], so it is possible that the surface is also partially remelted, removing powder particles that have stuck there.

Another important parameter that influences surface roughness of the parts is the carrier gas flow rate. It is noted that a high velocity of carrier gas flow causes increased surface agitation/ disturbance at the melt pool surface and decreased surface roughness. Increased surface disturbance this time assisted by the speed of incoming particles at high flow rates may again increase assimilation reducing surface roughness by reduction of partially assimilated particles.

7.5.2 Melt pool size

Creation of the melt pool during the laser cladding is due to melting of the substrate and the powder impinging on and being assimilated into the melt pool. The negative correlation between powder mass flow and melt pool depth can be explained by the thermodynamics of the melt pool. With an increase in powder mass flow rate, the amount of heat absorbed by the substrate is decreased due to the shadowing effect of the powder and the energy required assimilating it to the melt pool. This causes the decrease in depth of the melt pool inside the substrate.

The increase in the length of the melt pool with powder mass flow rate can be attributed to the higher amount of melted powder. With the increase in powder mass flow, more powder is available to be melted, therefore increasing the length of the melt pool, provided that the process is in the mass limited parameter range [278] and laser power is sufficient to melt more powder [279].

The area of the melt pool is of course dependent on the combination of melt pool length and depth. The combined effect is for the melt pool area to increase with increasing powder flow rate, indicating that the increase in melt length is numerically more significant than the reduction in depth. This is not surprising – energy is used more efficiently in melting powder than it is in melting the substrate where conduction losses are significant. At higher powder mass flow, a greater proportion of energy reaching the substrate is conveyed as heated particles rather than the incident laser flux. This increase in the melt pool area is higher in magnitude in case of pulsed wave deposition as compared to the continuous wave deposition. This can be attributed to the above effect being very marked at the high peak power observed during the pulsed deposition process.

The effect of carrier gas flow rate on melt pool depth suggests that an increase in carrier gas flow rate increases the speed of powder hitting the melt pool which leads to a deeper but shorter melt pool. This increase in depth of the pool is numerically less significant than the reduction in length of the pool. This can be attributed to the change in powder flow characteristics and ricocheting powder.

The Marangoni flow in the pool is proportional to the square of the melt pool size and has significant implication for overall melt pool shape [280]. The increase in melt pool size in the case of pulsed wave deposition suggests more vigorous Marangoni flow. This increase will not only ensure good mixing of elements within the melt pool, but may also contribute to the increased agitation at the surface of the melt pool. EDX of the sample shows higher dilution and a greater proportion of Ti-6Al-4V elements in the melt pool in the case of pulsed deposition (Figure 7.10b). In both samples there is an even distribution of Ti throughout the pool, suggesting vigorous Marangoni flow driven mixing.

7.6 Conclusions

An image analysis technique has been developed to measure the surface disturbance and the melt pool cross section size during laser direct metal deposition. Pulsed and continuous beam mode deposition of Inconel 718 on a Ti-6Al-4V thin wall with a range of powder mass flow rates and carrier gas flow rates has been tested.

Results showed that increased powder flow rate, increased carrier gas flow rate and using the laser in pulsed mode all increase the mean surface disturbance of the pool and affect the mean area of the melt pool. Inverse relations between the surface disturbance of the melt pool and the surface

roughness of the part were obtained. It is suggested that increased melt pool disturbance can reduce the presence of partially assimilated surface particles and thus actually have a beneficial effect for the process. Under tested conditions the overall melt pool area increased with the increase in powder flow rate; the carrier gas flow rates also seemed to play important roles in determining the melt pool size. Increase in gas flow rate lead to a small and shorter pool, possibly due to changes in powder stream characteristics or ricocheting powder.

Chapter 8. Parametric Study of Development of Ni-Steel Functionally Graded Materials by Direct Laser Metal Deposition

8.1 Introduction

The concept of Functionally Graded Materials (FGMs) was proposed in 1984 by material scientists in the Sendai area in Japan as a means of preparing thermal barrier materials [221]. FGMs are a class of advanced materials of which the composition and microstructure change gradually from one side to the other, resulting in a corresponding variation in the properties [222]. The materials can be designed for specific function and applications. Moreover, a graded change in material allows a reduction of stress concentrations appearing near a sharp interface between two different phases. Today, the FGM concept extends over a variety of materials fields all across the world. FGMs have found their place in various fields like bio-medical, automotive and aerospace, electronics, optics, and nuclear applications, reactor components and energy conversion [281, 282].

Nickel and steel alloys are widely used in power and nuclear industries. It is known that austenitic welds are resistant to hot cracking, stress and severe impacts during service conditions [283, 284]. While Inconel 718 alloy is appropriate in applications where high temperatures are observed and the atmosphere is highly carburising and oxidising [285, 286]. These unique properties of nickel and stainless steel alloys present its application in oil refineries where such conditions exist. But, these two alloys are often joined together by fusion welding that result in weak resistance to solidification

cracking [287]. To overcome this problem of cracking, functionally grading of Nickel-Steel alloy represents a viable solution.

This chapter, reports an investigation on the development of continuously graded Stainless Steel 316L and Inconel 718 thin wall structure made by direct laser metal deposition process. Various laser power levels and powder mass flow rates of SS316L and Inconel 718 during the deposition of Nickel-Steel graded structure have been investigated. Microstructure characterization and phase identification are performed by optical microscopy and X-ray diffraction technique. XRD results show the presence of the NbC and Fe_2Nb phases formed during the deposition of Stainless steel 316L- Inconel 718 graded structure. Mechanical testing such as hardness, wear resistance and tensile testing has been carried out on the graded structures. The effect of experimental parameters on the microstructure, hardness and wear resistance are correlated and discussed.

8.2 Previous Work

There are several techniques such as die compaction [288-290], plasma spraying [291], slip casting [292] and powder metallurgy [293] which are currently used for producing FGMs. Die compaction and plasma spraying are generally applied for fabrication of functionally graded coatings and the FGM coatings made by plasma spraying are not fully dense. Although powder metallurgy can be utilized for producing bulk FGMs, the shapes and sizes are usually limited because of the use of dies for pressure-aided densification. The LDMD process is able to fabricate complex prototypes in near-net shape, leading to time and machining cost savings. A variety of metals and alloys have been deposited by the process, such as H13 materials like steel [294], WC-Co [295], and Stellite.

The application of laser cladding process to manufacture metal-ceramic FGM was first accomplished by Jasim *et al* [296]. Later on various researchers have applied this concept to build a range of FGMs for various applications. Pei and De Hosson [223] produced AlSi40 FGM using a Nd:YAG laser where as Thivillon *et al* [297] analysed the fabrication of Co based Stellite 6 and Nickel super alloy Inconel 625 by the laser deposition technique. Ouyang, Mei and Kovacevic [298] developed a WC-(NiSiB alloy) ceramet/tool steel FGM by laser cladding technique for high-temperature tribological applications. Lin *et al* [299] investigated the solidification behaviour and the morphological evolution during the compositional gradient of stainless steel to Rene88DT.

8.3 Experimental procedure

The Laserline LDL 160-1500 1.5 *kW* Diode laser described in detail in chapter 4 was used for this laser deposition study. A Stainless Steel 316L substrate was positioned such that the beam was orthogonal to the surface and of size 2.5 *mm* (slow axis) x 3.5 *mm* (fast axis) at the deposition point. The build materials were Stainless Steel 316L and Inconel 718. A FST PF-2/2 Disc-type powder feeder, containing two powder canisters with a capacity of 1.5 *litres* each was used to deliver Stainless Steel 316L powder (50-120 μm particle diameter) and Inconel 718 (53 – 150 μm diameter) respectively. Powder morphology and elemental composition of the Stainless Steel 316L and Inconel 718 powders are given in the Figures 8.1 and 8.2.

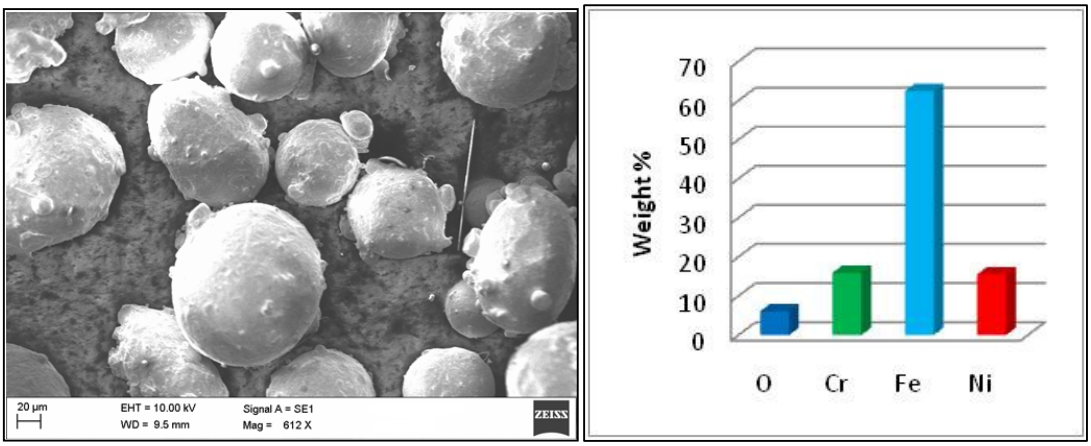

Figure 8.1: Stainless steel 316L powder morphology and elemental composition (wt %)

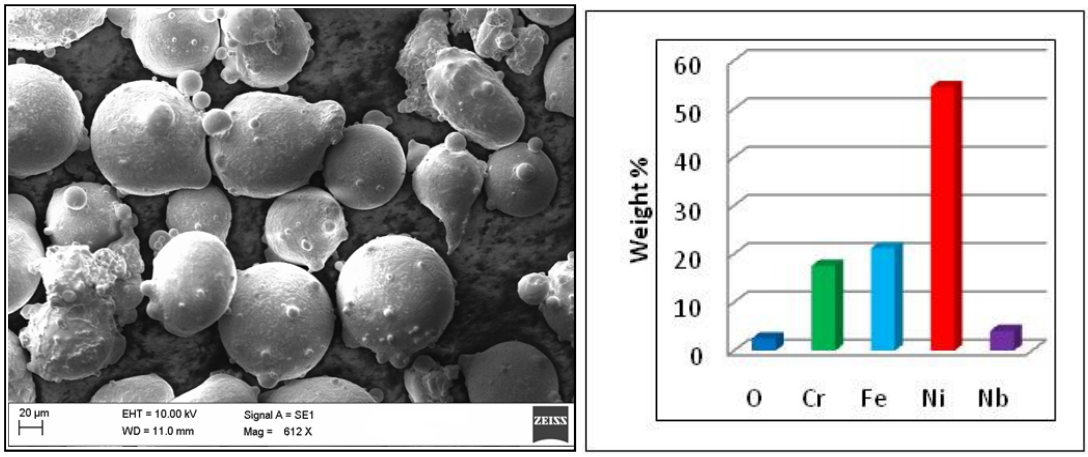

Figure 8.2 : Inconel 718 powder morphology and elemental composition (wt %)

SS 316L and Inconel 718 powders were initially weighted separately and then mixed with stirrer for 30 minutes according to the desired weight percentage. Grading of two materials was achieved by continuously depositing 3 layers of 100 wt% SS316L on SS316L substrate block and then increasing the weight percentage of Inconel 718 by 25% after every 3 layers and vice versa for SS316L powder. Powders were conveyed to the melt pool by argon gas from a coaxial nozzle. A two-channel powder feeder was used, allowing mixing of the powders in the nozzle before deposition. The nozzle was positioned in line with the slow axis of the laser beam. The process parameters used in the experiments are shown in Table 8.1.

Table 8.1: Experimental process parameters

Sample No.	Power *(W)*	Powder mass flow rate *(g/s)*
1	450	0.674
2	550	0.674
3	650	0.674
4	750	0.674
5	450	0.832
6	550	0.832
7	650	0.832
8	750	0.832

Before the experiment, the SS316L substrate was sand blasted in a Guyson sand blaster and then degreased using ethanol. The movement in x and y axis (horizontal plane) was controlled by a CNC table. The volume surrounding the whole setup was kept in an argon-filled chamber (glove-box). Prepared thin-walled samples were sectioned in a traverse planes, mounted in a Streur epoxy resin and polished to 4000 *grit size*. All samples were electrolytically etched in 10% oxalic acid using a 6 *V* DC potential. The graded microstructures were studied by means of optical microscopy technique. Energy dispersive x-ray spectroscopy (EDX) analysis was used to investigate the elemental composition. Micro-hardness testing was carried out on the cross-sectional planes of the built walls. Wear testing was carried out using a Teer Coatings (POD-2) pin on disk wear tester, in which samples were subjected to wear by rotation in contact with a WC-Co ball.

8.4 Results

8.4.1 Macrostructure and Dimensions

All parameter combinations formed thin continuous wall structures. All of the samples produced for analysing the effect of power and powder flow rates were well adhered to the substrate, with no signs of track discontinuity and appeared structurally sound. One of the graded walls is shown in Figure 8.3.

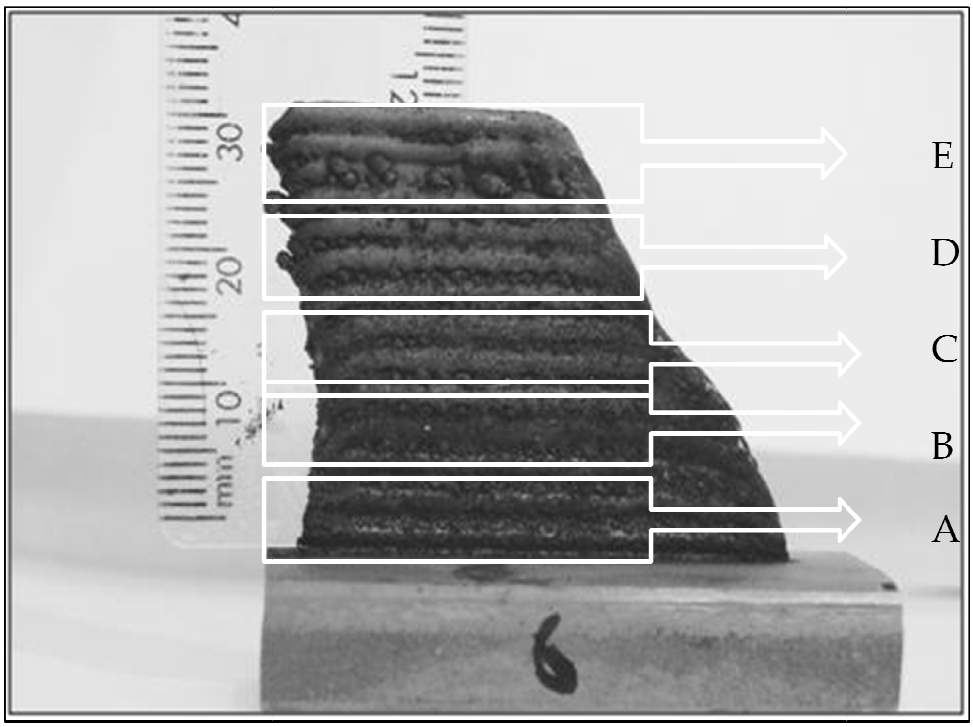

Figure 8.3: Direct laser metal deposited SS316L/ Inconel 718 functionally graded Sample (A) 100% SS 316L, (B) 75% SS 316L, (C) 50% SS 316L, (D) 25% SS 316L, (E) 0% SS 316L

Analysis of the track dimensions revealed a marked trend towards larger deposits with increasing power. The variation in layer height and layer width with the primary input variables of delivered power and powder mass flow rate are shown in Figures 8.4 and 8.5 respectively.

Mean layer heights ranging from 0.54 *mm* to 0.76 *mm* were observed for low powder flow rate deposition samples, while mean layer height range for high

powder flow rate deposition is between 0.63 *mm* and 0.84 *mm*, with track height increasing with increasing power. Similar trends were observed for track width, with the lowest mean layer width of 1.31 *mm* obtained at a power of 450 *W* and 1.65 *mm* at a power of 750 *W* for the low powder flow rate condition. At the high powder flow rate, a lowest mean layer width of 1.37 *mm* at 450 *W* and a highest mean layer width of 1.68 *mm* at 750 *W* were observed.

For all the samples, layer dimensions were limited by the available laser power; however when laser power is increased above a critical, increase in layer height and width starts to plateau. This shows that when laser power is increased above a critical value, below optimal quantities of powder are available to utilise all the laser power, consequently the deposition moves from a laser power limited regime to a powder limited regime. This explains the flattening off of the findings in Figures 8.4 and 8.5.

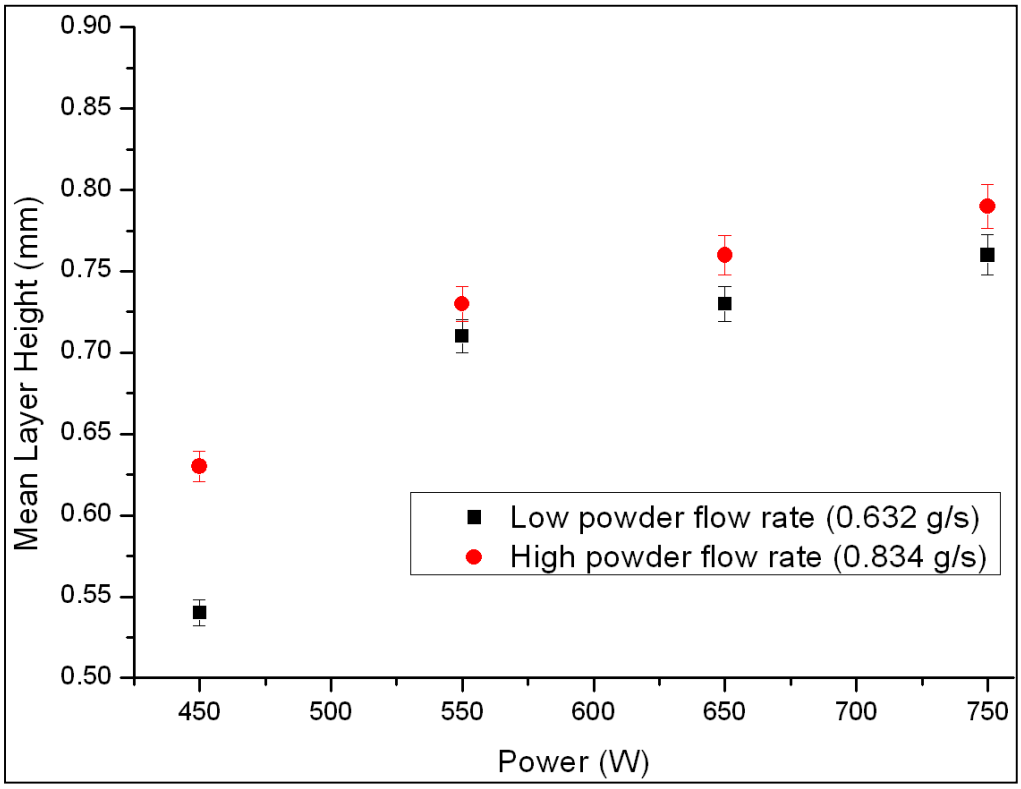

Figure 8.4: Effect of laser power and powder flow rate on mean layer height

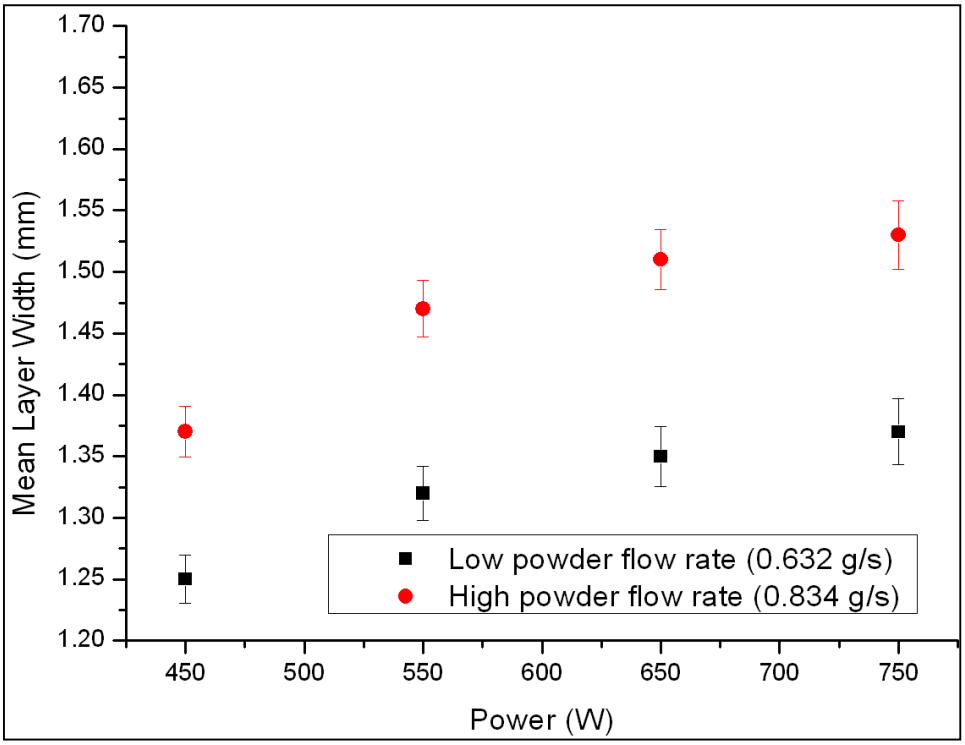

Figure 8.5: Effect of laser power and powder flow rate on mean layer width

8.4.2 Microstructure

The multi-layered walls showed good bonding between the layers. It was noted that columnar dendritic growth has prevailed in the all the FGM structures as shown in Figure 8.6. At the edges of the cross-section, columnar to cellular dendritic growth transitions were observed and these structures was also seen to prevail at layer boundaries throughout the parts as shown in Figure 8.7. No cracks were found but some porosity was visible in all functionally graded LDMD structures.

The microscopic characteristics of samples produced under each value of powder flow rate are not significantly different apart from their secondary dendritic arm spacing (SDAS).

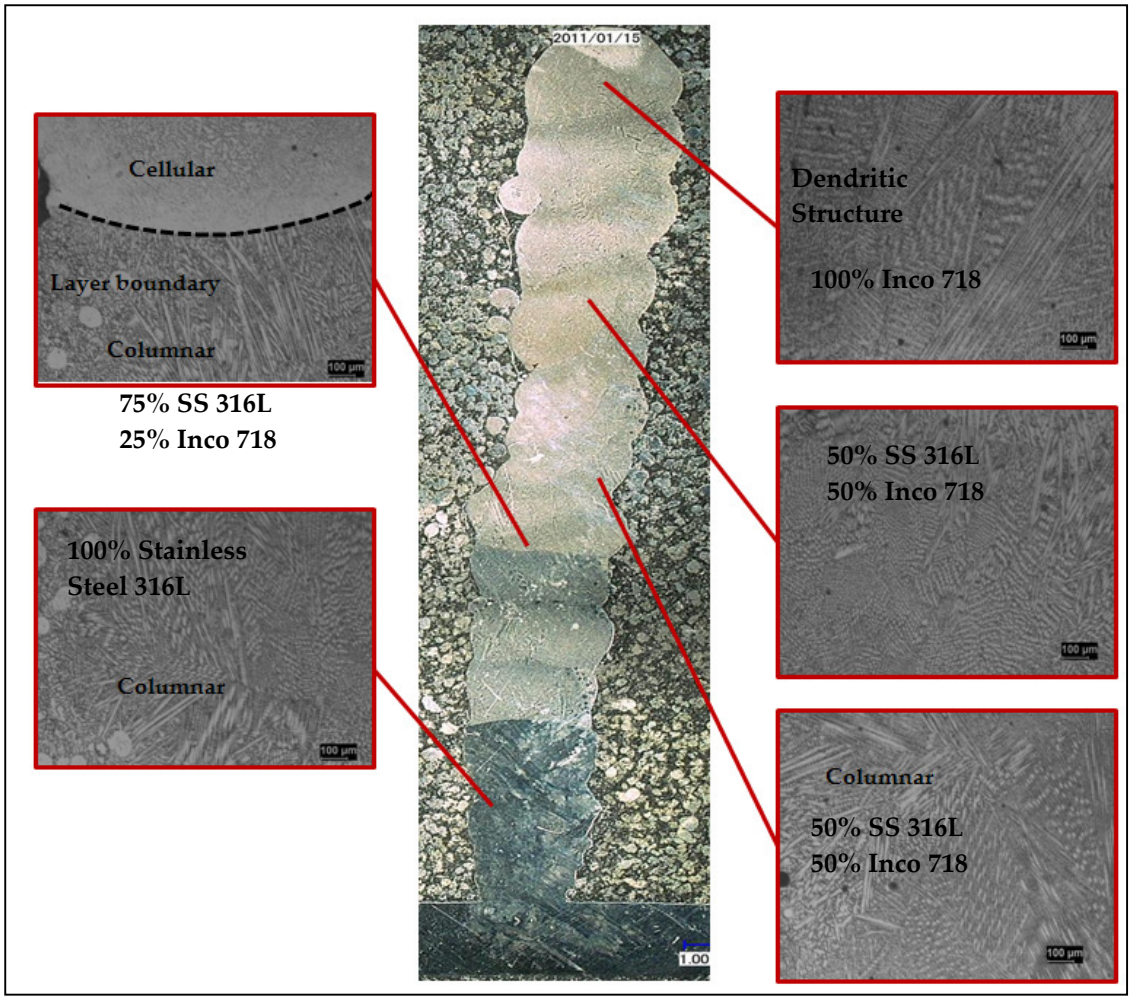

Figure 8.6: Sample 3 transverse cross section showing the Inconel 718 addition along the wall

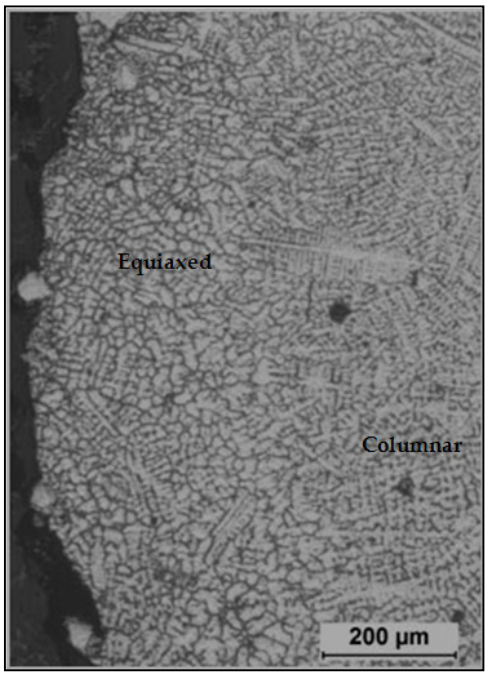

Figure 8.7: Cellular grain structure observed at the side of the wall in sample 4

The secondary dendrite arm spacing (SDAS) was measured for each layer of all the samples and their average was taken. Plots of average SDAS for 0.674 *g/s* and 0.874 *g/s* powder flow rate deposition are shown in Figures 8.8 and 8.9. For the range of parameters analysed, SDAS ranging from 4.49 *μm* to 8.44 *μm* for low powder flow rate deposition were measured, with the highest SDAS being produced with the 100% Inconel 718 powder. While under high powder flow rate conditions, the SDAS measured was in the range 4.13 *μm* to 7.76 *μm*. This trend clearly suggests that with increased powder flow rate, SDAS is decreased. This effect can be attributed to the rapid quenching that leads to the finer dendritic structure observed during high powder flow rate deposition process. Moreover, SDAS increased with the height of the build showing that the local solidification time also increased somewhat with increasing distance from the substrate, which acts as a heat sink. The increased solidification times arise from a lower average cooling rate with distance from the substrate. This is because the average thermal gradient in the build direction decreases as the distance from the substrate increases.

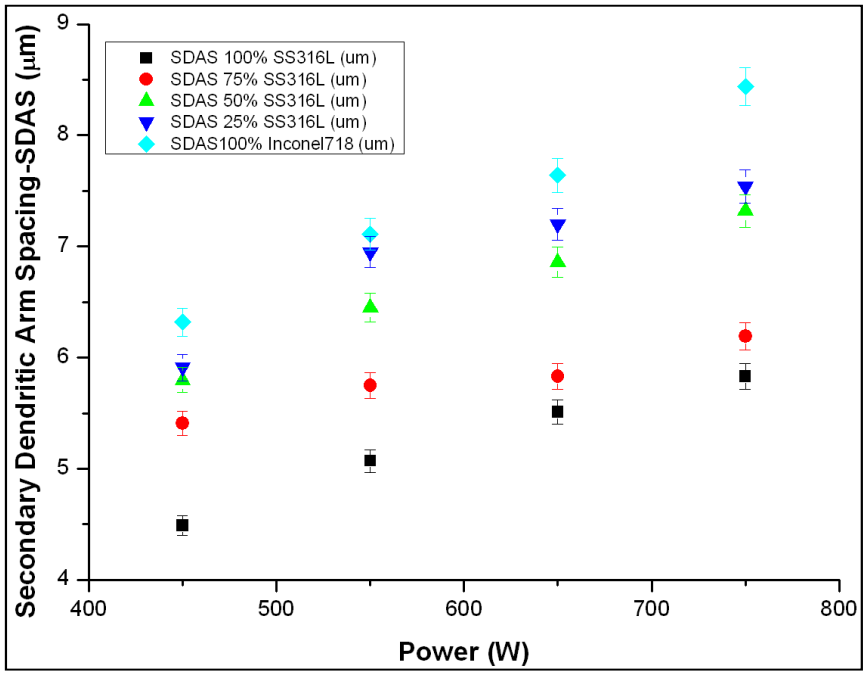

Figure 8.8: Change in Mean SDAS from bottom to top of the wall at low powder flow rate

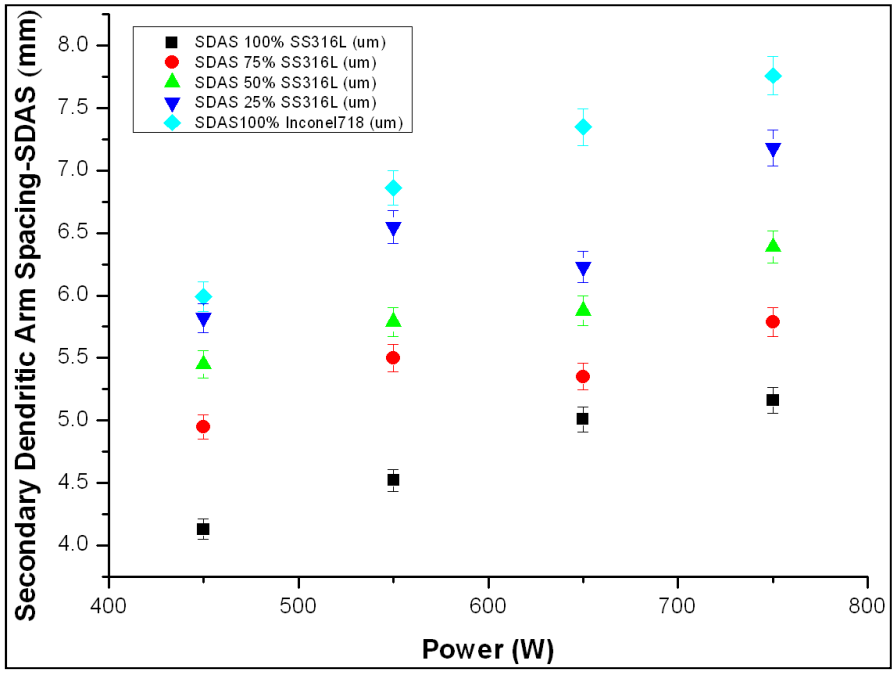

Figure 8.9: Change in Mean SDAS from bottom to top of the wall at high powder flow rate

8.4.3 Phase analysis using X-ray diffraction technique

Figure 8.10 (a-e) shows the XRD patterns from representative wall sections taken perpendicular to the gradient direction for sample 8. Similar patterns were obtained for the rest of the samples. Figure 8.10 (a, b) shows that structures produced with 100 and 75 percent of SS316L were entirely austenitic with minimum degree of ferrite. It also indicates lack of clear orientation of microstructure. As the Inconel 718 weight percentage increases new phases comprising of Niobium Carbide (NbC) and Fe_2Nb are formed as shown in Figure 8.10 (c-e). Quantification of the phases was not possible.

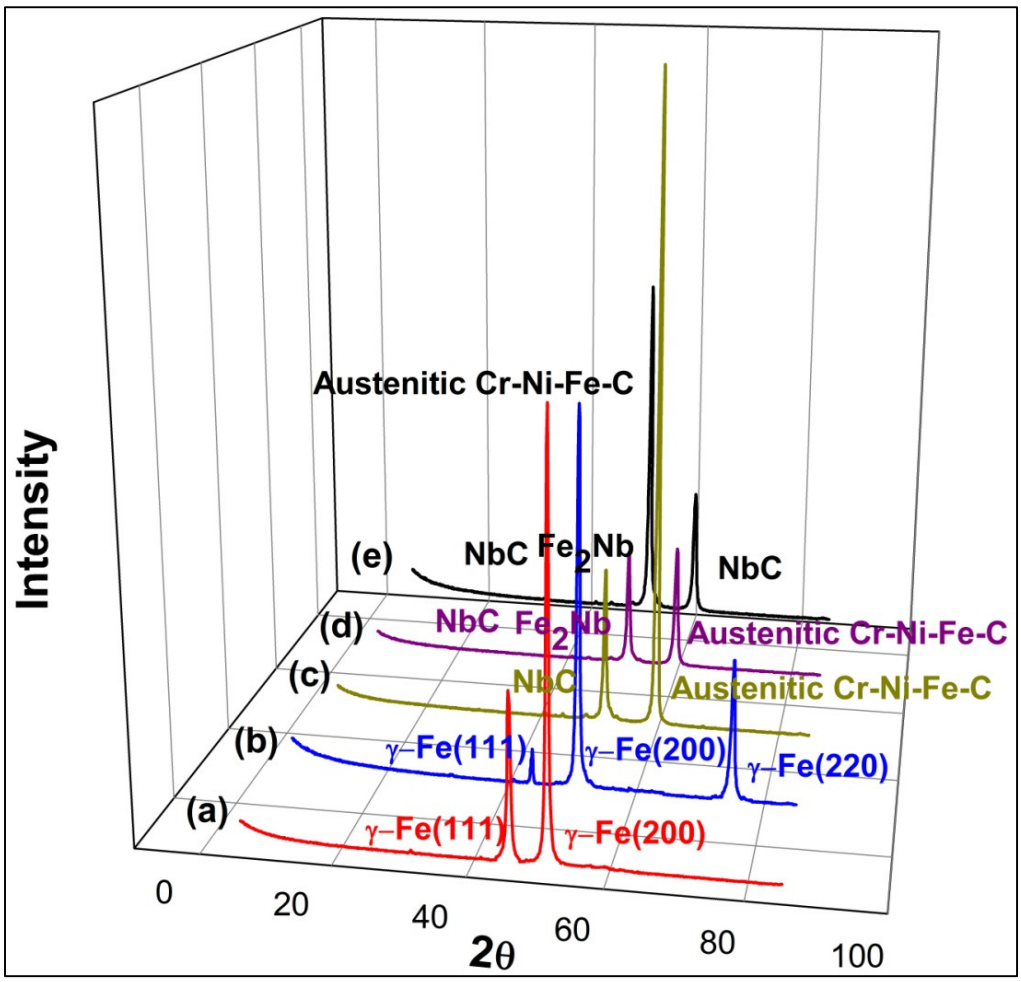

Figure 8.10: (a-e) XRD Patterns at different location along the SS 316L -Inco 718 gradient obtained for sample 8. (a) 100% SS 316L, (b) 75% SS 316L, (c) 50% SS 316L, (d) 25% SS 316L, (e) 0% SS 316L

8.4.4 Tensile testing

In all samples moderately ductile fracture took place with only a moderate amount of deformation. For all samples, fracture started initially at the stainless steel 316L side which then propagated rapidly to the Inconel 718 side. Cross-section of the fractured surface of sample 1 is shown in Figure 8.11.

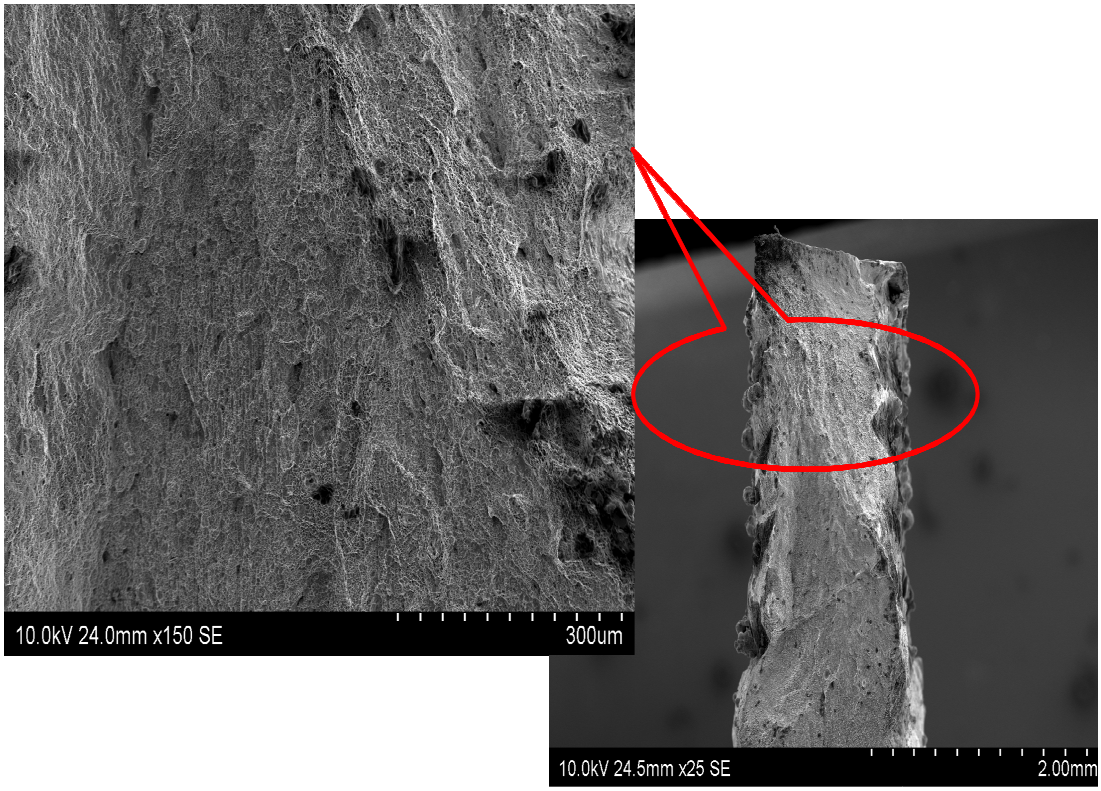

Figure 8.11: Fractured surface of sample 1 with enlarged view of the surface

.

The summary of the tensile strength data plotted versus laser power in Figure 8.12 shows a trend for a decrease in tensile strength at high laser powers. Moreover, tensile strength seems to increase with the increase in power flow rate. Low powder flow rate in the deposition process is found to yield tensile strengths of 526 *MPa* to 573.5 *MPa*. While high powder flow rate in the deposition process yields tensile strength ranging between 531 *MPa* and 596 *MPa*. It can also be seen that at high powder flow rates, high tensile strength values are obtained. Reduction of tensile strength can be explained by the fact that grains get larger in size with the increasing heat input and these offer less resistance to the applied load [300].

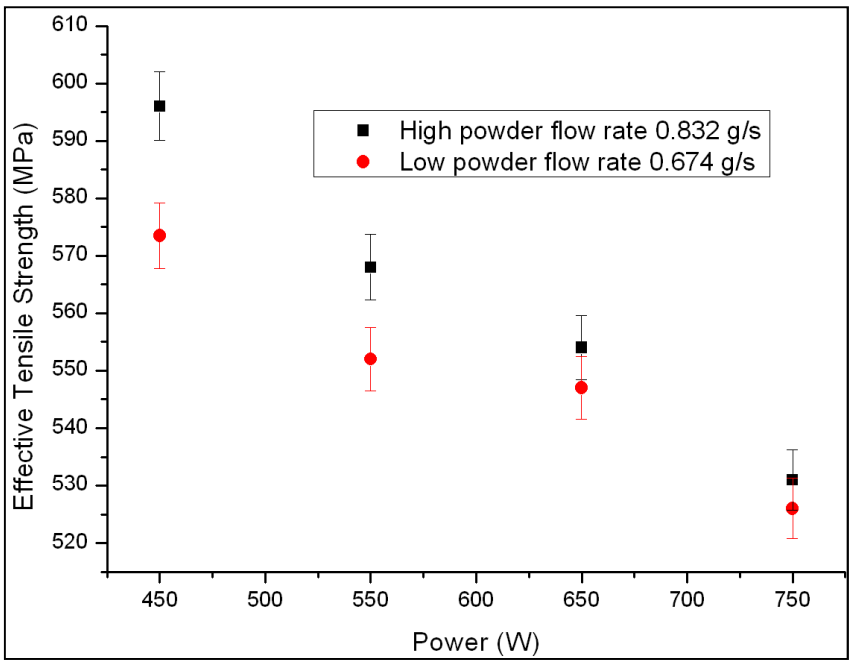

Figure 8.12: Tensile strength variation as a function of power at different powder flow rates

8.4.5 Hardness distribution

Vickers micro-hardness measurements were made along the length of the walls of samples deposited at different powder flow rates and power levels. The results are plotted in Fig. 8.13 as a function of the number of layers from the substrate. Figure 8.13 (a) shows an approximately parabolic distribution of hardness with a maximum measured hardness of 186.1 $HV_{0.1}$ in the final layer and 168.1 $HV_{0.1}$ in the first layer with high powder flow rate deposition. Hardness values of 155.6 $HV_{0.1}$ and 179.3 $HV_{0.1}$ are observed in the bottom and top layer respectively for low powder flow rate deposition. For the other three power levels, similar hardness variation measurements are observed. Furthermore, high powder flow rate deposition case results in a higher level of hardness compared to the low powder flow rate case. Figure 8.13 (a-d) clearly show that, within the multilayer builds studied, the hardness initially decreased until weight percentage of Inconel 718 was approximately

increased to 50%. From this percentage onwards, increase in hardness of layers was observed.

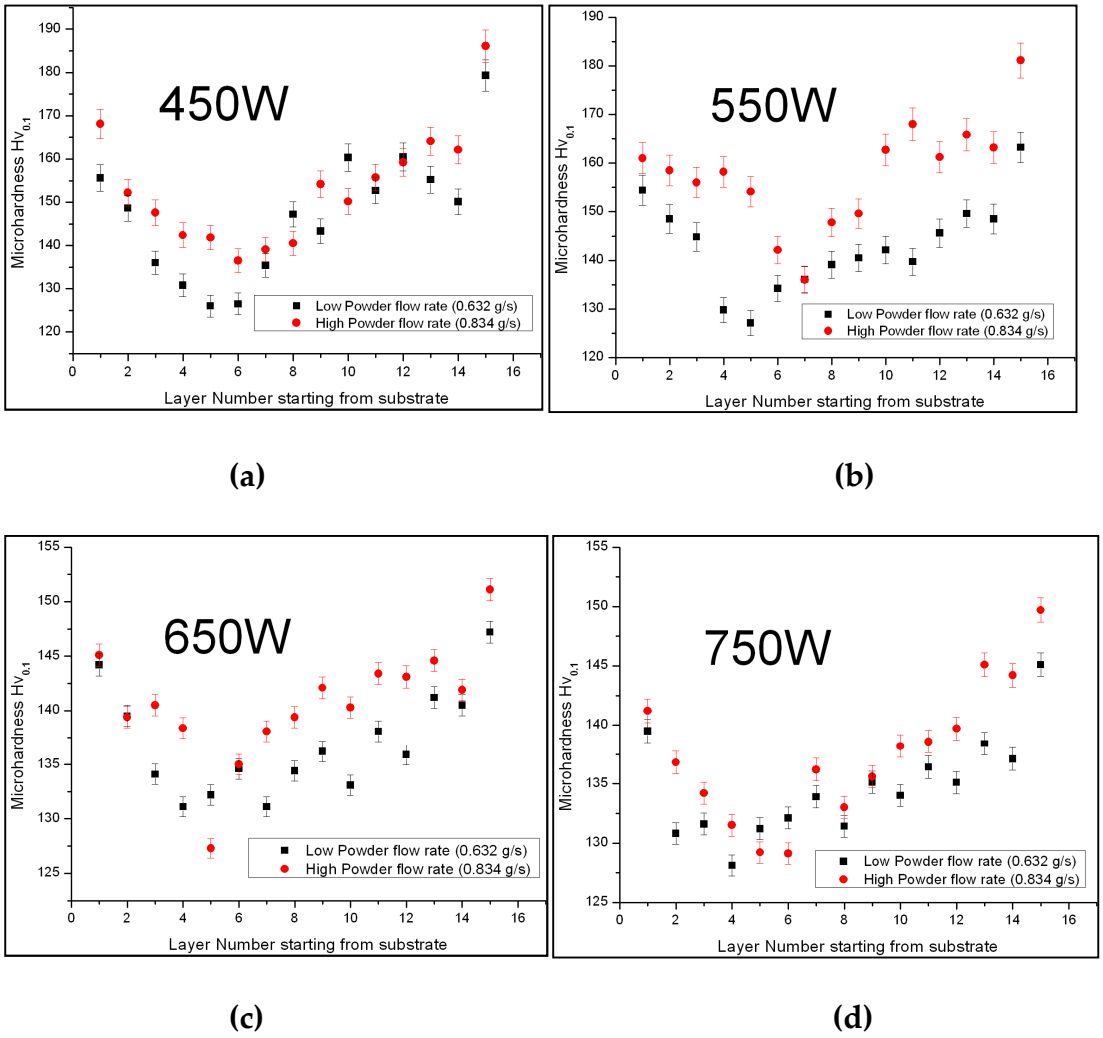

Figure 8.13: Hardness profiles at various powers under different powder flow rates

It is worth noting that there is a significant increase in the hardness in the top layers of all the samples. This could be explained by the fact that the final layer is not reheated, unlike the reheating experienced by the other layers beneath it. Lack of post deposition heat treatment is attributed to the increase in hardness.

8.4.6 Wear testing

All the sample walls were separated from the 316L substrate, longitudinally sectioned and mounted on a Teer Coatings (POD-2) pin on disk wear tester. The calculations for the evaluation of the specific wear rate were done by employing the software available with the machines supplied by Teer coatings Ltd, UK.

Figures 8.14 and 8.15 show optical and surface profiler images of the wear track on the surface of sample 2 following testing under 20 *N* load and sliding speed of 30 *mm/s*.

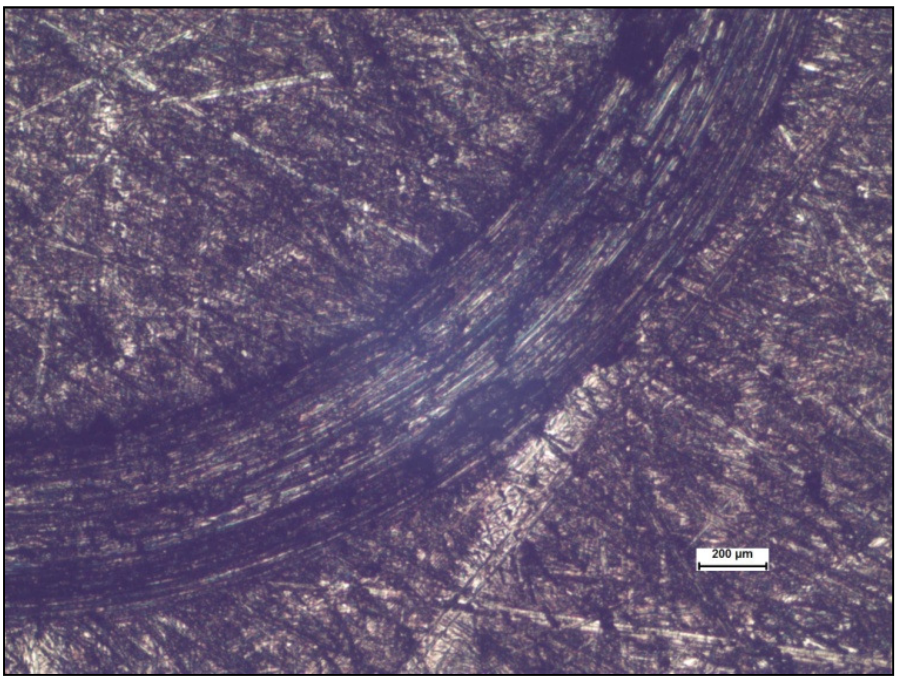

Figure 8.14: Optical profile of wear track track in sample2 25% SS31675% Inconel 718 composition by weight after testing under 20 N load

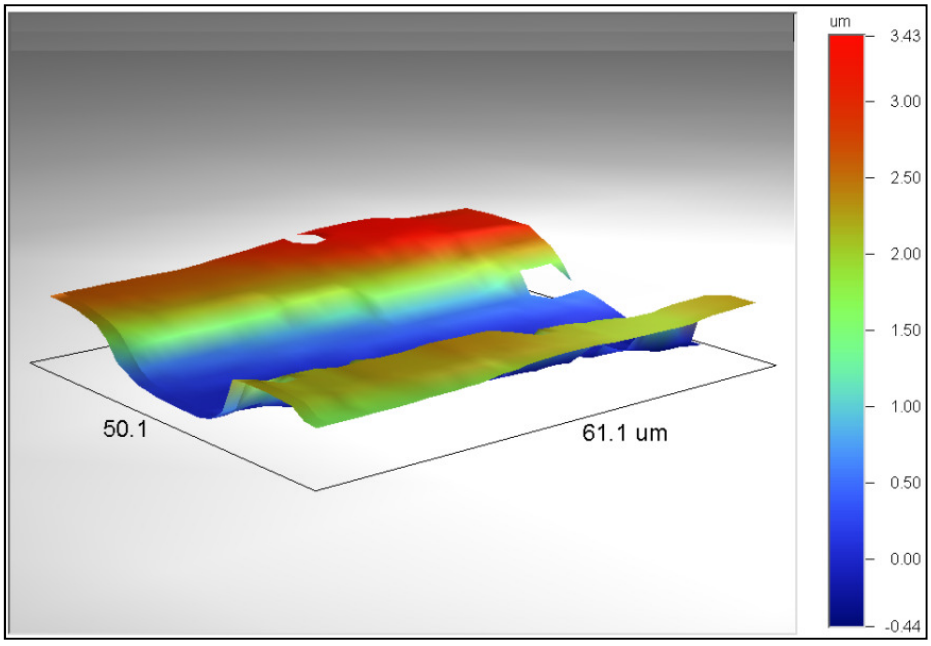

Figure.8.15: 3D surface profiler image of the wear track in sample2 25% SS31675% Inconel 718 composition by weight after testing under 20 N load

In Figure 8.16, the variations in mean specific wear rate for different power levels are shown. Instead of individual wear rate of each layer, a mean specific wear rates for three layers of constant composition were calculated due to limitation imposed by the diameter of the WC-Co ball used in the test. In all the samples, the mean specific wear rate (MSWR) followed an inverse relation to the hardness as the composition was changed from Stainless steel 316L to Inconel 718. In the first three layers of 100% SS316L MSWR is low; it then increases when Inconel 718 is added in the next three layers. After the addition of more Inconel 718 in the next 9 layers MSWR reduces. This trend is noted for all the samples. Overall MSWR is high at higher power levels used as compared to the MSWR observed at low powers levels.

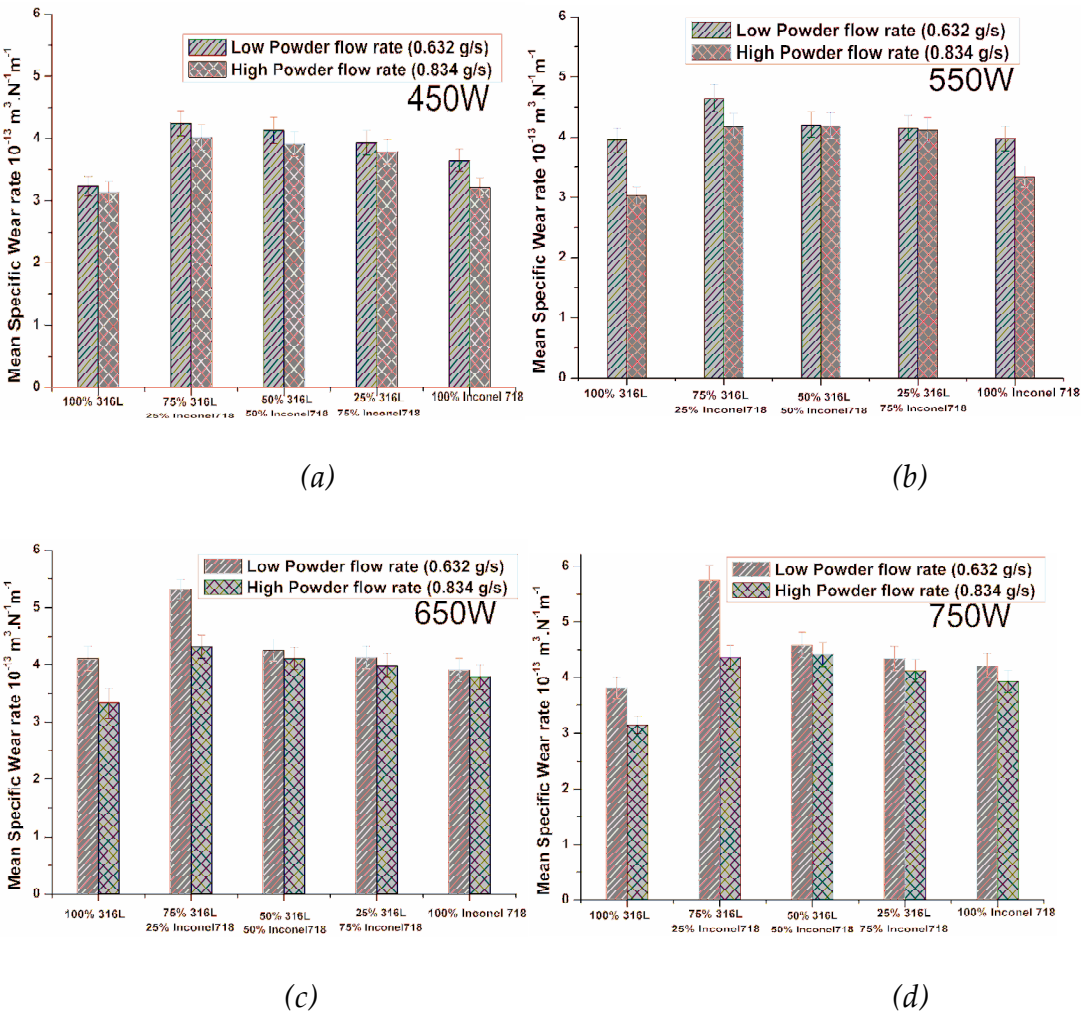

Figure 8.16: Means Specific wear rate along the gradient for various powers for 20N load and sliding speed of 30 mm/s (a) 450W (b) 550W (c) 650W (d) 750W

8.5 Discussion

Varying laser power and powder flow rate has shown some scope for controlling high power diode laser deposition microstructures. Minimising power and maximising powder flow rate is found to produce the finest grain structure, however these changes in microstructure come at the expense of changes in layer height and width.

Refinement of grain structure or the decrease in secondary dendritic arm spacing was found to decrease with increasing power. As the cooling rate decreases there is enough time for small dendrite arms to melt and disappear;

when this occurs, the secondary dendrite arm spacing of the alloys increases [301]. Moreover, the slower the cooling rate during solidification, the longer the time available for grain coarsening.

This characteristics echoes that reported by Wu *et al* [302] for titanium alloys and Griffith *et al* [169] for austenitic stainless steel and has been attributed to the effect of high cooling rates at low powers resulting in fine grain structures. It has also been noted that the SDAS increased with the height of the build, suggesting that the local solidification time also increased somewhat with increased distance from the substrate, which acts as a heat sink. The increased solidification times arise from a lower average cooling rate with distance from the substrate. This is because the average thermal gradient in the build direction decreases as the distance from the substrate increases.

Analysis of the tensile strength of the graded structure produced under various operating condition during high powder diode laser deposition yielded an inverse relation between the tensile strength and laser power. As it has been discussed above that laser power affects the grain size and SDAS, which in turn controls the ultimate strength of the material, lower SDAS values are obtained at low power which yields higher tensile strength in the material.

It is interesting to note that the hardness distribution in the samples followed an approximate parabolic curve unlike conventional single material deposition, in which the hardness of the material decreases when measured along the height of the samples starting from the substrate [87]. XRD patterns confirm the increasing presence of NbC and Fe_2Nb when the Inconel 718 percentage is increased. According to Fujita *et al* [303] NbC and Fe_2 Nb improve the strength of the material. This can justify the increase in hardness when more Inconel 718 is added and more Nb is present to form NbC.

An inverse relation is obtained for the wear rate and hardness of laser deposited SS316L and Inconel 718 graded walls. It is well known that wear

resistant materials can be obtained by reinforcing soft phases with harder phases [304, 305]. Nb is being used to modify stainless steels to get a good combination of thermal fatigue resistance, high temperature strength, corrosion resistance, for example in automotive exhaust systems [303, 306]. The presence of hard Niobium Carbide (NbC) and Fe_2 Nb in the laser deposited samples not only increased their hardness but also their wear resistance. Using such functional grading techniques, it provides a means to select hardness and wear resistance according to the end user's s own specific need.

8.6 Conclusions

With the ultimate goal of being able to manufacture novel graded structures of Stainless Steel 316L and Inconel 718 by using a diode laser deposition process, a set of parametric studies have been undertaken to analyse the effect of laser power and powder mass flow rate.

In the endeavour to determine the functional characteristics of diode laser deposited functionally graded walls of Stainless Steel 316L and Inconel 718, high resolution optical and scanning electron microscopy, XRD, tensile testing, micro hardness testing and wear rate testing have been employed. From the results generated the following conclusions can be drawn:

1. Laser deposition process is a feasible method of manufacturing functionally grading of SS316L and Inconel 718 materials.
2. Secondary dendritic arm spacing (SDAS) is strongly dependant on the power and solidification time during the manufacture of Ni-Steel FGM.
3. Effect of laser power and powder flow rate is inversely proportional to the tensile strength of the functional part.
4. Generation of carbide like NbC will create an opportunity to selectively control the hardness and wear resistance of the functional material.

5. The graded microstructure structure can be useful for applications where details of the loading conditions are known and the microstructure could be designed to best suit the loading for each section of a component.

Chapter 9. Conclusions and Future Work

9.1 Conclusions

This thesis has covered a wide range of aspects of diode laser deposition of dissimilar and functionally graded materials. Although conclusions for each set of work are included within the result sections, brief summaries of the findings are as follows:

9.1.1 LDMD of Inconel 718 nickel alloy to Ti-6Al-4V titanium alloy

- Duty cycle seems to have no significant effect on the crack development.
- Presence of two brittle phases Ti_2Ni and $TiNi_3$ were observed in all the deposited samples.
- Brittle phases and the amount of in-process stress dictate the crack formation in the clad.
- Clad thickness seems to have a significant effect on the debonding of the clad from the substrate.
- Clads with low powder flow rate of 0.358 g/s does not show any sign of cracking.

9.1.2 Finite element modelling of Titanium and Nickel Alloys LDMD process

- A three-dimensional thermal and structural finite element model of nickel and titanium alloy laser deposition process was developed using heterogeneous mesh and temperature dependant properties.

- Transient nature of continuous wave and pulsed wave deposition LDMD process has been implemented by using element birth and death technique available in ANSYS.
- Calculated and experimental temperature and residual stress results are in good agreement.

9.1.3 Melt pool stability during deposition of Inconel 718 on Ti-6Al-4V

- An image-based analysis technique has been developed in MATLAB® to measure the melt pool surface disturbance and the melt pool size during LDMD of Inconel 718 on Ti-6Al-4V.
- High powder flow rate and carrier gas flow rate and using the laser in pulsed mode increase the mean melt pool surface disturbance and affect the mean area of the melt pool.
- The overall melt pool area increased with the increase in powder flow rate; the carrier gas flow rates also seemed to play important roles in determining the melt pool size.
- Increase in carrier gas flow rate lead to a small and shorter pool, possibly due to changes in powder stream characteristics or recoiling powder.
- It has been observed that with the increase in melt pool surface disturbance, low level of surface roughness of the deposited part can be achieved.

9.1.4 LDMD of functionally graded Inconel 718 and Stainless steel 316L.

- Functionally grading of Inconel 718 and Stainless steel using LDMD process provides an alternative method of manufacturing. During the manufacture of Inconel 718 and stainless steel 316L graded structure,

dendritic growth was observed and secondary dendritic arm spacing (SDAS) dependency on power and solidification time was observed.

- Effect of laser power and powder flow rate is inversely proportional to the tensile strength of the functional part.
- Generation of carbide like NbC will create an opportunity to selectively control the hardness and wear resistance of the functional material. This opens up the opportunity to change these properties on and when required basis

9.2 Recommendations Future Work

This work presented in this dissertation opens new opportunities for further research. As a direct result of the work presented in this dissertation the following suggestions can be made.

9.2.1 Modelling

- A number of imaging techniques such as computerised X-Ray tomography can be used to produce detailed 3D images that may be used for physics based modelling. By using such techniques structures manufactured by LDMD process can be explored based on its original structure instead of conventional method of assuming pre-defined geometry. These original structures can be tested using any commercial finite element package.
- Modelling of the residual stress fields especially for the functionally graded structures is an important step that needs to be taken.
- Application of the such models to optimise LDMD process for various applications

9.2.2 Testing

- Investigating and documentation of the thermo-mechanical properties of alloys developed using LDMD process such as conductivity, surface tension temperature coefficient and yield stress etc. This data will be useful for thermo-structural modelling which is currently unknown for many alloys.
- The effect of different types of carrier gas on the melt pool stability should be tested.
- Effect of shield and/or carrier gas in LDMD process is nozzle dependant. By using different types of nozzles i.e. lateral and coaxial; elucidating the effect of shielding gas on the deposited structures needs to be made.
- Measuring residual stresses in the FGM using neutron diffraction techniques.
- Examination of the performance of components manufactured using laser deposition should be performed, ideally in comparison with traditionally manufactured components.
- Exploitation of more materials to build FGMs.

References

1. Zhao, X., J. Chen, X. Lin, and W. Huang, 2008 *Study on microstructure and mechanical properties of laser rapid forming Inconel 718.* Materials Science and Engineering: A. **478**(1-2): p. 119-124.
2. Zhang, W.J., B.V. Reddy, and S.C. Deevi, 2001 *Physical properties of TiAl-base alloys.* Scripta Materialia. **45**(6): p. 645-651.
3. Boivineau, M.M., 2006 *Thermophysical properties of solid and liquid Ti-6Al-4V (TA6V) alloy.* International Journal of Thermophysics. **27**(2): p. 507-29.
4. Wu, X., 1999 *In situ formation by laser cladding of a TiC composite coating with a gradient distribution.* Surface and Coatings Technology. **115**(2-3): p. 111-115.
5. Cirakoglu, M., S. Bhaduri, and S.B. Bhaduri, 2002 *Processing and characterization of Ti-B-based functionally graded materials produced by microwave-activated combustion synthesis.* Journal of Materials Research. **17**(11): p. 2823-30.
6. Yarrapareddy, E., S. Zekovic, S. Hamid, and R. Kovacevic, 2006 *The development of nickel-tungsten carbide functionally graded materials by a laser-based direct metal deposition process for industrial slurry erosion applications.* Proceedings of the Institution of Mechanical Engineers, Part B: Journal of Engineering Manufacture. **220**(12): p. 1923-1936.
7. *The Electromagnetic Spectrum* [cited 2010 01 December]. Available from: http://www.nasa.gov/centers/langley/science/FIRST.html.
8. Steen, W.M., 2003 *Laser material Processing*. 3rd Edition ed: Springer-Verlag London Limited.
9. Silfvast, W.T., 2004 *Laser Fundamentals*. Second ed: Cambridge University Press.
10. Beesley, M.J., 1976 *Lasers and their applications*. Second ed., London: Halsted Press.
11. Beesley, M. J., 1971 *Lasers and Their Applications*. London: Taylor & Francis.
12. Einstein, A., 1916 *A Simple Experiment to Demonstrate Ampère's Molecular Currents.* Deutsche Physikalische Gesellschaft. **18**: p. 138.
13. Steen, W.M., 1996 *Laser Materials Processing*. 2nd ed., Berlin: Springer.
14. Schilling, B. W., 2003 *Encyclopaedia of Optical Engineering, Section: Lasers*: Taylor & Francis.
15. Elijah Kannatey-Asibu, J., 2009 *Principles of laser materials processing*: John Wiley & Sons, Inc.
16. Ion, J.C., 2005 *Laser processing of engineering materials: principles, procedure and industrial application*: Elsevier, Butterworth-Heinemann.

17. Nathan, M.I., W.P. Dumke, G. Burns, F.H. Dill, Jr., and G. Lasher, 1962 *Stimulated emission of radiation from GaAs P-N junctions.* Applied Physics Letters. **1**(3): p. 62-64.
18. Tonshoff, H.K., A. Berndt, M. Sturmer, D. Golla, and J. Schumacher, 1994 *Diode lasers for material processing.* Journal De Physique. **4**(4): p. 59-63.
19. Ready, J.F., 1998 *Industrial applications of lasers*. 2nd ed., ed: Academic Press Limited.
20. *Brightness* [cited 2009 13 September]. Available from: http://www.rp-photonics.com/brightness.html.
21. *Laser Machining Processes* [cited 2010 08 November]. Available from: http://www.columbia.edu/cu/mechanical/mrl/ntm/level1/ch02/html/l1c02s07.html.
22. Luxon, J.T. and D.E. Parker, 1985 *Industrial lasers and their applications* Prentice-Hall, Inc.
23. Ion, J.C., 2005 *Laser processing of engineering materials: principles, procedure and industrial application*: Elsevier Butterworth-Heinemann. 589.
24. Silfvast, W.T., 2004 *Laser fundamentals* 2nd ed: Cambridge University Press. 670.
25. Ready, J.F., 2001 *LIA Handbook of Laser Materials Processing*: Laser Institute of America, Magnolia Publishing, Inc
26. Toyserkani, E., A. Khajepour, and S. Corbin, 2004*Laser Cladding*: CRC press LLC. 260.
27. Joseph, J.B., B. J. W, D.L. Bourell, R.H. Crawford, H.L. Marcus, and K.P. McAlea, 1997 *Solid Freeform Fabrication: A New Direction in manufacturing with Research and Applications in Thermal Laser Processing.*
28. Mazumder, J., D. Dutta, N. Kikuchi, and A. Ghosh, 2000 *Closed loop direct metal deposition: art to part.* Optics and Lasers in Engineering. **34**(4-6): p. 397.
29. Zhang, K., W. Liu, and X. Shang, 2007 *Research on the processing experiments of laser metal deposition shaping.* Optics & Laser Technology. **39**(3): p. 549-557.
30. *Laser Engineered Net Shaping* [cited 2010 10 December]. Available from: http://www.optomec.com/site/products_3.
31. *Direct Metal Deposition System* [cited 2010 10 December]. Available from: http://www.pomgroup.com/index.php?option=com_content&task=view&id=33&Itemid=90.
32. Pelletier, J.M., M.C. Sahour, M. Pilloz, and A.B. Vannes, 1993 *Influence of processing conditions on geometrical features of laser claddings obtained by powder injection.* Journal of Materials Science. **28**(19): p. 5184-5188.

33. Xiong, Z., G.-x. Chen, and X.-y. Zeng, 2009 *Effects of process variables on interfacial quality of laser cladding on aeroengine blade material GH4133.* Journal of Materials Processing Technology. **209**(2): p. 930-936.
34. Zhong, M., W. Liu, G. Ning, L. Yang, and Y. Chen, 2004 *Laser direct manufacturing of tungsten nickel collimation component.* Journal of Materials Processing Technology. **147**(2): p. 167-173.
35. Choi, J., L. Han, and Y. Hua, 2005 *Modeling and experiments of laser cladding with droplet injection.* Journal of Heat Transfer-Transactions of the Asme. **127**(9): p. 978-986.
36. Yang, Y. and H.C. Man, 2000 *Microstructure evolution of laser clad layers of W-C-Co alloy powders.* Surface and Coatings Technology. **132**(2-3): p. 130-136.
37. Fellowes, F.C.J., W.M. Steen, and S.R.J. Saunders, 1991 *Deposition of silica coatings on incoloy 800H substrates using a high power laser.* Surface and Coatings Technology. **45**(1-3): p. 425-434.
38. Tan, H., J. Chen, F. Zhang, X. Lin, and W. Huang, 2010 *Estimation of laser solid forming process based on temperature measurement.* Optics & Laser Technology. **42**(1): p. 47-54.
39. Tan, H., J. Chen, F. Zhang, X. Lin, and W. Huang, 2010 *Process analysis for laser solid forming of thin-wall structure.* International Journal of Machine Tools and Manufacture. **50**(1): p. 1-8.
40. Lin, J., 1999 *Temperature analysis of the powder streams in coaxial laser cladding.* Optics & Laser Technology. **31**(8): p. 565-570.
41. Huang, F., Z. Jiang, X. Liu, J. Lian, and L. Chen, 2009 *Microstructure and properties of thin wall by laser cladding forming.* Journal of Materials Processing Technology. **209**(11): p. 4970-4976.
42. Xu, X., X. Lin, M. Yang, J. Chen, and W. Huang, 2009 *Microstructure evolution in laser solid forming of Ti-50 wt% Ni alloy.* Journal of Alloys and Compounds. **480**(2): p. 782-787.
43. Paulo Davim, J., C. Oliveira, and A. Cardoso, 2008 *Predicting the geometric form of clad in laser cladding by powder using multiple regression analysis (MRA).* Materials & Design. **29**(2): p. 554-557.
44. Hua, T., C. Jing, L. Xin, Z. Fengying, and H. Weidong, 2008 *Research on molten pool temperature in the process of laser rapid forming.* Journal of Materials Processing Technology. **198**(1-3): p. 454-462.
45. Qu, H.P., P. Li, S.Q. Zhang, A. Li, and H.M. Wang, 2010 *Microstructure and mechanical property of laser melting deposition (LMD) Ti/TiAl structural gradient material.* Materials & Design. **31**(1): p. 574-582.
46. Pashby, I.R., S.H. Mok, and J. Folkes.2004 *Direct diode laser deposition of titanium alloys*. San Francisco, CA, United states: Laser Institute of America.

47. Pantelis, D., H. Michaud, and M. de Freitas, 1993 *Wear behaviour of laser surface hardfaced steels with tungsten carbide powder injection.* Surface and Coatings Technology. **57**(2-3): p. 123-131.
48. Wang, H.M., P. Jiang, and Y.F. Liu.2002 *State of the art prospects on laser surface modifications of titanium alloys for the aerospace industries*. in *Lasers in Material Processing and Manufacturing*. Shanghai, China: SPIE-Int. Soc. Opt. Eng.
49. Yang, X.-C., J.-J. Wang, S.-Y. Gao, Y.-S. Wang, Z.-C. Zhang, and Y. Tang.2002 *A new co-axial powder feeder without carrying gas for laser direct materials deposition*. in *Lasers in Materials Processing and Manufacturing*. Shanghai, China: The International Society for Optical Engineering.
50. de Damborenea, J., A.J. Vázquez, and B. Fernández, 1994 *Laser-clad 316 stainless steel with Ni---Cr powder mixtures.* Materials & Design. **15**(1): p. 41-44.
51. Hidouci, A., J.M. Pelletier, F. Ducoin, D. Dezert, and R. El Guerjouma, 2000 *Microstructural and mechanical characteristics of laser coatings.* Surface & Coatings Technology. **123**(1): p. 17-23.
52. Grujicic, M., Y. Hu, G.M. Fadel, and D.M. Keicher, 2001 *Optimization of the LENS Rapid fabrication process for in-flight melting of feed powder.* Journal of Materials Synthesis and processing. **9**(5): p. 223-233.
53. Kobryn, P.A., E.H. Moore, and S.L. Semiatin, 2000 *The effect of laser power and traverse speed on microstructure, porosity, and build height in laser-deposited Ti-6Al-4V* 2003 ASME Summer Heat Transfer Conference (HT2003). **43**(4): p. 299-305.
54. Roberts, I.A., C.J. Wang, R. Esterlein, M. Stanford, and D.J. Mynors, 2009 *A three-dimensional finite element analysis of the temperature field during laser melting of metal powders in additive layer manufacturing.* International Journal of Machine Tools and Manufacture. **49**(12-13): p. 916-923.
55. Lee, H.-K., 2008 *Effects of the cladding parameters on the deposition efficiency in pulsed Nd:YAG laser cladding.* Journal of Materials Processing Technology. **202**(1-3): p. 321-327.
56. Wen, S.Y., Y.C. Shin, J.Y. Murthy, and P.E. Sojka, 2009 *Modeling of coaxial powder flow for the laser direct deposition process.* International Journal of Heat and Mass Transfer. **52**(25-26): p. 5867-5877.
57. Pinkerton, A. and L. Li, 2004 *An analytical model of energy distribution in laser direct metal deposition.* Proceedings of the Institution of Mechanical Engineers, Part B: Journal of Engineering Manufacture. **218**(4): p. 363-374.
58. Foroozmehr, E., D. Lin, and R. Kovacevic, 2009 *Application of vibration in the laser powder deposition process.* Journal of Manufacturing Processes. **11**(1): p. 38-44.

59. Yang, N., 2009 *Concentration model based on movement model of powder flow in coaxial laser cladding.* Optics & Laser Technology. **41**(1): p. 94-98.
60. Alemohammad, H., S. Esmaeili, and E. Toyserkani, 2007 *Deposition of Co-Ti alloy on mild steel substrate using laser cladding.* Materials Science and Engineering: A. **456**(1-2): p. 156-161.
61. Han, L., K. Phatak, and F. Liou, 2004 *Modeling of laser cladding with powder injection.* Metallurgical and Materials Transactions B. **35**(6): p. 1139-1150.
62. Xiong, Y., J.E. Smugeresky, and J.M. Schoenung, 2009 *The influence of working distance on laser deposited WC-Co.* Journal of Materials Processing Technology. **209**(10): p. 4935-4941.
63. de Oliveira, U., V. Ocelik, and J.T.M. De Hosson, 2005 *Analysis of coaxial laser cladding processing conditions.* Surface & Coatings Technology. **197**(2-3): p. 127-136.
64. Doubenskaia, M., P. Bertrand, and I. Smurov.2003 *Optical monitoring of Nd:YAG laser cladding* in *Symposium H on Photonic Processing of Surfaces, Thin Films & Devices of the EMRS 2003 Spring Conference*. Strasbourg, France: Elsevier.
65. Vreeling, J.A., V. Ocelik, Y.T. Pei, D.T.L. Van Agterveld, and J.T.M. De Hosson, 2000 *Laser melt injection in aluminum alloys: on the role of the oxide skin* Acta Materialia **48**(17): p. 4225-4233.
66. Anandkumar, R., A. Almeida, R. Vilar, V. Ocelík, and J.T.M. De Hosson, 2009 *Influence of powder particle injection velocity on the microstructure of Al-12Si/SiCp coatings produced by laser cladding.* Surface and Coatings Technology. **204**(3): p. 285-290.
67. Sun., S.J. and M. Brandt, 2008 *Investigation of Hastelloy C laser clad melt pool size and its effect on clad formation.* Key Engineering Materials. **384**: p. 213-227.
68. Partes, K. and G. Sepold, 2008 *Modulation of power density distribution in time and space for high speed laser cladding.* Journal of Materials Processing Technology. **195**(1-3): p. 27-33.
69. Majumdar Dutta , J., A. Kumar, and L. Li, 2009 *Direct laser cladding of SiC dispersed AISI 316L stainless steel.* Tribology International. **42**(5): p. 750-753.
70. Zekovic, S., R. Dwivedi, and R. Kovacevic, 2007 *Numerical simulation and experimental investigation of gas-powder flow from radially symmetrical nozzles in laser-based direct metal deposition.* International Journal of Machine Tools and Manufacture. **47**(1): p. 112-123.
71. Pinkerton, A.J., W. Wang, and L. Li, 2008 *Component repair using laser direct metal deposition.* Proceedings of the Institution of Mechanical Engineers, Part B: Journal of Engineering Manufacture. **222**(7): p. 827-836.

72. Syed, W.U.H., A.J. Pinkerton, and L. Li, 2004 *A comparative study of wire feeding and powder feeding in direct diode laser deposition for rapid prototyping.* (Submitted to Applied Surface Science).
73. Syed, W.U.H., A.J. Pinkerton, Z. Liu, and L. Li, 2007 *Coincident wire and powder deposition by laser to form compositionally graded material.* Surface and Coatings Technology. **201**(16-17): p. 7083-7091.
74. Syed, W.U.H., A.J. Pinkerton, and L. Li, 2006 *Combining wire and coaxial powder feeding in laser direct metal deposition for rapid prototyping.* Applied Surface Science. **252**(13): p. 4803-4808.
75. Tuominen, J., M. Honkanen, J. Hovikorpi, J. Vihinen, P. Vuoristo, and T. Mantyla. 2003 *Corrosion resistant nickel superalloy coatings laser-clad with a 6 kW high power diode laser (HPDL),* in *First International Symposium on High-Power Laser Macroprocessing*, I. Miyamoto, et al., Editors, Spie-Int Soc Optical Engineering: Bellingham. p. 59-64.
76. Furumoto, T., T. Ueda, N. Kobayashi, A. Yassin, A. Hosokawa, and S. Abe, 2009 *Study on laser consolidation of metal powder with Yb:fiber laser--Evaluation of line consolidation structure.* Journal of Materials Processing Technology. **209**(18-19): p. 5973-5980.
77. Angelastro, A., *Characterization Of Colmonoy 227-F Samples Obtained By Direct Laser Metal Deposition.* Advanced materials research. **83**(2): p. 842-9.
78. Kusuhara, T., *Formation Of Ni-Base Self-fluxing Alloy Layers By Diode Laser Cladding With Powder Feeder.* AIP conference proceedings. **1282**: p. 123-6.
79. LIA handbook of laser materials processing 2001 Ready, J.F. and D.F. Farsoneds., Laser Institute of America Magnolia Publishing, Inc. .
80. Fu, Y., A. Loredo, B. Martin, and A.B. Vannes, 2002 *A theoretical model for laser and powder particles interaction during laser cladding.* Journal of Materials Processing Technology. **128**(1-3): p. 106-112.
81. Lin, J.M., 1999 *Concentration mode of the powder stream in coaxial laser cladding.* Optics and Laser Technology. **31**(3): p. 251-257.
82. Lin, J.M., 1999 *A simple model of powder catchment in coaxial laser cladding.* Optics and Laser Technology. **31**(3): p. 233-238.
83. Nowotny, S., S. Scharek, F. Kempe, and E. Beyer.2003 *COAXn: Modular system of powder nozzles for laser beam build-up welding*.
84. Pinkerton, A.J. and L. Li, 2004 *The significance of deposition point standoff variations in multiple-layer coaxial laser cladding (coaxial cladding standoff effects).* International Journal of Machine Tools and Manufacture. **44**(6): p. 573-584.
85. Jeng, J.Y., S.C. Peng, and C.J. Chou, 2000 *Metal Rapid Prototype Fabrication Using Selective Laser Cladding Technology.* The International Journal of Advanced Manufacturing Technology. **16**(9): p. 681-687.

86. F. Schneebeli, O. Braun, B. Tanner, and R. Dekumbis. 1993*Method of production of workpieces by welding equipment* U.P. Office, Editor.
87. Hussein, N.I.S., J. Segal, D.G. McCartney, and I.R. Pashby, 2008 *Microstructure formation in Waspaloy multilayer builds following direct metal deposition with laser and wire.* Materials Science and Engineering: A. **497**(1-2): p. 260-269.
88. Medrano, A., J. Folkes, J. Segal, and I. Pashby.2009 *Fibre laser metal deposition with wire: Parameters study and temperature monitoring system*. Lisboa, Portugal: SPIE.
89. Kim, J.-D. and Y. Peng, 2000 *Plunging method for Nd : YAG laser cladding with wire feeding.* Optics and Lasers in Engineering. **33**(4): p. 299.
90. Breinan, E.M. and B.H. Kear, 1983 *Rapid solidification laser processing at high power density.* Laser material processing: p. 235-295.
91. Nurminen, J., J. Riihimaki, J. Nakki, and P. Vuoristo.2007 *Hot-wire cladding process studies*. Orlando, FL, United states: Laser Institute of America.
92. Syed, W.U.H. and L. Li, 2005 *Effects of wire feeding direction and location in multiple layer diode laser direct metal deposition.* Applied Surface Science. **248**(1-4): p. 518.
93. Sun, Z. and M. Kuo, 1999 *Bridging the joint gap with wire feed laser welding.* Journal of Materials Processing Technology. **87**(1-3): p. 213.
94. Syed, W.U.H., A.J. Pinkerton, and L. Li, 2005 *A comparative study of wire feeding and powder feeding in direct diode laser deposition for rapid prototyping.* Applied Surface Science. **247**(1-4): p. 268.
95. Kim, J.-D. and Y. Peng, 2000 *Plunging method for Nd : YAG laser cladding with wire feeding.* Optics and Lasers in Engineering. **33**(4): p. 299-309.
96. Rongshi, X., C. Kai, Z. Tiechuan, G. Ambrosy, and H. Hugel.2002 *Influence of wire addition direction in CO2 laser welding of aluminum*. USA: SPIE-Int. Soc. Opt. Eng.
97. Fallah, V., S.F. Corbin, and A. Khajepour, 2010 *Solidification behaviour and phase formation during pre-placed laser cladding of Ti45Nb on mild steel.* Surface and Coatings Technology. **204**(Compendex): p. 2400-2409.
98. Powell, J., P.S. Henry, and W.M. Steen, 1988 *Laser cladding with preplaced powder analysis of thermal cycling and dilution.* Surface Engineering. **4 (2)**: p. 141-149.
99. Cheng, F.T., K.H. Lo, and H.C. Man, 2004 *A preliminary study of laser cladding of AISI 316 stainless steel using preplaced NiTi wire.* Materials Science and Engineering a-Structural Materials Properties Microstructure and Processing. **380**(1-2): p. 20-29.
100. Weerasinghe, V.M. and W.M. Steen.1983 *Laser Cladding with Pneumatic Powder Delivery*. Los Angeles, CA, USA: ASM.
101. Weerasinghe, V.M. and W.M. Steen, 1987 *Laser Cladding With Blown Powder.* Metal construction. **19**(10): p. 581-585.

102. Resch, M., A.F. Kaplan, and D. Schuoecker.2001 *Laser-assisted generating of three-dimensional parts by the blown powder process*. USA: SPIE-Int. Soc. Opt. Eng.
103. Zhou, M.Y., J.T. Xi, and J.Q. Yan, 2004 *Modeling and processing of functionally graded materials for rapid prototyping.* Journal of Materials Processing Technology. **146**(3): p. 396.
104. Koc, B., 2004 *Adaptive layer approximation of free-form models using marching point surface error calculation for rapid prototyping.* Rapid Prototyping Journal. **10(5)**: p. 270-280.
105. Luo, R.C., and J.H. Tzou, 2004. *Implementation of a new adaptive slicing algorithm for the rapid prototyping manufacturing system.* IEEE/ASME Transactions on Mechatronics. **9(3)**: p. 593-600.
106. Ma, W., W.-C. But, and P. He, 2004 *NURBS-based adaptive slicing for efficient rapid prototyping.* Computer-Aided Design. **36(13)**: p. 1309.
107. Liu, J. and L. Li, 2004 *In-time motion adjustment in laser cladding manufacturing process for improving dimensional accuracy and surface finish of the formed part.* Optics & Laser Technology. **36**(6): p. 477-483.
108. Lewis, G.K. and E. Schlienger, 2000 *Practical considerations and capabilities for laser assisted direct metal deposition.* Materials & Design. **21**(4): p. 417.
109. Li, L., 2006 *Repair of directionally solidified superalloy GTD-111 by laser-engineered net shaping.* Journal of Materials Science. **41**(23): p. 7886-7893.
110. Kobryn, P.A., E.H. Moore, and S.L. Semiatin, 2000 *Effect of laser power and traverse speed on microstructure, porosity, and build height in laser-deposited Ti-6Al-4V.* Scripta Materialia. **43**(4): p. 299-305.
111. Katayama, S., M. Mizutani, and A. Matsunawa.2003 *Development of porosity prevention procedures during laser welding*. USA: SPIE-Int. Soc. Opt. Eng.
112. Morgan, R.H., A.J. Papworth, C. Sutcliffe, P. Fox, and W. O'Neill, 2002 *High density net shape components by direct laser re-melting of single-phase powders.* Journal of Materials Science. **37**(15): p. 3093-3100.
113. Goswami, G.L., D. Kumar, A.K. Grover, A.L. Pappachan, and M.K. Totlani, 1999 *Control of defects during laser surface alloying.* Surface Engineering. **15**(1): p. 65-70.
114. Steen, W.M., V.M. Weerasinghe, and P. Monson.1986 *Some aspects of the formation of laser clad tracks*. USA.
115. Susan, D.F., J.D. Puskar, J.A. Brooks, and C.V. Robino, 2006 *Quantitative characterization of porosity in stainless steel LENS powders and deposits.* Materials Characterization. **57**(1): p. 36-43.
116. Hua, Y. and J. Choi, 2005 *Feedback control effects on dimensions and defects of H13 tool steel by direct metal deposition process.* Journal of Laser Applications. **17**(2): p. 118-126.

117. Choi, J. and Y. Chang, 2005 *Characteristics of laser aided direct metal/material deposition process for tool steel.* International Journal of Machine Tools and Manufacture. **45**(4-5): p. 597-607.
118. Liang, W. and F. Sergio, 2007 *Process Modeling in Laser Deposition of Multilayer SS410 Steel.* Journal of Manufacturing Science and Engineering. **129**(6): p. 1028-1034.
119. Ng, G., A. Jarfors, G. Bi, and H. Zheng, 2009 *Porosity formation and gas bubble retention in laser metal deposition.* Applied Physics A: Materials Science & Processing. **97**(3): p. 641-649.
120. Ahsan, M.N., C.P. Paul, L.M. Kukreja, and A.J. Pinkerton, *Porous structures fabrication by continuous and pulsed laser metal deposition for biomedical applications; modelling and experimental investigation.* Journal of Materials Processing Technology. **In Press, Corrected Proof**.
121. Gao, F., J. He, E. Wu, S. Liu, D. Yu, D. Li, S. Zhang, and Y. Tian, 2003 *Hardness of Covalent Crystals.* Physical Review Letters. **91**(1): p. 015502.
122. Liu, M.Y., B. Shi, C. Wang, S.K. Ji, X. Cai, and H.W. Song, 2003 *Normal Hall-Petch behavior of mild steel with submicron grains.* Materials Letters. **57**(19): p. 2798-2802.
123. Takaki, S., K. Kawasaki, and Y. Kimura, 2001 *Mechanical properties of ultra fine grained steels.* Journal of Materials Processing Technology. **117**(3): p. 359-363.
124. Wang, J., S. Yan, J. Xie, Z. Liu, J. Li, and W. Wang, *Effect of cooling rate on the microstructure of ZA48 alloy.* Journal of Wuhan University of Technology--Materials Science Edition. **25**(5): p. 811-813.
125. Griffith, M.L., M.E. Schlienger, L.D. Harwell, M.S. Oliver, M.D. Baldwin, M.T. Ensz, M. Essien, J. Brooks, C.V. Robino, J.E. Smugeresky, W.H. Hofmeister, M.J. Wert, and D.V. Nelson, 1999 *Understanding thermal behavior in the LENS process.* Materials & Design. **20**(2-3): p. 107-113.
126. Mazumder, J., A. Schifferer, and J. Choi, 1999 *Direct materials deposition: designed macro and microstructure.* Materials Research Innovations. **3**(3): p. 118-131.
127. Gorman, P., J.E. Smugeresky, and D.M. Keicher.2002 *Evaluation of property dependence on build rate for LENS powder metal deposition*. in *Rapid Prototyping of Materials. Proceedings of Symposium, 7-10 Oct. 2002*. Warrendale, PA, USA: TMS - Miner. Metals & Mater. Soc.
128. Zhang, Y. and L. Shi.2003 *Research on laser direct metal deposition*. in *First International Symposium on High-Power Laser Macroprocessing*. Osaka, Japan: SPIE.
129. Zhang, Y. and L. Shi.2003 *Research on laser direct metal deposition*. in *Proceedings of the SPIE*.

130. Zhang, Y., M. Xi, S. Gao, and L. Shi, 2003 *Characterization of laser direct deposited metallic parts.* Journal of Materials Processing Technology. **142**(2): p. 582-585.
131. Kurz, W., 2001 *Solidification microstructure-processing maps: Theory and application.* Advanced Engineering Materials. **3**(Copyright 2001, IEE): p. 443-4.
132. Bontha, S., N.W. Klingbeil, P.A. Kobryn, and H.L. Fraser, 2009 *Effects of process variables and size-scale on solidification microstructure in beam-based fabrication of bulky 3D structures.* Materials Science and Engineering: A. **513-514**: p. 311-318.
133. Fisher, D.J. and W. Kurz, 1980 *A theory of branching limited growth of irregular eutectics.* Acta Metallurgica. **28**(6): p. 777-794.
134. Kurz, W. and D.J. Fisher, 1981 *Dendrite growth at the limit of stability: tip radius and spacing.* Acta Metallurgica. **29**(1): p. 11-20.
135. Kurz, W. and R. Trivedi, 1994 *Rapid solidification processing and microstructure formation.* Materials Science & Engineering A: Structural Materials: Properties, Microstructure and Processing. **179-80(pt 1), 46-51**.
136. Gäumann, M., C. Bezençon, P. Canalis, and W. Kurz, 2001 *Single-crystal laser deposition of superalloys: processing-microstructure maps.* Acta Materialia. **49**(6): p. 1051-1062.
137. Khedkar, P. and P. Nash, 1986 *RELATIONSHIP OF DAS TO COOLING RATE IN SOLIDIFIED U-700 ALLOY.* Journal of Materials Science Letters. **5**(12): p. 1273-1274.
138. William, H., G. Michelle, E. Mark, and S. John, 2001 *Solidification in direct metal deposition by LENS processing.* JOM. **53**(9): p. 30.
139. Hofmeister, W., M. Wert, J. Smugeresky, J.A. Philliber, M. Griffith, and M. Ensz, 1999 *Investigating solidification with the laser engineered net shaping (LENS) process.* JOM. **51(7).**
140. Zheng, B., Y. Zhou, J.E. Smugeresky, J.M. Schoenung, and E.J. Lavernia, 2008 *Thermal behavior and microstructure evolution during laser deposition with laser-engineered net shaping: Part II. Experimental investigation and discussion.* Metallurgical and Materials Transactions A: Physical Metallurgy and Materials Science. **39**(9): p. 2237-2245.
141. Guo, W. and A. kar, 1998 *Interfacial instability and microstructural growth due to rapid solidification in laser processing.* Acta Materialia. **46**(10): p. 3485.
142. Guo, W. and A. Kar.1999 *Microstructural analysis and performance evaluation in laser cladding of stainless steel on the surface of plain carbon steel*. in *Proceedings of Elevated Temperature Coatings: Science and Technology III.TMS Annual Meeting*. San Diego, CA, USA.

143. Pinkerton, A.J., M. Karadge, W.U.H. Syed, and L. Lin, 2006 *Thermal and microstructural aspects of the laser direct metal deposition of waspaloy.* Journal of Laser Applications. **18**(3): p. 216-26.
144. Grujicic, M., G. Cao, and R.S. Figliola, 2001 *Computer simulations of the evolution of solidification microstructure in the LENS(TM) rapid fabrication process.* Applied Surface Science. **183**(1-2): p. 43-57.
145. Yin, H. and S.D. Felicelli, 2010 *Dendrite growth simulation during solidification in the LENS process.* Acta Materialia. **58**(4): p. 1455-1465.
146. Jendrzejewski, R. and G. Sliwinski, 2007 *Investigation of temperature and stress fields in laser cladded coatings.* Applied Surface Science. **254**(4): p. 921-925.
147. Jendrzejewski, R., G. Sliwinski, M. Krawczuk, and W. Ostachowicz, 2006 *Temperature and stress during laser cladding of double-layer coatings.* Surface and Coatings Technology. **201**(6): p. 3328-3334.
148. Bendeich, P., N. Alam, M. Brandt, D. Carr, K. Short, R. Blevins, C. Curfs, O. Kirstein, G. Atkinson, T. Holden, and R. Rogge, 2006 *Residual stress measurements in laser clad repaired low pressure turbine blades for the power industry.* Materials Science and Engineering: A. **437**(1): p. 70-74.
149. Nickel, A.H., D.M. Barnett, and F.B. Prinz, 2001 *Thermal stresses and deposition patterns in layered manufacturing.* Materials Science and Engineering A. **317**(1-2): p. 59-64.
150. Foroozmehr, E. and R. Kovacevic, 2010 *Effect of path planning on the laser powder deposition process: thermal and structural evaluation.* The International Journal of Advanced Manufacturing Technology. **51**(5): p. 659-669.
151. Dai, K. and L. Shaw, 2001 *Thermal and stress modeling of multi-material laser processing.* Acta Materialia. **49**(20): p. 4171-4181.
152. Dai, K. and L. Shaw, 2002 *Distortion minimization of laser-processed components through control of laser scanning patterns.* Rapid Prototyping Journal. **8**(5): p. 270-276.
153. Beuth, J. and N. Klingbeil, 2001 *The role of process variables in laser-based direct metal solid freeform fabrication.* JOM. **53**(9): p. 36-39.
154. Grum, J. and M. Znidarsic, 2004 *Microstructure, microhardness, and residual stress analysis of laser surface cladding of low-carbon steel.* Materials and Manufacturing Processes. **19**(Copyright 2004, IEE): p. 243-58.
155. Picasso, M., C.F. Marsden, J.-D. Wagniere, A. Frenk, and M. Rappaz, 1994 *A Simple but Realistic Model for Laser Cladding.* Metall. Mater. Trans. B. **25B**(2): p. 281-291.
156. Chen, W., X. Zhang, J. Bao, Y. Wang, T. Li, P. Jiang, and H. Zhang.1998 *Sensing and control system of process quality in CO[sub 2] laser deep-penetration welding*. in *Laser Processing of Materials and Industrial Applications II*. Beijing, China: SPIE.

157. Rangaswamy, P., T. Holden, R. Rogge, and M. Griffith, 2003 *Residual stresses in components formed by the laserengineered net shaping (LENSrG) process.* The Journal of Strain Analysis for Engineering Design. **38**(6): p. 519-527.
158. Rangaswamy, P., M.L. Griffith, M.B. Prime, T.M. Holden, R.B. Rogge, J.M. Edwards, and R.J. Sebring, 2005 *Residual stresses in LENS® components using neutron diffraction and contour method.* Materials Science and Engineering: A. **399**(1-2): p. 72-83.
159. R.J.Moat, A.J.Pinkerton, D.J.Hughes, L.Li, P.J.Withers, and M.Preuss.2007 *Stress distribution in multilayer laser deposited waspaloy parts measured using neutron diffraction*. in *26th International Congress on Applications of Lasers & Electro-Optics (ICALEO)*. Orlando, FL USA.
160. Pratt, P., 2008 *Residual stress measurement of laser-engineered net shaping AISI 410 thin plates using neutron diffraction.* Metallurgical and Materials Transactions; A; Physical Metallurgy and Materials Science. **39**(13): p. 3155-63.
161. Li, Y.Y., H. Yang, X. Lin, W. Huang, J. Li, and Y. Zhou, 2002 *Laser direct forming of metal components: Technical characterizations.* Proceedings of SPIE--the international society for optical engineering. **4915**: p. 395.
162. Kumar, A.V. and A. Dutta, 2004 *Electrophotographic Layered Manufacturing.* Journal of Manufacturing Science and Engineering. **126**(3): p. 571.
163. Kim, J.-D. and Y. Peng, 2000 *Melt pool shape and dilution of laser cladding with wire feeding.* Journal of Materials Processing Technology. **104**(3): p. 284-293.
164. Smugeresky, J.E., D.M.M.O. Keicher, J.A. Romero, M.L. Griffith, and L.D. Harwell.1997 *Laser Engineered Net Shaping (LENS) process: optimization of surface finish and microstructural properties*. in *Proceedings of the 1997 International Conference on Powder Metallurgy and Pariculate Materials*. Chicago, IL, USA.
165. Utsumi, A., T. Hino, J. Martsuda, T. Tasoda, M. Yoneda, M. Katsumura, T. Yano, and T. Araki.2003 *Effect of laser power on clad metal in laser-TIG combined metal cladding*. in *First International Symposium on High-Power Laser Macroprocessing*.
166. Kurz, W. and D.J. Fischer, 1990*Fundamentals of solidification*. Zurich, Switzerland: Trans Tech Publications Limited.
167. Pryds, N.H. and X. Huang, 2000 *The Effect of Cooling Rate on the Microstructures Formed during Solidification of Ferritic Steel.* Metallurgical and Materials Transactions A. **31**(12): p. 3155-3166.
168. Gorman, P., J.E. Smugeresky, and D.M. Keicher.2002 *Evaluation of property dependence on build rate for LENS powder metal deposition*. in *Proceedings of the Symposium on Rapid Prototyping of Materials at the TMS Fall Meeting*. Columbus, OH, USA.

169. Griffith, M.L., M.T. Ensz, J.D. Puskar, C.V. Robino, J.A. Brooks, J.A. Philliber, J.E. Smugeresky, and W.H. Hofmeister.2000 *Understanding the microstructure and properties of components fabricated by Laser Engineered Net Shaping (LENS).* San Francisco, CA: Materials Research Society.
170. Pelletier, J.M., M.C. Sahour, M. Pilloz, and A.B. Vannes, 1993 *Influence of processing conditions on geometrical features of laser claddings obtained by powder injection.* Journal of materials science. **28**(19): p. 5184 - 5188.
171. Lin, F. and W. Sun, 2001 *Warping Analysis in Laminated Object Manufacturing Process*

Journal of Manufacturing Science and Engineering,. **123** (4): p. 739-753.
172. Choi, J., S.K. Choudhuri, and J. Mazumder, 2000 *Role of preheating and specific energy input on the evolution of microstructure and wear properties of laser clad Fe-Cr-C-W alloys.* Journal of Materials Science. **35**(13): p. 3213-19.
173. Gugliotti, M., M.S. Baptista, and M.J. Politi, 2002 *Laser-induced Marangoni convection in the presence of surfactant monolayers.* Langmuir;. **18**(25): p. 9792 - 9798.
174. Limmaneevichitr, C. and S. Kou, 2000 *Visualization of Marangoni convection in simulated weld pools containing a surface-active agent.* Welding Journal. **79**(11): p. 324S-330S.
175. Palmer, S.J., 1976 *The effect of temperature on surface tension.* Physics Education. **11**(2): p. 119-20.
176. Voelkel, D.D. and J. Mazumder, 1990 *Visulalization of Laser Melt Pool* Applied Optics. **29**(12): p. 1718-1720.
177. Anthony, T.R. and H.E. Cline, 1977 *Surface Rippling Induced by Surface Tension Gradient during Laser surface Melting and Alloying.* Journal of Applied Physics. **48**(9): p. 3888-3894.
178. Kumar, A. and S. Roy, 2009 *Effect of three-dimensional melt pool convection on process characteristics during laser cladding.* Computational Materials Science. **46**(2): p. 495-506.
179. Limmaneevichitr, C. and S. Kou, 2000 *Experiments to simulate effect of Marangoni convection on weld pool shape.* Welding Journal (Miami, Fla). **79**(8): p. 231s-237s.
180. Chan, C.L., 1988 *Effect of surface tension gradient driven convection in a laser melt pool: Three-dimensional perturbation model.* Journal of applied physics. **64**(11): p. 6166-74.
181. Lei, Y.P., H. Murakawa, Y.W. Shi, and X.Y. Li, 2001 *Numerical analysis of the competitive influence of Marangoni flow and evaporation on heat surface temperature and molten pool shape in laser surface remelting.* Computational Materials Science. **21**(3): p. 276-290.
182. Tsotridis, G., H. Rother, and E.D. Hondros, 1989 *Marangoni flow and the shapes of laser-melted pools.* Die Naturwissenschaften. **76**(5): p. 216 -218.

183. Brooks, R. and P. Quested, 2005 *The surface tension of steels.* Journal of Materials Science. **40**(9): p. 2233-2238.
184. Kreutz, E.-W. and N. Pirch.1990 *Melt dynamics in surface processing with laser radiation: calculations and applications*. in *CO2 Lasers and Applications II*. The Hague, Netherlands: SPIE.
185. Anthony, T.R. and H.E. Cline, 1977 *Surface rippling induced by surface-tension gradients during laser surface melting and alloying.* Journal of applied physics. **48**(9): p. 3888-94.
186. Meriaudeau, F., F. Truchetete, C. Dumont, E. Renier, and P. Bolland.1996 *Acquisition and image processing system able to optimize laser cladding process*. Beijing, China: IEEE.
187. Yu, Y.P., C.W. Chen, and K. Mukherjee, 2000 *Measurement of temperature distributions during laser cladding process.* Journal of Laser Applications. **12**(3): p. 126-30.
188. Justin, K. and M. Jyoti. 1998*Apparatus and methods for monitoring and controlling multi-layer laser cladding*, 6122564: US. Patent
189. Dilthey, U., D. Fuest, and W. Scheller, 1995 *Laser welding with filler wire.* Optical and Quantum Electronics. **27**(12): p. 1181-1191.
190. Dèmure, O., P. Aubry, F. Chaventon, and L. Sabatier.2000 *Evaluation of Rapid Prototyping with Filler Wire and CO_2 or YAG Laser*. in *19th International Congress on Applications of Lasers and Electro-Optics ICALEO 2000*. LIA
191. Grant, K. and D.W. Winston. 1995*Fuzzy logic-controlled laser processing*, U. Patent, Editor: USA.
192. Betteridge, W., 1984*Nickle and its alloys*: Ellis Horwood Limited. 211.
193. Reed, R.C., 2006*The Superalloys Fundamentals and Applications*: Cambridge University Press.
194. Oradei-Basile, A. and J.F. Radavich.1998 *A Current T-T-T Diagram for Wrought Alloy 718*. in *Proceedings of TMS, Superalloys 718, 625 and Derivatives, 325.*
195. Pereira, J.M. and B.A. Lerch, 2001 *Effects of heat treatment on the ballistic impact properties of Inconel 718 for jet engine fan containment applications.* International Journal of Impact Engineering. **25**(8): p. 715-733.
196. Blackwell, P.L., 2005 *The mechanical and microstructural characteristics of laser-deposited IN718.* Journal of Materials Processing Technology. **170**(1-2): p. 240-246.
197. ASM International Properties and Selection:Irons, Steels and High Performance Alloys
1990 Committee, A.I.H.10th ed. Vol. 1.
198. Fukuhara, M. and A. Sanpei, 1993 *Elastic moduli and internal frictions of Inconel 718 and Ti-6Al-4V as a function of temperature.* Journal of Materials Science Letters. **12**(14): p. 1122-1124.

199. Leyens, C. and M. Peters, 2003*Titanium and Titanium Alloys Fundamentals and Applications*: WILEY-VCH Verlag GmbH & Co. KGaA, Weinheim.
200. Matthew J. Donachie, J., 2000*Titanium: A Technical Guide*: ASM International.
201. Richter, K., W. Behr, and U. Reisgen, 2007 *Low heat welding of titanium materials with a pulsed Nd:YAG laser.* Materialwissenschaft und Werkstofftechnik. **38**(1): p. 51-56.
202. Bergmann, J.P., 2005 *Mechanical behaviour of overlap joints of titanium.* Science and Technology of Welding and Joining. **10**(1): p. 50-60.
203. *Metallurgy of Titanium and its Alloys* Bhadeshia, H.K.D.H. [cited 2010 20 December]. Available from: http://www.msm.cam.ac.uk/phase-trans/2004/titanium/titanium.html.
204. Budinski, K.G., 1991 *Tribological properties of titanium alloys.* Wear. **151**(2): p. 203-217.
205. Molinari, A., G. Straffelini, B. Tesi, and T. Bacci, 1997 *Dry sliding wear mechanisms of the Ti6Al4V alloy.* Wear. **208**(1-2): p. 105-112.
206. Sun, R.L., D.Z. Yang, L.X. Guo, and S.L. Dong, 2001 *Laser cladding of Ti-6Al-4V alloy with TiC and TiC+NiCrBSi powders.* Surface and Coatings Technology. **135**(2-3): p. 307-12.
207. Meng, Q.W., L. Geng, and B.Y. Zhang, 2006 *Laser cladding of Ni-base composite coatings onto Ti-6Al-4V substrates with pre-placed B4C + NiCrBSi powders.* Surface and Coatings Technology. **200**(16-17): p. 4923-4928.
208. William D. Callister, J., 2000*Materials science and engineering: an introduction*. 5th ed: John Wiley & Sons.
209. Hackerman, N. and D.I. Marshall, 1948 *Passivity of chromium.* Journal of the Electrochemical Society. **93**: p. 49-54.
210. MCGUIRE, M., 2008*Stainless steels for design engineers*: ASM International.
211. SSINA. 1998*Design Guidelines for Selection and Use of Stainless Steel*.
212. Keicher, D. and J. Smugeresky, 1997 *The laser forming of metallic components using particulate materials.* JOM Journal of the Minerals, Metals and Materials Society. **49**(5): p. 51-54.
213. Peckner, D. and I.M. Bernstein, 1977 *Handbook of Stainless Steels*: Mcgraw-Hill.
214. Andrew, J.P., S. Waheed Ul Haq, and L. Lin, 2006 *An experimental and theoretical investigation of combined gas- and water-atomized powder deposition with a diode laser.* Journal of Laser Applications. **18**(1): p. 73-80.
215. *Diode Lasers Applications Overview* [cited 2010 07 December]. Available from: http://www.laserline-inc.com/index.php.
216. Technologies, F.S. 1999*FST PF-X/X Powder Feeder Operating Manual*.

217. Smallman, R.E. and A.H.W. Ngan, 2007*Physical Metallurgy and Advanced Materials*. Seventh ed: Elsevier Ltd.
218. Hand book of hard coatings:Deposition technologies, properties and applications.2001 Bunshah, R.F. Vol. Noyes Publications / William Andrew Publishing, LLC
219. *Fastcam APX RS* [cited 2011 15 January]. Available from: http://www.photron.com/index.php?cmd=product_general&product_id=11.
220. *Copper Vapour Laser (CVL)* [cited 2011 15 January]. Available from: http://www.oxfordlasers.com/imaging/laser/cvl.
221. Koizumi, M., 1997 *FGM activities in Japan.* Composites Part B:Engineering. **28**(1-2): p. 1-4.
222. Liu, W. and J.N. DuPont, 2003 *Fabrication of functionally graded TiC/Ti composites by Laser Engineered Net Shaping.* Scripta Materialia. **48**(9): p. 1337.
223. Pei, Y.T. and J.T.M. De Hosson, 2000 *Functionally graded materials produced by laser cladding.* Acta Materialia. **48**(10): p. 2617.
224. Yarrapareddy, E., S. Zekovic, S. Hamid, and R. Kovacevic, 2006 *The development of nickel-tungsten carbide functionally graded materials by a laser-based direct metal deposition process for industrial slurry erosion applications.* Proceedings of the Institution of Mechanical Engineers, Part B (Journal of Engineering Manufacture). **220**(B12): p. 1923-36.
225. Klingbeil, N.W., J.L. Beuth, R.K. Chin, and C.H. Amon, 2002 *Residual stress-induced warping in direct metal solid freeform fabrication.* International Journal of Mechanical Sciences. **44**(Compendex): p. 57-77.
226. Domack, M.S. and J.M. Baughman, 2005 *Development of nickel-titanium graded composition components.* Rapid Prototyping Journal. **11**(1): p. 41-51.
227. Lin, X., T.M. Yue, H.O. Yang, and W.D. Huang, 2007 *Solidification Behavior and the Evolution of Phase in Laser Rapid Forming of Graded Ti6Al4V-Rene88DT Alloy.* Metallurgical and Materials Transactions A. **38**(1): p. 127-137.
228. Seretsky, J. and E.R. Ryba, 1976 *Laser welding of dissimilar metals: Titanium to Nickel.* Welding Journal (Miami, Fla). **55**(7): p. 208-211.
229. Chatterjee, S., T.A. Abinandanan, and K. Chattopadhyay, 2006 *Microstructure development during dissimilar welding: Case of laser welding of Ti with Ni involving intermetallic phase formation.* Journal of Materials Science. **V41**(3): p. 643.
230. Chatterjee, S., T.A. Abinandanan, and K. Chattopadhyay, 2008 *Phase formation in Ti/Ni dissimilar welds.* Materials Science and Engineering: A. **490**(1-2): p. 7-15.

231. Rahman, M., W.K.H. Seah, and T.T. Teo, 1997 *The machinability of inconel 718.* Journal of Materials Processing Technology. **63**(1-3): p. 199-204.
232. Cole, C.E., S.C. Noden, J.R. Tyrer, and P.A. Hilton.1998 *The application of diffractive optical elements in high power laser material processing*. Orlando, FL, USA: Laser Institute of America.
233. Ignatiev, M., I. Smurov, and G. Flamant, 1994 *Real-time optical pyrometer in laser machining.* Measurement Science and Technology. **5**(5): p. 563.
234. Donachie, M.J. and S.J. Donachie, 2002*Superalloys: A Technical Guide*: ASM International.
235. Xinhua, W., L. Jing, J. Mei, C. Mitchell, P.S. Goodwin, and W. Voice, 2004 *Microstructures of laser-deposited Ti-6A1-4V.* Materials & Design. **25**(2): p. 137-44.
236. Kelly, S.M. and S.L. Kamper, 2004 *Microstructural evolution in laser-deposited multilayer Ti-6Al-4V builds: Part 1. Microstructural characterization.* Metallurgical and Materials Transactions A: Physical Metallurgy and Materials Science. **35 A**(6): p. 1861-1867.
237. Hofmeister, W., M. Griffith, M. Ensz, and J. Smugeresky, 2001 *Solidification in direct metal deposition by LENS processing.* JOM. **53**(9): p. 30.
238. Zhao, H., D.R. White, and T. Debroy, 1999 *Current issues and problems in laser welding of automotive aluminum alloys.* International Materials Reviews. **44**(6): p. 238-266.
239. Moat R, Pinkerton A, Hughes D, Li L, Preuss M, and W.P. J.29 October 2007 *Stress Distributions in Multilayer Laser Deposited Waspaloy Parts Measured using Neutron Diffraction*. in *26th International Congress on Applications of Lasers and Electro-optics (ICALEO)*. USA.
240. Weerasinghe, V.M. and W.M. Steen.1983 *Computer Simulation Model For Laser Cladding*. Boston, Mass, USA: ASME.
241. Kar, A. and J. Mazumder, 1987 *One-dimensional diffusion model for extended solid solution in laser cladding.* Journal of Applied Physics. **61**(Copyright 1987, IEE): p. 2645-55.
242. Picasso, M. and M. Rappaz, 1994 *Laser-powder-material interactions in the laser cladding process.* Journal De Physique. **4**(Compendex): p. 27-33.
243. Toyserkani, E., 2003 *Three-dimensional finite element modeling of laser cladding by powder injection: effects of powder feedrate and travel speed on the process.* Journal of Laser Applications. **15**(3): p. 153-60.
244. Toyserkani, E., A. Khajepour, and S. Corbin, 2004 *3-D finite element modeling of laser cladding by powder injection: effects of laser pulse shaping on the process.* Optics and Lasers in Engineering. **41**(6): p. 849.
245. Qi, H. and J. Mazumder, 2006 *Numerical simulation of heat transfer and fluid flow in coaxial laser cladding process for direct metal deposition.* Journal of Applied Physics. **100**(2).

246. Bontha, S., N.W. Klingbeil, P.A. Kobryn, and H.L. Fraser, 2006 *Thermal process maps for predicting solidification microstructure in laser fabrication of thin-wall structures.* Journal of Materials Processing Technology. **178**(Copyright 2006, The Institution of Engineering and Technology): p. 135-42.
247. Kelly, S.M. and S.L. Kampe, 2004 *Microstructural evolution in laser-deposited multilayer Ti-6Al-4V builds: Part II. Thermal Modeling.* Metallurgical and Materials Transactions A: Physical Metallurgy and Materials Science. **35 A**(Compendex): p. 1869-1879.
248. Liang, W. and S. Felicelli, 2007 *Process modeling in laser deposition of multilayer SS410 steel.* Transactions of the ASME. Journal of Manufacturing Science and Engineering. **129**(Copyright 2008, The Institution of Engineering and Technology): p. 1028-34.
249. P.J. Withers, 2006 *Residual Stress: Definition.* Encyclopedia of Materials: Science and Technology: p. 8110-8112.
250. Chin, R.K., J.L. Beuth, and C.H. Amon.1996 *Thermomechanical modeling of successive material deposition in layered manufacturing*. in *Proceedings of the 1996 Solid Freeform Fabrication Symposium*. Austin, Texas.
251. Klingbeil, N.W., J.L. Beuth, R.K. Chin, and C.H. Amon.1998 *Measurement and Modeling of Residual Stress-Induced Warping in Direct Metal Deposition Processes*. in *Proc. Solid Freeform Fabrication*.
252. Ghosh, S. and J. Choi.2003 *3-Dimensional transient residual stress finite element analysis for laser aided direct metal deposition process*. in *ICALEO 2003 - 22nd International Congress on Applications of Laser and Electro-Optics, October 13, 2003 - October 16, 2003*. Jacksonville, FL, United states: Laser Institute of America.
253. Ghosh, S. and J. Choi, 2005 *Three-dimensional transient finite element analysis for residual stresses in the laser aided direct metal/material deposition process.* Journal of Laser Applications. **17**(Compendex): p. 144-158.
254. Bruckner, F., D. Lepski, and E. Beyer, 2007 *Modeling the influence of process parameters and additional heat sources on residual stresses in laser cladding.* Journal of Thermal Spray Technology. **16**(Copyright 2009, The Institution of Engineering and Technology): p. 355-73.
255. Loucas, P., H. Tobias, and F.Z. Michael, 2007 *Interaction between laser beam, process effects, and structural properties during welding using models based on the finite element analysis.* Journal of Laser Applications. **19**(3): p. 189-196.
256. Plati, A., J.C. Tan, I.O. Golosnoy, R. Persoons, K. van Acker, and T.W. Clyne, 2006 *Residual Stress Generation during Laser Cladding of Steel with a Particulate Metal Matrix Composite.* Advanced Engineering Materials. **8**(7): p. 619-624.
257. A.M. de Deus. 2004*A Thermal and Mechanical Model of Laser Cladding* in *Mechanical Engineering*, PhD Thesis,University of Illinois.

258. Labudovic, M., D. Hu, and R. Kovacevic, 2003 *A three dimensional model for direct laser metal powder deposition and rapid prototyping.* Journal of Materials Science. **38**(1): p. 35.
259. Kumar, S. and S. Roy, 2004 *A parametric study of a blown powder laser cladding and alloying process using a two-dimensional conduction model.* Proceedings of the Institution of Mechanical Engineers, Part C: Journal of Mechanical Engineering Science. **218**(7): p. 703-709.
260. Rao, S.S., 2004*The Finite Element Method in Engineering (Fourth Edition)* Elsevier Inc.
261. Pinkerton, A.J. and L. Li, 2004 *An analytical model of energy distribution in laser direct metal deposition.* Proceedings of the Institution of Mechanical Engineers, Part B (Journal of Engineering Manufacture). **218**(B4): p. 363-74.
262. ANSYS. 2007*ANSYS Theory Reference*.
263. Pinkerton, A.J. and L. Li, 2003 *An investigation of the effect of pulse frequency in laser multiple-layer cladding of stainless steel.* Applied Surface Science. **208-209**: p. 405-410.
264. Hu, Y., C. Chen, and K. Mukherjee, 1998 *Innovative laser-aided manufacturing of patterned stamping and cutting dies: Processing parameters.* Materials and Manufacturing Processes. **13**(3): p. 369-387.
265. Milewski, J.O., G.K. Lewis, J. Fonseca, and R.B. Nemec, 2000 *Laser powder deposition of a near net shape injection mold core - a case study.* Materials and Manufacturing Processes. **15**(2): p. 247-258.
266. Kizaki, Y., H. Azuma, S. Yamazaki, H. Sugimoto, and S. Takagi, 1993 *Phenomenological studies in laser cladding. Part I. Time-resolved measurements of the absorptivity of metal powder.* Japanese Journal of Applied Physics, Part 1: Regular Papers and Short Notes and Review Papers. **32**(1 A): p. 205-212.
267. Hua, Y. and J. Choi.2003 *Feedback control effects on dimensions and defects of H13 tool steel by DMD process*. Jacksonville, FL, United states: Laser Institute of America.
268. Jichang, L. and L. Lijun, 2004 *In-time motion adjustment in laser cladding manufacturing process for improving dimensional accuracy and surface finish of the formed part.* Optics and Laser Technology. **36**(6): p. 477-83.
269. Pinkerton, A.J., 2006 *Thermal and microstructural aspects of the laser direct metal deposition of waspaloy.* Journal of Laser Applications. **18**(3): p. 216-26.
270. Schwendner, K.I., R. Banerjee, P.C. Collins, C.A. Brice, and H.L. Fraser, 2001 *Direct laser deposition of alloys from elemental powder blends.* Scripta Materialia. **45**(10): p. 1123-1129.
271. Han, L., 2005 *Thermal behavior and geometry model of melt pool in laser material process.* Journal of heat transfer. **127**(9): p. 1005-14.

272. Pinkerton, A.J. and L. Li, 2003 *The effect of laser pulse width on multiple-layer 316L steel clad microstructure and surface finish.* Applied Surface Science. **208-209**(SUPPL): p. 411.
273. Pinkerton, A.J. and L. Li, 2003 *An investigation of the effect of pulse frequency in laser multiple-layer cladding of stainless steel.* Applied Surface Science. **208-209**: p. 405-10.
274. Sun, S., Y. Durandet, and M. Brandt.2004 *Correlation between melt pool temperature and clad formation in pulsed and continuous wave Nd:Yag laser cladding of stellite 6*. in *PICALO 2004 - 1st Pacific International Conference on Applications of Laser and Optics*. Melbourne, VIC, Australia: Laser Institute of America.
275. Sun, S. and M. Brandt.2004 *Comparison between continuous wave and pulsed Nd:YAG laser cladding of stellite 6*. San Francisco, CA, United states: Laser Institute of America.
276. Canny, J., 1986 *A computational approach to edge detection.* IEEE Transactions on Pattern Analysis and Machine Intelligence. **PAMI-8**(6): p. 679-98.
277. P.V.C., H. 1962*Method and means for recognising complex patterns, Technical report*, U.S.P.O. 3069654, Editor: USA.
278. Kaplan, A.F.H., B. Weinberger, and D. Schuocker.1997 *Theoretical analysis of laser cladding and alloying*. USA: SPIE-Int. Soc. Opt. Eng.
279. DuPont, J.N. and A.R. Marder, 1996 *Dilution in single pass arc welds.* Metallurgical and Materials Transactions B: Process Metallurgy and Materials Processing Science. **27**(3): p. 481-489.
280. Drezet, J.-M., S. Pellerin, C. Bezencon, and S. Mokadem, 2004 *Modelling the Marangoni convection in laser heat treatment.* Journal de physique.IV (Proceedings). **120**: p. 299-306.
281. Sun, G., G. Li, S. Hou, S. Zhou, W. Li, and Q. Li, 2010 *Crashworthiness design for functionally graded foam-filled thin-walled structures.* Materials Science and Engineering A. **527**(7-8): p. 1911-1919.
282. Bandyopadhyay, A., B. Krishna, W. Xue, and S. Bose, 2009 *Application of Laser Engineered Net Shaping (LENS) to manufacture porous and functionally graded structures for load bearing implants.* Journal of Materials Science: Materials in Medicine. **20**(0): p. 29-34.
283. Kacar, R. and O. Baylan, 2004 *An investigation of microstructure/property relationships in dissimilar welds between martensitic and austenitic stainless steels.* Materials & Design. **25**(4): p. 317-29.
284. Meola, C., A. Squillace, F.M.C. Minutolo, and R.E. Morace, 2004 *Analysis of stainless steel welded joints: a comparison between destructive and non-destructive techniques.* Journal of Materials Processing Technology. **155-156**: p. 1893-9.

285. Zhao, S., X. Xie, and G.D. Smith, 2004 *The oxidation behavior of the new nickel-based superalloy Inconel 740 with and without Na2SO4 deposit.* Surface and Coatings Technology. **185**(2-3): p. 178-183.
286. Jian, L., C.Y. Yuh, and M. Farooque, 2000 *Oxidation behavior of superalloys in oxidizing and reducing environments.* Corrosion Science. **42**(9): p. 1573-1585.
287. Robinson, J.L. and M.H. Scott, 1980 *Liquation cracking during the welding of austenitic stainless steels and nickel alloys.* Philosophical Transactions of the Royal Society of London A (Mathematical and Physical Sciences). **295**(1413): p. 105-17.
288. Leushake, U., A.N. Winter, B.H. Rabin, and B.A. Corff, 1999 *General aspects of FGM fabrication by powder stacking.* Materials Science Forum. **308-311**: p. 13-18.
289. Watanabe, R., A. Kawasaki, M. Tanaka, and J.-F. Li, 1993 *Fabrication of SiC-AlN/Mo functionally gradient material for high temperature use.* International Journal of Refractory Metals and Hard Materials. **12**(4): p. 187-193.
290. Gooch, W.W.A., 1999 *Development and ballistic testing of a functionally gradient ceramic/metal applique.* Materials science forum. **308**: p. 614-621.
291. Y.Miaymoto, W.A.Kaysser, B.H.Rabin, A.Kawasaki, and R. G.Ford, 1999*Functinally graded materials:design, processing, and applications*: Kluwer Academic Publishers. 330.
292. Marple, B.R. and J. Boulanger, 1994 *Graded Casting of Materials with Continuous Gradients.* Journal of the American Ceramic Society. **77**(10): p. 2747-2750.
293. Thummler, F. and R. Oberacker, 1993*An introduction to powder metallurgy*. Institute of Materials series on powder metallurgy: Institute of Materials,London. 177-180.
294. Watkins, K.G. and E. Fearon.2003 *A method of layer height control in direct laser fabrication of 304L stainless steel*. Jacksonville, FL, United states: Laser Institute of America.
295. Valsecchi, B., B. Previtali, M. Vedani, and G. Vimercati, *Fiber laser cladding with high content of WC-Co based powder.* International Journal of Material Forming. **3**(SUPPL. 1): p. 1127-1130.
296. Jasim, K.M., R.D. Rawlings, and D.R.F. West, 1993 *Metal-ceramic functionally gradient material produced by laser processing.* Journal of Materials Science. **28**(10): p. 2820-2826.
297. Thivillon, L., P. Bertrand, B. Laget, and I. Smurov, 2009 *Potential of direct metal deposition technology for manufacturing thick functionally graded coatings and parts for reactors components.* Journal of Nuclear Materials. **385**(2): p. 236-241.
298. Ouyang, J.H., H. Mei, and R. Kovacevic.2002 *Rapid prototyping and characterization of a WC-(NiSiB alloy) cermet/tool steel functionally graded*

material (FGM) synthesized by laser cladding. Warrendale, PA, USA: TMS - Miner. Metals & Mater. Soc.

299. Lin, X., T.M. Yue, H.O. Yang, and W.D. Huang, 2005 *Laser rapid forming of SS316L/Rene88DT graded material.* Materials Science and Engineering A. **391**(1-2): p. 325.
300. Quan, Y.J., Z.H. Chen, X.S. Gong, and Z.H. Yu, 2008 *Effects of heat input on microstructure and tensile properties of laser welded magnesium alloy AZ31.* Materials Characterization. **59**(10): p. 1491-1497.
301. Campbell, J., 2003*Castings (Second Edition)*: Butterworth-Heinemann.
302. Wu, X., J. Liang, J. Mei, C. Mitchell, P.S. Goodwin, and W. Voice, 2004 *Microstructures of laser-deposited Ti-6Al-4V.* Materials & Design. **25**(2): p. 137-144.
303. Fujita, N., K. Ohmura, and A. Yamamoto, 2003 *Changes of microstructures and high temperature properties during high temperature service of Niobium added ferritic stainless steels.* Materials Science and Engineering A. **351**(1-2): p. 272-281.
304. Aksoy, M., M.B. Karamis, and E. Evin, 1996 *An evaluation of the wear behaviour of a dual-phase low-carbon steel.* Wear. **193**(2): p. 248-252.
305. Wang, A. and H.J. Rack, 1991 *Transition wear behavior of SiC-particulate- and SiC-whisker-reinforced 7091 Al metal matrix composites.* Materials Science and Engineering: A. **147**(2): p. 211-224.
306. Yazawa, Y., Y. Ozaki, Y. Kato, and O. Furukimi, 2003 *Development of ferritic stainless steel sheets with excellent deep drawability by {1 1 1} recrystallization texture control.* JSAE Review. **24**(4): p. 483-488.

Appendix A: APDL used for the thermal modelling of Laser Direct Metal Deposition process

---

```
/SOLU
/NERR,0,,,,
LSCLEAR, ALL
ANTYPE,TRANS
TRNOPT,FULL
LUMPM,0
NROPT,FULL
RESCONTROL,NORESTART,ALL, LAST, 0
OUTPR, ALL,ALL
OUTRES, ALL,ALL
IC,ALL,TEMP,293
ASEL,S,LOC,Y,0,0
ASEL,A,LOC,Z,0,0
ASEL,A,LOC,x,0,0
ASEL,A,LOC,x,48e-3,48e-3
ASEL,A,LOC,z,-50e-3,-50e-3
ASEL,A,,,92
ASEL,A,,,62
ASEL,A,,,4
ASEL,A,,,56
ASEL,A,,,84
ASEL,A,,,75
ASEL,A,,,95
```

```
ASEL,A,,,82
SFA,ALL,1,CONV,20,293
ASEL,ALL
CMSEL,S,FULL CLAD,ELEM
EKILL,ALL
ALLSEL,ALL
multipro,'start',3
   *cset,1,3,st_ep,'Enter the Number of Time Step',
   *cset,4,6,tm_sp,'Enter the Time Step Size',
   *cset,7,9,po_er,'Enter the Laser Power',
multipro,'end'
CO_01=0
COUNT=0
*DO,i_1,1,st_ep,1
COUNT=COUNT+1
CMSEL,S,BEAM%COUNT%,ELEM
SFE,BEAM%COUNT%,4,HFLUX,,po_er
ESEL, ALL
CMSEL,S,CLAD%COUNT%,ELEM
EALIVE,ALL
ALLSEL,ALL
NEQIT,1000
NSUBST,1,1,1
AUTOTS,1
EQSLV,SPAR
LNSRCH,1
CO_01=CO_01+tm_sp
TIME,CO_01
SOLVE
```

```
SFEDELE,BEAM%COUNT%,4,HFLUX
*ENDDO
CO_01 = CO_01+6000
TIME,CO_01
NSUBST,5,10,1
OUTPR, ALL,ALL
OUTRES,ALL,LAST
AUTOTS,1
EQSLV,SPAR
LNSRCH,1
NEQIT,500
ALLSEL,ALL
SOLVE
FINISH
```

Appendix B: APDL used for the structural modeling of Laser Direct Metal Deposition process

---

```
/SOLU
/NERR,0,,,,
LSCLEAR, ALL
CMSEL,S,Full Clad
ekill,all
ALLSEL,ALL
ASEL,S,LOC,Y,11e-3,11e-3
NSLA,S,1
D,ALL, ,0, , , ,UX,UY,UZ, , ,
LSEL,S,,,10
LSEL,A,,,124
LSEL,A,,,149
LSEL,A,,,52
LSEL,A,,,157
LSEL,A,,,154
NSLL,S,1
D,ALL, ,0, , , ,UX,UY,UZ, , ,
ALLSEL,ALL
count=0
Co_01=0
*DO,i_1,1,22,1
Co_01=Co_01+0.4375
count=count+1
```

```
ANTYPE,TRANS
TRNOPT,FULL
LUMPM,0
AUTOTS,1
CNVTOL,F, , , 2, ,
CUTCONTROL,PLSLIMIT,1
LNSRCH,1
NEQIT,100
NSUBST,1,1,1
CMSEL,S,CLAD%count%
EALIVE,ALL
ESEL,S,LIVE
ALLSEL,ALL
ESEL,ALL
LDREAD,TEMP,,,Co_01, ,'CW','rth','..\Thermal Results\'
TIME,Co_01
SOLVE
*ENDDO
CO_01 = CO_01+6000
TIME,CO_01
ANTYPE,TRANS
TRNOPT,FULL
LDREAD,TEMP,,,Co_01, ,'CW','rth','..\Thermal Results\'
TIME,CO_01
LUMPM,0
AUTOTS,-1
CNVTOL,F, , , 2, ,
CUTCONTROL,PLSLIMIT,1
LNSRCH,1
```

```
NEQT,300
DELTIM,600, , ,1
SOLVE
FINISH
```

Appendix C: Image Analysis Code developed in MATLAB

```
function [DEV, MAX, LENGTH, Dmm] = ripple(imageFile)
THRESHOLD   = 5; % Range: 1 to 50
 DILATION    = 12; % Range: 2 to 20
TOLERANCE   = 30;% Range: 5 to 100 (connecting line-segments)
 imageFile='R1_v3.bmp';
 img0 = imread(imageFile);
 img1  = 255-rgb2gray(img0); %
figure(1);subplot(2,3,1);imshow(img1);
img2 = histeq(img1);
figure(1);subplot(2,3,2);imshow(img2);
img3 = 255*(img2>160); %
figure(1);subplot(2,3,3);imshow(img3);
img4 = 255*(img3>240); %
edg1 = edge(img4,'canny'); % edg2 = 255*(edg1>0);
se = strel('disk', DILATION );
edg3 = imdilate(edg2,se);
figure(1);subplot(2,3,4);imshow(edg3);
[Ht,T,R] = hough(edg3,'ThetaResolution', 1 );
MaxIntensity = max(max(Ht));
thresh = MaxIntensity-THRESHOLD;
Ht2 = 255*(Ht>thresh);
HP  = houghpeaks(Ht2);
th = T(HP(:,2)); ro = R(HP(:,1));
 % figure(2);imshow(Ht, [0 255] );
% figure(2);hold on;
```

```
% plot(HP(:,2),HP(:,1),'s','color','white');
% hold off;
lines = houghlines(edg3,T,R,HP,'FillGap',5,'MinLength',7);
LL = length(lines);
figure(1);subplot(2,3,5);imshow(edg2);hold on;
max_len = 0;
for k = 1:LL
xy = [lines(k).point1; lines(k).point2];
plot(xy(:,1),xy(:,2),'LineWidth',2,'Color','green');
len = norm(lines(k).point1 - lines(k).point2);
if ( len > max_len)
max_len = len;
xy_long = xy;
end
end
hold off;
dtr = bwdist(edg2);
figure(1);subplot(2,3,6);
imshow(dtr, [0 255] );
figure(3);imshow(img0, [0 255] );hold on;
szDTR = size(dtr);
DEV=0;
TL=0;
Xmax = -1;
Xmin = -1;
Ymax = -1;
Ymin = -1;
for k = 1:LL
x1 = lines(k).point1(1);
```

```
y1 = lines(k).point1(2);
x2 = lines(k).point2(1);
y2 = lines(k).point2(2);
dd = sqrt( (x2-x1)'*(y2-y1) );
if(dd>TOLERANCE)
if(Xmax<0),Xmax=x1;end
if(Ymax<0),Ymax=y1;end
if(Xmin<0),Xmin=x1;end
if(Ymin<0),Ymin=y1;end
if(Xmax<x1),Xmax=x1;end
if(Xmax<x2),Xmax=x2;end
if(Xmin>x1),Xmin=x1;end
if(Xmin>x2),Xmin=x2;end
 if(Ymax<y1),Ymax=y1;end
if(Ymax<y2),Ymax=y2;end
if(Ymin>y1),Ymin=y1;end
if(Ymin>y2),Ymin=y2;end
end
m  = (y2-y1)/(x2-x1);
X  = x1:x2;
Y  = round(m*(X-x1) + y1);
Nxy= length( X );
td = zeros(1,Nxy);
for i=1:Nxy
 x = X(i);
 y = Y(i);
if(x<szDTR(1) && y<szDTR(2) )
td(i) = dtr( Y(i), X(i) );
DEV = [ DEV td(i) ];
```

```
end
end
plot( X, Y,'g.');
plot( X, Y-td-10, 'r');
end
PT1 = [ xy_long(1,1); xy_long(1,2)];
PT2 = [ xy_long(2,1); xy_long(2,2)];
plot( [PT1(1) PT2(1)], [PT1(2) PT2(2)], 'b*');
plot( [Xmin Xmax], [Ymin Ymax], 'r*');
hold off;
DEV     = sum(DEV)/length(DEV);
MAX     = sqrt( (PT1(2)-PT2(2))*(PT1(1)-PT2(1)) );
LENGTH  = sqrt( (Ymax-Ymin)*(Xmax-Xmin) );
Dmm = (2.4/220)*DEV;
end
```